COLLEGE SCIENCES
DOCTORAL DE LA MER
BRETAGNE ET DU LITTORAL

UBO
Université de Bretagne Occidentale

HABILITATION A DIRIGER DES RECHERCHES

L'UNIVERSITE
DE BRETAGNE OCCIDENTALE

ECOLE DOCTORALE N° 598

Par

Stéphan Ker

Imagerie et caractérisation sismique multirésolution du sous-sol marin : contribution à l'étude haute résolution des systèmes gaz/hydrates de gaz

Présentée à Brest le 8 avril 2024

Composition du jury

Président :	**Pascal Tarits**	Professeur, Geo-Ocean, IUEM, UBO
Rapporteurs :	**Stéphane Garambois**	Professeur, ISTerre, Université Grenoble Alpes
	Mark Noble	Maître de Recherche, Centre de Géosciences, Mines Paris Tech
	Alessandra Ribodetti	Chargée de Recherche, HDR, IRD, Géoazur, Université Côte d'Azur
Examinatrices :	**Sara Bazin**	Physicienne, HDR, Geo-Ocean, IUEM, UBO
	Donatienne Leparoux	Directrice de Recherche, Université Gustave Eiffel

Table des matières

Résumé 5

1 Curriculum vitae 7

1.1 Formation 7

1.2 Expériences professionnelles 7

1.3 Principaux projets de recherche et d'expertise réalisés à l'Ifremer 7

1.4 Encadrements d'étudiants et de chercheur post-doctorat 9

1.4.1 Encadrement de Masters 9

1.4.2 Encadrement de thèses 9

1.4.3 Encadrement de postdoc 10

1.5 Autres activités de recherche 10

2 Liste de publications 13

2.1 Publications de rang A 13

2.2 Conférences, ouvrages, rapports techniques et jeux de données 15

3 Travaux de recherche 17

Introduction 17

3.1 Analyse sismique multi-échelle par réponse en ondelettes 20

3.1.1 Le concept de réponse en ondelettes et son application en sismique réflexion 20

3.1.2 Optimisation de la correction de source pour la fusion des données multifréquences SYSIF et reconstruction du profil d'impédance 22

3.1.3 Extension de la réponse en ondelettes en présence d'atténuation 24

3.1.4 Application à l'analyse de la réflectivité de la thermocline saisonnière 30

3.1.5 Bilan sur l'analyse sismique multi-échelle 35

3.2 Développement de la sismique près du fond multidéport 36

3.2.1 Sismique très haute résolution près du fond avec l'engin remorqué SYSIF 36

3.2.2 Développements instrumentaux et méthodologiques associés à l'acquisition multidéport près du fond SYSIF 38

3.2.3 Détermination précise de la variabilité de la forme de l'antenne de réception et *datuming* des données SYSIF 42

3.2.4 Bilan sur la sismique très haute résolution près du fond 47

3.3 Caractérisation sismique et son intégration dans une approche multidisciplinaire pour l'étude des systèmes gaz/hydrates de gaz 49

3.3.1 Gaz dans les sédiments marins et contribution de la caractérisation sismique 49

3.3.2 Caractérisation multi-échelle des interfaces complexes associées à la présence de gaz libre dans les sédiments marins 50

3.3.3 Caractérisation des *pockmarks* 51

3.3.4 Mise en évidence de la dynamique du système hydrate de la mer Noire 54
3.3.5 Bilan sur la caractérisation sismique et perspectives à court terme 61
3.4 Perspectives de développements de la caractérisation sismique haute résolution à partir de l'acquisition sur le fond de mer par fibre optique et OBS 65
3.4.1 Contexte de l'acquisition en fond de mer : émergence des mesures distribuées sur fibre optique 65
3.4.2 Caractérisation sismique à partir des mesures réparties sur fibre optique 66
3.4.3 Projets en cours sur les mesures acquises en fond de mer 69
Références 74
4 Sélection d'articles 83

Résumé

La partie superficielle de la colonne sédimentaire en contact avec l'océan est le siège de nombreux processus géologiques actifs, souvent associés à des circulations de fluides, potentiellement sources d'aléas marins. Depuis les années 1990, l'Ifremer s'est spécialisé dans le développement de la sismique réflexion adaptée à l'étude haute résolution des sédiments marins et des processus géologiques proches du fond de mer. Mes travaux au sein de l'Ifremer contribuent à l'amélioration de la résolution de l'imagerie sismique et à la caractérisation des sédiments marins superficiels par des développements technologiques et méthodologiques. Ils s'intègrent dans une approche pluridisciplinaire en géosciences indispensable à la compréhension des processus géologiques complexes. Mon activité de recherche s'articule autour de quatre thématiques. La première est d'exploiter la grande richesse fréquentielle des sources sismiques pour développer plus en avant l'analyse sismique multi-échelle qui repose sur la théorie des ondelettes. J'ai adapté cet outil analytique en développant une technique de correction des effets de distorsions de source par des travaux menés en collaboration avec l'Université de Rennes. Son application en sismique en fait un outil efficace et novateur permettant de définir la morphologie des réflecteurs, de fusionner des données acquises par différentes sources, ou encore d'évaluer la détectabilité des réflecteurs. Le développement d'une méthode de compensation de l'atténuation sismique permet d'étendre le domaine d'application de l'analyse multi-échelle aux milieux anélastiques. La seconde thématique consiste à améliorer la résolution de l'imagerie sismique très haute résolution par grande profondeur d'eau avec le développement d'une capacité multidéport de l'engin sous-marin SYSIF remorqué en fond de mer. Les innovations instrumentales et méthodologiques adaptées aux spécificités d'acquisition par grand fond et réalisées en étroite collaboration avec les équipes techniques d'Ifremer permettent d'atteindre une résolution métrique de l'image du sous-sol et de caractériser les sédiments superficiels avec une précision encore inégalée. Les développements associés à ces deux premières thématiques de recherche ont été mis à profit dans la troisième thématique dédiée à l'intégration de la caractérisation sismique dans l'étude pluridisciplinaire des systèmes sédimentaires comportant du gaz libre et des hydrates de gaz. La contribution majeure de cette approche pluridisciplinaire fut de révéler un état transitoire de la zone de stabilité des hydrates de gaz dans le secteur roumain de la mer Noire suite aux changements des conditions environnementales depuis le dernier épisode glaciaire. L'apport de la caractérisation sismique multirésolution avec acquisition de surface et près du fond a été essentiel pour définir l'état actuel du système hydrate. Une caractérisation plus précise du système hydrate est en cours, reposant sur l'exploitation des données sismiques multirésolution de surface acquises avec une large gamme d'incidence. J'ai débuté plus récemment des travaux de recherche concernant les dispositifs de réception posés sur le fond de mer et plus particulièrement sur l'utilisation de la fibre optique des câbles sous-marins pour mesurer le taux de déformation dynamique. L'émergence de cette nouvelle technique de mesure géophysique est l'opportunité de développer la sismique passive en milieu marin au travers de nombreux projets de collaborations scientifiques et d'utiliser les ondes de surface pour déterminer les propriétés de cisaillement des sédiments marins. Ces futurs travaux porteront dans un premier temps sur l'étude de la réponse instrumentale du capteur « fibre optique ». La tomographie des sédiments superficiels à partir des ondes de Scholte par corrélation du bruit ambiant permettra ensuite d'enrichir les capacités de caractérisation des sédiments marins.

1 Curriculum vitae

Stéphan Ker

Né le 4 juillet 1974 à Brest

Cadre de recherche à l'Ifremer – UMR 6538 Geo-Ocean – Equipes ALMA/ANTIPOD

Adresse : Ifremer – Centre de Brest – 1625 Rte de Sainte-Anne, 29280 Plouzané

ORCID : 0000-0002-4393-3965

Page internet Ifremer : https://annuaire.ifremer.fr/cv/17027/

H-Index : 15

1.1 Formation

- 2012 Doctorat en Géophysique – Institut de Physique du Globe – Paris – « Développement de méthodes d'imagerie par grand fond et analyse multi-échelle par ondelettes pour la caractérisation à haute résolution du sous-sol marin »
  Directeur de thèse : Dominique Gibert, co-directeur : Yves Le Gonidec

- 2000 Ingénieur spécialisé en exploration géophysique – ENSPM – Rueil-Malmaison – sujets : Traitement antimultiple en sismique réflexion (Ifremer – Brest) et Imagerie sismique sub-basaltique (*Geoscience Research Center* – ELF – Londres)

- 1997 DEA de géophysique « Mécanique des milieux géophysiques et environnement » – Université Joseph Fourier – Grenoble – sujet : Imagerie géophysique du sous-sol par géoradar

1.2 Expériences professionnelles

- Depuis mars 2007 : cadre de recherche en géophysique à l'Ifremer

- Septembre 2000 à mars 2007 : ingénieur de recherche à l'IFP (devenu IFPen) – Projets R&D : Imagerie sismique sub-basaltique (SIMBA), imagerie sismique multicomposante, inversion stratigraphique

- Novembre 1997 à août 1998 : service militaire effectué au sein de la Marine Nationale

1.3 Principaux projets de recherche et d'expertise réalisés à l'Ifremer

- SYSIF (2007-2015) : Développement de la sismique remorquée près du fond de mer
  - Responsable du projet : Bruno Marsset
  - Financement industriel et financement CARNOT
  - Travaux : développement instrumental et méthodologique pour l'obtention d'une imagerie à très haute résolution par grande profondeur d'eau

- ERIG3D (2008-2012) : Etude des aléas marins dans le golfe de Guinée
    - Responsable du projet : Michel Voisset
    - Projet de recherche collaborative entre l'Ifremer et TOTAL
    - Responsable du volet géophysique du projet
    - Travaux : imagerie sismique très haute résolution SYSIF et ultra haute résolution (AUV)

- MSA (2012-2016) : Analyse sismique multi-échelle des réflecteurs sédimentaires et des structures océaniques
    - Responsable du projet
    - Collaboration avec Géosciences Rennes, IPGP et le Laboratoire d'Océanographie Physique et Spatiale (LOPS)
    - Travaux : développement de la technique de la réponse en ondelettes appliquée aux données sismiques, analyse de réflecteurs sismiques complexes

- GHASS (2015-2019) : Etude pluridisciplinaire du système hydrate du secteur roumain de la mer Noire et possible relation avec les instabilités sédimentaires
    - Responsable du projet et chef de mission de la campagne océanographique éponyme (2015)
    - Projet impliquant l'ensemble des équipes de recherche de Géosciences marines de l'Ifremer et collaboration avec GeoEcoMar (Roumanie), Geomar (Allemagne), NGI (Norvège) et l'Université de Barcelone (Espagne)
    - Travaux : imagerie sismique haute et très haute résolution, contribution à l'approche pluridisciplinaire de caractérisation du système hydrate

- AMETISTE (2019-2021) : Prise en compte des vitesses de propagation des sédiments dans la propagation acoustique
    - Responsable du projet : Elodie Marquès (SHOM)
    - Collaboration avec le SHOM
    - Travaux : développement de l'acquisition long-déport pour la caractérisation sismique haute-résolution de surface

- Projet R&D avec Technip (2019-2020) - responsable d'une expertise technique menée par l'Ifremer (confidentiel)

- GHASS2 (2020-2025) : Second volet du projet GHASS portant sur le cycle du méthane des sédiments marins jusqu'à l'hydrosphère
    - Responsable du projet : Vincent Riboulot
    - Financement ANR Blame (ANR-18-CE01-0007) et européen DOORS (doi : 10.3030/101000518)
    - Responsable du premier leg de la campagne (2021) et du volet géophysique
    - Travaux : imagerie sismique basse et haute résolution, contribution à l'approche pluridisciplinaire de caractérisation du système hydrate

- Projet Bruit-FM (2022-2025) : Exploitation des signaux cachés dans le bruit sismologique large-bande de fond de mer

- Responsable du projet : Wayne Crawford (IPGP)
- Financement ANR (ANR-21-CE01-0031)
- Responsable Ifremer et d'un WP
- Travaux : Séparation de signaux enregistrés par les sismomètres de fond de mer

- Projet Focus (2018-2025) étude de la déformation du fond marin par réflectométrie laser sur fibre optique des câbles sous-marins
  - Responsable du projet : Marc-André Gutscher (CNRS/Geo-Ocean)
  - Financement ERC
  - Collaboration : Geomar et Université de Kiel (Allemagne), INGV, INFN-LNS et Université de Catane (Italie)
  - Travaux : étude de la réponse instrumentale et apport de la mesure DAS (taux de déformation) depuis 2022

1.4 Encadrements d'étudiants et de chercheur post-doctorat

1.4.1 Encadrement de Masters

- Marion Jaud, 2008, master de recherche (UBO)/diplôme d'ingénieur (ENSIETA), durée de 5 mois, co-encadrement avec Yannick Thomas « Imagerie sismique haute résolution : application à l'étude des hydrates de gaz »

- Paul Lubrano Lavadera, 2009, ingénieur EOST stage de fin d'étude, durée de 5 mois, « Inversion par forme d'onde des données sismiques haute résolution »

- Céline Bernard, 2017, master de recherche (UBO)/diplôme d'ingénieur (ENSTA), durée de 5 mois, « Estimation de la concentration en gaz dans les sédiments marins superficiels à partir des paramètres sismiques »

- Giuseppe Cappelli, 2020, master de recherche Université de Naples, durée de 5 mois, co-encadrement avec Shane Murphy, « Comparing different techniques in travel time computation »

- Achille Métral, 2022, master de recherche (UBO)/diplôme d'ingénieur (ENSTA), durée de 5 mois, « Analyse des signaux acoustiques de rorqual enregistrés par un réseau d'OBS dans l'Océan Arctique »

1.4.2 Encadrement de thèses

- Florent Colin, 2018-2020, « Caractérisation des systèmes gaz/hydrates de gaz de la mer Noire par imagerie sismique haute résolution remorquée en fond de mer (SYSIF) » co-encadrement avec Bruno Marsset et direction de thèse Pr Pascal Tarits – UBO – EDSML

- Giuseppe Cappelli, 2023-2025, « L'analyse des données de réflectométrie laser (BOTDR et DAS) sur des câbles de fibre-optique sous-marins », participation à l'encadrement avec Lionel Quetel (IDIL) et Shane Murphy (Geo-Ocean), direction de thèse par Marc-André Gutscher (CNRS/Geo-Ocean) – UBO – EDSML

1.4.3 Encadrement de postdoc

- Simon Rebeyrol, 2022-2023, « Séparation de signaux enregistrés par les sismomètres de fond de mer », projet ANR Bruit-FM.

1.5 Autres activités de recherche

Campagnes océanographiques :

- Direction de trois campagnes
  - TECHAUV (2009) doi: 10.17600/9060190
  - GHASS (2015) doi :10.17600/15000500
  - GHASS 2 (2021) doi : 10.17600/18001358
  -
- Participation à vingt campagnes océanographiques (CO) ou d'essais (CE).
  - Sismique près du fond :
    C0 : ERIG3D (2008), JCR269 (2011), PRISME2 (2013), GHASS (2015)
    CE : EXOCET et EXOCET2 (2007), ESSNAUT (2009), ESSYPEN (2013)
  - Sismique HR et THR :
    CO : BOBGEO (2009), GASCOGNE3 (2018), CARAPASS (2019), SOUSACOU (2021), GHASS2 (2021)
    CE : ESSISM2 (2015), ESSIMSOURCE (2018)
  - Sismique HR 3D (CO) : MARMESONET (2009) et FUTUNA 2 (2011)
  - Sondeur de sédiment sur AUV (CE) ESSED (2007), TECHAUV (2009)
  - Mesures piézométrique et déploiements de sismomètres de fond de mer
    CO : CAGE20-6 (2020)

Campagne de mesures à terre :

- Campagnes de mesures du taux de déformation dynamique par réflectométrie laser (DAS) sur les câbles sous-marins de Catane et Capo Passero en mer Ionienne (novembre 2023)

Participation à jury de thèse : Examinateur, thèse de Judith Flamme, « Nouvelle approche de l'étude du sous-sol marin : application conjointe de l'électromagnétisme, de la sismique multitrace et de la géotechnique», EDSML, soutenance mai 2021.

Participation au jury de soutenance Master 2 : membre expert, Master 2 géophysique marine (UBO), septembre 2023

Reviewer pour une douzaine de revues de rang A (GJI, JGR solid earth and Ocean, Geophysics, Near Surface Geophysics, Marine and Petroleum geology, Ocean Engineering, Geophysical Prospecting, International Journal of Greenhouse Gas Control, Journal of Natural Gas Science and Engineering, Interpretation).

Enseignements : Intervention en Master 2 géophysique marine (UBO) et école d'ingénieurs (ISEN) (de 2008 à 2010)

Participation à comités : Membre suppléant de la commission nationale de la flotte océanographique de 2019-2022.

2 Liste de publications

2.1 Publications de rang A

Rebeyrol, S., **Ker, S**., Crawford, W., Duval, L. (2024). Revisiting the OBS compliance signal removal, a stationary-based approach, en révision pour *Geophysical Journal International*.

Fabre, M., Riboulot, V., Loncke, L., **Ker, S**., Ballas, G., Thomas, Y., Ion, G., Sultan, N. (2024). Slow dynamics of hydrate systems revealed by a double BSR. *Geophysical Research Letters*, *51*, e2023GL106284.

Dupré, S., Foucher, J.-P., Pierre, C., Decker, C., Westbrook, G., **Ker, S**., Olu - Le Roy, K., Donval, J.-P., Charlou, J.-L., Blanc-Valleron, M.-M., Nouzé, H. (2023). Methane-flow system within the Nyegga pockmark field, offshore mid-Norway. *Frontiers in Earth Science*, 11, 1250619 (24p.).

Szitkar, F., Dyment, J., Pelleter, E., Thomas, Y., Marsset, B., **Ker, S.,** Fouquet, Y. (2022). Effusive and explosive volcanism on the northern Futuna Ridge, Lau Basin: A combined bathymetric, magnetic and seismic investigation. *Journal of Volcanology and Geothermal Research*, 431, 107646.

Garziglia, S., Sultan, N., Thomas, Y., **Ker, S.**, Marsset, B., Bompais, X., Woerther, P., Witt, C., Kopf, A., Apprioual, R. (2021). Assessing spatio-temporal variability of free gas in surficial cohesive sediments using tidal pressure fluctuations. *Journal of Geophysical Research: Earth Surface*, 126(10), e2021JF006131 (26p.).

Chazallon, B., Rodriguez, C.T., Ruffine, L., Carpentier, Y., Donval, J-P., **Ker, S.**, Riboulot, V. (2021). Characterizing the variability of natural gas hydrate composition from a selected site of the Western Black Sea, off Romania. *Marine and Petroleum Geology*, 124, 104785 (15p.).

Ruffine, L., Deusner, C., Haeckel, M., Kossel, E., Toucanne, S., Chéron, S., Boissier, A., Schmidt, M., Donval, J-P., Scholz, F., Guyader, V., **Ker, S.**, Riboulot, V. (2021). Effects of postglacial seawater intrusion on sediment geochemical characteristics in the Romanian sector of the Black Sea. *Marine and Petroleum Geology*, 123, 104746.

Ker, S. & Le Gonidec, Y. (2020). Filtering of a Ricker wavelet induced by anelastic seismic wave propagation and reflection. *Journal of Geophysics and Engineering*, 17(5), 838-851.

Colin, F., **Ker, S.**, Riboulot, V., Sultan, N. (2020). Irregular BSR: evidence of an ongoing reequilibrium of a gas hydrate system. *Geophysical Research Letters*, 47(20), e2020GL089906 (10p.).

Colin, F., **Ker, S.**, Marsset, B. (2020). Fine-scale velocity distribution revealed by datuming of very-high-resolution deep-towed seismic data: Example of a shallow-gas system from the western Black Sea. *Geophysics*, 85(5), B181-B192.

Ker, S., Thomas, Y., Riboulot, V., Sultan, N., Bernard, C., Scalabrin, C., Ion, G, Marsset, B. (2019). Anomalously deep BSR related to a transient state of the gas hydrate system in the western Black Sea. *Geochemistry Geophysics Geosystems*, 20(1), 442-459.

Ballas, G., Garziglia, S., Sultan, N., Pelleter, E., Toucanne, S., Marsset, T., Riboulot, V., **Ker, S.** (2018). Influence of early diagenesis on geotechnical properties of clay sediments (Romania, Black Sea). *Engineering Geology*, 240, 175-188.

Ker, S. & Le Gonidec, Y. (2018). Fractional integration of seismic wavelets in anelastic media to recover multiscale properties of impedance discontinuities. *Geophysics*, 83(2), V61-V71.

Marsset, B., **Ker, S.,** Thomas, Y., Colin, F. (2018). Deep-towed high resolution seismic imaging II: Determination of P-wave velocity distribution. *Deep-sea Research Part I-oceanographic Research Papers*, 132, 29-36.

Marsset, T., Ruffine, L., **Ker, S.**, Cauquil, E., Gay, A. (2018). Types of fluid-related features controlled by sedimentary cycles and fault network in deepwater Nigeria. *Marine and Petroleum Geology*, 89(Part.2), 330-349.

Riboulot, V., **Ker, S.**, Sultan, N., Thomas, Y., Marsset, B., Scalabrin, C., Ruffine, L., Boulart, C., Ion, G. (2018). Freshwater lake to salt-water sea causing widespread hydrate dissociation in the Black Sea. *Nature Communications*, 9(117), 1-8.

Goswami, B. K., Weitemeyer, K. A., Bunz, S., Minshull, T. A., Westbrook, G., **Ker, S.**, Sinha, M. C. (2017). Variations in pockmark composition at the Vestnesa Ridge: Insights from marine controlled source electromagnetic and seismic data. *Geochemistry Geophysics Geosystems*, 18(3), 1111-1125.

Riboulot, V., Cattaneo, A., Scalabrin, C., Gaillot, A., Jouet, G., Ballas, G., Marsset, T., Garziglia, S., **Ker, S.** (2017). Control of the geomorphology and gas hydrate extent on widespread gas emissions offshore Romania. *Bulletin De La Société Géologique De France*, 188(4), 26 (1-12).

Ker, S., Le Gonidec, Y., Marié, L. (2016). Multifrequency seismic detectability of seasonal thermoclines assessed from ARGO data. *Journal of Geophysical Research: Oceans*, 121(8), 6035-6060.

Riboulot, V., Sultan, N., Imbert, P., **Ker, S.** (2016). Initiation of gas-hydrate pockmark in deep-water Nigeria: Geo-mechanical analysis and modelling. *Earth and Planetary Science Letters*, 434, 252-263.

Goswami, B. K., Weitemeyer, K. A., Minshull, T. A., Sinha, M. C., Westbrook, G., Chabert, A., Henstock, T. J., **Ker, S.** (2015). A joint electromagnetic and seismic study of an active pockmark within the hydrate stability field at the Vestnesa Ridge, West Svalbard margin. *Journal of Geophysical Research: Solid Earth*, 120(10), 6797-6822.

Ker, S., Le Gonidec, Y., Marié, L., Thomas, Y., Gibert, D. (2015). Multiscale seismic reflectivity of shallow thermoclines. *Journal of Geophysical Research: Oceans*, 120(3), 1872-1886.

Marsset, B., Menut, E., **Ker, S.**, Thomas, Y., Regnault, J-P., Leon, P., Martinossi, H., Artzner, L., Chenot, D., Dentrecolas, S., Spychalski, B., Mellier, G., Sultan, N. (2014). Deep-towed High Resolution multichannel seismic imaging. *Deep-sea Research Part I-oceanographic Research Papers*, 93, 83-90.

Ker, S., Le Gonidec, Y., Marsset, B., Westbrook, G., Gibert, D., Minshull, T. A. (2014). Fine-scale gas distribution in marine sediments assessed from deep-towed seismic data. *Geophysical Journal International*, 196(3), 1466-1470.

Ker, S., Le Gonidec, Y., Gibert, D. (2013). Multiresolution seismic data fusion with a generalized wavelet-based method to derive subseabed acoustic properties. *Geophysical Journal International*, 195(2), 1370-1383.

Riboulot, V., Cattaneo, A., Sultan, N., Garziglia, S., **Ker, S.**, Imbert, P., Voisset, M. (2013). Sea-level change and free gas occurrence influencing a submarine landslide and pockmark formation and distribution in deepwater Nigeria. *Earth and Planetary Science Letters*, 375, 78-91.

Ker, S., Le Gonidec, Y., Gibert, D. (2012). Multiscale seismic attributes: source-corrected wavelet response and application to high-resolution seismic data. *Geophysical Journal International*, 190(3), 1746-1760.

Ker, S., Le Gonidec, Y., Gibert, D., Marsset, B. (2011). Multiscale seismic attributes: A wavelet-based method and its application to high-resolution seismic and ground truth data. *Geophysical Journal International*, 187(2), 1038-1054.

Sultan, N., Riboulot, V., **Ker, S.**, Marsset, B., Geli, L., Tary, J-B., Klingelhoefer, F., Voisset, M., Lanfumey, V., Colliat, J-L., Adamy, J., Grimaud, S. (2011). Dynamics of fault-fluid-hydrate system around a shale-cored anticline in deepwater Nigeria. *Journal of Geophysical Research: Solid Earth*, 116(B12110).

Ker, S., Marsset, B., Garziglia, S., Le Gonidec, Y., Gibert, D., Voisset, M., Adamy, J. (2010). High-resolution seismic imaging in deep sea from a joint deep-towed/OBH reflection experiment: application to a Mass Transport Complex offshore Nigeria. *Geophysical Journal International*, 182(3), 1524-1542.

Sultan, N., Marsset, B., **Ker, S.**, Marsset, T., Voisset, M., Vernant, A-M., Bayon, G., Cauquil, E., Adamy, J., Colliat, J. L., Drapeau, D. (2010). Hydrate dissolution as a potential mechanism for pockmark formation in the Niger delta. *Journal of Geophysical Research: Solid Earth*, 115(B08101), 1-33.

Plaza-Faverola, A., Westbrook, G. K., **Ker, S.**, Exley, R. J. K., Gailler, A., Minshull, T. A., Broto, K. (2010). Evidence from three-dimensional seismic tomography for a substantial accumulation of gas hydrate in a fluid-escape chimney in the Nyegga pockmark field, offshore Norway. *Journal of Geophysical Research: Solid Earth*, 115(B08104), 1-24.

Marsset, T., Marsset, B., **Ker, S.**, Thomas, Y., Le Gall, Y. (2010). High and very high resolution deep-towed seismic system: Performance and examples from deep water Geohazard studies. *Deep-sea Research Part I-oceanographic Research Papers*, 57(4), 628-637.

Garziglia, S., Sultan, N., Cattaneo, A., **Ker, S.**, Marsset, B., Riboulot, V., Voisset, M., Adamy, J., Unterseh, S. (2010). Identification of Shear Zones and Their Causal Mechanisms Using a Combination of Cone Penetration Tests and Seismic Data in the Eastern Niger Delta. *Advances in Natural and Technological Hazards Research*, 28, 55-65.

2.2 Conférences, ouvrages, rapports techniques et jeux de données

Sélection de conférence depuis 2018

Trivedi, A., Sarkar, S., **Ker, S**., Minshull, T. A (2023): An improved Weichselian seismic stratigraphic framework of the Kongsfjorden-Isfjorden Interfan region off western Svalbard from high-frequency deep-towed seismic data and its implication on fluid migration and methane venting, EGU General Assembly 2023, Vienna, Austria, 24–28 Apr 2023.

Murphy, S., Garreau, P., Palano, M., **Ker, S**., Quetel, L., Jousset, P., Riccobene, G., Aurnia, S., Currenti, G., Gutscher, M.-A (2022): Strain evolution on a submarine cable during the 2020-2021 Etna eruption, EGU General Assembly 2022, Vienna, Austria, 23–27 May 2022.

Fabre, M., Loncke, L., Riboulot, V., Sultan, N., **Ker, S**. (2021): Slope instabilities and gas hydrates dissociation in the western Black Sea since the last glacial maximum, EGU General Assembly 2022, Vienna, Austria, 23–27 May 2022.

Colin, F., **Ker, S**., Marsset, B. (2019). Wave-equation datuming applied to very high-resolution deep-towed multichannel seismic data. Near Surface Geoscience 2019. 8 - 12 September 2019, The Hague, The Netherlands.

Colin, F., **Ker, S.**, Marsset, B., Damy, G. (2019). Very high-resolution deep towed multi-channel seismic imaging: Solving the impact of variable array shape on data processing. EGU General Assembly 2019. 7-12 April 2019, Vienna.

Ker, S., Riboulot, V., Sultan, N., Thomas, Y., Marsset, B., Scalabrin, C., Ruffine, L., Boulart, C., Ion, G., 2018. From a freshwater lake to a salt-water sea causing widespread hydrate dissociation in the Black Sea. 20th International Sedimentological Congress, Québec, Canada, August 13-17.

Participation à ouvrages scientifiques

Sultan, N., Ruffine, L., Garziglia, S., Ker, S., Vanneste, M., Humphrey, G. (2018). Seabed Gas Hydrates. In Encyclopedia of Maritime and Offshore Engineering. 2018. J. Carlton, P. Jukes and Y. S. Choo (Eds) ISBN: 9781118476352

Ruffine, L., Broseta, D., Desmedt, A. (2018). Gas Hydrates 2: Geoscience Issues and Potential Industrial Applications, chapter 2 Geophysical Approach. ISTE- Wiley.

Rapports techniques

Rédaction d'une quinzaine de rapports de mission, de comptes rendus d'acquisition et d'analyse consultables sur archimer à l'exception des rapports confidentiels (https://archimer.ifremer.fr).

Jeux de données

Thomas, Y., Marsset, B., Dupont, P., **Ker, S.**, Riboulot, V. (2023). Depth-migrated High Resolution seismic reflection profiles and interval velocity models in the western Black Sea. SEANOE. doi.org/10.17882/96701

Colin, F., **Ker, S.**, Marsset, B. (2021). SYSIF seismic data acquired in the western Black Sea. SEANOE. doi.org/10.17882/75247

Colin, F., **Ker, S.**, Marsset, B., Thomas, Y. (2020). Irregular BSR: evidence of an on-going reequilibrium of a gas hydrate system. SEANOE. doi.org/10.17882/74866

3 Travaux de recherche

Introduction

La partie superficielle (*i.e.* les 500 premiers mètres) de la colonne sédimentaire en contact avec l'océan est le siège de nombreux processus géologiques actifs, d'aléas marins et constitue une archive climatique et océanique. Pour étudier les sédiments marins superficiels, les chercheurs en géosciences marines ont recours à deux types de mesures : 1) les mesures directes du sous-sol marin collectées *in situ* par des pénétromètres ou pratiquées sur des carottes sédimentaires, limitées à des épaisseurs sous le fond de l'eau généralement inférieures à 50 m et à un nombre de sites très réduit et 2) des mesures indirectes qui permettent de couvrir une large surface pour définir la bathymétrie (acoustique sous-marine) et des coupes en profondeur avec des techniques d'imagerie du sous-sol. La sismique réflexion est une méthode d'imagerie indirecte particulièrement efficace pour étudier les bassins sédimentaires avec plus d'un siècle de développements techniques et méthodologiques associés à des activités industrielles mobilisant des moyens financiers colossaux. Cette méthode consiste à émettre des ondes sismiques et à enregistrer les ondes réfléchies aux différentes interfaces du sous-sol pour obtenir une image du de celui-ci. L'imagerie sismique en 3D est devenue un prérequis standard pour l'exploration pétrolière et gazière et pour la surveillance de l'exploitation. Cependant, afin de pouvoir imager des réservoirs situés à plusieurs kilomètres de profondeur, il est nécessaire d'utiliser des ondes de basses fréquences fournissant une imagerie avec une résolution verticale décamétrique. La limitation de la résolution est due au phénomène d'atténuation sismique affectant le contenu haute fréquence de l'onde sismique au cours de sa propagation. Il fut donc nécessaire de développer une branche de la sismique réflexion haute voire très haute résolution pour imager et caractériser le sous-sol marin superficiel à une échelle métrique voire submétrique en adéquation avec une résolution appropriée à l'étude des sédiments superficiels et une analyse combinée avec les mesures directes. L'Ifremer, motivé par ses thématiques de recherche et par les besoins de la communauté scientifique nationale, s'est spécialisée dans ce domaine en développant des dispositifs spécifiques émettant un contenu fréquentiel plus élevé mais avec une profondeur de pénétration limitée. Dans la période 1990-2010, l'Ifremer a ainsi mis au point et opéré des dispositifs de sismique 2D et 3D haute et très haute résolution avec des dispositifs tractés très proches de la surface de l'eau ou en surface, un dispositif hybride avec source en surface et des récepteurs tractés près du fond (PASISAR) et un système sismique (source et récepteur) très haute résolution remorqué près du fond (SYSIF).

Mes activités de recherche au sein de l'Ifremer ont contribué à ces développements techniques et méthodologiques portant sur l'amélioration de la résolution de l'imagerie sismique et de la caractérisation des sédiments marins superficiels. J'ai également participé à l'intégration des informations obtenues par la sismique dans une approche pluridisciplinaire associant toutes les disciplines des géosciences indispensables à la compréhension des processus géologiques complexes.

Mon activité de recherche s'articule autour de quatre thématiques.

Analyse sismique multi-échelle

L'analyse sismique multi-échelle exploite la grande richesse fréquentielle des sources sismiques dans le but d'augmenter la résolution verticale et d'extraire de nouveaux attributs qualifiés de

multi-échelles. Cette analyse multi-échelle repose sur la théorie mathématique des ondelettes et consiste à développer plus en avant la technique de la réponse en ondelettes pour des données sismiques acquises en incidence normale dans un milieu élastique. Cette technique permet de définir la morphologie des réflecteurs et de fusionner des données acquises par différentes sources augmentant ainsi la résolution verticale de l'image sismique. Appliqué aux données issues de la sismique très haute résolution, elle permet de comparer directement les données sismiques et *in situ* dans le domaine des ondelettes et d'estimer l'impédance acoustique. Le développement de la correction des effets de l'atténuation sismique permet d'étendre le domaine de validité de l'analyse sismique multi-échelle à des milieux anélastiques. La réponse en ondelettes est également un outil de modélisation très efficace pour étudier la réponse sismique des réflecteurs complexes en fonction de la fréquence. En plus de la caractérisation des sédiments, j'ai pu démontrer l'apport de cette analyse en l'appliquant à l'imagerie haute résolution de la thermocline superficielle, une interface clé de l'Océan. Le développement d'une formulation analytique de la réponse en ondelettes d'un modèle de thermocline et la modélisation à partir de mesures *in situ* ARGO ont permis de comprendre la réponse sismique de la thermocline en fonction de la fréquence et d'évaluer sa détectabilité.

Développement de la sismique très haute résolution multidéport remorquée en fond de mer

Le système sismique SYSIF remorqué près du fond a été conçu pour réaliser une imagerie avec une résolution métrique du sous-sol marin par grande profondeur impossible à obtenir avec des dispositifs de surface. S'agissant d'une acquisition monodéport (incidence normale), les premiers développements associés à ce dispositif ont été consacrés à l'optimisation de la résolution verticale. Dans une seconde phase, sujet de ce volet, l'objectif a été d'améliorer la résolution horizontale et de pouvoir déterminer les vitesses des ondes de compression en dotant SYSIF d'une capacité d'acquisition multidéport. Pour remplir cet objectif, nous avons conçu une antenne de réception, déterminé avec précision l'évolution de la forme de cette antenne au cours de l'acquisition et développé des techniques de traitement et d'imagerie adaptées à la géométrie complexe de cette acquisition près du fond.

Caractérisation sismique des systèmes gaz/hydrates de gaz

La compréhension des systèmes sédimentaires renfermant du méthane sous forme de gaz libre ou piégé dans des solides appelés hydrates de gaz nécessite une approche pluridisciplinaire. Pour une part importante de mon activité, j'ai contribué à cet effort collectif par le développement de la composante géophysique en proposant un arsenal d'imagerie et de caractérisation adapté à ce type de milieu. Les développements réalisés en sismique près du fond et en analyse sismique multi-échelle s'inscrivent dans ce cadre. L'approche de sismique multirésolution avec acquisition haute résolution de surface et très haute résolution près du fond a contribué à mieux définir la distribution de gaz libre dans la colonne sédimentaire, à mieux caractériser des structures géomorphologiques et comprendre leur genèse. Cette approche s'est montrée également très efficace pour l'étude des systèmes hydrates et l'imagerie de leur limite de stabilité. Sa contribution majeure a révélé, au cours du projet GHASS, un état transitoire de la zone de stabilité des hydrates de gaz dans le secteur roumain de la mer Noire en réponse aux changements des conditions environnementales depuis le dernier épisode glaciaire.

Perspectives de développement de l'acquisition en fond de mer

Cette thématique récente repose sur l'utilisation des dispositifs de réception sur le fond de mer et plus particulièrement sur l'utilisation de la fibre optique des câbles sous-marins pour caractériser le sous-sol marin. L'acquisition de mesures réparties sur fibre optique consiste à mesurer le taux de déformation dynamique par réflectométrie laser. L'émergence de cette nouvelle technique de mesure géophysique, caractérisée par un échantillonnage spatial dense, offre la possibilité d'une part de compléter la caractérisation du sous-sol marin avec une approche de sismique active associant réception conventionnelle en surface et sur le fond par fibre optique. D'autre part, elle offre une très grande opportunité de développer la sismique passive en milieu marin et d'utiliser les ondes de surface pour déterminer les propriétés de cisaillement des sédiments marins superficiels. Une étape importante dans le développement des applications géophysiques des mesures réparties sur fibre optique réside dans la caractérisation de la réponse instrumentale du « capteur fibre ».

3.1 Analyse sismique multi-échelle par réponse en ondelettes

Cette thématique repose sur des développements associés à la théorie mathématique des ondelettes. Les objectifs sont d'améliorer la résolution verticale des données sismiques acquises avec des sources d'émission caractérisées par un large contenu fréquentiel, de développer des nouveaux attributs sismiques permettant la caractérisation de la géométrie des réflecteurs et d'accéder à l'impédance acoustique.

3.1.1 Le concept de réponse en ondelettes et son application en sismique réflexion

La réponse en ondelettes

La caractérisation sismique multi-échelle par réponse en ondelettes repose sur les propriétés mathématiques de la transformée en ondelettes. Cette caractérisation multi-échelle a été initiée dans le domaine ultrasonore en cuve acoustique par Le Gonidec et al. (2002) et a été prolongée dans le domaine des ondes sismiques par Gesret et al. (2010). La réponse en ondelettes notée R a pour principe de propager des sources acoustiques ou sismiques de même forme mais de contenu fréquentiel différent (donc de résolution différente) dans un milieu d'impédance p :

$$R[\xi, p](t, a) \equiv (D_a \xi \otimes p)(t), \qquad \text{eq. 1.1}$$

où $D_a \xi = a^{-1} \xi(t/a)$ est l'opérateur de dilatation appliqué à l'ondelette sismique ξ avec a la dilatation qui permet de modifier le contenu fréquentiel et t le temps double de propagation. $\otimes$ est l'opérateur de propagation des ondes sismiques dans le milieu. Pour une propagation 1D, la réponse en ondelettes R est le produit de convolution de la famille d'ondelettes dilatées avec la séquence de réflectivité r du milieu. La réponse en ondelettes R est donc la transformée en ondelettes W de la réflectivité r :

$$\begin{aligned} R[\xi, p](t, a) &= D_a \xi(t) * r(t), \qquad \text{eq. 1.2} \\ &= W[\xi, r](t, a)\,. \end{aligned}$$

Le Gonidec et al. (2002) ont montré que si l'approximation de Born est valide (i.e. régime de diffusion simple), la réponse en ondelettes est équivalente à la transformée en ondelettes de l'impédance p dans le domaine spatial réalisée avec une ondelette analysante avec un ordre de dérivation supplémentaire $(n+1)$: $aR[\xi_n, p](t, a) \Leftrightarrow W[\xi_{n+1}, p](z, a)$. La transformée en ondelettes W et la réponse en ondelettes R partagent les mêmes propriétés multi-échelles. Parmi ces propriétés figure l'utilisation des lignes d'extrema comme support condensé de l'information multi-échelle. Les lignes d'extrema permettent d'analyser la morphologie des discontinuités du milieu et de déterminer leurs dimensions caractéristiques (Mallat & Hwang, 1992 ; Le Gonidec et al., 2002).

Réponse en ondelettes obtenue à partir d'une expérience sismique : la correction de source

Dans le cadre de ma thèse, j'ai proposé d'étendre l'utilisation de la réponse en ondelettes à l'imagerie sismique. Au cours d'une expérience de sismique réflexion, il n'est pas possible d'émettre des signaux de même forme avec des contenus fréquentiels différents. Cependant si le spectre de la source est suffisamment large, nous avons pu démontrer que l'on pouvait obtenir la réponse en ondelettes à partir de la transformée en ondelettes de la trace sismique $s(t) * r(t)$. Ceci est possible grâce à une méthode dite de correction de source qui consiste à substituer la source émise $s(t)$ par un signal $b(t)$ qui est une ondelette analysante de contenu fréquentiel identique mais de nature à être en accord avec la théorie des ondelettes. Cette substitution repose

sur les propriétés de $s(t)$ après le traitement de déconvolution de signature. En effet, après déconvolution, $s(t)$ est un élément neutre de la convolution car étant à phase nulle et ayant un spectre d'amplitude plat. La recherche du modèle de source $b(t)$ se fait en minimisant au sens des moindres carrés l'expression $b(t) * s(t) \simeq b(t)$. Le modèle de source b et la famille d'ondelettes analysantes $D_a\xi(t)$, utilisée pour la transformée en ondelettes de la trace sismique, sont recherchés parmi des dérivées de fonctions Levy-alpha stable L d'ordre respectif m et n car leur convolution produit une famille de dérivées de la même fonction Levy-alpha stables d'ordre $l = m + n$ (Ker et al., 2012). La famille d'ondelettes analysantes devient $D_{a_e}\xi_e(t) = D_a\xi(t) * b(t)$ avec l'ondelette analysante effective $\xi_e = \frac{d^l}{dt^l}L(t)$ et a_e la dilatation effective. La réponse en ondelettes $\tilde{R}$ obtenue à partir d'une expérience sismique est donc équivalente à la transformée en ondelettes de la réflectivité mais dans une gamme de dilatation limitée par le contenu fréquentiel de la source initiale :

$$\begin{aligned} \tilde{R}[\xi, p](t, a) &= [D_a\xi(t) * b(t)] * r(t) \\ &= A \times D_{a_e}\xi_e(t) * r(t) \\ &= A \times W[\xi_e, r](t, a_e)\,. \end{aligned} \qquad \text{eq. 1.3}$$

Où A est un facteur de correction d'amplitude. Cette approche a été appelée la réponse en ondelettes par correction de source (Ker et al., 2012).

La réponse en ondelettes par correction de source a été appliquée aux données sismiques acquises sur un même profil (campagne ERIG3D) par le système de sismique remorquée près du fond SYSIF (cf. détails sur SYSIF en partie 3.2.1) à l'aide de deux sources de type transducteur Janus-Helmholtz (figure 1.1) : source Hautes Fréquences (HF) [220-1050 Hz] et source Très Hautes Fréquences (THF) [580-2200 Hz]. La méthode de correction de source, reposant sur l'utilisation de dérivées entières de fonctions Gaussiennes, a permis d'obtenir une réponse en ondelettes en fusionnant les deux contributions sur la gamme de fréquence [220-2200 Hz]. Les amplitudes sismiques multi-échelles, définies par les lignes d'extrema de la réponse en ondelettes, ont permis de caractériser la géométrie des réflecteurs (Ker et al., 2012) et constituent un nouvel attribut sismique dit multi-échelle. Cependant la procédure de correction de source n'était pas optimale dans la gamme de dilatation associée à la transition entre les composantes HF et THF. Il a été également noté que la localisation de la dilatation associée au maximum d'une ligne d'extrema ne dépendait pas uniquement de la morphologie du réflecteur mais aussi de la complexité de l'ondelette analysante.

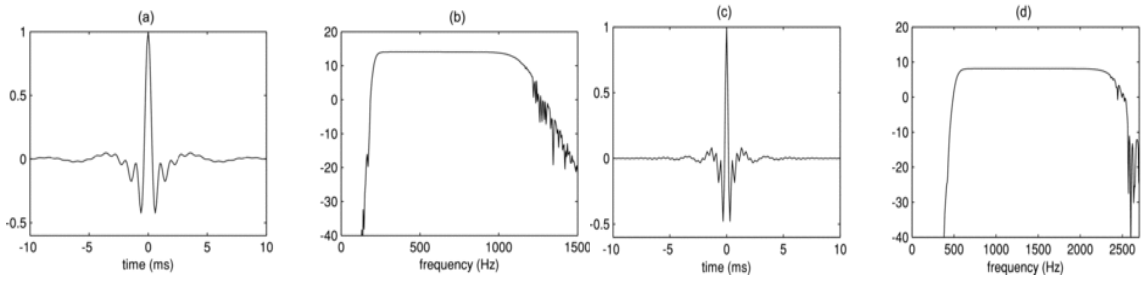

Figure 1.1 : Signatures (a et c) et spectres d'amplitudes (b et d) associés aux transducteurs HF et THF du système sismique SYSIF après déconvolution de signature

3.1.2 Optimisation de la correction de source pour la fusion des données multifréquences SYSIF et reconstruction du profil d'impédance

J'ai poursuivi après ma thèse le développement de la réponse en ondelettes appliquée aux données SYSIF avec Yves Le Gonidec (Géosciences Rennes) et Dominique Gibert (IPGP) avec pour objectifs d'améliorer la méthode de correction de source et d'exploiter les attributs multi-échelles pour la caractérisation de réflecteurs sismiques.

Correction de source avec dérivées fractionnaires de Gaussienne

Nous avons pu démontrer que parmi les fonctions Lévy-alpha stable, les fonctions Gaussiennes associées à la distribution normale caractérisée par le paramètre de stabilité $\alpha = 2$ possédaient le support fréquentiel le plus compact et étaient donc optimales pour se substituer à la source $s(t)$. De plus, nous avons étendu la recherche de l'ordre de dérivation m du modèle de source $b(t)$ de $\mathbb{N}^+$à $\mathbb{R}^+$. C'est-à-dire que nous ne limitons pas la recherche à des dérivées entières de fonctions Gaussiennes mais nous étendons la recherche aux dérivées fractionnaires. Ceci a pour avantages de limiter la complexité de l'ondelette analysante et d'optimiser la fusion quand plusieurs sources existent comme pour le cas des données SYSIF. Nous avons également introduit une nouvelle paramétrisation du modèle de source reposant sur la notion de résolution temporelle de la source sismique. La source sismique $s(t)$ après déconvolution peut être assimilée à une ondelette de Klauder caractérisée par sa résolution temporelle $T_s = 1/B$ où B est la largeur de bande de fréquence. Le modèle de source $b(t)$ est une dérivée de Gaussienne $\frac{d^m}{dt^m} exp\left(\frac{t^2}{a_b^2}\right)$ avec pour paramètres son ordre de dérivation m et sa dilatation a_b. Le modèle source $b(t)$ doit posséder la même résolution temporelle que la source $s(t)$ et ses paramètres sont reliés à la résolution temporelle T_s par la relation $T_s = \delta_m a_b$, où le facteur δ_m est uniquement dépendant de l'ordre de dérivation m. Dans le prolongement de ce formalisme, au lieu de représenter l'ondelette analysante effective $\xi_e(t)$ en fonction de la dilatation effective, il est possible de la représenter en fonction de la dilatation dominante a_d correspondant à la résolution temporelle de l'ondelette effective T_d. La dilatation dominante est obtenue avec la relation $a_d = \delta_l a_e$. La dilatation dominante permet d'utiliser la résolution temporelle de l'ondelette analysante et fournit une représentation où la localisation des extrema ne dépend plus de la complexité de l'ondelette tout en respectant le formalisme des ondelettes (Ker et al., 2013).

Application aux données SYSIF et reconstruction de l'impédance

La nouvelle paramétrisation du modèle de source permet d'optimiser l'ordre de dérivation pour chacune des deux sources SYSIF. En limitant l'ordre de dérivation à $l = 5$ pour la famille des ondelettes effectives assurant ainsi une complexité réduite, l'optimisation de la recherche des ordres de dérivation a abouti à des valeurs différentes pour les deux sources HF et THF (respectivement 4.9 et 4.6 pour l'ordre de dérivation m et 682 et 342 µs pour la dilatation a_b). Après convolution avec des familles d'ondelettes possédant un ordre de dérivation complémentaire à m pour obtenir l, la fusion des deux sources SYSIF génère une famille d'ondelettes dans la gamme de dilatation dominante $\mathcal{R}_{a_d}$= [620 ; 3260 µs]. L'erreur relative par rapport à des ondelettes de référence ne dépasse pas 10 % soit une amélioration de 10 % par rapport à la précédente approche. La figure 1.2 illustre la comparaison entre les réponses en ondelettes obtenues en a) modélisant la propagation de la famille d'ondelettes dans un milieu caractérisé par un profil d'impédance issu de mesures *in situ* (Ker et al., 2011) constituant la référence, b) en appliquant la correction de signature avec des ordres de dérivation entiers pour les modèles de source, et c) en utilisant des ordres fractionnaires. La continuité au niveau de la

zone de transition entre les composantes HF et THF est fortement améliorée et les lignes d'extrema des réflecteurs A et B (figure 1.2 d et e) sont en très bon accord avec celles extraites de la réponse en ondelettes de référence démontrant l'efficacité de la nouvelle approche.

Fort de ces résultats et du fait que la réponse en ondelettes est la transformée en ondelettes de la réflectivité, nous avons appliqué une transformée en ondelettes inverse à la réponse en ondelettes obtenue dans la gamme de dilatation limitée $\mathcal{R}_{a_d}$. L'intégration de la réflectivité permet ensuite d'obtenir un profil d'impédance relative en considérant l'approximation de Born valide. La figure 1.3 illustre la reconstruction du profil d'impédance à partir de la réponse en ondelettes associées aux données sismiques acquises avec les deux composantes HF et THF et comparée au profil d'impédance *in situ* de référence (figure 1.3 a et b), et quand les deux composantes sont fusionnées (figure 1.3 c). L'application de la reconstruction de l'impédance relative au profil acquis par les deux sources SYSIF est présentée en figure 2.2 de la section consacrée à la sismique près du fond. La résolution verticale de ce profil d'impédance relative est de 38 cm.

La réponse en ondelettes permet ainsi de fournir deux types d'attributs sismiques : l'amplitude sismique multi-échelle qui est un attribut géométrique et l'impédance relative qui est un attribut/quantité physique. Ces deux attributs complètent l'arsenal de caractérisation sismique. La fusion de sources réalisée dans le domaine des ondelettes permet d'augmenter la résolution verticale de ces attributs.

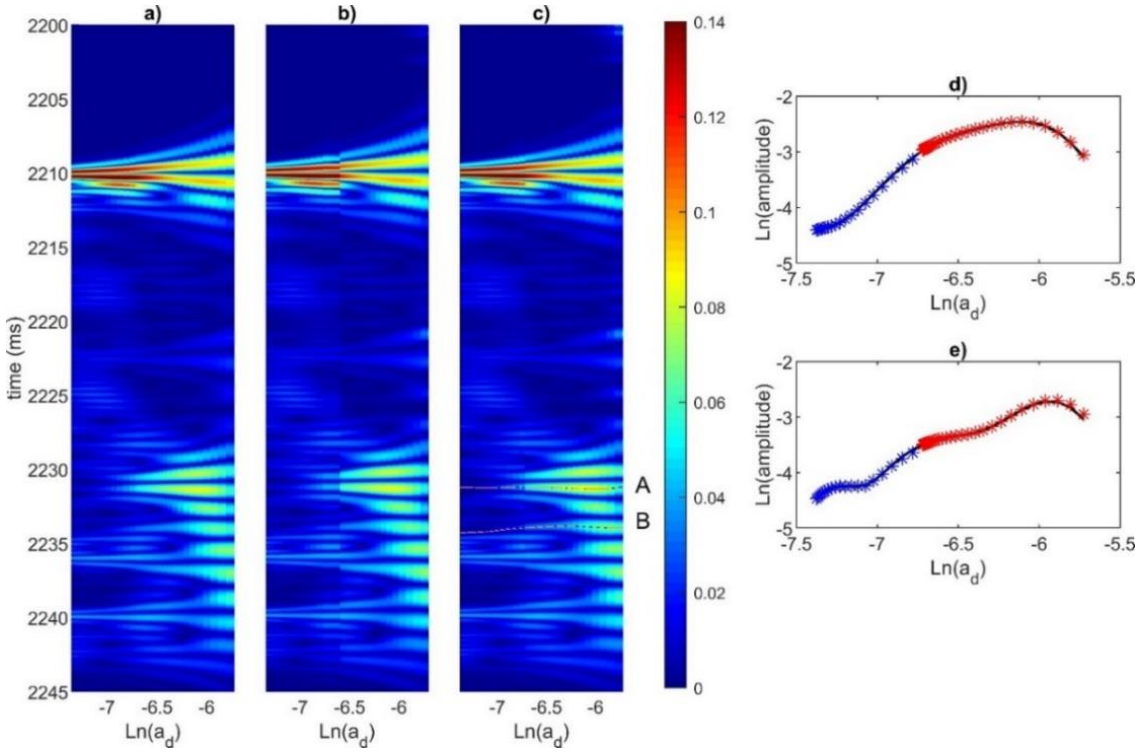

Figure 1.2 : Réponses en ondelettes associées au profil d'impédance *in situ* : a) référence, b) obtenue après correction de source appliquée aux signatures HF et THF de SYSIF avec la méthode exploitant des dérivées entières pour le modèle de source et c) avec une optimisation associée à l'utilisation des dérivées fractionnaires de Gaussiennes. Les lignes d'extrema issues de la fusion des sources SYSIF HF (rouge) et THF (bleu) associées aux réflecteurs A et B (d et e) sont comparées à celles issues de la réponse en ondelettes de référence (en noir).

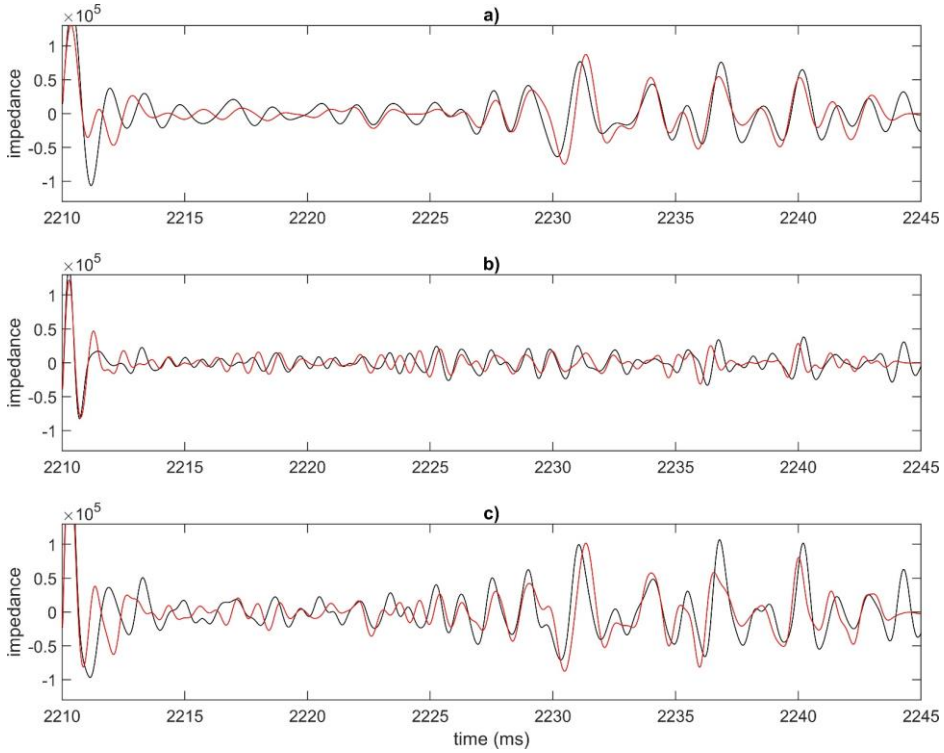

Figure 1.3 : Impédances relatives reconstruites à partir de la transformée en ondelettes inverse appliquée à la réponse en ondelettes obtenues à partir des données sismiques SYSIF (courbes noires) et modélisée avec le profil d'impédance mesuré *in situ* (courbes rouges) pour les deux gammes fréquentielles HF (a) et THF (b) et quand les deux composantes sont fusionnées (c).

3.1.3 Extension de la réponse en ondelettes en présence d'atténuation

Réponse en ondelettes d'un milieu anélastique

Dans un milieu anélastique, l'atténuation sismique modifie les propriétés de l'ondelette source ξ en introduisant une perte d'amplitude, une modification du contenu fréquentiel et de la phase. L'ondelette sismique φ se propageant dans le milieu anélastique varie en fonction de la profondeur (et du temps double de propagation τ), elle a pour expression :

$$\varphi(z,t) = \frac{1}{2\pi}\int_{-\infty}^{+\infty} \hat{\xi}(\omega)\exp(-\beta z)\exp\left[i\omega\left(t-\frac{z}{\gamma}\right)\right] \qquad \text{eq. 1.4}$$

où $\hat{\xi}(\omega)$ est la transformée de Fourier de l'ondelette source ξ avec ω la fréquence angulaire. β est le facteur d'atténuation et γ la vitesse de phase de l'ondelette sismique. Dans le cadre du modèle Kolsky-Futterman (Kolsky, 1956; Futterman, 1962) qui décrit une atténuation linéaire avec la fréquence, le facteur d'atténuation et la phase sont définis par :

$$\beta = \frac{\omega}{2cQ} \qquad \text{eq. 1.5}$$

$$\frac{1}{\gamma} = \frac{1}{c}\left(1 - \frac{1}{\pi Q} Ln\left(\frac{\omega}{\omega_h}\right)\right), \qquad \text{eq. 1.6}$$

où Q est le facteur de qualité, c et ω_h sont respectivement la vitesse de phase et la fréquence de référence. La figure 1.4 illustre les effets de l'atténuation sur la forme d'onde et le spectre d'une ondelette sismique issue d'une ondelette source de type dérivée seconde de Gaussienne (Ricker).

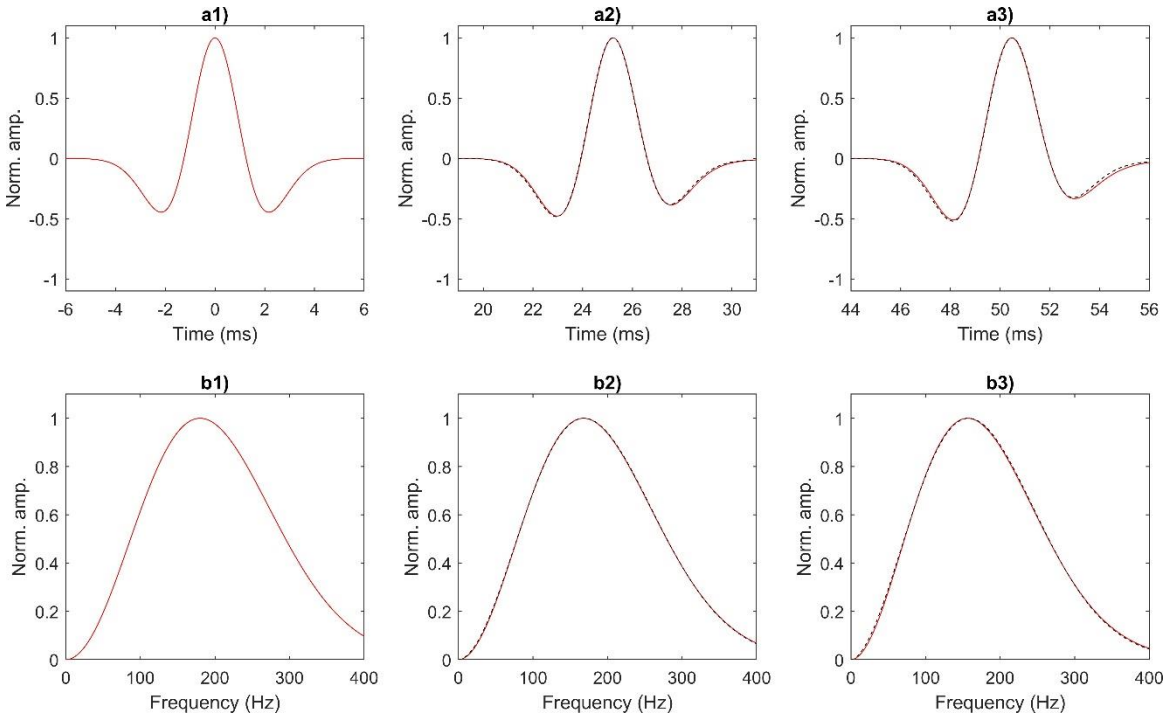

Figure 1.4 : En rouge, ondelettes sismiques normalisées ayant subi une atténuation (facteur de qualité Q = 50) suivant le modèle de Kolsky-Futterman pour des temps de propagation de 25 ms (a2-b2) et 50 ms (a3-b3). L'ondelette source propagée est de type Ricker avec un pic de fréquence à 180 Hz (a1-b1). Représentation dans le domaine temporel (a1-a3) et dans le domaine fréquentiel (b1-b3). En noir, les modèles de dérivées de Gaussiennes optimaux pour chaque ondelette.

Dans un milieu anélastique, la réponse en ondelettes a pour expression :

$$\tilde{R}[\xi, p](t, a) = \int_0^\infty D_a \varphi(z, t) r(z)\, dz. \qquad \text{eq. 1.7}$$

Les conséquences de la modification des propriétés de l'ondelette sismique pour la réponse en ondelettes sont la perte des propriétés de l'analyse par ondelettes et empêche l'extraction des attributs sismiques multi-échelles. Ceci est illustré en figure 1.5 qui représente les modélisations d'une réponse en ondelettes dans un milieu élastique présentant une discontinuité de type Heaviside (figure 1.5a) et dans un milieu anélastique présentant le même réflecteur et caractérisé par une unique valeur de Q. La réponse en ondelettes du milieu élastique présente la même forme, celle d'une dérivée cinquième de Gaussienne (figure 1.5 b), quel que soit la dilatation. Cette forme est celle de l'ondelette analysante car la réflectivité se réduit à un Dirac (Le Gonidec et al., 2002). L'amplitude multi-échelle est une constante (figure 1.5 d). En présence d'atténuation et avec des propriétés de réflexion anélastique négligeables, la réponse en ondelettes ne présente plus la même forme selon la dilatation et l'amplitude maximale croit de manière monotone en fonction de la dilatation (figure 1.5 d).

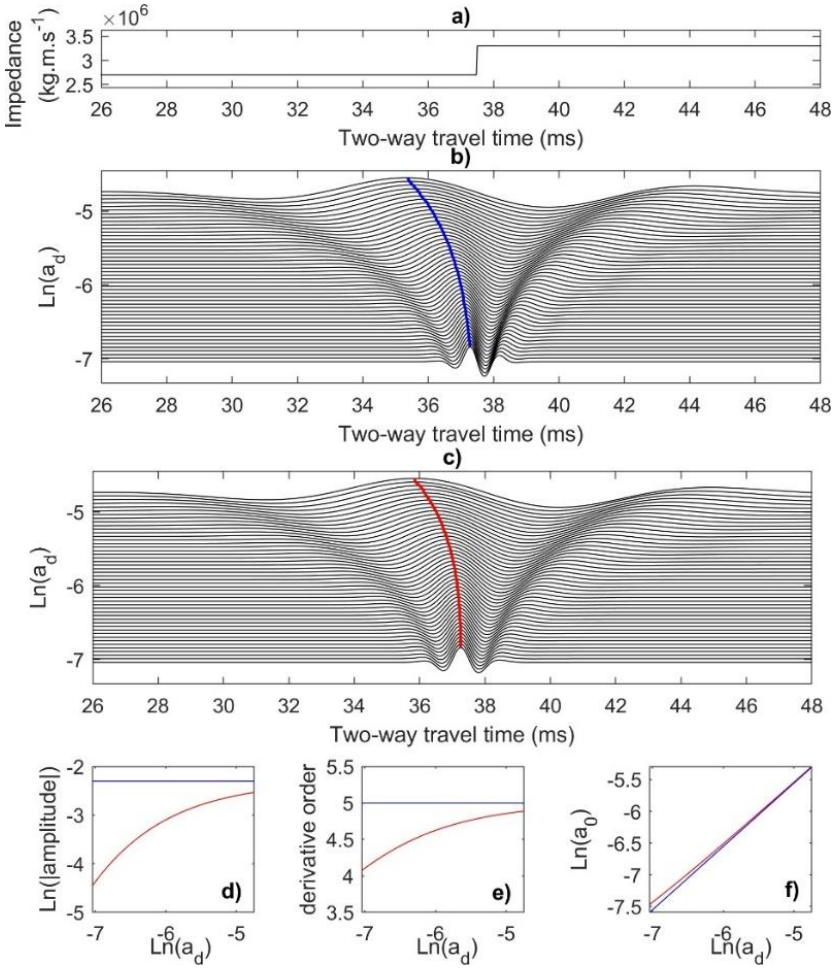

Figure 1.5: Réponses en ondelettes associées à une discontinuité de type Heaviside (a) obtenues dans un milieu élastique (b) et anélastique (c). Comparaisons pour le milieu élastique (bleu) et le milieu anélastique (rouge) des d) amplitudes multi-échelles extraites des lignes d'extrema, e) variation des ordres de dérivation et f) dilatation des ondelettes constituant la réponse en ondelettes.

Quasi-conservation du caractère Gaussien de l'ondelette sismique

Si l'on considère que l'ondelette source émise est une dérivée de Gaussienne d'ordre α et de fréquence angulaire $\omega_0 = 2/a_0$ avec pour expression dans le domaine temporel $\xi(t) = \Omega \frac{d^\alpha}{dt^\alpha} \exp\left(-\frac{\omega_0^2 t^2}{4}\right)$, le phénomène d'atténuation décrit par le modèle de Kolsky-Futterman a pour effet de casser la symétrie de l'ondelette et de décaler le contenu fréquentiel vers les basses fréquences (figure 1.4). Les paramètres de l'ondelette ξ, α et ω_0 ne sont pas conservés au cours de la propagation et nous constatons une décroissance des valeurs des paramètres de l'ondelette (figure 1.5). Cette décroissance suggère que le phénomène d'atténuation peut être considéré comme équivalent à une intégration fractionnaire de ξ et que l'ondelette affectée par l'atténuation $\varphi_\tau(t) = \varphi(z,t)$ peut être approximée par : $\varphi_\tau(t) \simeq \Omega' \frac{d^{\alpha'}}{dt^{\alpha'}} \exp\left(-\frac{\omega_0'^2 t^2}{4}\right)$ où l'ordre de dérivation $\alpha'<\alpha$. Les paramètres α' et ω_0' sont évalués par la méthode de Wang (2015) exploitant le centroïde et l'écart-type du spectre de puissance de $\varphi_\tau(t)$. Les modèles optimaux de dérivées de Gaussiennes correspondant aux ondelettes atténuées sont présentés en figure 1.4 et démontrent la validité de l'approximation qui a été également testée pour différentes valeurs de l'ordre de dérivation initial de l'ondelette (Ker & Le Gonidec, 2018).

Compensation de l'atténuation

La quasi-conservation du caractère gaussien de l'ondelette sismique au cours de la propagation dans un milieu anélastique implique que les effets de l'atténuation peuvent être approximés par un filtre $F_\tau(t)$ appartenant aux fonctions Lévy-alpha stables et que $\varphi_\tau(t) = \xi(t) * F_\tau(t)$. Le fait de pouvoir approximer l'atténuation de l'ondelette à chaque temps de propagation τ, peut être mis à profit pour compenser les effets de distorsions sur la réponse en ondelettes et restaurer les propriétés multi-échelles. Notre objectif est de compenser les effets d'atténuation pour obtenir une famille d'ondelettes partageant la même forme pour toute la gamme de dilatations considérées quel que soit le temps de propagation. Nous identifions dans un premier temps la forme de l'ondelette la plus atténuée pour un temps de propagation maximum. Ceci va nous permettre de fixer la forme de la famille d'ondelettes analysantes caractérisée par l'ordre de dérivation $\bar{\alpha}$. La procédure de compensation repose sur l'application d'un filtre qui modifie la forme de l'ondelette à chaque temps de propagation τ pour passer de l'ordre de dérivation α' à $\bar{\alpha}$ et ainsi conserver une forme unique. Nous avons défini un filtre de forme variable en fonction du temps constitué par : 1) un terme de correction d'amplitude κ, 2) une intégration fractionnaire $\nu = \alpha' - \bar{\alpha}$, 3) un terme gaussien où $\omega_s = \sqrt{\bar{\omega}_0^2 - \omega'^2_0}$ qui compense le décalage de fréquence, 4) un terme de correction du décalage de temps τ_s. Dans le domaine de Fourier, le filtre a pour expression :

$$\hat{h}(\omega) = \kappa(i\omega)^{-\nu} exp\left(-\frac{\omega^2}{\omega_s^2}\right) exp(-i\omega\tau_s). \qquad \text{eq. 1.8}$$

Ce filtrage est appliqué en utilisant la convolution non-stationnaire (Margrave, 1998) où la réponse impulsionnelle $h(t)$ est calculée pour chaque valeur de τ qui a pour expression dans le domaine temporel :

$$h(t) = \kappa \frac{t^{\nu-1}}{\Gamma(\nu)} * exp\left(-\frac{1}{4}\omega_s^2(t-\tau_s)^2\right). \qquad \text{eq. 1.9}$$

Exemple d'application sur données synthétiques avec la source SYSIF

Nous avons appliqué cette méthode de compensation de l'atténuation aux données sismiques modélisées à partir de la source SYSIF HF (figure 1.1 a) et d'un profil d'impédance issu de mesures *in situ* (Ker et al., 2013) en appliquant une propagation anélastique de type Kolsky-Futterman avec Q=50. Après correction de source, la réponse en ondelettes est associée à une dérivée cinquième de Gaussienne (figure 1.6 a). Les lignes d'extrema extraites des réponses en ondelettes obtenues pour le milieu élastique et anélastique (figures 1.6 a et b) pour deux réflecteurs montrent l'importance de la distorsion (figures 1.6 c et d). Pour appliquer la méthode de compensation, nous avons sélectionné le temps maximal de 41 ms supérieur à celui des deux réflecteurs d'intérêt et l'ordre de dérivation $\bar{\alpha}$=4. La réponse en ondelettes compensée est présentée en figure 1.6 e et superposée à une réponse en ondelettes du milieu élastique avec α = 4. Les amplitudes multi-échelles sont restituées avec une erreur inférieure à respectivement 5 et 10 % pour les réflecteurs A et B, démontrant l'efficacité de la méthode de compensation (figures 1.6 f et g).

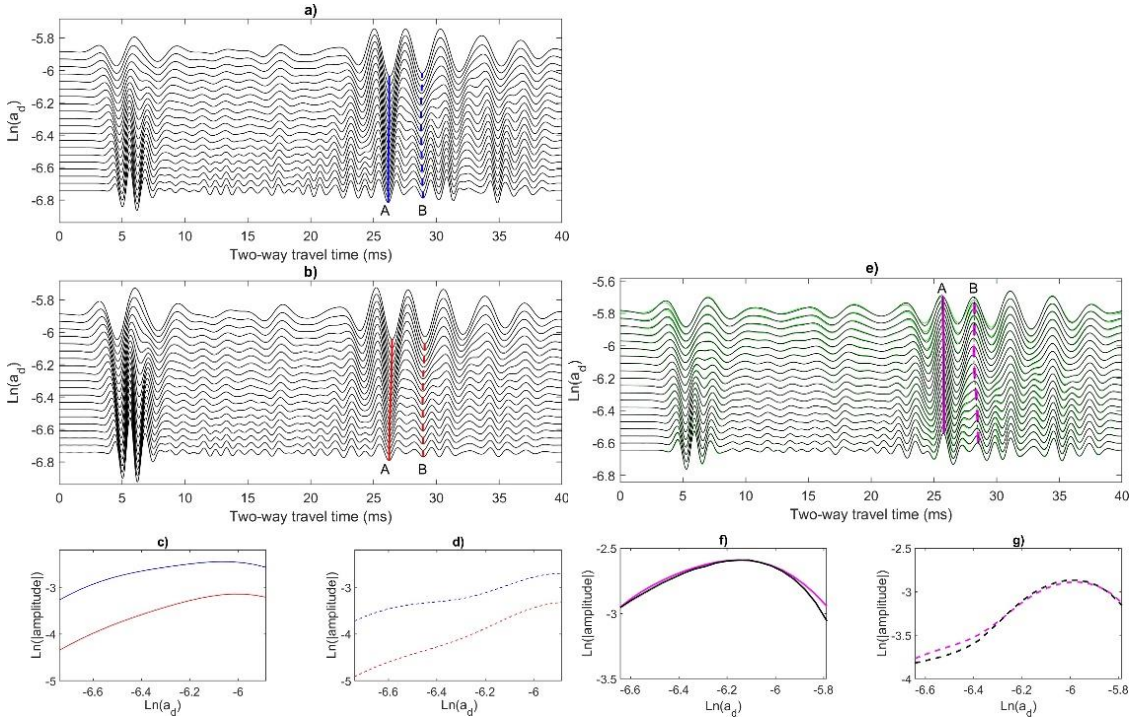

Figure 1.6 : Réponses en ondelettes associées à des données sismiques synthétiques (source SYSIF HF et profil d'impédance issu de mesures *in situ*), pour un milieu élastique (a) et anélastique (b) en considérant une atténuation caractérisée par Q=50 et les lignes d'extrema associées aux réflecteurs A et B (c et d). Réponse en ondelettes (e) et lignes d'extrema après compensation d'atténuation (f et g) comparées avec les résultats obtenus dans un milieu élastique avec une réponse en ondelettes associée à un ordre de dérivation de 4 (au lieu de 5 pour a et b).

Etude de l'impact de la propagation et de la réflexion anélastique sur les attributs sismiques

Dans le travail précédent nous avons considéré que la contribution de l'anélasticité au coefficient de réflexion était négligeable. Mais pour de forts contrastes de facteur de qualité tels que ceux associés aux réservoirs carbonatés (Adam *et al.* ,2009; Takam Takougang & Bouzidi, 2018), d'huiles lourdes (Gurevich *et al.* 2008) ou encore des sédiments comportant des hydrates de gaz (Marin-Moreno *et al.,* 2017) la contribution est importante voire dominante (Bourbié & Nur, 1984). Notre objectif était donc de quantifier les effets cumulés de la propagation et de la réflexion dans un milieu anélastique stratifié (deux couches) sur les attributs sismiques, notamment la fréquence pic souvent utilisée pour l'estimation du facteur de qualité Q. Nous avons considéré la propagation 1D d'une onde plane. La vitesse des ondes de compression est complexe et est exprimée selon le modèle de Kjartansson (1979) :

$$v^*(\omega) \approx c\left(\frac{\omega}{\omega_h}\right)^{\frac{1}{\pi Q}}\left[1+\frac{i}{2Q}\right] \qquad \text{eq. 1.10}$$

Pour développer une approche quantitative d'évaluation des effets de propagation et de réflexion associés à l'anélasticité, nous avons défini les filtres associés à ces contributions. Seuls sont développés ici les modules de ces filtres, les phases sont décrites dans Ker & Le Gonidec (2020). Les modules associés à la propagation M_p et à la réflexion M_r ont pour expression :

$$M_p(\omega) = exp\left(-\frac{\omega\tau}{2Q_1}\right) = exp\left(-\frac{2\omega}{\pi\Gamma}\right), \qquad \text{eq. 1.11}$$

$$M_r(\omega) = \frac{|\eta|}{4}\sqrt{1+16D(\omega)^2}, \qquad \text{eq. 1.12}$$

avec le rapport $\Gamma = \frac{4Q_1}{\pi\tau}$ qui possède la dimension d'une fréquence, le paramètre $\eta = \frac{1}{Q_2} - \frac{1}{Q_1}$ qui quantifie le contraste anélastique et le paramètre $D(\omega) = \frac{R_E}{\eta} + \frac{1}{2\pi} Ln\left(\frac{\omega}{\omega_h}\right)$ avec R_E le coefficient de réflexion élastique. Le filtre prenant en compte la propagation anélastique jusqu'à un réflecteur donné puis la réflexion à l'interface séparant les deux milieux anélastiques est par conséquent $M(\omega) = M_p(\omega)M_r(\omega)$. M possède un comportement qui dépend du rapport R_E/η. Pour $\frac{R_E}{\eta} \leq 0$, le filtre M est un filtre passe-bas car M_p et M_r sont deux fonctions qui décroissent de manière monotone avec la fréquence. Pour $\frac{R_E}{\eta} > 0$, M_r, qui présente un extremum, peut agir soit comme un filtre passe-bas soit comme un filtre passe-haut. Il est important de noter que pour le second cas, le filtre cumulatif peut générer des inversions de phase. La figure 1.7 illustre le module (a1-3) et la phase (b1-3) du filtre cumulatif pour les cas R_E négatif, nul et positif en fonction de la fréquence normalisée $f_n = \omega/\omega_h$ et du paramètre η. Une propagation de 100 ms avec un facteur de qualité $Q = 100$ est considérée dans le milieu supérieur.

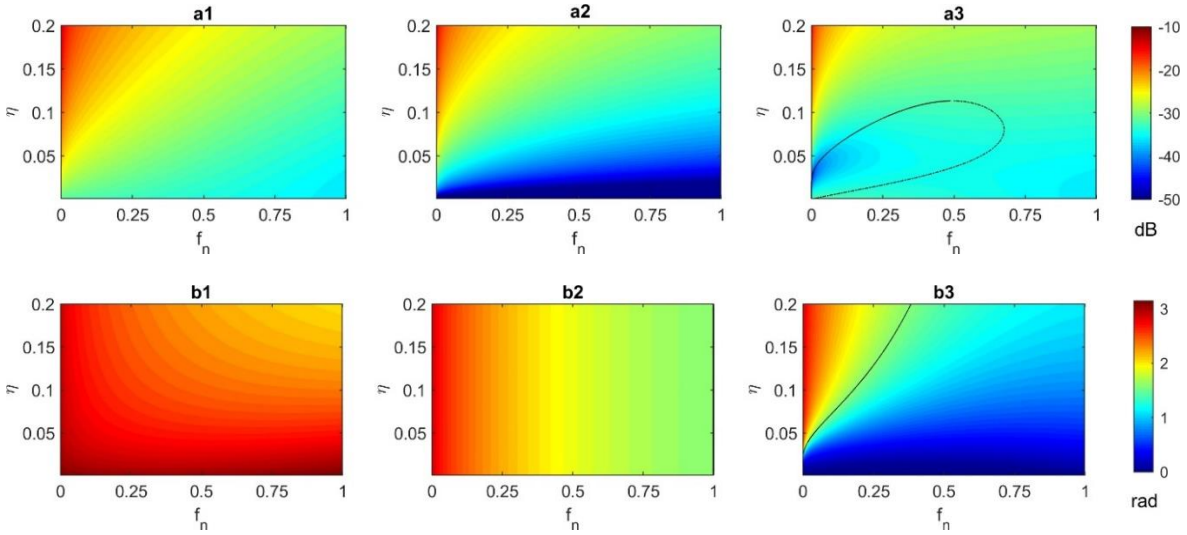

Figure 1.7 : Module (a1-3) et phase (b1-3) du filtre cumulatif pour R_E négatif, nul et positif en fonction de $f_n$et η. Pour a-3, la ligne noire continue représente les valeurs maximales et la ligne en pointillée les valeurs minimales. Pour b3, la ligne noire continue représente la quadrature de phase.

Nous avons ensuite analysé l'impact du filtre cumulatif d'atténuation sur une ondelette sismique de type Ricker en extrayant des attributs sismiques associés au pic du spectre d'amplitude de l'ondelette sismique atténuée à savoir la fréquence pic, l'amplitude et la phase qui lui sont associées. La forme d'onde de l'ondelette réfléchie est présentée en figure 1.8 a-c pour R_E négatif, nul et positif. Pour le cas positif la rotation de phase est bien marquée pour les petites valeurs de η (figure 1.8 c). Les attributs sismiques quantifient précisément l'impact du filtre cumulatif. Pour la fréquence pic d'une valeur initiale de 50 Hz, réduite à 48 Hz par la propagation anélastique, pour R_E négatif, sa valeur décroit jusqu'à 44 Hz pour une grande valeur de η. Pour R_E positif, la valeur évolue de 48 à 46 Hz en présentant une valeur maximale à 52 Hz. Cette augmentation possible de la fréquence pic est un phénomène inattendu mais qui ne se produit que si les contrastes élastiques et anélastiques sont de signe opposé. Les techniques de quantification du facteur de qualité qui reposent sur la fréquence pic sont le plus souvent appliquées en négligeant la contribution de la réflexion anélastique ce qui peut donc entrainer une erreur dans l'estimation du facteur de qualité.

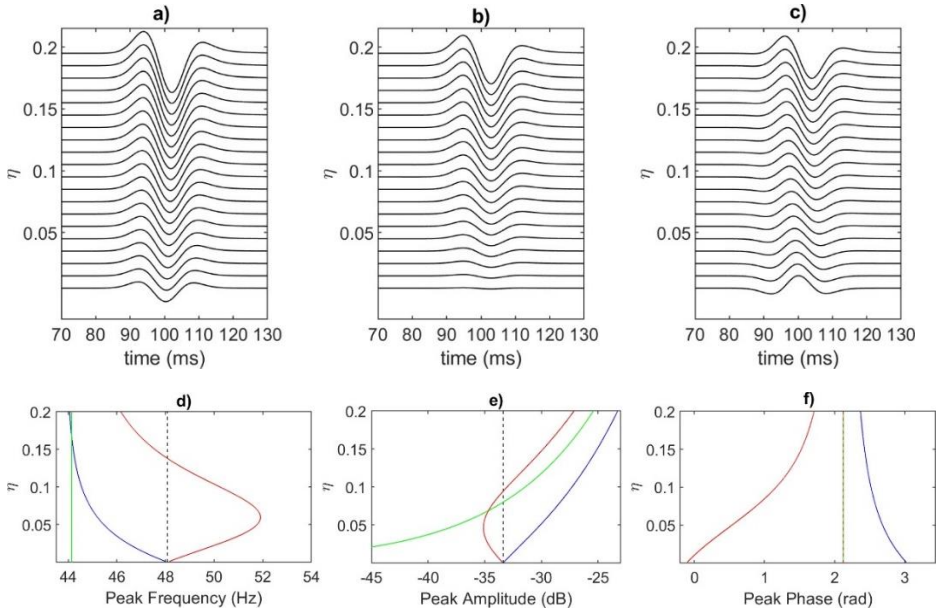

Figure 1.8 : Formes d'onde de l'ondelette sismique affectée par les effets de propagation et de réflexion anélastiques pour différentes valeur de η et R_E négatif, nul et positif respectivement (a-c), d) valeurs du pic de fréquence, de l'amplitude (d) et phase correspondante (f) pour R_E négatif (en bleu), nul (en ver) et positif (en rouge). Les courbes en pointillées représentent les valeurs associées à la seule propagation.

3.1.4 Application à l'analyse de la réflectivité de la thermocline saisonnière

Sismique océanographique appliquée à l'imagerie de la thermocline

La technique de la sismique réflexion a été appliquée avec succès à partir des années 2000 à l'imagerie des structures thermo-halines de l'océan profond de petites échelles telles que les ondes internes (Holdbrook & Fer, 2005) ou de méso-échelles comme les gyres (Biescas et al., 2008 ; Ménesguen et al., 2012). La réflectivité de la colonne d'eau est contrôlée par les variations d'impédance acoustique verticale fonction de la pression, la température et la salinité des masses d'eau selon l'équation d'état de l'eau de mer (Sallarès et al., 2009). La réflectivité associée aux structures océaniques est un ordre de grandeur plus faible que celle des sédiments marins et montre une grande dépendance au contenu fréquentiel de la source sismique (Hobbs et al., 2009). La sismique appliquée à l'océanographie a permis d'imager les structures thermo-halines profondes, mais elle avait été peu employée pour l'étude de structures superficielles à des profondeurs inférieures à 150 m. L'étude de la couche superficielle de l'Océan et de son interaction avec l'atmosphère est d'une très grande importance pour la compréhension et la modélisation des systèmes climatiques. Observer les structures thermohalines superficielles avec des résolutions appropriées le long de profils demeure difficile et l'intérêt d'une méthode de télédétection comme la sismique réflexion est certain. Une première application de la sismique océanographique a permis d'imager la thermocline saisonnière avec succès en juin 2012 dans le golfe de Gascogne lors de la campagne ASPEX avec l'utilisation d'une source de surface très haute fréquence (*Sparker*) avec une fréquence pic de 500 Hz (Piété et al, 2013). Réalisée trois mois plus tard, la campagne IFOSISMO a échoué à imager la thermocline pourtant marquée par un différentiel de température de 4°C, et a montré la nécessité de mieux comprendre la réflectivité de la thermocline et sa dépendance fréquentielle. Nous avons analysé cette réflectivité grâce aux développements analytiques de la réponse en ondelettes effectués dans le cadre d'un modèle de thermocline.

Réponse en ondelettes associée à la thermocline

La thermocline est une zone de transition entre deux masses d'eau. Son profil vertical de température peut être défini en première approximation (figure 1.9) par la fonction erreur de Gauss (erf) :

$$T(z) = T_0 - \frac{\Delta T}{2}\left(1 + erf\left(\frac{z-z_0}{\Delta z/4}\right)\right), \qquad \text{eq. 1.13}$$

où T_0 est la température du milieu supérieur, ΔT l'écart de température, Δz l'épaisseur de la thermocline et z_0 la profondeur du barycentre de la thermocline. Le modèle de thermocline est comparé en figure 1.9 aux mesures *in situ* réalisées avec des sondes pendant la campagne IFOSISMO. Les mesures *in situ* du golfe de Gascogne ont montré que la salinité était quasi-constante et que les variations des masses volumiques étaient négligeables. Les contrastes d'impédance responsables des réflexions sismiques sont donc contrôlés par la vitesse qui est elle-même fonction des variations de température. Le gradient vertical du modèle de température décrit par l'équation 1.13 a pour expression :

$$\frac{dT(z)}{dz} = \frac{-\Delta T}{\sqrt{2\pi}}\frac{1}{\kappa\Delta z}exp\left(\frac{-(z-z_0)^2}{2(\kappa\Delta z)^2}\right), \qquad \text{eq. 1.14}$$

où $\kappa = 1/(4\sqrt{2})$.

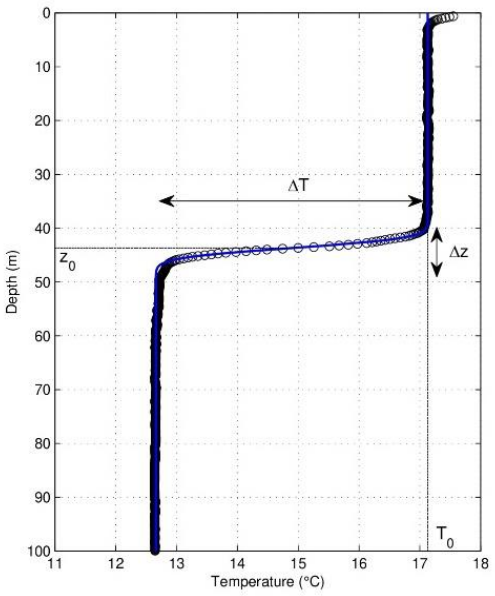

Figure 1.9 : Modèle de profil vertical de température de la thermocline représentée par une fonction erf (courbe bleue) et comparé à la thermocline saisonnière mesurée pendant la campagne IFOSISMO (cercles noirs).

Ce gradient qui s'exprime en fonction d'une Gaussienne permet de faire intervenir la propriété de stabilité des fonctions Lévy-alpha stable et permet le calcul analytique de la réponse en ondelettes. En utilisant une dérivée de Gaussienne d'ordre n comme ondelette analysante ξ_n et en linéarisant la relation entre la vitesse et la température, la réponse en ondelettes a pour expression :

$$R[\xi_n, v](t, a) = r_0\left(\frac{a}{a'}\right)^{n+1}\frac{1}{a'}\xi_n\left(\frac{t-t_0}{a'}\right). \qquad \text{eq. 1.15}$$

Le signal sismique réfléchi par une thermocline modélisée par une fonction erreur avec l'ondelette sismique ξ_n est une ondelette de même nature (*i.e.* une dérivée de Gaussienne d'ordre n) mais avec une dilatation différente $a' = \sqrt{a^2 + 2\left(\frac{\kappa\Delta z}{v}\right)^2}$ qui dépend de l'épaisseur de la thermocline et de la vitesse v. Si n=2 (ondelette de type Ricker), l'amplitude maximale $\mathcal{A}$ de la réponse en ondelettes R (*i.e.* l'amplitude sismique multi-échelle) a pour expression :

$$\mathcal{A} = \mathcal{A}_0 \left(1 + 2\left(\frac{\pi\kappa\Delta z}{\lambda}\right)^2\right)^{-\frac{3}{2}} \qquad \text{eq. 1.16}$$

où l'on a introduit la longueur d'onde de l'ondelette sismique $\lambda = \pi v a$. Cette amplitude peut être exprimée en dB sous la forme :

$$\mathcal{A}^{dB} = \mathcal{A}_0^{dB} + \Lambda^{dB} \qquad \text{eq. 1.17}$$

avec $\mathcal{A}_0^{dB} = 20\log(\mathcal{A}_0)$

$$\Lambda^{dB} = -30\log\left(1 + \left(\frac{4\lambda}{\pi\Delta z}\right)^{-2}\right).$$

L'amplitude sismique multi-échelle est donc constituée de deux termes, le premier est le coefficient de réflexion $\mathcal{A}_0 = \frac{v(T_0-\Delta T) - v(T_0)}{v(T_0-\Delta T) + v(T_0)}$ et le second est un terme d'atténuation qui dépend du rapport entre la longueur d'onde du signal sismique et l'épaisseur de la thermocline $\lambda/\Delta z$. Ce dernier terme est responsable de la dépendance de l'amplitude multi-échelle $\mathcal{A}$ de la thermocline envers la fréquence du signal sismique. L'évolution de Λ^{dB} en fonction de $\lambda/\Delta z$ est présentée en figure 1.10. Quand $\lambda \gg \Delta z$, la thermocline se comporte comme un réflecteur de type Heaviside mais pour $\lambda < \Delta z$ le terme d'atténuation fait décroitre considérablement l'amplitude multi-échelle. Les amplitudes multi-échelles issues des mesures *in situ* d'ASPEX et d'IFOSIMO, auxquelles $\mathcal{A}_0^{dB}$ a été soustrait, sont en bon accord avec le modèle. On constate que l'expérience IFOSISMO est associée à une forte valeur de Λ^{dB}=-22.6 dB pour le rapport $\lambda/\Delta z = 0.45$. Ce qui a pour conséquence de réduire très fortement son amplitude ($\mathcal{A}^{dB} = -71.3$ dB). Un dispositif plus basse fréquence avec une fréquence pic de 180 Hz au lieu de 400 Hz aurait permis d'imager la thermocline lors de la campagne IFOSISMO en réduisant le terme Λ^{dB} (Ker et al., 2015).

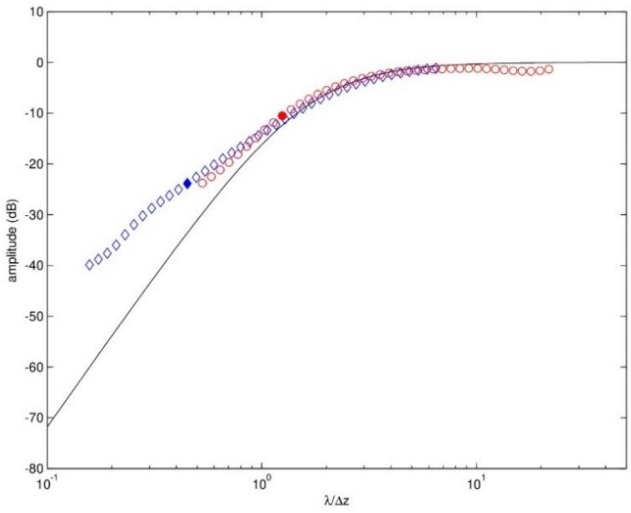

Figure 1.10 : Terme d'atténuation issu du modèle erf de thermocline en fonction du rapport entre la longueur d'onde sismique λ et l'épaisseur de la thermocline Δz (en noir) et comparé à celui des thermoclines mesurées *in situ* lors des campagnes ASPEX (rouge) et IFOSISMO (bleu). Les symboles pleins indiquent le rapport $\lambda/\Delta z$ associées aux expériences sismiques.

Etude multifréquence de la réflectivité de la thermocline saisonnière et de la détectabilité sismique

L'application de la sismique océanographique à l'étude de la thermocline est donc rendue difficile par le manque d'adéquation probable entre les paramètres de l'expérience sismique (contenu fréquentiel, puissance d'émission, profondeur d'immersion, etc…) et la faiblesse de la réflectivité sismique de la thermocline. Au-delà du modèle erf de thermocline et des campagnes ASPEX et IFOSIMO, nous souhaitions avoir une connaissance plus approfondie des propriétés de la thermocline saisonnière du type de celle présente dans le golfe de Gascogne et proposer une première quantification de sa détectabilité en fonction des capacités des systèmes d'acquisition sismique.

Pour réaliser une étude de la distribution de la réflectivité de la thermocline saisonnière (Ker et al., 2016), nous avons exploité plusieurs jeux de mesures hydrographiques acquis par les enregistreurs autonomes ARGO présents dans le Golfe de Gascogne au cours des années 2011, 2012 et 2014. Près de 1000 profils verticaux de température et de salinité ont permis de calculer la réflectivité de la colonne d'eau, d'étudier son évolution au cours de l'année et de confirmer le contrôle de la température sur la réflectivité (figure 1.11 a-c). Une relation linéaire entre le coefficient de réflexion et le gradient de température a pu être montrée (figure 1.11 d) avec un coefficient de corrélation de plus de 0.85. Les images sismiques de ces structures thermohalines superficielles sont donc des images du gradient de température.

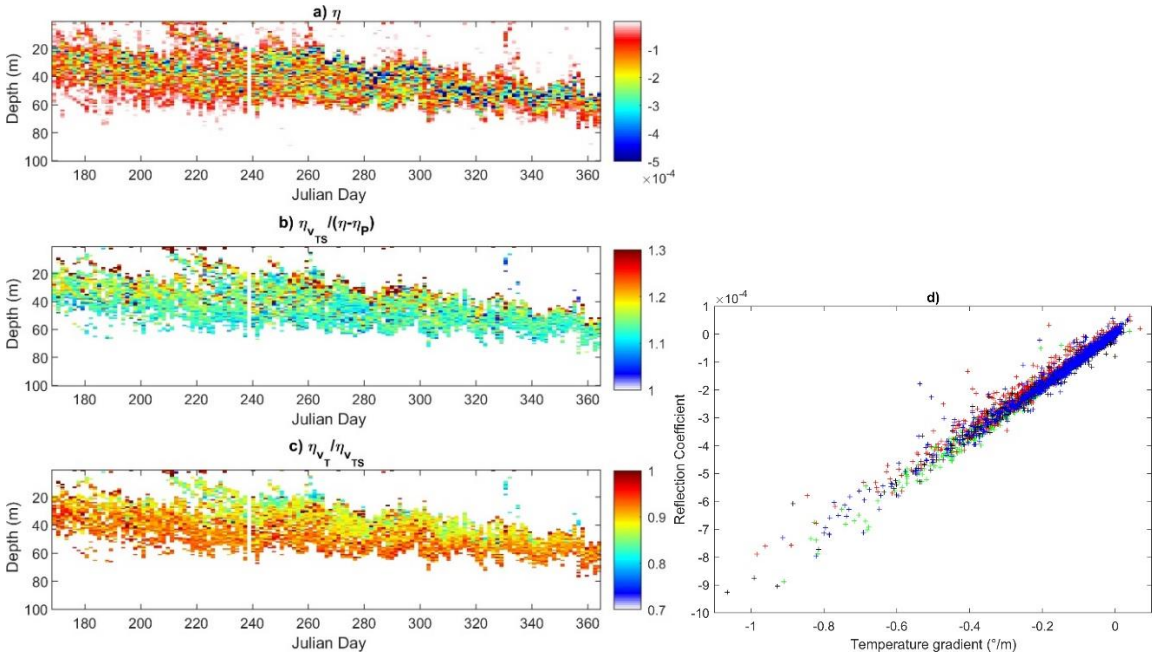

Figure 1.11 : valeurs de la réflectivité estimées à partir des données hydrographiques quand a) la pression, la température et la salinité sont prises en compte, b) contribution de la vitesse à la réflectivité, c) rapport des contributions de la vitesse à la réflectivité entre la contribution seule de la température et avec la température et la salinité, d) coefficient de réflexion en fonction du gradient de température.

Nous avons utilisé l'amplitude multi-échelle sismique pour étudier la réponse sismique multifréquence de la thermocline. Cette étude s'est appuyée sur la modélisation des réponses en ondelettes des thermoclines en utilisant les mesures *in situ* et l'extraction des lignes d'extrema associées aux réflecteurs les plus énergétiques. Ceci nous a permis de définir la profondeur et la dépendance fréquentielle de ces réflecteurs. Cette approche a fourni la première distribution statistique de l'amplitude de la réflexion sismique $\mathcal{A}$, dépendante de la fréquence, associée à la

thermocline dans la gamme [50-300 Hz]. Les amplitudes multi-échelles sont réparties dans une gamme de 20 dB centrée entre -100 dB à 50 Hz et -113 dB à 300 Hz (figure 1.12). Une analyse similaire a été réalisée dans la gamme [50-1000 Hz] à partir de données ARGO haute résolution mais sur seulement 69 profils (figure 1.13).

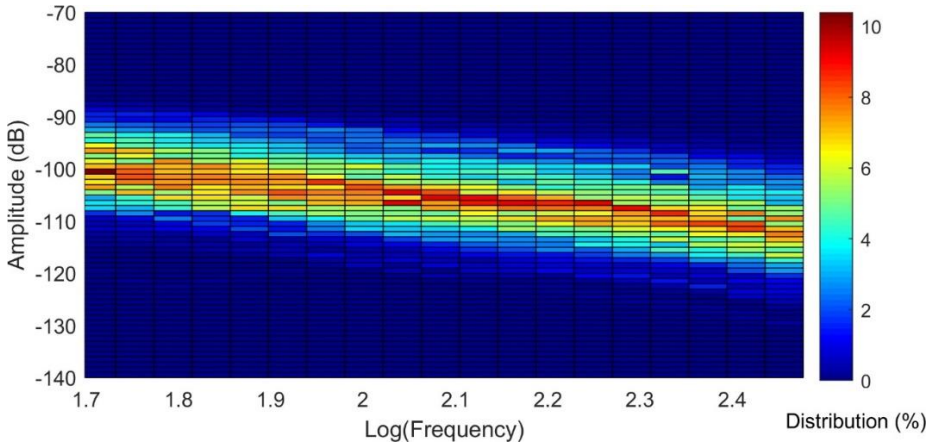

Figure 1.12 : Distribution des amplitudes multi-échelles dans la gamme 50-300 Hz obtenues à partir des données des flotteurs ARGO dans le golfe de Gascogne.

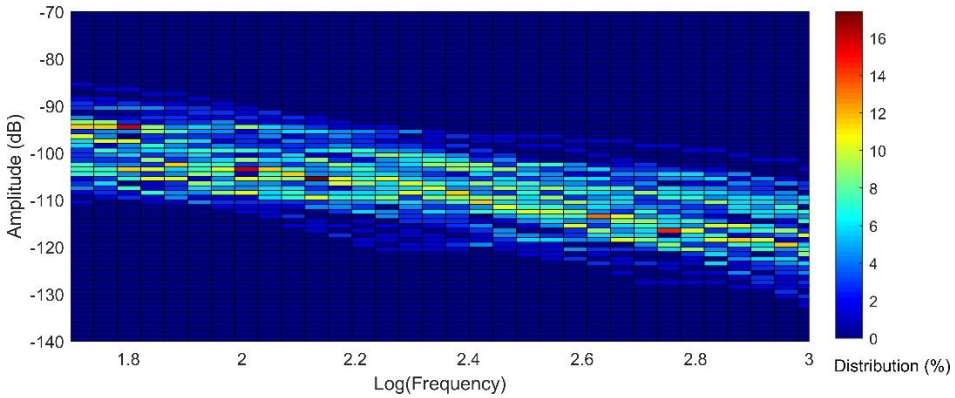

Figure 1.13 : Distribution des amplitudes multi-échelles dans la gamme 50-1000 Hz obtenues à partir des données haute résolution (69 profils) des flotteurs ARGO dans le golfe de Gascogne.

La détectabilité sismique de la thermocline doit satisfaire l'inégalité $\mathcal{S} + \mathcal{A} \geq \mathcal{T} + \mathcal{N}$ avec $\mathcal{S}$ qui qualifie l'émission de la source et les gains de réception et de traitement, $\mathcal{T}$ est le seuil de détection (fixé à 6 dB) et $\mathcal{N}$ le niveau de bruit de l'expérience sismique. Nous avons rassemblé tous les termes non dépendants du réflecteur dans un seul terme $\mathcal{C} = \mathcal{S} - \mathcal{T} - \mathcal{N}$ qui mesure la capacité globale d'une expérience sismique à détecter un réflecteur. Les dispositifs caractérisés par une valeur de $\mathcal{C}$ proche de 100 dB utilisés durant les campagnes ASPEX et IFOSISMO peuvent détectés seulement 2 % des thermoclines. Une valeur de $\mathcal{C}$ > 120 dB associée à une fréquence centrale entre [200-300 Hz] permettrait une détection de 90 % des thermoclines. Les systèmes sismiques actuels qui sont mis en œuvre depuis des petits navires ne possèdent pas de telles caractéristiques (contenu fréquentiel, puissance d'émission…). Des développements instrumentaux spécifiques sont nécessaires afin de faire de l'imagerie sismique de la thermocline, un outil efficace de détection et d'analyse.

3.1.5 Bilan sur l'analyse sismique multi-échelle

L'analyse sismique multi-échelle appliquée à des données sismiques avec un contenu fréquentiel large telles que celles acquises par SYSIF, permet grâce à la correction de source de réaliser une transformée en ondelettes de la réflectivité et d'utiliser les lignes d'extrema pour analyser la morphologie des discontinuités d'impédance. Elle permet la fusion de sources pour augmenter la résolution verticale. Grâce à la transformée inverse, il est également possible de reconstruire l'impédance relative. Limitée à un régime de diffusion simple, à une incidence normale et à un milieu non atténuant, cette analyse multi-échelle est d'une très grande utilité pour la comparaison avec des mesures *in situ* pour des sédiments marins meubles de type hémipélagique. La correction de l'effet de l'atténuation sur la forme des ondelettes permet de conserver les propriétés de la transformée en ondelettes pour l'analyse de milieux anélastiques. Au-delà de l'application aux données SYSIF, l'analyse sismique multi-échelle est un formidable outil pour modéliser la réponse sismique et quantifier la détectabilité des réflecteurs comme nous avons pu le démontrer avec l'exemple de la thermocline saisonnière.

Articles associés

Ker, S. & Le Gonidec, Y. (2020). Filtering of a Ricker wavelet induced by anelastic seismic wave propagation and reflection. *Journal of Geophysics and Engineering*, 17(5), 838-851.

Ker, S. & Le Gonidec, Y. (2018). Fractional integration of seismic wavelets in anelastic media to recover multiscale properties of impedance discontinuities. *Geophysics*, 83(2), V61-V71.

Ker, S., Le Gonidec, Y., Marié, L. (2016). Multifrequency seismic detectability of seasonal thermoclines assessed from ARGO data. *Journal of Geophysical Research: Oceans*, 121(8), 6035-6060.

Ker, S., Le Gonidec Y., Marié, L., Thomas, Y., Gibert, D. (2015). Multiscale seismic reflectivity of shallow thermoclines. *Journal of Geophysical Research: Oceans*, 120(3), 1872-1886.

Ker, S., Le Gonidec, Y., Gibert, D. (2013). Multiresolution seismic data fusion with a generalized wavelet-based method to derive subseabed acoustic properties. *Geophysical Journal International*, 195(2), 1370-1383.

3.2 Développement de la sismique près du fond multidéport

L'objectif de cette thématique est d'améliorer la résolution de l'imagerie sismique du sous-sol marin par grande profondeur d'eau et de pouvoir estimer les vitesses de propagation dans les sédiments superficiels en développant une capacité multidéport à l'engin remorqué en fond de mer SYSIF.

3.2.1 Sismique très haute résolution près du fond avec l'engin remorqué SYSIF

Intérêt de la sismique près du fond

L'obtention d'une imagerie sismique de résolution métrique à sub-métrique (*i.e.* sismique très haute résolution THR) des sédiments marins superficiels par des dispositifs d'acquisition déployés proches de la surface de la mer souffre de plusieurs limitations dès que la hauteur d'eau dépasse 500 m. La première limitation est la puissance d'émission des sources acoustiques hautes-fréquences (> 200 Hz), de l'ordre de 190-220 dB ref. 1 μPa @ 1 m, insuffisante pour contrecarrer les pertes en transmission associées à la divergence sphérique (par exemple 33 dB pour une hauteur d'eau de 1000 m). La seconde limitation est la précision des analyses de vitesse de propagation limitée par une faible gamme d'incidence angulaire. En effet, les relatifs faibles déports entre la position de la source et les récepteurs, inférieurs à la profondeur des réflecteurs ciblés, ne permettent pas d'obtenir une couverture angulaire suffisante pour une détermination précise des vitesses. Or la connaissance précise du champ de vitesse de propagation est nécessaire pour obtenir une résolution horizontale optimale. Enfin, la troisième limitation est une forte empreinte des échos latéraux enregistrés pour les profils acquis en deux dimensions, du fait d'une largeur de la zone de Fresnel dépendante de la hauteur d'eau (Marsset et al., 2010 ; Ker et al., 2010). A titre d'exemple, la zone de Fresnel pour une fréquence de 500 Hz atteint 40 m pour une hauteur d'eau de 1000 m. Pour réduire fortement l'impact de ces limitations, l'ensemble du système d'acquisition sismique doit être tracté près du fond. Avant le développement d'un système sismique intégralement placé près du fond, l'étape intermédiaire fut de développer dans les années 1970, un système de réception près du fond en conservant la source en surface (Bryan, 1979; Lewis et al., 1979). A l'Ifremer, le système Pasisar marqua cette étape (Nouzé et al., 1997). Le premier système de sismique remorqué intégralement en fond de mer fut le DTAGS (*Deep Towed Acoustics and Geophysics System*) développé par le *National Research Laboratory* aux Etats-Unis dans les années 1980 et 1990 (Fagot, 1986 ; Rowe & Gettrust, 1993).

Challenges de la sismique près du fond

Le premier challenge pour la réalisation d'un système sismique remorqué en fond de mer est de faire fonctionner une source acoustique et des récepteurs dans un environnement caractérisé par des fortes pressions hydrostatiques. Le développement d'hydrophones opérant par grand fond fut réalisé dans les années 1960 à partir de céramiques piézoélectriques. Celui de la source est plus récent (années 1990) et s'appuie sur des sources avec une cavité ouverte et d'amplificateurs de puissance déportés dans l'engin tracté près du fond. Le second challenge est de maîtriser le positionnement, par grande profondeur d'eau, de la source et des récepteurs en s'appuyant sur le positionnement acoustique moins précis que celui obtenu avec le système GPS. Le troisième challenge est de développer des protocoles d'acquisition et de traitement des données spécifiques à cette géométrie d'acquisition par grand fond afin d'obtenir une imagerie à très haute résolution des structures superficielles. L'expérience du DTAGS a montré que plusieurs limitations empêchaient d'atteindre une résolution optimale de l'image sismique. La première limitation est associée aux paramètres d'acquisition : l'altitude très grande du DTGAS entre 350 et 500 m choisie pour éviter les interférences entre les arrivées directes et réfléchies et la faible récurrence de tirs de 20-30 s réduisent fortement la pénétration, la résolution, la gamme d'angles d'incidence et l'échantillonnage spatial (Chapman et al., 2002). La seconde limitation est due à l'approche pour déterminer le positionnement des récepteurs qui s'appuie sur l'exploitation des temps d'arrivées

directes et réfléchies sur la surface de l'eau. Cette approche ne fournit pas une précision suffisante et des corrections statiques doivent être appliquées (Walia & Hannay, 1999; He et al., 2009). Enfin, les analyses de vitesses conventionnelles (correction de courbure normale) ne sont pas réalisées directement du fait des profondeurs différentes de la source et des récepteurs mais après des corrections statiques pour propager les données vers une même profondeur d'acquisition. L'utilisation de corrections statiques à la place de corrections dynamiques affecte la cohérence des signaux et introduit des incertitudes importantes dans l'estimation des vitesses (He et al., 2009).

Développement de l'engin remorqué SYSIF

Dans le cadre de l'étude des aléas géologiques marins, l'Ifremer a décidé de développer dans les années 2000 sous la direction de Bruno Marsset, une technologie d'acquisition sismique THR monocapteur près du fond de mer qui a abouti à la réalisation du système opérationnel SYSIF (Système Sismique remorqué en Fond de mer) en 2007 en collaboration étroite avec le service « systèmes sous-marins » de l'Ifremer dirigé par Pierre Léon. SYSIF permet d'acquérir des données sismiques grâce à la technologie des transducteurs Janus-Helmholtz développée par Yves Le Gall (Ifremer). Le transducteur Janus-Helmholtz est composé d'un moteur piézoélectrique (Janus) formé par un pilier de céramiques inséré entre deux pavillons identiques. Cette structure est montée à l'intérieur d'un boîtier cylindrique ouvert en son milieu, créant ainsi l'évent de ce transducteur (Le Gall, 1999). Le couplage entre le moteur Janus et la cavité délimitée par le boîtier cylindrique permet de générer un signal large bande. Ce type de transducteur présente les avantages de fonctionner par grande immersion et de la répétitivité de l'émission. Son plus faible niveau d'émission (196 dB ref. 1 μPa @ 1 m) par rapport aux sources de type *sparker* ou piézoélectrique de surface est compensé par des durées d'émission plus grandes, plusieurs dizaines de millisecondes. SYSIF peut être opéré avec une résolution dépendante du choix du transducteur installé au sein de l'engin remorqué avec deux gammes de fréquences possibles qui sont : 220-1050 Hz ou 580-2200 Hz avec des signaux modulés linéairement en fréquence (*chirp*) sur des durées de 100 et 50 ms respectivement. Le dispositif de réception est constitué par une antenne de réception (flûte sismique ou *streamer*) avec deux éléments : le premier est un hydrophone unitaire, le second est une antenne de 6 hydrophones. Le positionnement de l'engin est obtenu avec une balise acoustique à base courte. L'engin est également instrumenté d'une centrale d'attitude, d'un altimètre et d'un capteur d'immersion (figure 2.1). L'engin est remorqué à la vitesse de 2 nœuds à une altitude quasi constante fixée entre 50 et 100 m. La récurrence de tirs est optimisée afin d'éviter de faire coïncider l'enregistrement des réflexions primaires avec celui des réflexions multiples de tirs précédents tout en assurant un bon échantillonnage spatial (Ker et al., 2010).

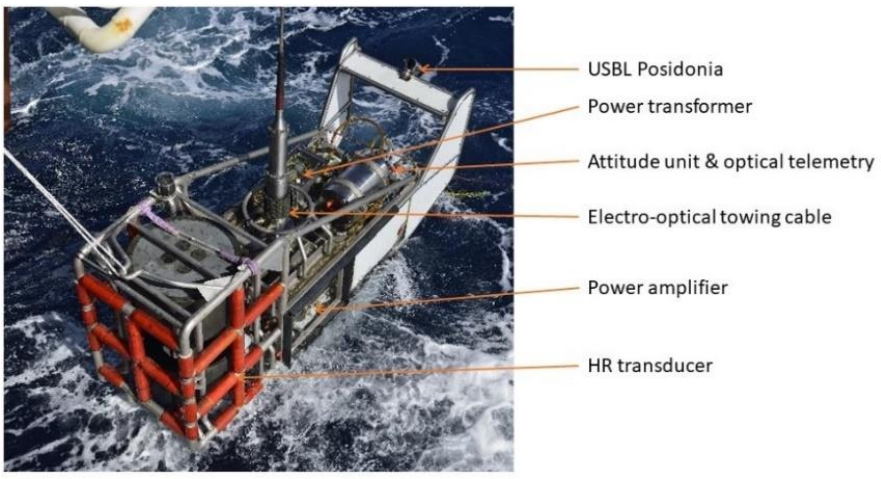

Figure 2.1 : Engin sismique remorqué près du fond SYSIF

Au cours de ma thèse, j'ai pu contribuer à améliorer significativement la résolution verticale des profils sismiques SYSIF grâce à la déconvolution de la signature de la source acoustique en exploitant l'enregistrement en incidence normale de la signature en champ lointain des deux transducteurs. J'ai pu également démontrer la faisabilité d'une imagerie sismique exploitant une acquisition multidéport (Ker et al., 2010). Après ma thèse, j'ai poursuivi mes travaux sur la sismique près du fond monotrace en proposant une technique de fusion des données acquises par les deux transducteurs pour un même profil en exploitant les mesures de signatures en champ lointain (figure 2.2). Ceci a permis d'atteindre une résolution verticale de 38 cm pour le profil d'impédance acoustique. Le profil de masse volumique a été estimé à l'aide de la composante continue des données *in situ* (Ker et al., 2013) et du fait d'une vitesse de propagation quasi-constante à 1485 $m.s^{-1}$ (Ker et al., 2011). La technique de fusion est associée à une approche reposant sur l'analyse en ondelettes qui a été présentée dans le premier volet de mes travaux (cf. partie 3.1.2).

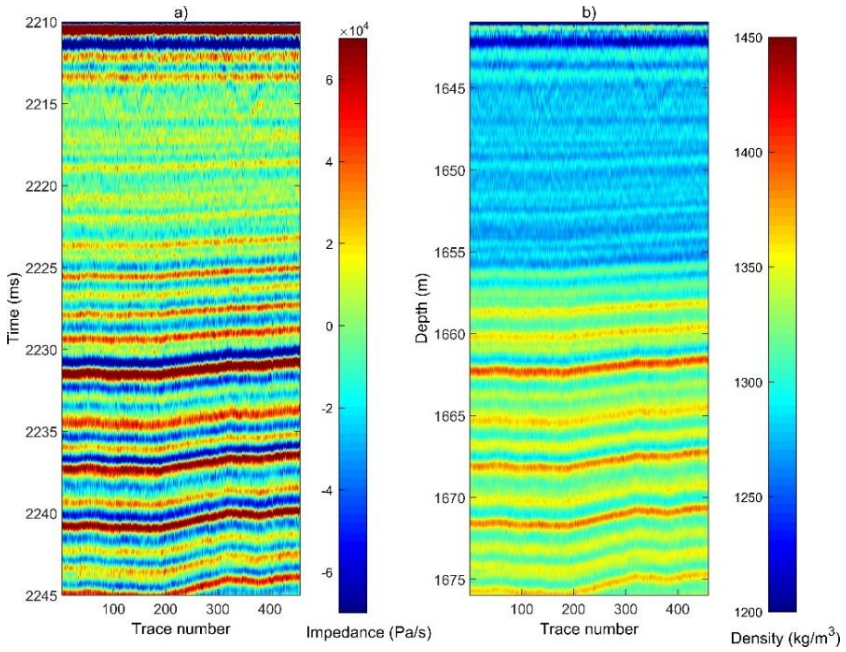

Figure 2.2 : Profils d'impédance relative (a) et de masse volumique (b) obtenus à partir de la fusion des données SYSIF acquises par les deux transducteurs (données de la campagne ERIG3D).

3.2.2 Développements instrumentaux et méthodologiques associés à l'acquisition multidéport près du fond SYSIF

En 2010, conforté par l'étude de faisabilité réalisée pendant ma thèse, il a été décidé de procurer à SYSIF une capacité d'acquisition multidéport avec le développement d'une antenne de réception multitrace ayant pour objectifs d'améliorer la résolution latérale et de permettre la détermination des vitesses de propagation. Les principaux challenges associés à cette acquisition multidéport étaient l'obtention d'un positionnement précis de la source et des récepteurs et le développement d'une séquence de traitement des données multitraces SYSIF.

Développements instrumentaux

Le développement de cette antenne de réception sous la direction de Bruno Marsset, effectué entre 2011 et 2013 avec un financement Carnot, repose sur l'utilisation d'hydrophones unitaires

numériques. La résolution recherchée requiert de proscrire les filtrages d'antenne dus à la sommation de plusieurs hydrophones proches, inévitables avec la géométrie complexe d'acquisition où l'altitude de la source évolue constamment en fonction de la bathymétrie entrainant des mouvements importants de l'antenne de réception. La numérisation se fait au sein même de la cavité cylindrique de l'hydrophone composé d'un empilement de céramiques. Le développement de la carte de numérisation effectué par Eric Menut (Ifremer) a permis d'intégrer le conditionnement du signal analogique (filtrage fréquentiel et pré-amplification), la conversion analogique-numérique, et de transmettre les données par protocole Ethernet via des commutateurs réseaux répartis le long de la flûte sismique. Pour aider au positionnement de chaque hydrophone, j'ai initié l'intégration à la carte numérique de capteurs MEMS (Micro Electro Mechanical Systems) mesurant le tangage, le roulis et le cap. La figure 2.3 présente l'intégration de la carte électronique dans un hydrophone HTI 90 (HighTech Inc.). Les commutateurs réseaux sont eux abrités dans des conteneurs en titane. La réalisation d'une antenne de réception a été finalisée en 2013 avec 52 hydrophones numériques espacés de 2 m sur une distance de 10 à 112 m et 8 commutateurs réseaux intégrés dans une flûte sismique par Sercel (Marsset et al., 2014). L'acquisition SYSIF multidéport a été testée pour la première fois lors de la campagne d'essai ESSYPEN (2013) et a ensuite été utilisée lors des campagnes océanographiques PRISME 2 (2013) et GHASS (2015).

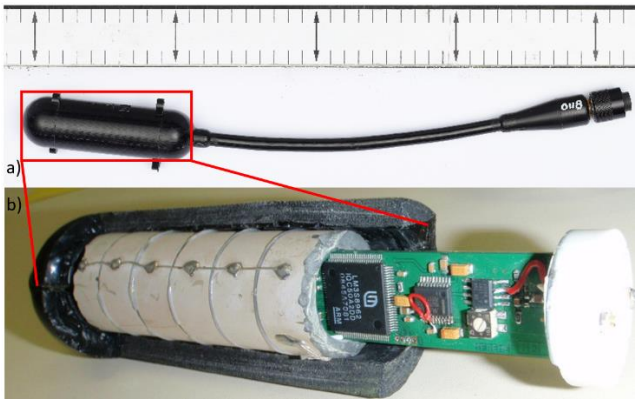

Figure 2.3 : a) hydrophone HTI et b) carte numérique insérée dans la cavité de l'hydrophone (l'échelle est de 10 cm entre deux fléches)

Développements méthodologiques

Les données sismiques multitraces THR acquises en grande profondeur d'eau par un engin remorqué près du fond ont nécessité le développement de méthodes de traitement adaptées à ce nouveau type de données. Afin d'augmenter la couverture angulaire pour l'analyse de vitesse et pour diminuer la zone de Fresnel, les profils SYSIF sont acquis à l'altitude de 50 m, posant le problème de la superposition des signaux associés aux arrivées directes et réfléchies. Du fait de la durée d'émission de 100 ms et de la proximité du fond, ces deux types de signaux interférent. Le traitement de signature, qui exploite la signature en champ lointain en incidence normale, est inopérant pour la déconvolution de l'arrivée directe. En effet, le transducteur Janus-Helmholtz n'étant pas omnidirectionnel, les signatures des arrivées directes et réfléchies sont très différentes (figure 2.4 a). Il a donc été nécessaire que nous développions une technique de suppression de l'arrivée directe à appliquer avant le traitement de signature. Pour supprimer l'arrivée directe, nous avons développé une approche dans le domaine temps-fréquence (Marsset et al., 2018). La représentation temps-fréquence que nous avons choisie est le spectrogramme obtenu à partir de la transformée de Fourier à court-terme qui permet une transformée inverse. Dans ce domaine

temps-fréquence, les arrivées directes et réfléchies sont bien séparées (figure 2.4 b) et l'application d'un masque sur l'arrivée directe permet, après transformée inverse, une suppression de cette arrivée directe dans le domaine temporel (figures 2.4 d et e).

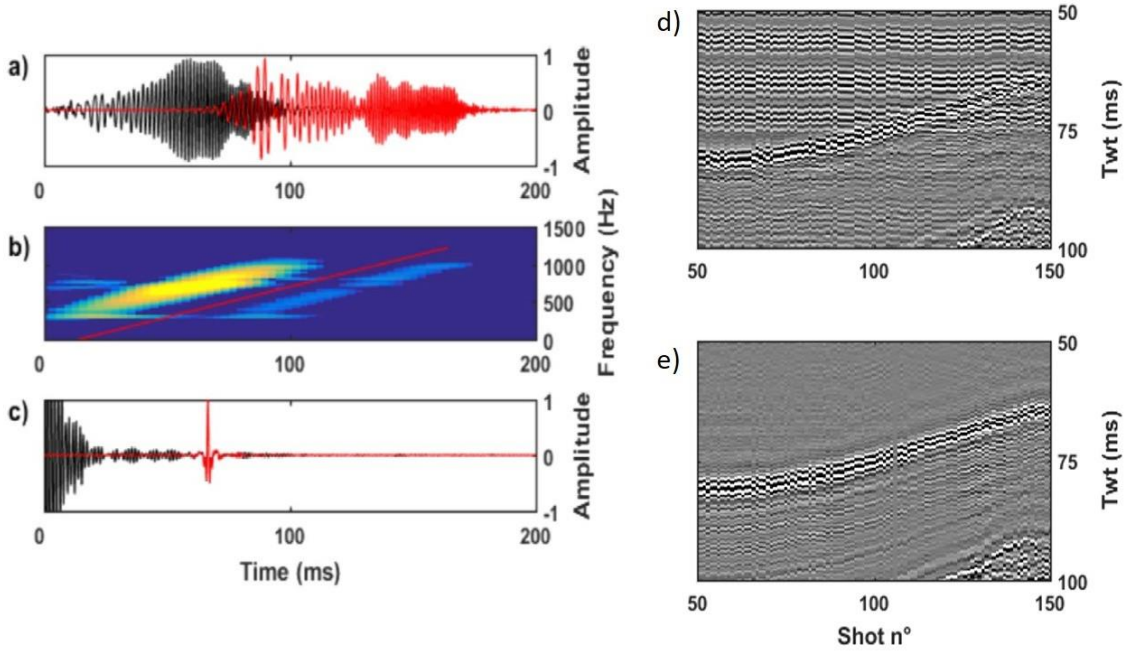

Figure 2.4 : a) arrivées directe avec une émission à 90° (en noire) et réfléchie avec une émission proche de l'incidence normale (en rouge), b) spectrogramme qui permet de séparer les deux arrivées, c) résultats de déconvolution avec la signature en incidence normale, d) collection récepteur commun où les arrivées directes horizontales interférent avec les arrivées réfléchies, e) même collection après la suppression de l'arrivée directe dans le domaine temps-fréquence.

Des développements méthodologiques ont été également nécessaires pour définir précisément le positionnement des hydrophones. Lors d'une acquisition sismique près du fond de mer, l'engin sous-marin portant la source est remorqué à une altitude quasi-constante au-dessus du fond marin, provoquant des variations de profondeur du système d'acquisition sismique. Les mouvements verticaux de la source se propagent le long de la flûte remorquée sous forme d'ondes mécaniques générant des variations dans les distances source-récepteur et dans la profondeur des récepteurs. La stratégie initiale de positionnement reposait sur l'exploitation des données d'attitude collectées par les capteurs MEMS. L'analyse de ces données a permis de mettre en évidence que seules les données de tangage subissaient des variations importantes au contraire des données de roulis et cap. Le traitement des données de tangage consiste en une première correction associée à une calibration des capteurs MEMS réalisée sur le pont puis en l'application d'un filtrage passe-bas. L'évolution de l'immersion de SYSIF lors de l'acquisition d'un profil et les données de tangage correspondantes sont illustrées par la figure 2.5. Il est intéressant de noter qu'une variation de l'immersion de la source impacte immédiatement la tête du *streamer* et que la déformation, qui se propage le long du *streamer*, impacte plus tardivement le dernier hydrophone (dans l'exemple de la figure 2.5, 100 s plus tard soit 50 tirs).

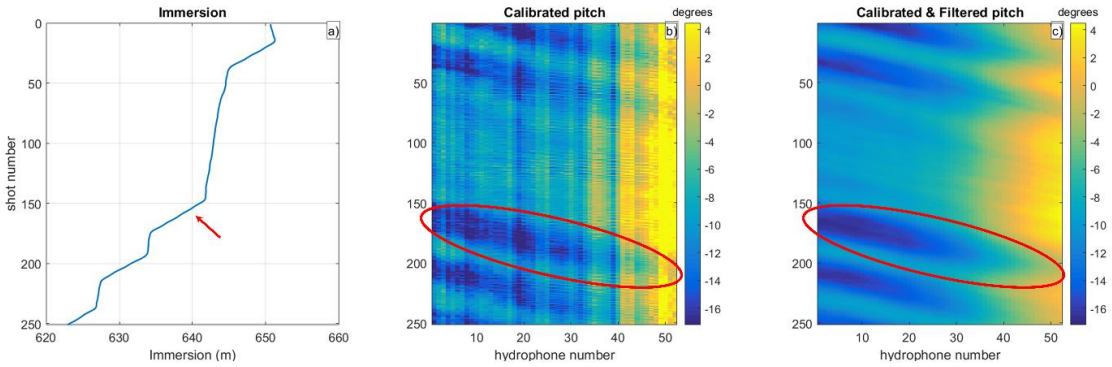

Figure 2.5 : a) Variation de l'immersion de l'engin remorqué (a) et valeurs de tangage des capteurs MEMS associées à ces variations d'immersion après calibration (b) et filtrage (c). L'impact d'une variation importante de l'immersion de la source sur la forme du streamer est souligné par la flèche rouge et les valeurs de tangage entourées.

Les données de tangage après traitement permettent de restituer la forme du *streamer* qui est considéré comme une courbe plane. La position de chaque hydrophones (x_r^i, z_r^i) est obtenue à partir de l'abscisse curviligne r^i, l'angle de tangage α et la distance entre le barycentre du transducteur et le point de traction du streamer $x_0 = 2.1$ m :

$$\begin{cases} x_r^i = x_0 + \int_0^{r^i} \cos[\alpha(r)]\, dr \\ z_r^i = \int_0^{r^i} \sin[\alpha(r)]\, dr \end{cases}, \qquad \text{eq. 2.1}$$

L'abscisse curviligne des hydrophones évolue entre 8 et 110 m avec un espacement de 2 m.

L'analyse de la variation de la forme du *streamer* associée à des sections de profil sans variation d'immersion de la source a révélé que la distribution des masses des équipements électroniques le long du *streamer* n'était pas uniforme et que le *streamer* avait tendance à plonger dans sa première partie puis à remonter à son extrémité (figure 2.6).

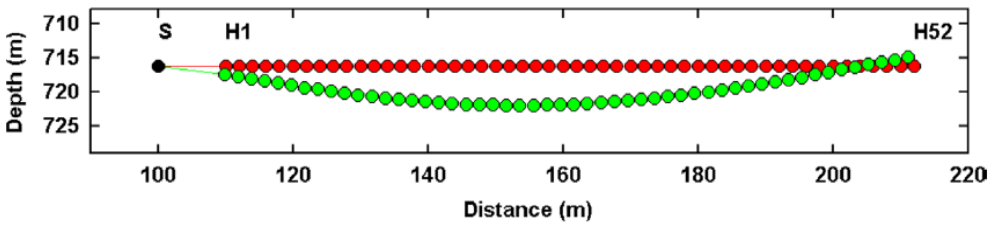

Figure 2.6 : Forme du streamer de SYSIF obtenue avec les données de tangage de capteurs MEMS (en vert) à comparer avec une forme idéale (en rouge).

La géométrie complexe, variant au cours du temps de l'acquisition multitrace SYSIF, rend inopérantes les techniques conventionnelles de traitement de sismique marine qui considèrent la source et les récepteurs à la même profondeur. Pour résoudre ce problème de géométrie, nous avons proposé d'utiliser la migration en profondeur avant sommation de Kirchhoff (Marsset et al., 2014). Cette technique de migration utilise le calcul des temps de trajet obtenus par la résolution de l'équation de l'Eikonal (Podvin & Lecomte, 1991) pour laquelle une géométrie d'acquisition complexe peut-être aisément prise en compte. Pour le traitement des données SYSIF, la migration est réalisée avec les données rassemblées en collection récepteur commun. Les données migrées sont ensuite rassemblées en collection image commune (*Common Image Gather*) pour être sommées. Cette approche de migration profondeur avant sommation permet l'analyse des

vitesses de propagation par le principe de focalisation des réflecteurs en profondeur comme illustré en figure 2.7 (Marsset et al., 2018).

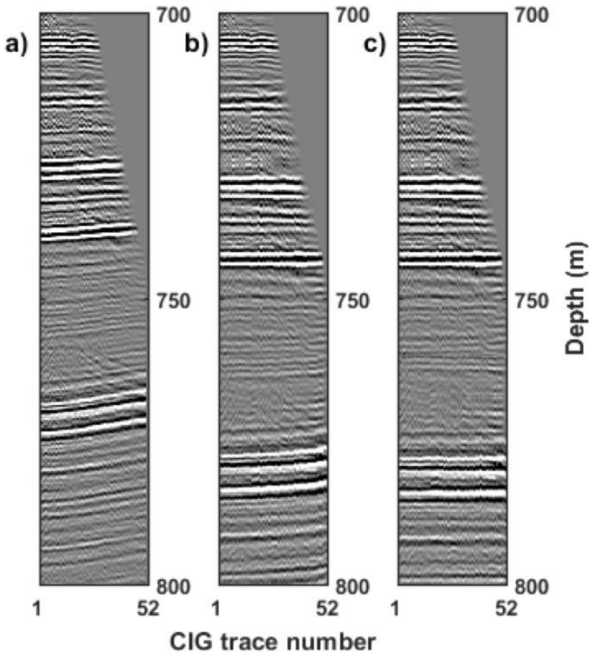

Figure 2.7 : Collection CIG (Common Image Gather) après migration profondeur avec un modèle de vitesse à une couche (1480 m.s^{-1}), deux couches (1480 m.s^{-1} ; 1700 m.s^{-1} @720 m), et trois couches (1480 m.s^{-1}, 1700 m.s^{-1} @720 m, 1700 m.s^{-1} @775 m).

Ces travaux ont permis d'obtenir, pour la première fois pour un système sismique près du fond, une imagerie avec une séquence de migration avant sommation permettant une augmentation de la résolution horizontale et une amélioration significative du rapport signal sur bruit. Cependant, nous avons toutefois constaté qu'une imprécision du traitement des données de positionnement entrainait une perte de résolution. De plus, il a été constaté une inadaptation de l'analyse de vitesse par migration avant sommation à traiter un large volume de données tel que celui de la campagne GHASS (30 profils pour une longueur totale de 300 km). C'est pourquoi, nous avons proposé un projet de thèse portant sur la résolution de ces deux problèmes afin de pouvoir traiter et analyser de manière plus efficace et exhaustive les données de la campagne GHASS dans le but de caractériser le système d'hydrates de gaz de la mer Noire.

3.2.3 Détermination précise de la variabilité de la forme de l'antenne de réception et *datuming* des données SYSIF

Détermination précise de la forme du streamer

Les travaux de thèse de Florent Colin (2018-2020) ont porté dans un premier temps sur une amélioration de notre connaissance de la forme variable du streamer au cours de l'acquisition du profil sismique. En effet, des différences de temps entre les arrivées réfléchies observées et modélisées à partir de la géométrie du streamer obtenue à partir des données MEMS démontrent que des variations de forme à petites longueurs d'onde affectent le streamer (figure 2.8). Une différence de temps de 0.8 ms correspond ainsi à une erreur de position de plus d'un mètre.

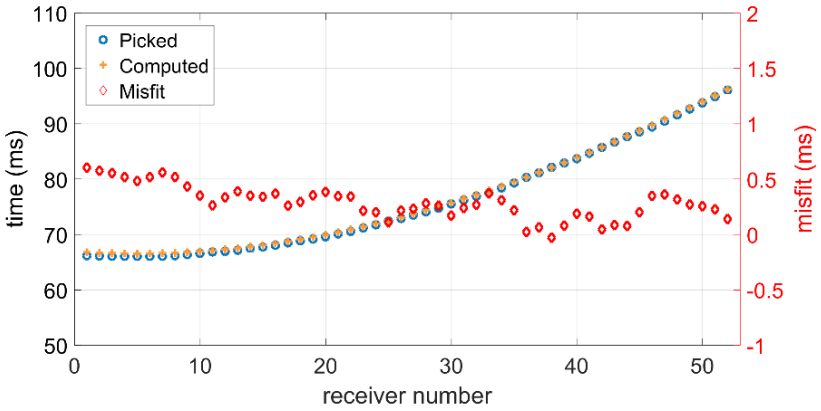

Figure 2.8 : Comparaison des temps de la réflexion sur le fond enregistrés par les hydrophones et calculés à partir de la géométrie MEMS et différence de ces temps de trajet (diamant rouge).

Pour réduire les erreurs de positionnement, une méthode de détermination des valeurs de tangage à partir de l'inversion des temps de trajet directs et réfléchis sur le fond de mer a été développée. Cette approche consiste à rechercher les valeurs de tangage optimales minimisant les différences de temps de trajet observés (t^i_{obs}) et calculés (t^i_{calc}) au sens des moindres carrés. La fonction coût de ce problème a pour expression :

$$S = \min_{\alpha(r)} \sum_i \{t^i_{calc}[\alpha(r^i)] - t^i_{obs}\}^2 \qquad \text{eq. 2.2}$$

La diminution de la fonction coût est réalisée avec une optimisation locale de type « région de confiance » (Conn et al., 2000) en considérant comme modèle initial la géométrie obtenue à partir des capteurs MEMS. Les valeurs de tangage obtenues par l'inversion conservent l'évolution basse-fréquence issue des capteurs MEMS mais montrent une évolution sinusoïdale à plus petite échelle (figure 2.9 a). Cette détermination précise des valeurs de tangage a révélé le comportement de festonnement du streamer provoqué par les masses plus importantes des commutateurs réseaux (figure 2.9 b).

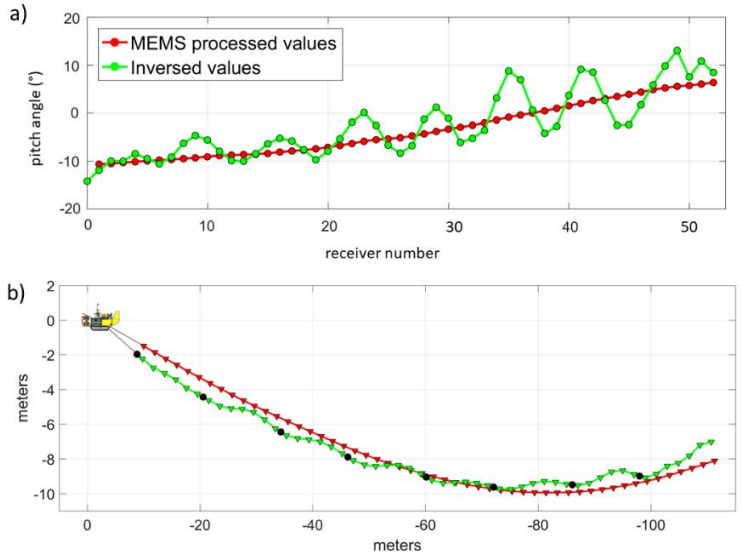

Figure 2.9 : a) Valeurs de tangage obtenues par les capteurs MEMS et améliorées par la procédure d'inversion, b) la forme du *streamer* déterminée après inversion des valeurs de tangage (en vert) montre des ondulations non révélées par la reconstruction à partir des capteurs MEMS (en rouge).

La figure 2.10 montre l'apport de l'amélioration du positionnement sur l'imagerie profondeur obtenue à partir de données multitraces SYSIF. L'amélioration du positionnement permet d'atteindre respectivement 0.65 et 1.6 m de résolutions horizontale et verticale pour une profondeur d'eau de 660 m, résolutions jamais atteintes jusqu'alors pour une imagerie sismique très haute résolution par grande profondeur d'eau (Colin et al., 2020a).

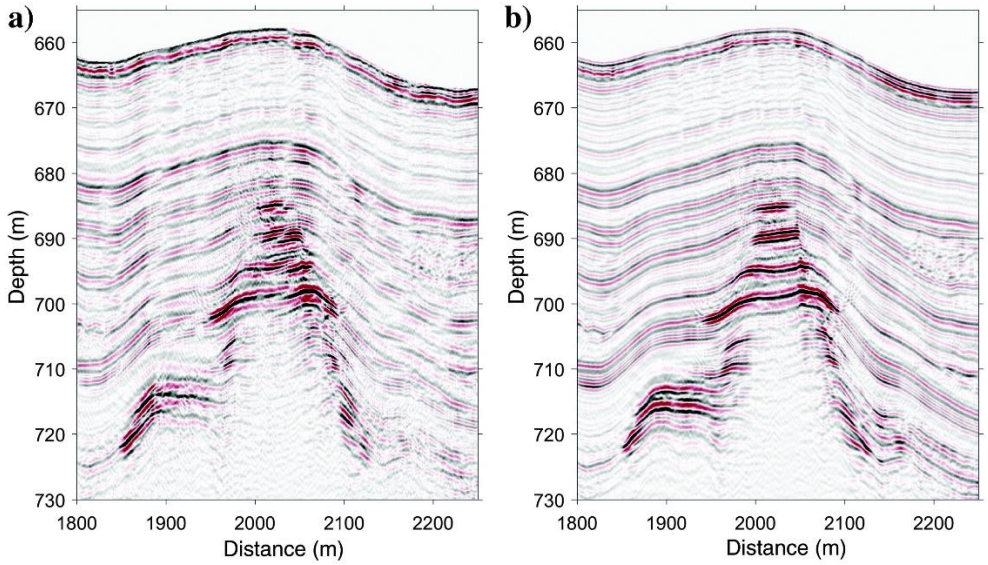

Figure 2.10 : Profil SYSIF en profondeur obtenu après migration avant sommation en utilisant la géométrie MEMS (a) et l'inversion des valeurs de tangage (b).

Datuming des données SYSIF

Une nouvelle approche pour gérer le problème de l'asymétrie de l'acquisition de sismique près du fond a été développée pendant la thèse de Florent Colin reposant sur l'adaptation de la technique du *datuming*, initialement introduit par Berryhill (1979), à la géométrie de l'acquisition sismique près du fond. Cette technique consiste à prolonger numériquement la propagation de manière à simuler une acquisition où la source et les récepteurs sont situés à la même profondeur, celle du plan de référence appelé le *datum*. La propagation au *datum* repose sur un prolongement de la propagation dans la colonne d'eau en utilisant la sommation de Kirchhoff. Les principales étapes de la technique du *datuming* adaptée aux données de sismique près du fond sont les suivantes :

1) Définition du plan de référence (le *datum*) et de la géométrie de l'acquisition après *datuming*,
2) Déplacement des récepteurs vers le *datum* en propageant les données initiales P_i triées en collection tir commun (CSG) pour obtenir les données intermédiaires p_j:

$$p_j = \sum_{i=0}^{M} A_{ij} \frac{\partial^{1/2}}{\partial t^{1/2}} P_i(t - \tau_{ij}), \qquad \text{eq. 2.3}$$

$$\text{avec } A_{ij} = \frac{\Delta x}{2\pi r_{ij} v} \cos(\vartheta_{ij}) \qquad \text{eq. 2.4}$$

τ_{ij} est le temps de trajet entre la position initiale du récepteur i et la position du récepteur sur le *datum* j. M définie la limite de contribution des récepteurs. M doit être défini par rapport au pendage maximal à imager. A_{ij} est le terme d'amplitude prenant en compte la divergence sphérique et l'obliquité avec v la vitesse de propagation associée au *datum*,

Δx est l'échantillonnage spatial, ϑ_{ij} est l'angle d'émergence et r_{ij} est la distance entre la position initiale du récepteur i et celle après *datuming* j.

3) Déplacement des sources vers le *datum* en propageant les données intermédiaires p triées en collections récepteur commun (CRG) pour obtenir les données après *datuming* P'_k:

$$P'_k = \sum_{j=0}^{N} A_{jk} \frac{\partial^{1/2}}{\partial t^{1/2}} p_j(t - \tau_{jk}) \qquad \text{eq. 2.5}$$

Avec N qui définit les limites de sommation par rapport à la position de la source.

4) La préservation des angles de propagation est assurée par une sélection variable avec le temps réalisée dans la collection point milieu commun (CMP).

La figure 2.11 illustre l'application du *datuming* aux données SYSIF avec la collection récepteur commun associée au dernier hydrophone qui n'est plus pénalisée par les variations d'immersion de la source et de l'hydrophone.

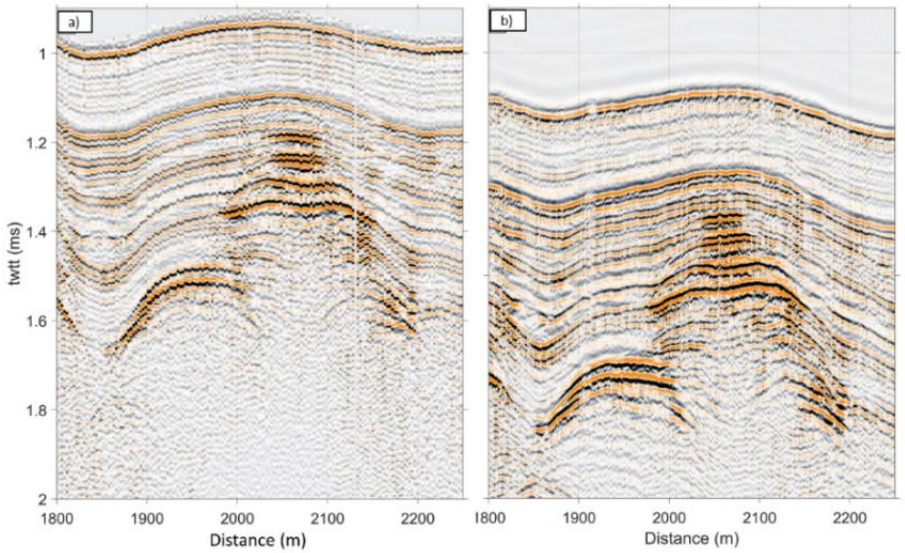

Figure 2.11 : Comparaison entre une collection récepteur commun (dernier récepteur) avant (a) et après *datuming* (b).

Les données SYSIF, une fois la procédure de *datuming* réalisée, peuvent être traitées et analysées de manière conventionnelle. L'analyse de vitesse exploitant la courbure normale (NMO) peut être ainsi mise en œuvre permettant une imagerie de l'ensemble des profils de la campagne GHASS dans un temps raisonnable. Une première application de ces nouvelles approches de traitement développées au cours de la thèse de Florent Colin a permis d'identifier et de caractériser des réservoirs de gaz comme illustré en figure 2.12 où un anticlinal renferme du gaz libre identifié par une vitesse plus faible de propagation proche de 1000 $m.s^{-1}$ (Colin et al., 2020a). L'analyse de vitesse (figure 2.12 b) a été réalisée tous les 10 m avec un pas de vitesse de 1 $m.s^{-1}$ pour la génération des panneaux de semblance (figure 2.12 a). L'incertitude temporelle du pointé de vitesse a été évalué à 0.45 ms permettant l'évaluation des incertitudes sur les vitesses d'intervalle (Hajnal & Sereda, 1981). Le gain en résolution de l'imagerie obtenue par migration profondeur en utilisant le champ de vitesse variable est illustré en figure 2.13.

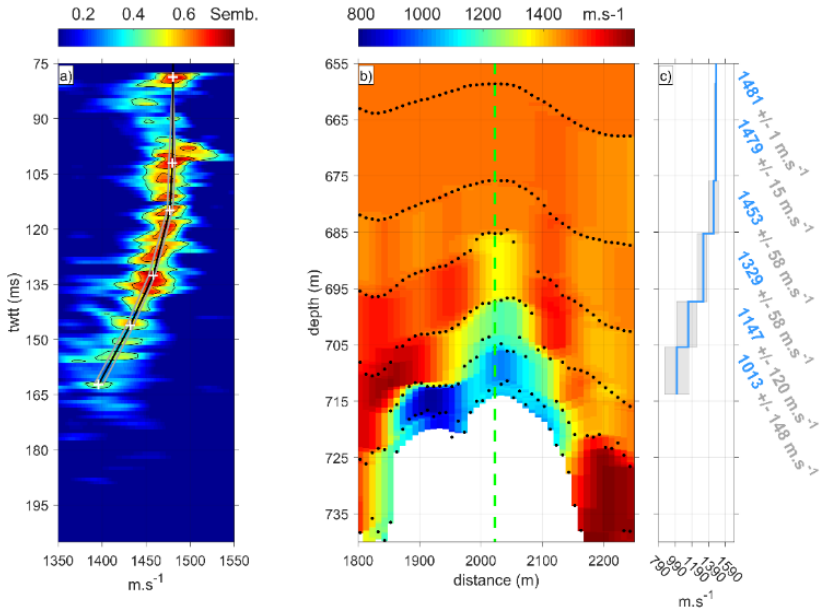

Figure 2.12 : Analyse de vitesse réalisée sur panneau de semblance (a), champ de vitesse (b) et profil vertical de vitesses avec incertitudes.

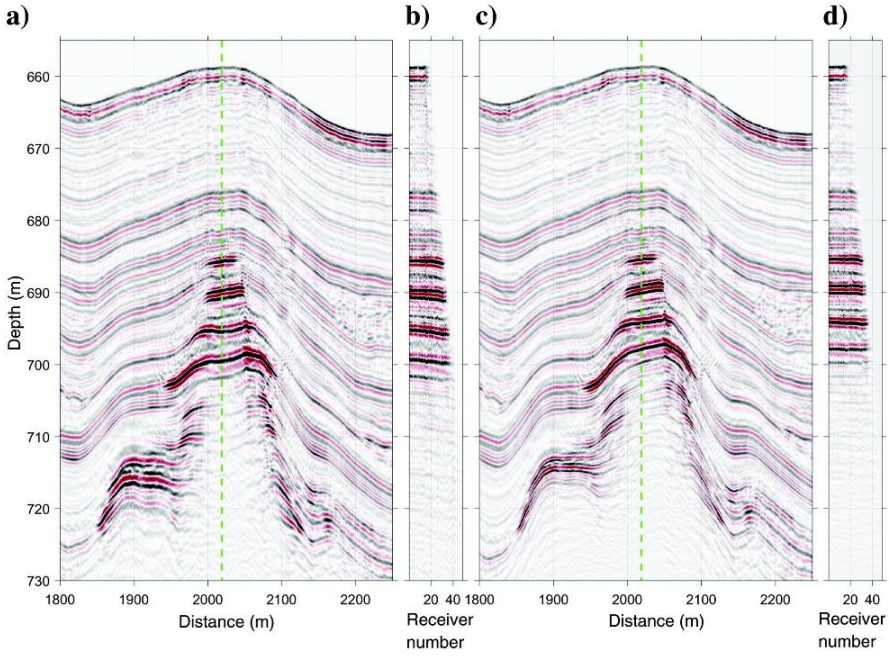

Figure 2.13 : Migration profondeur avant sommation d'une partie du profil SYSIF PL03PR06 (campagne GHASS) avec a) la vitesse constante de la couche d'eau et c) le champ de vitesses défini par l'analyse de vitesse avec les *CIG* correspondants (b et d)

Migration de type extrapolation du champ d'onde

Nous avons exploré les possibilités offertes par les méthodes de migration de type extrapolation du champ d'onde pour améliorer l'imagerie sismique SYSIF en présence de variation rapide du champ de vitesses. Si la méthode de Kirchhoff qui repose sur le tracé de rayon s'est montrée très efficace pour l'imagerie des données SYSIF, cette méthode repose sur des hypothèses fortes, en premier lieu celle de variation lisse du champ de vitesse. Les méthodes de migration de type

extrapolation du champ d'onde qui s'appuient sur la résolution de l'équation d'onde sont plus précises mais requièrent un plus gros effort de calcul. Une première application de ce type de méthode peut être réalisée après la phase de *datuming*. En effet, la géométrie d'acquisition simple et régulière après *datuming* permet d'utiliser des algorithmes de migration rapides et stables comme par exemple, la technique de migration par *phase shift plus interpolation* (PSPI) illustrée en figure 2.14 (Gazdag & Sguazzero, 1984). Il est à noter que le pas de la grille utilisé est de 10 cm.

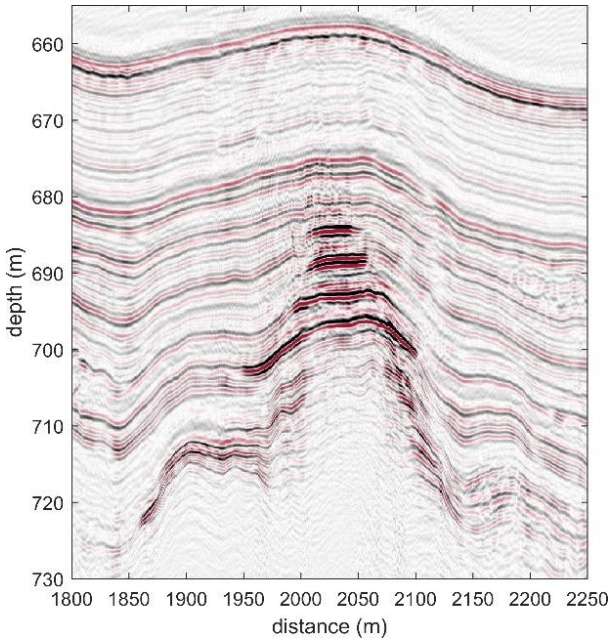

Figure 2.14 : Application d'une migration de type extrapolation du champ d'onde (méthode PSPI) aux données SYSIF après *datuming* (pas de grille 10 cm et fréquence d'échantillonnage de 5000 Hz)

3.2.4 Bilan sur la sismique très haute résolution près du fond

Après la phase de développement technologique de l'engin remorqué SYSIF, la phase de développement méthodologique a permis d'exploiter le potentiel des données. Le résultat est une imagerie sismique à très haute résolution permettant une analyse précise des structures géologiques superficielles à une résolution jamais obtenue jusqu'alors par grande profondeur d'eau. L'exploitation des données SYSIF a été essentielle pour les projets de recherche sur les aléas marins et les systèmes hydrates et est toujours en cours pour l'étude du système hydrate de la mer Noire. Ceci sera détaillé plus en avant dans le troisième volet de mes travaux de recherche.

D'autres systèmes de sismique près du fond ont été récemment développés avec notamment l'apparition du nouveau système chinois Kuiyang (Pei et al., 2022). Kuiyang possède pour particularités d'utiliser une source de type *sparker* spécifiquement conçue pour un fonctionnement en grande immersion avec une antenne d'émission multi-électrodes. Ce système comprend également des flotteurs au sein du streamer pour éviter les problèmes de distribution inhomogène de masse et une déformation trop importante du *streamer*. L'ajout de flotteurs évite le festonnement du *streamer* qui conserve ainsi une forme simple approximable par un polynôme de faible degré (Pei et al., 2023) et facilite la détermination précise des positions des hydrophones.

Articles associés

Colin, F., Ker, S., Marsset, B. (2020). Fine-scale velocity distribution revealed by datuming of very-high-resolution deep-towed seismic data: Example of a shallow-gas system from the western Black Sea. *Geophysics*, 85(5), B181-B192.

Ker, S., Le Gonidec, Y., Gibert, D. (2013). Multiresolution seismic data fusion with a generalized wavelet-based method to derive subseabed acoustic properties. *Geophysical Journal International*, 195(2), 1370-1383.

Marsset, B., Menut, E., Ker, S., Thomas, Y., Regnault, J-P., Leon, P., Martinossi, H., Artzner, L., Chenot, D., Dentrecolas, S., Spychalski, B., Mellier, G., Sultan, N. (2014). Deep-towed High Resolution multichannel seismic imaging. *Deep-sea Research Part I-oceanographic Research Papers*, 93, 83-90.

Marsset, B., Ker, S., Thomas, Y., Colin, F. (2018). Deep-towed high resolution seismic imaging II: Determination of P-wave velocity distribution. *Deep-sea Research Part I-oceanographic Research Papers*, 132, 29-36.

3.3 Caractérisation sismique et son intégration dans une approche multidisciplinaire pour l'étude des systèmes gaz/hydrates de gaz

L'objectif de cette thématique est de développer des méthodes d'imagerie et de caractérisation des systèmes sédimentaires comportant du méthane sous forme de gaz libre ou piégé sous forme solide. Les résultats d'imagerie et de caractérisation géophysique sont intégrés à l'étude pluridisciplinaire permettant une meilleure compréhension de ces systèmes et de leur dynamique. Ces travaux s'appuient en grande partie sur les développements présentés dans les sections précédentes : analyse multi-échelle et sismique près du fond.

3.3.1 Gaz dans les sédiments marins et contribution de la caractérisation sismique

Les sédiments marins superficiels (< 500 m sous le fond de l'eau) contiennent de grandes quantités de gaz, majoritairement du méthane qui existent sous différentes formes : dissoutes, gaz libre (bulles) ou piégées dans une structure solide appelée hydrate de gaz. Les hydrates de gaz, ou clathrates, sont des solides formés par des molécules d'eau formant des cages qui piègent des molécules de gaz tel que le méthane (Sloan & Koh, 2008) avec une capacité très importante (1 cm^3 d'hydrate renferme 164 cm^3 de méthane à pression atmosphérique). Leur découverte date des années 1970 et leur répartition couvre une grande partie des marges continentales. Ces hydrates de gaz constituent un puits de carbone stable sous certaines conditions environnementales de température, pression, salinité, etc. (Ruppel & Kessler, 2017) et sont susceptibles de se déstabiliser suite à des variations de ces conditions (Phrampus & Hornbach, 2012). La déstabilisation des hydrates peut libérer de grandes quantités de méthane dans les sédiments marins, altérant leurs propriétés mécaniques, dans la colonne d'eau voire potentiellement dans l'atmosphère. Les hydrates de gaz constituent par conséquent une source d'aléas géologiques (instabilités sédimentaires) et climatiques pouvant induire des évènements de réchauffement globaux rapides (hypothèse du *Clathrate Gun*, Hill et al., 2006 et Kennet et al., 2000).

La distribution du méthane contenu dans les sédiments marins superficiels sous forme de bulles ou piégée dans les hydrates est encore mal explorée. Il est essentiel de mieux évaluer ce puits de carbone, de comprendre son évolution en fonction des forçages environnementaux que sont les variations du niveau marin, de la température de l'Océan et d'évaluer les flux de gaz vers le fond de mer et les flux qui s'échappent du fond de mer. Au cours des vingt dernières années, le laboratoire Géosciences Marines, puis Geo-Ocean, a mené des travaux pluridisciplinaires sur l'étude des sédiments marins contenant du gaz libre et des hydrates de gaz dans le cadre notamment des projets ERIG3D et GHASS. Les développements de la sismique remorquée près du fond et de l'analyse multi-échelle présentés dans les sections précédentes ont contribué à la caractérisation sismique des systèmes de gaz libre et d'hydrates de gaz en association avec la sismique haute résolution de surface dans le cadre d'une analyse sismique multirésolution. Nous détaillerons dans cette section les travaux réalisés sur les réflecteurs sismiques associés à la présence de gaz libre, sur des structures géomorphologiques associées aux fluides et enfin sur l'étude du système hydrate de la mer Noire et de sa dynamique.

3.3.2 Caractérisation multi-échelle des interfaces complexes associées à la présence de gaz libre dans les sédiments marins

La pente continentale localisée à l'ouest de l'archipel du Svalbard dans l'Océan Arctique renferme des sédiments marins riches en gaz libre. Les méthodes acoustiques révèlent la présence de nombreuses émissions de gaz libre au niveau du fond marin (Westbrook et al., 2009). L'imagerie sismique haute résolution obtenue par un dispositif en surface avec une source composée de canons à air [30-150 Hz] permet d'identifier la présence de gaz libre dans les sédiments mais est limitée à une résolution de 4 m (Sarkar et al., 2012). L'étude à très haute résolution (~1 m) telle qu'obtenue par l'engin remorqué SYSIF s'est avérée essentielle pour mieux définir la répartition du gaz libre au sein des sédiments marins (Ker et al., 2014). Les profils SYSIF acquis en 2011 avec le transducteur HF [220-1050 Hz] ont mis en évidence des fortes réflexions (BS1 et BS2, figure 3.1) présentant des caractéristiques (amplitude, phase) différentes de celles présentes sur un profil acquis avec le dispositif de surface de plus basse résolution. Les points brillants caractérisés par des réflexions de polarité inverse sur le profil basse résolution, sont interprétés comme des interfaces avec une inversion d'impédance associée à la présence de gaz libre dans les sédiments marins qui fait chuter la vitesse de propagation des ondes sismiques. Or la polarité normale du point brillant BS1 sur le profil SYSIF ne confortait pas cette interprétation. En effet, une polarité positive laissait supposer la présence d'une lithologie caractérisée par une forte vitesse de propagation comme par exemple des hydrates ou des carbonates authigéniques souvent associés à la présence de gaz libre.

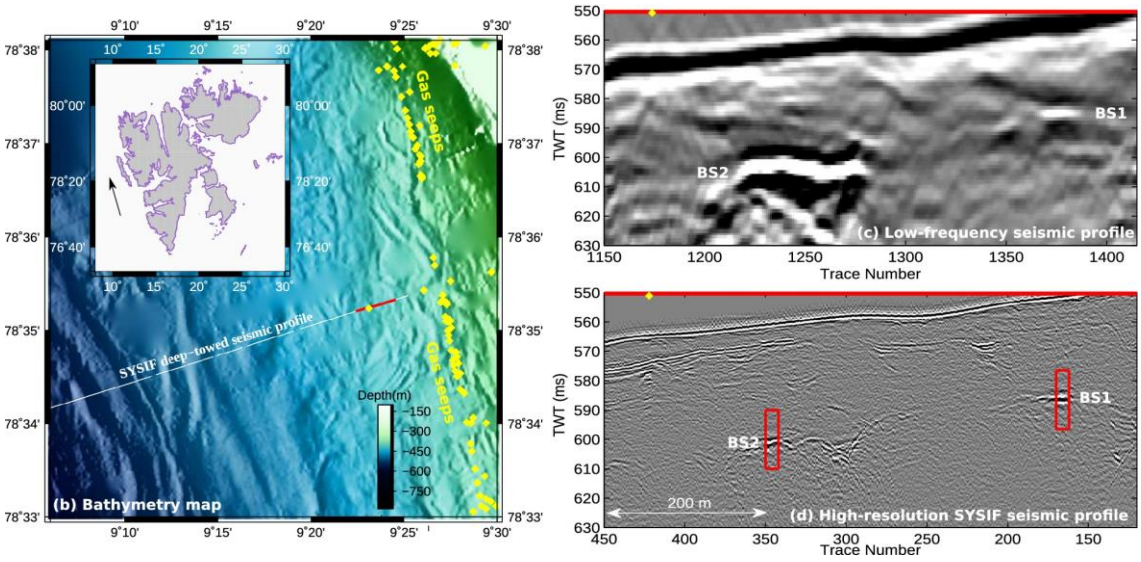

Figure 3.1 : a) Localisation de la zone d'étude située au large du Svalbard, b) localisation du profil sismique investigué avec deux résolutions et localisation des émissions sur le fond de mer, c) et d) analyse sismique multirésolution avec HR et THR respectivement (Ker et al., 2014).

Pour mieux analyser les formes d'ondes associées aux réflecteurs BS1 et BS2, nous avons utilisé l'analyse multi-échelle fournie par la réponse en ondelettes. La réponse en ondelettes associée au réflecteur BS1 présente un extremum de plus que l'ondelette effective (figure 3.2) après l'application de la correction de source présentée en section 3.1.2. De plus, la ligne d'extrema principale présente un maximum indiquant une morphologie complexe (Le Gonidec et al., 2002). La morphologie de la réponse en ondelettes et celle de l'attribut multi-échelle sont en accord avec une discontinuité d'impédance de type banc mince associée à une diminution de l'impédance (figures 3.2 c et d). L'épaisseur du banc mince, de l'ordre de 70 cm, a pu être évaluée à partir de la dilatation associée au maximum de l'attribut multi-échelle et d'une vitesse de propagation dans

le banc mince estimée à 1300 m.s^{-1} (Sarkar et al., 2012). Un second réflecteur de type Heaviside de polarité inverse (BS2) a confirmé la chute de vitesse associée à la présence de gaz libre mais a surtout révélé une décroissance d'amplitude aux petites échelles associée à un phénomène de diffusion multiple de l'onde sismique générée par une distribution hétérogène du gaz libre dans les sédiments dans des patches de dimension inframétrique.

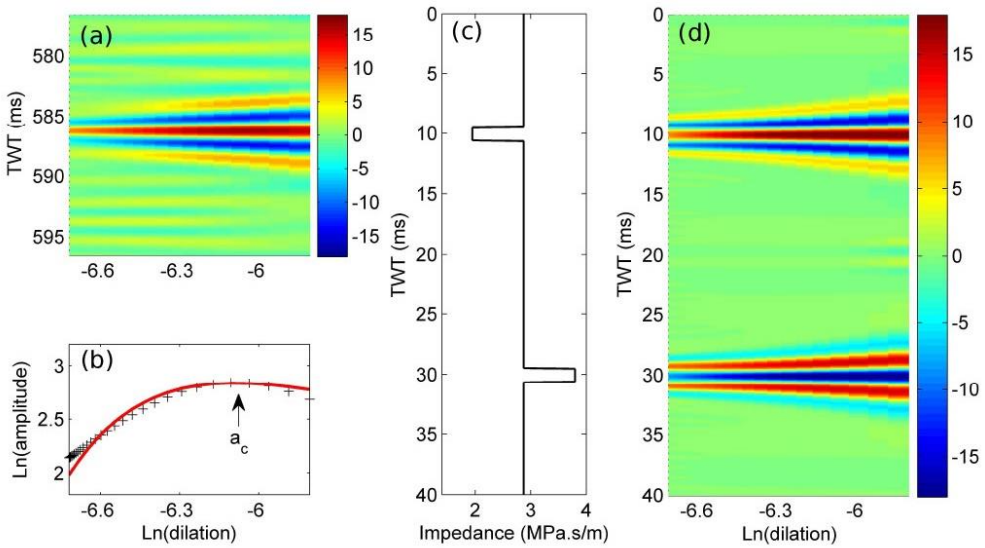

Figure 3.2 : a) analyse en ondelette du réflecteur BS1 et b) la ligne d'extrema associée, c) discontinuités d'impédance négative et positive de type banc mince et d) réponses en ondelettes associées (Ker et al., 2014).

L'analyse sismique multirésolution réalisée à partir des données de surface et près du fond et l'analyse mutiéchelle par ondelettes des données SYSIF apportent des informations précieuses sur les dimensions des zones où le gaz est stocké ou migre au sein de la colonne sédimentaire. De plus, elle permet de lever des ambiguïtés dans l'interprétation des données de surface. L'analyse conjointe des données sismiques haute et très haute résolution permet de mieux définir la distribution du gaz libre au sein de l'architecture sédimentaire observée au large du Svalbard contrôlée par la glaciation vistulienne (thèse de A. Trivedi encadré par S. Sarkar).

3.3.3 Caractérisation des *pockmarks*

L'étude des fonds marins a permis de mettre en évidence dans les années 1970, sur toutes les marges continentales actives et passives du monde, la présence de dépressions quasi-circulaires généralement de diamètre compris entre 20 et 200 m mais pouvant atteindre plus d'un kilomètre avec une profondeur de plusieurs dizaines voire centaines de mètres (Pilcher & Argent, 2007). Ces dépressions appelées *pockmarks* (figure 3.3 a) sont des figures d'échappement de fluides. Elles sont associées en profondeur à des cheminées verticales dévoilées par les profils sismiques qui sont des signatures de chemins de migration verticale des fluides (Hovland, 1984). L'étude des *pockmarks* est importante pour connaître leur potentiel rôle en tant que source d'instabilité du sous-sol marin mais aussi afin de mieux évaluer les quantités de fluide stockées et susceptibles de se libérer dans la colonne d'eau voire l'atmosphère. Ces structures morphologiques sont complexes et leur analyse nécessite une approche pluridisciplinaire associant étude géomorphologique, imagerie sismique, analyses sédimentologiques et géomécaniques.

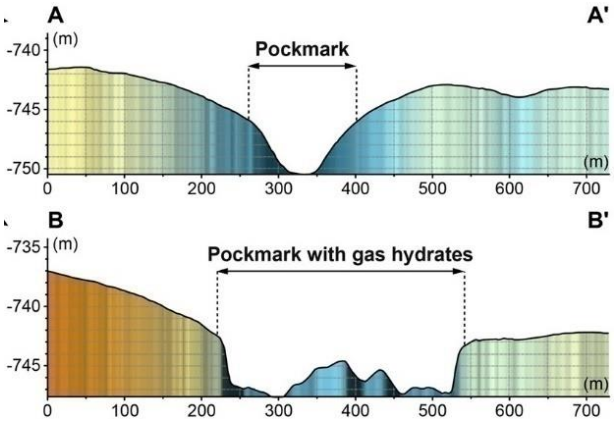

Figure 3.3 : Morphologie du fond marin associé aux deux types de pockmark, a) type 1 régulier quasi-circulaire, b) type 2 irrégulier associé à la présence d'hydrates de gaz dans les sédiments marins (Riboulot et al., 2016)

Etude des facteurs de formation des pockmarks

Dans le cadre du projet ERIG3D portant sur les aléas géologiques dans le golfe de Guinée, un champ de *pockmarks* associé à un glissement sous-marin situé à 120 m sous le fond de mer a été étudié par notre laboratoire. Il couvre une superficie de plus de 200 km^2 et constitue un réservoir secondaire de fluide provenant d'un réservoir plus profond (> 500 m). L'étude pluridisciplinaire dirigée par Vincent Riboulot a mis en évidence une chronologie de formation des *pockmarks* contrôlée par les variations du niveau marin avec un cycle de 100000 ans modifiant la pression hydrostatique au sein du glissement sous-marin (NG1). L'apport de la géophysique est essentiel pour fournir une imagerie à plusieurs échelles associant des acquisitions de surface à l'échelle « régionale » (sismique 3D dans ce cas) et la sismique près du fond pour atteindre une résolution en accord avec celle des mesures *in situ* sédimentologiques (carottes) et géotechniques réalisées dans les cinquante premiers mètres de sédiments (figure 3.4).

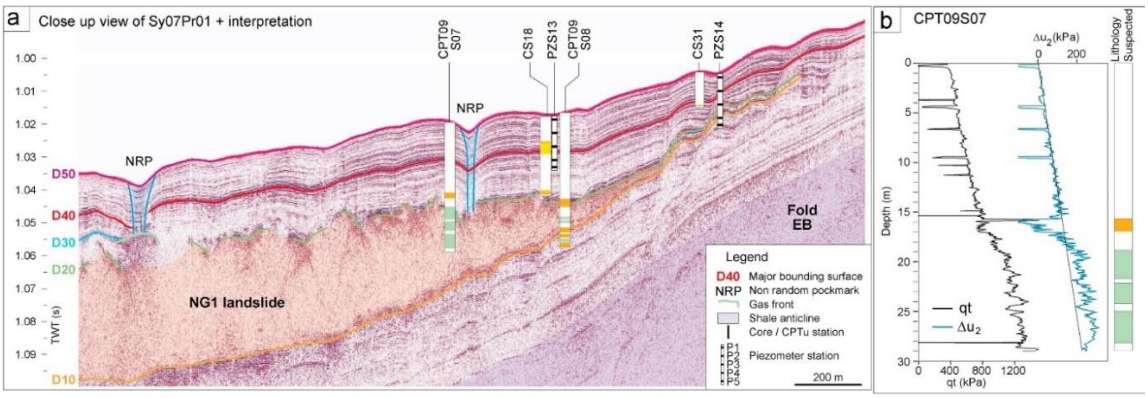

Figure 3.4 : a) Profil sismique SYSIF interprété avec localisations des mesures *in situ* géotechnique (CPT), piézométrique (PZ) et carottes (CS) montrant la connexion entre les *pockmarks* (NRP) et le glissement NG1 b) exemple de données géotechniques (résistance de pointe et différence de pression interstitielle) associées à la lithologie (Riboulot et al., 2013).

Au cours de ce même projet ERIG3D, les profils très haute résolution de SYSIF ont eu un rôle important pour dévoiler le mécanisme de formation des pockmarks initié par la dissolution des hydrates de méthane (Sultan et al., 2010 et 2014). Chaque stade d'évolution a pu être illustré par un profil sismique SYSIF. Un nouveau type de *pockmark* caractérisé par une morphologie irrégulière (figures 3.3b et 3.5) a pu être associé à la présence d'hydrates et à leur impact en terme

de fracturation grâce à une approche intégrant l'analyse des données sismiques très haute résolution SYSIF, sédimentologiques, géotechniques et la modélisation géomécanique (Riboulot et al., 2016).

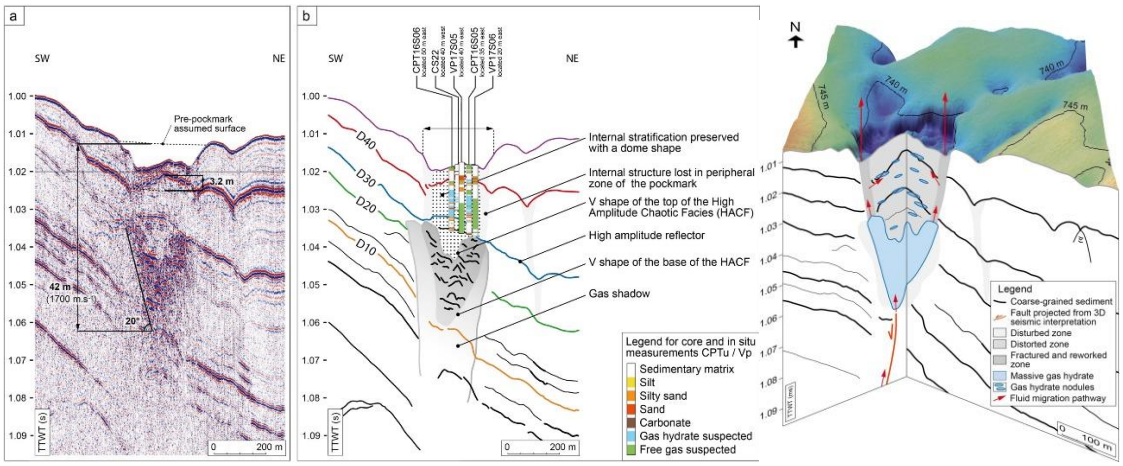

Figure 3.5 : a) Profil sismique SYSIF et b) interprétation avec localisations des mesures *in situ* géotechnique (CPT), piézométrique (PZ) et carottes (CS) réalisées dans le pockmark et c) et interprétation 3D du *pockmark* (Riboulot et al., 2016).

Composition des pockmarks : approche conjointe électromagnétique et sismique

En 2011, une collaboration avec le *National Oceanography Center* du Royaume-Uni a permis de mettre en œuvre une approche comportant deux méthodes d'imagerie géophysiques (électromagnétique et sismique) pour définir la répartition des hydrates de gaz et du gaz libre dans et autour d'un *pockmark* en domaine profond (> 1200 m) au large du Svalbard en Arctique au cours de la campagne JCR 269 (Goswani et al., 2015 & 2017). L'acquisition de mesures électromagnétiques a été réalisée avec la technique CSEM (*Controlled Source ElectroMagnetic*) comportant : 1) une source active (DASI) tractée à 50 m au-dessus du fond émettant un courant de 1 Hz de 81 A avec une antenne de dipôle horizontale de 100 m, 2) un récepteur électrique tracté trois axes Vulcan (Weitemeyer & Constable, 2010) et 3) 9 récepteurs électriques (2 composantes horizontales) posés sur le fond (*Ocean-Bottom Electric Field*). Différentes mesures sismiques ont été acquises : sismique haute résolution de surface et très haute résolution avec l'engin remorqué SYSIF. Deux sismomètres de fond de mer (OBS) ont été également déployés pour permettre la détermination des vitesses de propagation. Une première approche de combinaison des deux techniques géophysiques est de superposer les informations de structure fournies par la sismique réflexion et les valeurs de résistivité. Des valeurs fortes de résistivité (10 Ωm) sont systématiquement associées à la présence de *pockmarks* du fait de la présence de gaz libre et/ou d'hydrates de gaz (figure 3.6). Une seconde approche plus quantitative consiste à déterminer la saturation en hydrate et en gaz à partir des anomalies de résistivité et de vitesses obtenues à partir de calcul direct reposant sur la théorie des milieux effectifs (Goswani et al., 2015). Les anomalies positives de résistivité de 2-4 Ωm et de vitesse de propagation de 300 $m.s^{-1}$ fournissent des saturations en hydrate de plus de 50 % au cœur de la cheminée sous le *pockmark*.

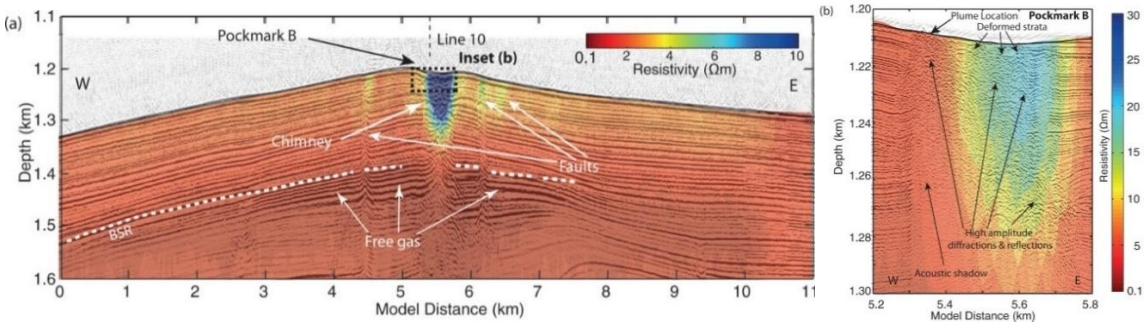

Figure 3.6 : Superposition des profils sismiques de surface air-gun (a) et SYSIF (b) avec les résistivités obtenues avec le CSEM (Goswani et al., 2017).

Pour une optimisation de cette approche conjointe associant les méthodes électromagnétique et sismique, il reste à franchir une dernière étape qui serait l'inversion conjointe des données électromagnétiques et sismiques en s'appuyant sur des modèles de milieux effectifs permettant le calcul des résistivités et des vitesses. Cette approche permettrait d'être plus discriminant sur la distribution des hydrates au sein des sédiments marins (Liu et al., 2020). Enfin, il est à noter que les *pockmarks* et les cheminées sont des objets très complexes en trois dimensions. Une avancée importante dans la compréhension de leur structure requiert une imagerie sismique 3D à très haute résolution qu'il reste difficile à envisager par grande profondeur d'eau.

3.3.4 Mise en évidence de la dynamique du système hydrate de la mer Noire

Stabilité des hydrates de méthane : exemple de la mer Noire

Il est considéré que la mer Noire renferme une grande quantité d'hydrates de gaz (Merey & Sinayuc, 2016). Cette présence est déduite de l'observation d'un réflecteur sismique qui marque la limite de stabilité des hydrates de gaz en profondeur. Ce réflecteur est appelé BSR (*Bottom Simulating Reflector*) car les premières expressions découvertes mimaient en profondeur la morphologie de la bathymétrie (Holbrook et al., 1996). Le BSR présente généralement un fort coefficient de réflexion et une inversion de phase associée au contraste négatif d'impédance entre les sédiments contenant des hydrates et ceux sous-jacents contenant du gaz libre (Davies et al., 2017). Le BSR a été cartographié dans le partie Ouest de la mer Noire avec des multiples BSR dans l'éventail profond du Danube (Popescu et al., 2006 et 2007). La mer Noire a connu de large bouleversement de conditions environnementales depuis le dernier épisode glaciaire (20 ka). Elle constitue ainsi un laboratoire naturel pour étudier la dynamique d'un système « hydrates de gaz » liée à ces variations et ses possibles conséquences sur la stabilité des sédiments marins. C'est pour ces raisons que fut initié le projet GHASS dont j'ai eu la responsabilité de 2015 à 2019. Ce projet, associé à une campagne océanographique réalisée en septembre 2015, avait pour objectifs d'identifier les couches sédimentaires renfermant des hydrates de gaz et/ou du gaz libre, d'étudier la dynamique du système et le possible lien avec la présence de nombreux glissements sous-marins et de déformations sédimentaires observées de part et d'autre du canyon du Danube.

Caractérisation de l'état actuel du système

a) Imagerie sismique

Pour réaliser la caractérisation du système hydrate du secteur roumain de la mer Noire, nous avons mis en œuvre : 1) une acquisition de sismique haute résolution de surface [40-170 Hz] avec un canon à air de petit volume (*mini-GI 24 ci*) immergé à 1.5 m et une flûte de 96 traces avec un

déport maximal de 650 m immergée à 2 m et un espacement entre traces de 6.25 m, 2) une acquisition de sismique très haute-résolution près du fond avec l'engin remorqué SYSIF avec la source HF [220 -1050 Hz] et la flûte de 52 hydrophones espacés de 2 m avec un déport maximal de 110 m et 3) des moyens d'investigations *in situ* (pénétromètre et piézomètre) et de prélèvement (carottiers) qui nous ont permis de collecter le premier échantillon d'hydrate de gaz de ce secteur et ainsi d'analyser la composition du gaz renfermé dans les hydrates. Grâce aux carottes sédimentaires, la composition minéralogique des sédiments a été évaluée (Riboulot et al., 2018).

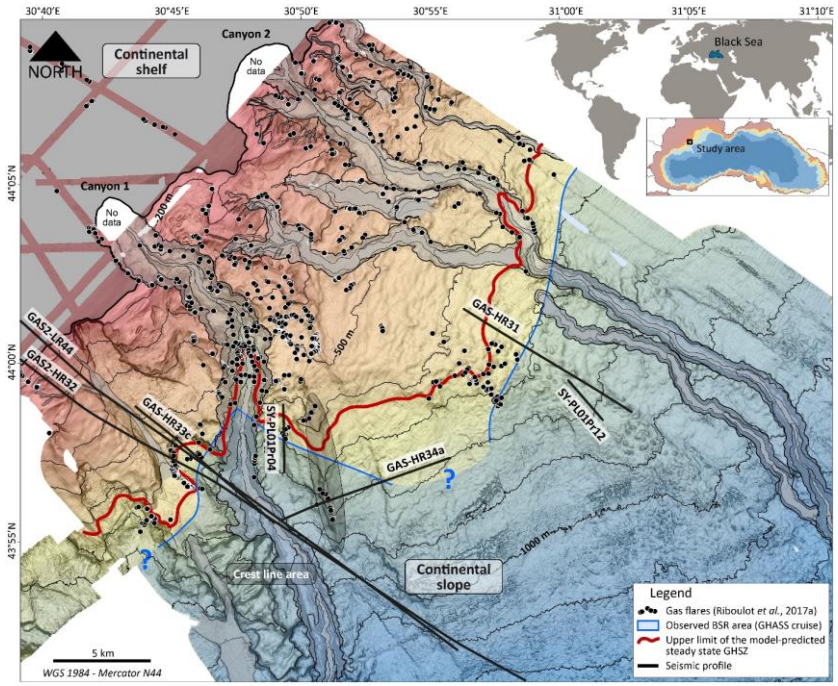

Figure 3.7: Carte présentant la zone d'étude du projet GHASS située dans le secteur ouest de la mer Noire. Les profils sismiques clés sont indiqués ainsi que la localisation du BSR et des sites d'échappements de fluide.

Outre les travaux d'imagerie associés à la sismique près du fond détaillés plus haut et une analyse conventionnelle (analyse de correction de courbure normale et migration après sommation) des profils de sismique haute résolution de surface, nous avons procédé avec Yannick Thomas à une imagerie profondeur avant sommation obtenue après une analyse de vitesse par migration profondeur de Kirchhoff itérative (Al-Yahya, 1989) pour des profils clés situés au cœur de la zone de stabilité des hydrates de gaz ou recoupant l'ensemble du système (figure 3.7). L'analyse des collections image commune (CIG) a été réalisée avec un espacement de 32 m. Les résolutions de l'imagerie sismique haute résolution de surface sont de 3.5 m verticalement et 15 m horizontalement. Les incertitudes sur les vitesses ont été estimées à ± 50 $m.s^{-1}$ jusqu'à 1000 m et dépassent ± 100 $m.s^{-1}$ à partir de 1200 m du fait de la gamme d'incidence très réduite.

L'analyse des profils sismiques a révélé que le BSR n'est pas toujours observé comme l'atteste le profil 34a, où le BSR est présent uniquement dans la partie Ouest de ce profil (figure 3.8). L'absence de BSR dans la partie Est procure une opportunité pour définir un profil de vitesse de référence (gradient linéaire de 0.68 s^{-1}) uniquement associé aux propriétés des sédiments. La présence de vitesses de propagation plus fortes (1700 - 2050 $m.s^{-1}$) ou plus faibles (1200 – 1500 $m.s^{-1}$) par rapport au profil de référence permet de délimiter les zones où les sédiments marins contiennent des hydrates de gaz ou du gaz libre (figure 3.8).

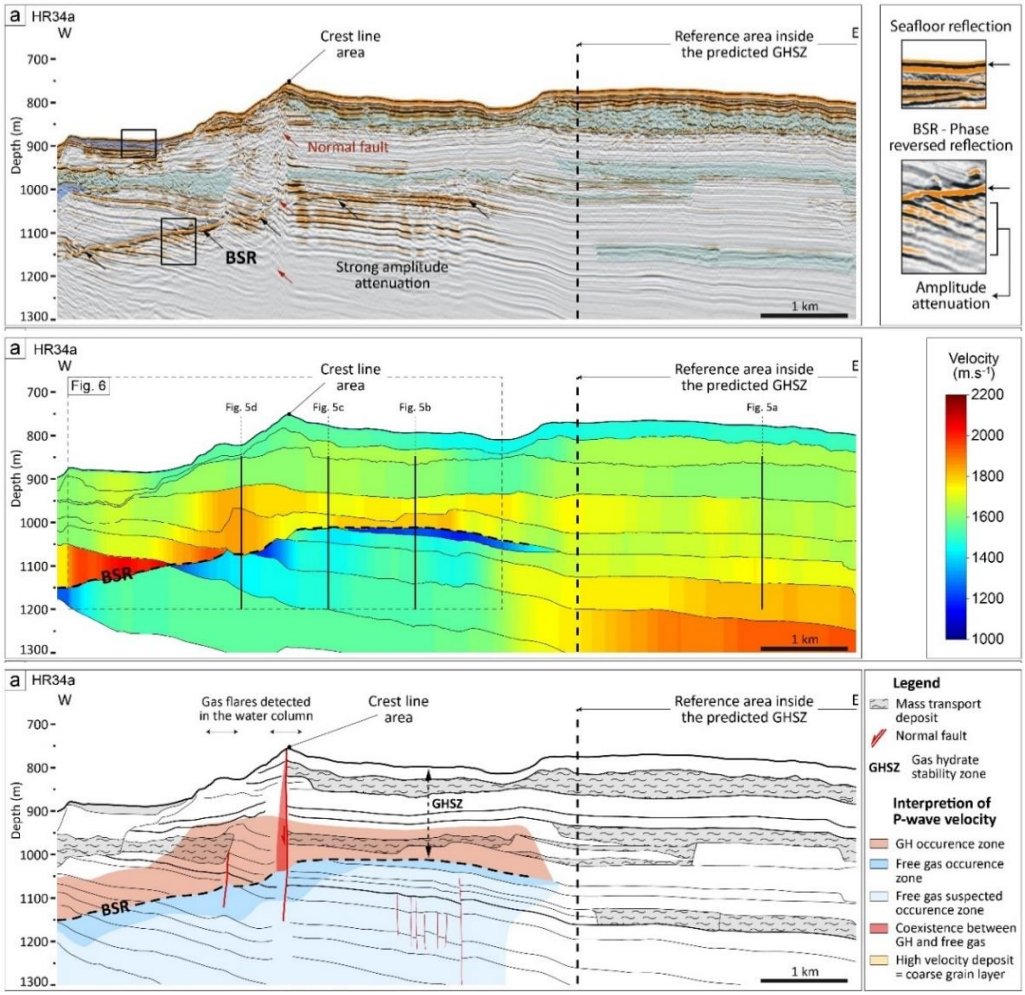

Figure 3.8 : Profil sismique haute résolution (34a) après migration profondeur avant sommation et le champ de vitesses associé (haut et centre). Interprétation géologique du profil sismique qui présente les zones à hydrates et gaz libre à partir des anomalies de vitesse (Ker et al., 2019).

b) Concentration en gaz libre et hydrate

Pour estimer les concentrations en hydrate et méthane sous forme de gaz libre, nous nous sommes appuyés sur des modèles effectifs associés à la théorie de la poroélasticité permettant de rendre compte des propriétés de propagation des ondes dans les milieux poreux. Selon la théorie de Gassmann, la pression du fluide mis en mouvement par le passage de l'onde sismique a eu le temps d'atteindre l'équilibre pour des fréquences supérieures à la fréquence caractéristique de Biot (Bourbié et al., 1987). La vitesse des ondes de compression se propageant dans un milieu poreux saturé par un seul fluide a pour expression $v_p = \sqrt{H/\rho}$ avec $H = L + f(K_s, K_f, \varphi)$, H et L étant les modules élastiques de l'onde P du milieu poreux saturé en fluide et sans fluide respectivement, avec K_s et K_f les modules d'incompressibilité des grains solides et du fluide et φ la porosité. Pour des milieux poreux avec plusieurs fluides, la propagation des ondes est différente du fait d'une diffusion de fluide hétérogène. La théorie de Gassmann reste valable pour deux cas extrêmes à très basses fréquences et très hautes fréquences (Müller et al., 2010) :

- à basse fréquence (limite de Wood, état quasi-statique), le module effectif d'incompressibilité du fluide est la somme harmonique des modules des différents fluides : $K_F = \left[\sum_{i=1}^{n} \frac{S_i}{K_{fi}}\right]^{-1}$ et le module de l'onde P est : $H_{wood} = L + f(K_s, K_F, \varphi)$,

- à haute fréquence (limite de Hill), l'équilibre n'a pas le temps d'être atteint et les différentes parties du milieu poreux sont à des pressions de fluide différentes, la théorie de Gassmann est appliquée à chaque zone individuelle et le module des ondes P est calculé à partir de la moyenne harmonique des modules : $H_{Hill} = \left[\sum_{i=1}^{n} \frac{S_i}{H(K_{fi})}\right]^{-1}$.

Les deux cas présentés sont des cas extrêmes d'un phénomène de relaxation. La théorie de la poroélasticité de Biot (Biot, 1956 a et b) permet de rendre compte des phénomènes de circulation de la phase fluide générée par le passage de l'onde. Le module de vitesse des ondes P, $H(\omega)$ est complexe et varie en fonction de la fréquence. Il quantifie les phénomènes d'atténuation et de dispersion des ondes sismiques. Pour préciser la quantification du gaz libre, il est possible d'utiliser en complément des vitesses de propagation, la mesure d'atténuation sismique fournie par le facteur de qualité. Des formulations analytiques du module complexe de vitesse des ondes de compression $H(\omega)$ et du facteur de qualité peuvent être obtenues avec le modèle de White et al. (1975) qui considère une répartition hétérogène en petites zones de gaz (patches). Ce modèle repose sur le concept de la circulation de fluide induite par le passage de l'onde sismique à la méso-échelle (> dimension des pores); il considère un milieu poreux équivalent constitué par une alternance périodique de deux couches saturées par deux fluides différents qui sont l'eau et le gaz libre (Carcione & Picotti, 2006).

Pour la quantification de la saturation en hydrate, deux cas de figure sont considérés pour rendre compte de la distribution des hydrates au sein des sédiments marins (Helgerud et al., 1999) : a) un cas où les hydrates sont distribués dans l'espace poreux sans contribuer à la matrice, le module effectif de la vitesse P est calculé par l'expression de H_{wood} en considérant le module d'incompressibilité de la phase fluide K_F calculé avec la moyenne harmonique de ceux de l'eau et des hydrates ; b) le cas où les hydrates participent à la matrice avec H calculé en considérant les hydrates faisant partie des grains solides contribuant à L et K_S.

Les anomalies de vitesses sont inversées en exploitant ces modèles de milieux effectifs pour obtenir des concentrations en hydrate et en gaz libre pour une partie du profil 34a. Cette inversion s'est déroulée en deux étapes :

1) Définition du profil de porosité dans la zone de référence du profil 34a à partir de l'inversion du profil de vitesse caractérisé par un gradient linéaire. Ceci est réalisé en considérant des sédiments normalement consolidés, une porosité qui évolue avec la profondeur (Terzaghi et al., 1996) et le modèle effectif développé par Dvorkin et al. (1999), en utilisant une composition minéralogique issue du forage DSP du site 380 (Calvert & Batchelor, 1978) et de l'analyse des carottes sédimentaires prélevées pendant la campagne (Ballas et al., 2018).
2) Définition des concentrations en hydrate de gaz et en gaz libre en exploitant l'écart (positif ou négatif) au profil de vitesse de référence en prenant en compte les hydrates ou le gaz libre dans les sédiments marins à l'aide de la théorie des milieux effectifs décrite plus haut. Pour les hydrates, les deux cas de figure ont été considérés suivant la répartition des hydrates dans les pores ou faisant partie de la matrice. Pour le méthane sous forme de gaz libre, le modèle White et al. (1975) a été utilisé. L'inversion du profil de vitesse a été obtenue avec une optimisation locale qui recherche la concentration en hydrate ou en gaz libre en minimisant au sens des moindres carrés les différences entre vitesses modélisées et déduites de la sismique. Pour le cas du gaz libre, le facteur de qualité est également pris en compte pour définir la taille caractéristique des patches de gaz. Il est important de noter que la dépendance fréquentielle de la vitesse de propagation et du facteur de qualité n'a pas été exploitée et qu'une valeur constante pour ces deux paramètres a été utilisée pour un intervalle de

temps/profondeur donné correspondant à la fréquence dominante du signal sismique dans cet intervalle. L'incertitude sur les valeurs de concentration a été évaluée à 30 %.

c) Etat actuel

La caractérisation géophysique a permis de décrire l'état actuel du système hydrate (figure 3.8 bas). Le BSR permet de délimiter la zone de stabilité des hydrates. La localisation des hydrates avec des concentrations moyennes significatives de 5 à 10 % se limite à la partie inférieure de la zone de stabilité des hydrates. On obtient une épaisseur variable qui augmente de la terminaison du système vers le large pour atteindre 200 m au-dessus du BSR dans le domaine profond. Le méthane sous forme de gaz libre est piégé sous le BSR avec une concentration moyenne de 5 %. Les hydrates en stockant le gaz libre agissent comme une barrière à la migration verticale du gaz vers le fond de mer, limitant les échappements de fluide du fond de mer à l'extérieur de la zone de stabilité des hydrates (figure 3.7). L'absence de BSR et de gaz libre dans certaines zones comme la zone de référence sont associées à l'absence de chemins de migration du gaz en provenance de réservoirs profonds. L'existence d'un système de failles au cœur de la zone de stabilité des hydrates permet un flux suffisamment important de gaz pour autoriser la coexistence d'hydrate et de gaz libre au niveau d'une zone de crête où des sorties de fluide ont été observées et des échantillons d'hydrates collectés.

Etat transitoire du système hydrate

a) Profondeur anormale du BSR

La stabilité des hydrates de gaz est contrôlée par la composition du gaz renfermé dans les hydrates, la température, la pression et la salinité des eaux interstitielles (Sloan, 2003). Lors de la campagne GHASS, les mesures *in situ* ont permis de définir la température en fond de mer à 9°, d'évaluer le gradient géothermique, d'identifier une composition du gaz piégé dans les hydrates à 99 % de méthane biogénique. L'analyse des eaux interstitielles menée sur les carottes prélevées pendant la campagne a révélé la présence d'un gradient de salinité de 22 psu en fond de mer pour atteindre 2 psu à 25 m de profondeur. Ce gradient de salinité est associé à l'histoire récente de la mer Noire. Ainsi, suite à la reconnexion avec la Méditerranée il y a 9 000 ans, la mer Noire a vu sa salinité augmenter de 2 psu (la mer Noire était alors un lac) pour se stabiliser à 22 psu en fond de mer depuis 2500 ans. Si l'intrusion de sel a des conséquences importantes sur les propriétés physico-chimiques des sédiments (Ruffine et al., 2021), elle modifie également les conditions de stabilité des hydrates du fait de la présence d'ions (Dickens & Quinby-Hunt, 1994). Les mesures *in situ* ont permis de réaliser des modélisations des conditions actuelles de la zone de stabilité des hydrates de gaz dans un état d'équilibre (Sultan et al., 2010). La comparaison entre la limite calculée de stabilité à l'équilibre avec la position du BSR montre que ce dernier est plus profond de 100 m (figure 3.9). Le BSR actuel se situe à une position intermédiaire entre la limite de stabilité calculée pour le dernier épisode glaciaire (température au fond de l'eau de 4°C et niveau marin plus bas de 100 à 150 m d'après Soulet et al., 2011) et actuelle pour un système à l'équilibre. Cette anomalie de profondeur du BSR indique que suite aux variations des conditions environnementales subies depuis le dernier épisode glaciaire, le système hydrate est dans un état transitoire qui tend vers un nouvel équilibre. Si un nouvel équilibre des conditions de pression et de température semble être atteint, le fait d'être toujours dans un état transitoire indique que le système hydrate possède un temps de latence pour retrouver un nouvel état d'équilibre. L'hypothèse d'une perméabilité faible et hétérogène des sédiments marins pourrait expliquer cette latence.

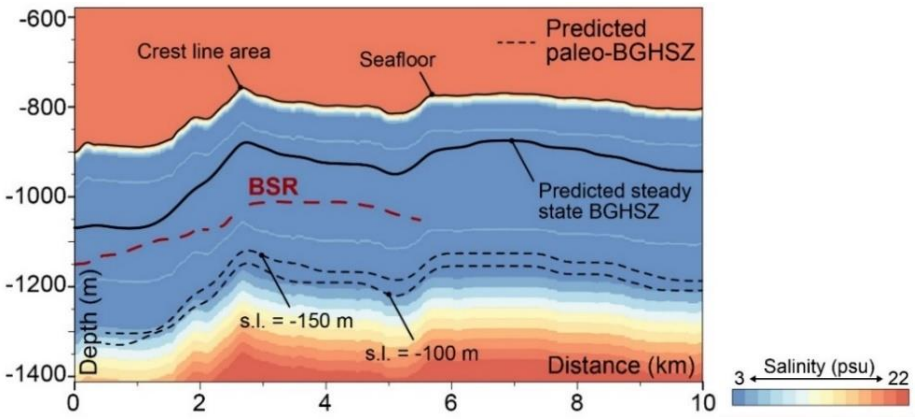

Figure 3.9 : Base de la zone de stabilité des hydrates prédite à l'équilibre dans les conditions actuelles (avec les paramètres mesurés *in situ*) et passée (paramètres de Soulet et al., 2011) à comparer avec la position du BSR.

b) BSR irrégulier

Les profils SYSIF permettant une imagerie à très haute résolution de la zone de stabilité des hydrates (1 m pour la résolution verticale et 3 m pour la résolution horizontale) ont révélé l'existence d'un BSR irrégulier (Colin et al., 2020b). Sur ces profils, si la tendance générale du BSR est de descendre (figure 3.10), on observe localement des réflexions de plus fortes amplitudes associées à la présence de gaz libre situées au-dessus de la tendance générale du BSR. Certaines de ces réflexions avec une polarité inverse sont caractérisées par une nature discontinue avec des hyperboles de diffraction, non focalisées par la migration, générées par des hétérogénéités d'une taille inférieure à 3 m. La distribution irrégulière du front de gaz associé au BSR est une observation directe de la migration en cours de la zone de stabilité. Ce BSR atypique correspond à une migration irrégulière de la zone de stabilité du fait des différences de perméabilité des sédiments qui génèrent une déstabilisation hétérogène des hydrates. La déstabilisation hétérogène des hydrates pourrait être associée à la présence de surpressions générées par une faible perméabilité qui faciliterait la recristallisation des hydrates ralentissant ainsi la migration de la zone de stabilité (Sultan, 2007).

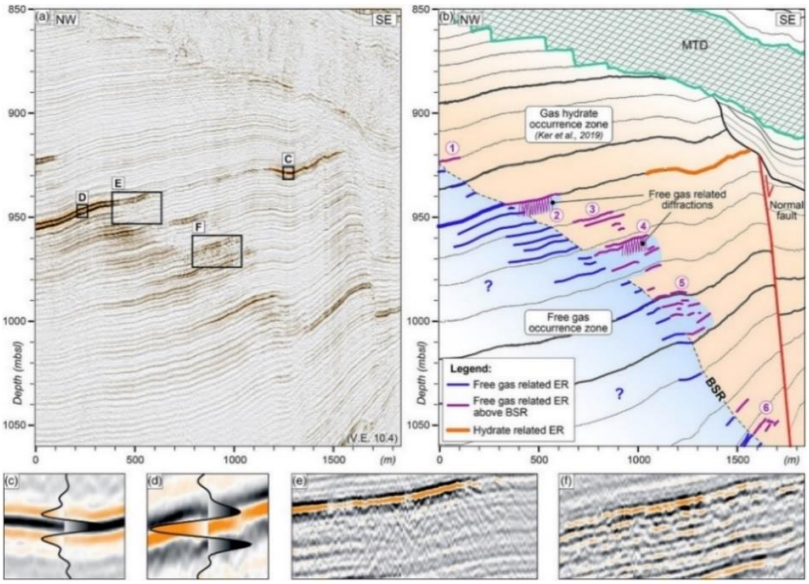

Figure 3.10 : a) Pofil Sysif (PL01PR12) montrant un BSR irrégulier et b) son interprétation. c) et d) polarité de réflecteurs clés, e) et f) réflecteurs présentant de nombreuses diffractions (Colin et al., 2020b).

c) Double BSR

Plusieurs profils sismiques haute résolution ont révélé la présence d'un double BSR étudié dans le cadre de la thèse de Maud Fabre (2021-2023). Les deux BSR recoupent la stratigraphie, sont parallèles au fond de l'eau et possèdent une polarité inverse en accord avec des chutes de vitesse des ondes de compression (figure 3.11). Le second BSR, situé 130 m plus profondément que le premier, est de plus faible amplitude et constitue la limite supérieure d'une zone caractérisée par une plus faible vitesse et une plus forte atténuation que celles de la couche située entre les deux BSR. La modélisation dynamique de la zone de stabilité des hydrates au cours des derniers 33.5 ka utilisant les conditions environnementales passées et présentes permet d'associer le premier BSR à la position actuelle de la limite de stabilité et le second BSR à la position de cette limite durant le dernier épisode glaciaire (entre -33.5 et -20 ka). La préservation de cette relique de l'ancienne limite de stabilité pourrait être associée à la faible perméabilité des sédiments et à la très grande période de stabilité (Fabre et al., en révision). La migration de la zone de stabilité des hydrates générée par des variations des conditions environnementales est un processus avec une dynamique lente dans les sédiments marins de faible perméabilité où la diffusion du gaz est dominante. L'ensemble de ces observations de profondeur anormale du BSR, de BSR irrégulier et de double BSR atteste de cette dynamique lente du système hydrate du secteur roumain de la mer Noire. Les hypothèses de conséquences catastrophiques associées à une déstabilisation rapide des hydrates (Clathrate gun) semblent écartées pour ce type de système hydrate.

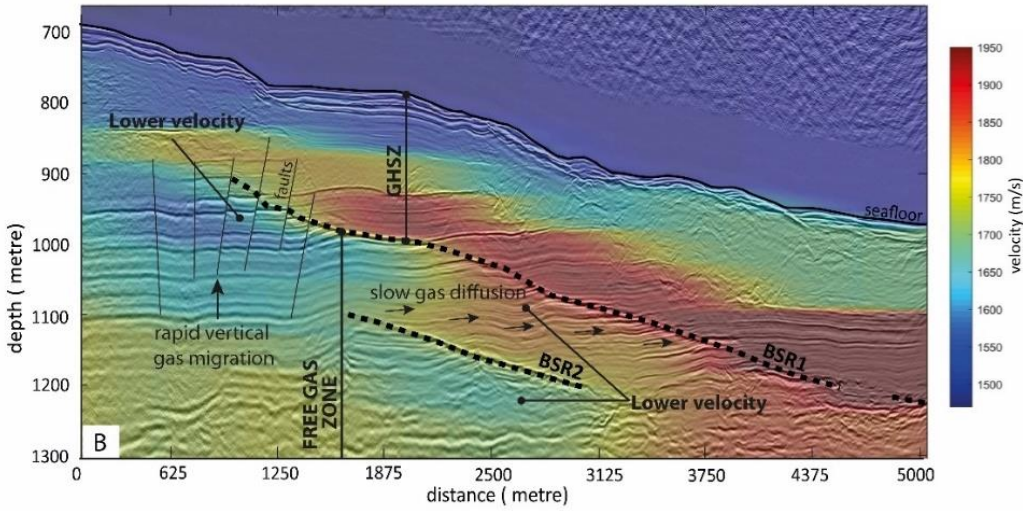

Figure 3.11 : Profil sismique haute résolution (profil HR33c) et champ de vitesses P surimposé. Les deux BSR sont associés à des chutes de vitesse (Fabre et al., en révision).

d) Impact de la salinité sur la déstabilisation

Un autre résultat important du projet GHASS fut de révéler que l'évolution en cours du gradient de salinité était une source de déstabilisation actuelle pour la partie superficielle du système hydrate (Riboulot et al., 2018). Les modélisations de la stabilité des hydrates montrent que la diffusion de sel dans les sédiments entraîne une géométrie atypique en forme de langue de la terminaison de la zone de stabilité (superposition avec un profil SYSIF en figure 3.12). La lente diffusion du sel contribue à la migration vers le large de la zone de stabilité. Ce processus de déstabilisation en cours pourrait être la cause principale des échappements de gaz observés à la limite du système hydrate dans une zone en cours de déstabilisation.

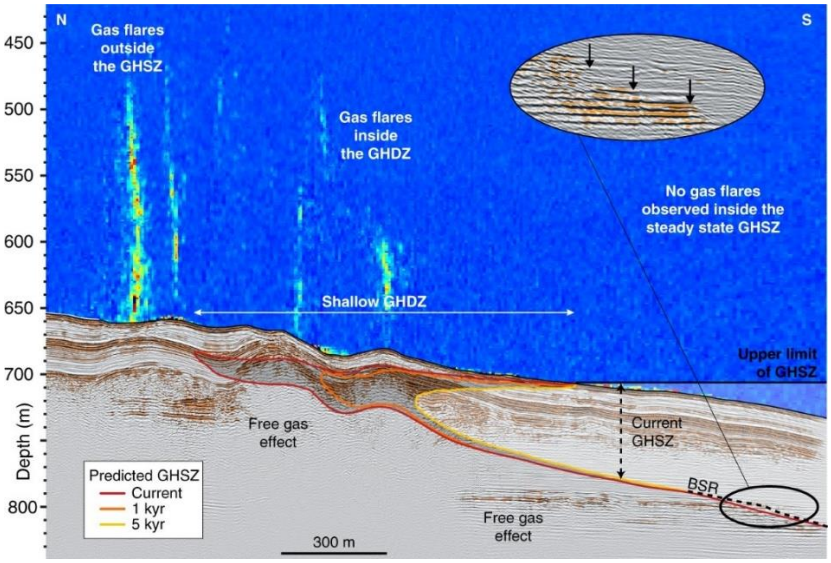

Figure 3.12 : Combinaison de l'échogramme issu des données acoustiques et profil SYSIF (PL01PR04) avec en superposition le calcul de la zone de stabilité des hydrates. La déstabilisation des hydrates due à la salinisation des sédiments marins pourrait être responsable des panaches acoustiques associés aux sorties de fluide (Riboulot et al., 2018).

3.3.5 Bilan sur la caractérisation sismique et perspectives à court terme

Bilan

Les développements réalisés dans le cadre des deux premières thématiques de recherche ont été incorporés à l'arsenal de caractérisation sismique des sédiments superficiels contenant des hydrates de gaz et/ou du gaz libre. En association avec une approche d'imagerie sismique multirésolution combinant sismique haute résolution de surface et très haute résolution près du fond, cet arsenal a permis de fournir des outils efficaces pour analyser et caractériser quantitativement les réflecteurs clés associés à la présence de gaz libre. Une approche pluridisciplinaire incorporant analyses géophysiques, géomorphologiques, géochimiques et modélisation reposant sur des paramètres mesurés *in situ* a permis de mieux comprendre la formation et la composition des *pockmarks* et de révéler la dynamique actuelle du système hydrate du secteur roumain de la mer Noire dans le cadre du projet GHASS. Une seconde phase de ce projet nommée GHASS2 (2020-2025), coordonnée par Vincent Riboulot, associée au projet ANR BLAME (2020-2024) et européen DOORS (2021-2025) est en cours pour : 1) caractériser le système gaz dans sa globalité du réservoir à l'hydrosphère dans le secteur nord du canyon du Danube, 2) quantifier les flux de gaz à l'interface eau/sédiments (bilan méthane et carbone) et étudier l'éventuel passage à l'atmosphère, 3) contraindre l'évolution temporelle de la zone de stabilité des hydrates depuis le dernier épisode glaciaire et analyser la déstabilisation actuelle liée au gradient de salinité. Ce second volet du projet GHASS s'appuie sur les travaux pluridisciplinaires réalisés pendant les trois legs de la campagne GHASS2 (2021).

Perspectives à court terme

A court terme, je vais poursuivre mes travaux de caractérisation et d'imagerie associés aux données sismiques de la campagne GHASS2 (2021) avec Estelle Théréau et Yannick Thomas. Au cours de la campagne GHASS2, nous avons acquis des données sismiques de surface avec deux résolutions différentes : une gamme pour la basse résolution et grande pénétration [5 - 92 Hz] et une gamme haute résolution [10 – 280 Hz] (Thomas et al., 2021). Le choix d'une acquisition basse

résolution a été motivé par la volonté d'imager l'intégralité des réservoirs de gaz profonds. La présence de dauphins pendant le déroulement de la campagne a eu pour conséquence de devoir réduire de 12 dB la puissance d'émission de la sismique BR et donc de fortement limiter nos capacités à imager les structures profondes. Les données sismiques ont été acquises avec des déports maximaux de 3000 et 6000 m respectivement. Pour rappel, le déport maximal du système sismique HR de GHASS était de 650 m.

Estelle Théréau et Yannick Thomas ont réalisé les phases de traitement des données de positionnement et du traitement conventionnel des données sismiques pour obtenir une imagerie après sommation (Théréau et Thomas, 2023). Il a été noté que l'apport des grands déports permet une plus grande précision dans l'analyse de vitesses démontrée en figure 3.13. Il est toutefois à constater la limite de l'approximation classique à deux termes de la correction de courbure normale qui se manifeste sur les longs déports.

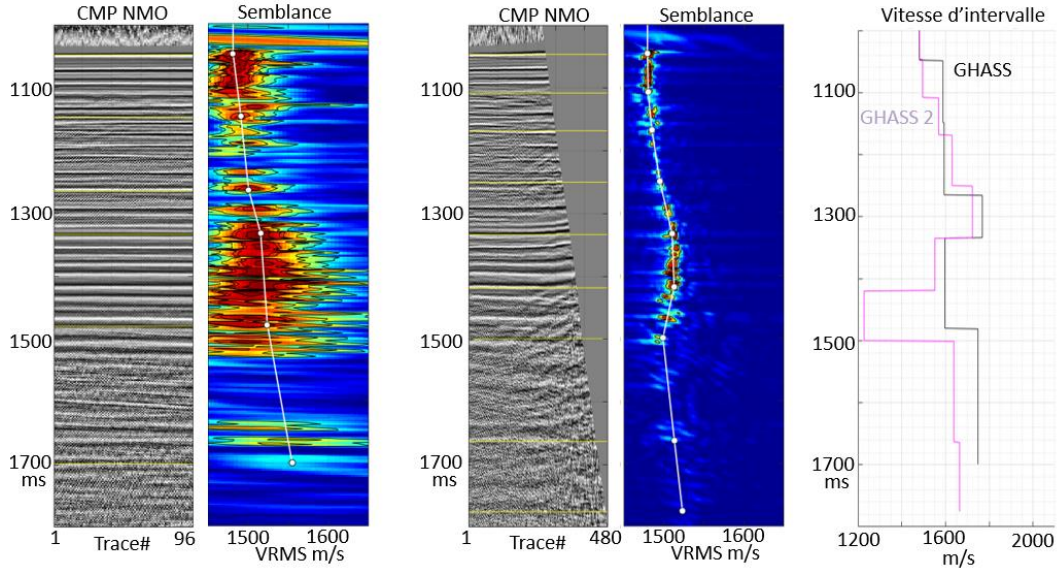

Figure 3.13 : Analyses de vitesse RMS sur les données de sismique haute résolution. Comparaison entre les données de la campagne GHASS (2015, streamer de 650 m) et celles de la campagne GHASS2 (2021, streamer de 3000 m) à la même localisation (zone de la crête). Collection CMP et panneau de semblance pour le profil 34a (GHASS) et le profil 23 (GHASS2), comparaison des vitesses d'intervalle issues des deux lois de vitesses quadratiques pointées (Théréau et Thomas, 2023).

L'exploitation des données sismiques de la campagne GHASS2 avec 21 profils haute résolution (1000 km) et 9 profils basse résolution (470 km) nous permettra de :

1) réaliser une délimitation plus précise des zones à hydrates et à gaz libre, en particulier de mieux définir l'extension des réservoirs de gaz libre grâce à l'acquisition basse fréquence [5 - 92 Hz]. L'identification des réservoirs profonds est quant à elle incertaine du fait du manque de puissance d'émission de la source basse résolution,

2) caractériser de manière quantitative les BSR irréguliers et des doubles BSR en exploitant les anomalies de vitesses, la dépendance fréquentielle de l'amplitude du BSR et l'atténuation dans la zone de gaz libre avec les deux résolutions (exemple du double BSR en figure 3.14),

3) améliorer l'évaluation des quantités en hydrate et en gaz libre initiée dans le projet GHASS avec une plus grande précision de l'analyse de vitesse fournie par les longs déports et l'utilisation de modèles effectifs plus performants prenant en compte la distribution des hydrates dans des

fractures ou des veines (Wei et al., 2021) et un modèle non-périodique pour la distribution du gaz libre de type *random patchy saturation* (Müller & Gurevich, 2004) ;

4) préciser le lien entre dynamique des hydrates et instabilités sédimentaires depuis le dernier épisode glaciaire.

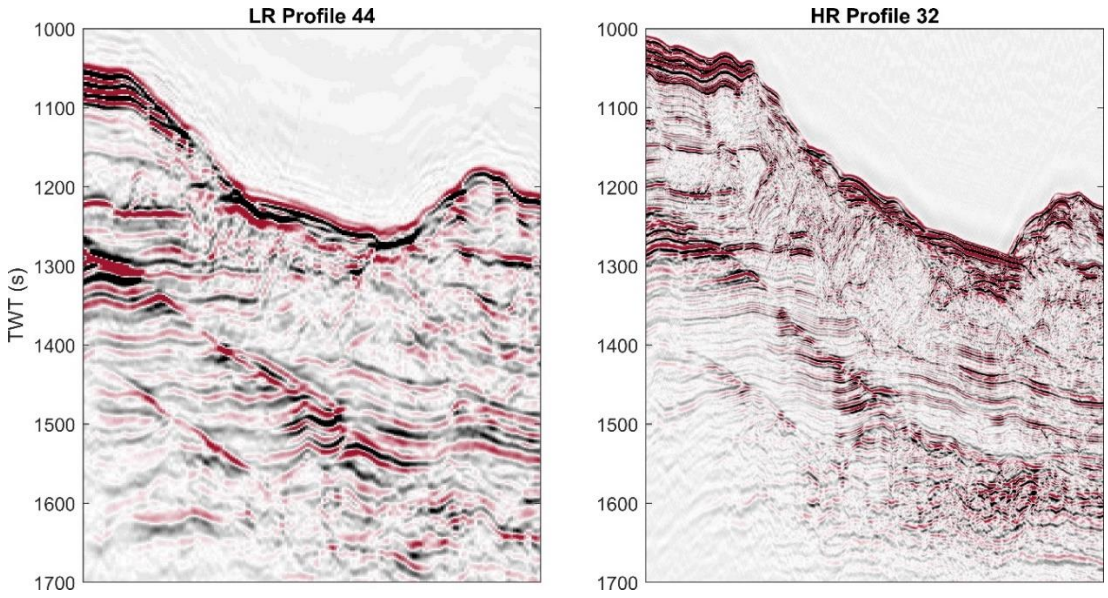

Figure 3.14 : Double BSR observé sur deux profils de la campagne GHASS2 proche l'un de l'autre et acquis avec les deux types de résolution (basse résolution et haute résolution)

La maîtrise de l'acquisition des données avec grands déports associée à celle de la modularité de la source sismique que nous avons pu obtenir depuis les campagnes du SHOM CARAPASS (2019) et SOUSACOU (2021), réalisées dans le cadre du projet AMETISTE dirigé par Elodie Marches (SHOM), et GHASS2 ouvrent la voie à une optimisation de l'acquisition sismique de surface. Cela permet d'améliorer l'imagerie et caractérisation à haute résolution des aléas marins, des architectures sédimentaires et des structures océaniques. Des développements méthodologiques seront encore nécessaires pour exploiter pleinement le potentiel de ces données grands déports en terme d'imagerie et d'inversion.

Articles associés

Colin, F., Ker, S., Riboulot, V., Sultan, N. (2020). Irregular BSR: Evidence of an ongoing reequilibrium of a gas hydrate system, *Geophysical Research Letters*, 47(20), e2020GL089906 (10p.).

Fabre, M., Riboulot, V., Loncke, L., Ker, S., Ballas, G., Thomas, Y., Ion, G., Sultan, N. (2024). Slow dynamics of hydrate systems revealed by a double BSR, *Geophysical Research Letters*, 51, e2023GL106284.

Goswami, B. K., Weitemeyer, K. A., Bunz, S., Minshull, T. A., Westbrook, G., Ker, S., Sinha, M. C. (2017). Variations in pockmark composition at the Vestnesa Ridge: Insights from marine controlled source electromagnetic and seismic data. *Geochemistry Geophysics Geosystems*, 18(3), 1111-1125.

Goswami, B. K., Weitemeyer, K. A., Minshull, T. A., Sinha, M. C., Westbrook, G., Chabert, A., Henstock, T. J., Ker, S. (2015). A joint electromagnetic and seismic study of an active pockmark within the hydrate stability field at the Vestnesa Ridge, West Svalbard margin. *Journal of Geophysical Research: Solid Earth*, 120(10), 6797-6822.

Ker, S., Thomas, Y., Riboulot, V., Sultan, N., Bernard, C., Scalabrin, C., Ion, G, Marsset, B. (2019). Anomalously deep BSR related to a transient state of the gas hydrate system in the western Black Sea. *Geochemistry Geophysics Geosystems*, 20(1), 442-459.

Ker, S., Le Gonidec, Y., Marsset, B., Westbrook, G., Gibert, D., Minshull, T. A. (2014). Fine-scale gas distribution in marine sediments assessed from deep-towed seismic data. *Geophysical Journal International*, 196(3), 1466-1470.

Riboulot, V., Ker, S., Sultan, N., Thomas, Y., Marsset, B., Scalabrin, C., Ruffine, L., Boulart, C., Ion, G. (2018). Freshwater lake to salt-water sea causing widespread hydrate dissociation in the Black Sea. *Nature Communications*, 9(117), 1-8.

Riboulot, V., Sultan, N., Imbert, P., Ker, S. (2016). Initiation of gas-hydrate pockmark in deep-water Nigeria: Geo-mechanical analysis and modelling. *Earth and Planetary Science Letters*, 434, 252-263.

Riboulot, V., Cattaneo, A., Sultan, N., Garziglia, S., Ker, S., Imbert, P., Voisset, M. (2013). Sea-level change and free gas occurrence influencing a submarine landslide and pockmark formation and distribution in deepwater Nigeria. *Earth and Planetary Science Letters*, 375, 78-91.

3.4 Perspectives de développements de la caractérisation sismique haute résolution à partir de l'acquisition sur le fond de mer par fibre optique et OBS

L'objectif de cette thématique est de développer la caractérisation du sous-sol marin avec des dispositifs de réception en fond de mer, en particulier ceux associés aux mesures distribuées sur fibre optique. Une caractérisation plus complète des propriétés physiques du sous-sol est possible avec l'enregistrement des ondes de surface par ces dispositifs permettant la détermination des vitesses de cisaillement. Malgré l'utilisation de fibres en géophysique de puits depuis maintenant une dizaine d'année, les défis en termes de mise en œuvre et de protocole de traitement restent ambitieux, notamment pour la caractérisation quantitative. L'exploitation de ces données passent par une maîtrise de la chaîne d'acquisition, par des développements en traitement adéquats et par des collaborations entre laboratoires de recherche et l'industrie. L'Ifremer s'est récemment investie dans ce domaine par l'acquisition d'équipements de pointe et par le recrutement de nouvelles compétences. La collaboration à des projets européens notamment avec l'IUEM est également une formidable opportunité pour progresser dans cette application en géosciences de la fibre optique.

3.4.1 Contexte de l'acquisition en fond de mer : émergence des mesures distribuées sur fibre optique

L'acquisition avec des sismomètres situés sur le fond de mer permet, en plus de l'enregistrement des signaux associés aux ondes de compression, celui des ondes de cisaillement et de surface. Ces instruments permettent également d'enregistrer le signal de *compliance* qui résulte de la déformation du sous-sol générée par les ondes de gravité (vagues, houles). La technologie des sismomètres de fond de mer a largement progressé ces dernières années avec notamment la mise en œuvre des sismomètres large-bande (*Ocean Bottom Seismometer*/OBS; Janiszewski et al., 2022) et des nodes (*Ocean Bottom Node*/OBN). Par contre, le nombre souvent très réduit d'instruments disponibles par la communauté scientifique limite fortement les études à haute résolution spatiale réalisables avec ces instruments.

L'émergence récente de la technique de mesures réparties sur fibre optique par réflectométrie laser autorise désormais l'acquisition de mesures sur le fond avec des dimensions de l'antenne de réception pouvant atteindre plusieurs dizaines de kilomètres avec une résolution spatiale de quelques mètres (Hartog, 2017, Lindsey et al., 2019) et une résolution temporelle élevée ($\geq$1 kHz). Ces mesures de réflectométrie peuvent être réalisées sur des fibres optiques dédiées ou sur des fibres optiques d'opportunité comme celles des câbles de télécommunications. Les mesures distribuées de type DVS ou DAS (*Distributed Vibration/Acoustic Sensing*) reposent sur la réflectométrie exploitant la rétrodiffusion de Rayleigh d'une impulsion laser émise par un équipement optique appelé interrogateur (Hartog, 2017). La sensibilité de la fibre à son étirement ou à sa contraction permet de mesurer le taux de déformation dynamique associé au passage des ondes. Une première application en géophysique a été associée à l'acquisition de profils sismiques verticaux dans les puits de forage (Johannessen et al., 2012). Très rapidement, la communauté des sismologues a détecté le potentiel de cette nouvelle technique associée aux infrastructures de câbles de télécommunications pour augmenter considérablement la surveillance des activités sismiques (Jousset et al., 2018) en particulier dans le domaine océanique où la couverture spatiale est très pauvre (Lindsey et al., 2019 ; Sladen et al., 2019 ; Williams et al., 2019).

Dans le cadre de l'imagerie géophysique, les mesures sur fibre peuvent être réalisées lors de campagnes d'acquisition mettant en œuvre des sources actives (Taweesintananon et al., 2021; Bachrach et al., 2023). Ces nouvelles données sont complémentaires des acquisitions de surface

et autorisent une meilleure caractérisation du sous-sol avec l'obtention d'images associées aux ondes de compression et aux ondes converties PS. Mais la grande opportunité de ce type de mesure réside dans l'acquisition de longues séries temporelles appliquées à l'étude de la sismique passive dans le domaine marin. L'acquisition de longue durée, associée à des longueurs de dispositifs de plusieurs dizaines de kilomètres, permet d'exploiter le bruit sismique pour caractériser le sous-sol à l'aide de l'interférométrie par corrélation du bruit sismique ambiant (Spica et al., 2020 ; Cheng et al., 2021 ; Williams et al., 2021). Le développement de l'écoute passive marine par fibre optique ouvre ainsi la voie à une amélioration sans précédent de la mesure du bruit sismique associé à l'interaction Océan-Terre solide et à la surveillance de l'évolution temporelle des propriétés du sous-sol.

3.4.2 Caractérisation sismique à partir des mesures réparties sur fibre optique

Mes travaux de recherche associés aux mesures réparties sur fibre optique vont porter, tout d'abord, sur l'étude de la réponse instrumentale du capteur « fibre optique », prés-requis indispensable avant toute caractérisation. Puis ils porteront sur la détermination des profils de vitesses des ondes de cisaillement avec des sources actives ou à partir de la corrélation de bruit.

Etude de la réponse instrumentale

La réponse instrumentale du capteur « fibre optique » est complexe et nécessite des travaux portant sur son analyse, sa caractérisation et sa calibration. Une première composante de la réponse instrumentale du capteur « fibre » est liée à l'interrogateur réalisant les mesures optiques. La seconde composante qui module la sensibilité du capteur « fibre » est associée aux propriétés de la fibre, celles du câble et à sa mise en œuvre.

Principe de la mesure DAS

Les mesures distribuées sur fibre optique des câbles sous-marins au moyen de la technique DAS sont des mesures du taux de déformation longitudinale le long de la fibre optique (Hartog, 2017). Le taux de déformation est obtenu à partir du déphasage du signal optique mesuré entre des émissions laser successives.

$$\Delta\dot{\Phi} = \frac{4\pi n \zeta L}{\lambda}\dot{\epsilon} \qquad \text{eq. 4.1}$$

Où $\Delta\dot{\Phi}$ est la dérivée temporelle du déphasage, $\dot{\epsilon}$ la dérivée temporelle de la déformation longitudinale, n l'indice de réfraction, ζ le coefficient photo-élastique, L la distance de jauge et λ la longueur d'onde de l'impulsion laser. Les mesures DAS ne sont pas des mesures ponctuelles, elles sont obtenues en considérant un segment de fibre, appelé distance de jauge L, afin d'obtenir une mesure robuste du déphasage des signaux laser. Cette acquisition est équivalente à un filtrage d'antenne du taux de déformation qui limite la gamme des nombres d'ondes échantillonnés. Elle agit comme un filtre passe-bas et peut introduire des creux dans la réponse spectrale (Yang et al., 2022). Le traitement des mesures optiques est réalisé au sein de l'interrogateur. La connaissance de la séquence et des paramètres de traitement est déterminante pour estimer de manière précise le taux de déformation moyen associé à la distance de jauge.

Propriétés de la fibre optique

Deux caractéristiques de la fibre optique sont importantes dans le cadre des mesures DAS et dans l'étude de la réponse instrumentale. La première est l'atténuation (en dB/km) qui impacte la portée de la mesure en fonction de la longueur d'onde utilisée et du bruit intrinsèque de l'interrogateur (Hartog, 2017). La seconde est l'aménagement de la fibre optique au sein du

câble, à savoir libre (*loose*) ou serré (*tight*) qui différent par la possibilité de la fibre de se déplacer ou non librement au sein du câble. L'aménagement peut impacter la sensibilité de la mesure comme semble l'indiquer l'étude menée par Trafford et al. (2022).

Couplage avec le sous-sol marin et nature du câble

La qualité du couplage du câble avec le sous-sol marin a bien sûr un impact sur la sensibilité de la mesure DAS. De plus il existe deux types de câbles sous-marins : les câbles optiques (e.g. câbles de télécommunication) et les câbles hybrides électro-optiques avec une masse linéique de plusieurs dizaines de kg/m (figure 4.1). Selon le type de câble, la nature et la constitution varient, influençant également la sensibilité de la fibre. Ces impacts sont à étudier et quantifier.

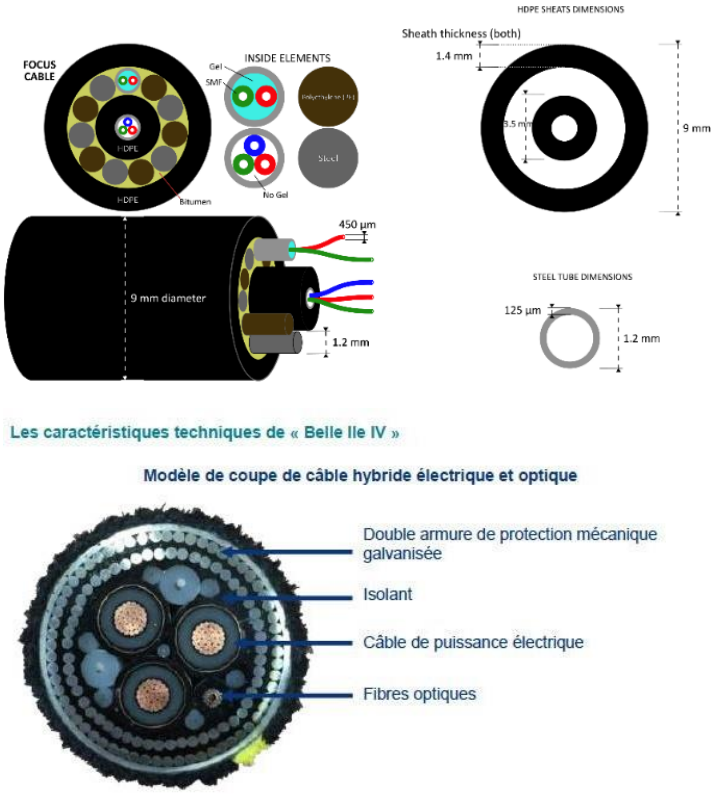

Figure 4.1 : Gauche : Description du câble sous-marin FOCUS de diamètre 9 mm avec 5 fibres optiques (source : G. Cappelli). Droite : Section du câble hybride sous-marin électro-optique (20 000 V) de 119 mm comportant 48 fibres optiques (Source Enedis).

La caractérisation des mesures DAS nécessitera de connaître précisément le positionnement du câble et de développer une méthodologie de calibration avec des mesures conventionnelles de déplacement.

Positionnement

La localisation précise du câble sous-marin est un prérequis pour des objectifs d'imagerie ou de caractérisation haute résolution du sous-sol marin. Un positionnement précis du câble est parfois difficile à obtenir suivant les conditions de mises en œuvre (fond accidenté, enfouissement). De plus, les distances le long du câble obtenues à partir du trajet optique sont très souvent supérieures aux distances vraies. Ce problème est dû à l'aménagement de la fibre optique de type libre et est connue sous le nom d'*overstuffing*. La longueur de fibre peut alors être supérieure à

celle du câble de 0.1 à 2.5% engendrant des erreurs de positionnement de plusieurs dizaines de mètres (Lumens, 2014). Pour des expériences de sismique active, il est impératif d'exploiter les trajets directs entre la source et la fibre pour déterminer précisément le positionnement du câble (Bachrach et al., 2023). Pour des expériences passives et suivant le degré de précision souhaité pour le positionnement, des sources comme les navires dont la position est connue, peuvent être exploitées.

Transformation déformation-vitesse/déplacement

Les mesures DAS diffèrent des mesures classiques faites en sismologie et en imagerie sismique qui sont associées soit au déplacement (vitesse et accélération) et acquises par les sismomètres, soit à la pression et mesurées par les hydrophones. Afin de comparer les mesures DAS aux mesures obtenues avec des géophones ou accéléromètres, il est nécessaire de développer des procédures de transformation des mesures du taux de déformation en mesures de vitesse. Cela permet aussi de bénéficier des traitements élaborés depuis plusieurs décennies en sismologie et en imagerie sismique. Dans le cas simple d'une onde plane, la relation entre le taux de déformation $\dot{\epsilon}$ et la vitesse horizontale v_h des particules est (Daley et al., 2016) :

$$\dot{\epsilon} = \frac{i\omega}{c_h} v_h \qquad \text{eq. 4.2}$$

Où c_h est la vitesse horizontale apparente de l'onde plane. La difficulté repose sur la détermination précise de c_h. Pour le cas où plusieurs ondes sont enregistrées qui possèdent une vitesse de propagation c_h différente, il faut développer des procédures capables d'appliquer un facteur $c_h/i\omega$ pour chaque onde. Des approches exploitant les domaines fk (transformée de Fourier 2D) et tau-p (transformée de Radon) ont été proposées avec des hypothèses de géométrie d'acquisition linéaire et d'échantillonnage spatial régulier (Bachrach et al., 2023). Une approche développée par Trabatonni et al. (2023) s'appuie sur des moyennes spatiales glissantes pour la conversion des données DAS en déplacements avec une limitation à des segments rectilignes.

Détermination des propriétés de cisaillement du sous-sol marin

Le module de cisaillement est un paramètre clé en géomécanique pour les études de stabilité du sous-sol marin. Cependant ce module est extrêmement difficile à déterminer à partir des ondes de compression enregistrées par des acquisitions de surface. En effet, cela nécessite d'utiliser les techniques d'inversion des formes d'onde extrêmement complexes à mettre en œuvre, au regard de la résolution, pour des fréquences élevées (> 100 Hz) et mal contraintes par l'absence de basses fréquences (Provenzano et al., 2017 ; Virieux & Operto, 2009). Les ondes de surface de type Scholte (Scholte, 1947) sont porteuses d'information sur ce module de cisaillement. Ces ondes de surface peuvent être générées par des sources actives (Klein et al., 2005 ; Wege et al., 2022) et enregistrées par des instruments de fond de mer (OBN) ou des flûtes d'hydrophones tractées près du fond (uniquement en petit fond). Mais la difficulté et le coût de ce type d'acquisition limitent fortement son utilisation en domaine marin contrairement au domaine terrestre. L'émergence des mesures réparties sur fibre, qui sont sensibles aux ondes se propageant longitudinalement comme les ondes de Scholte (Spica et al., 2020), offre la possibilité de développer l'utilisation des ondes de surface pour caractériser le sous-sol marin (Trafford et al., 2022).

Un premier type d'acquisition d'ondes de surface consiste à utiliser une source active (canon à air) et la fibre d'un câble sous-marin. Une première étude de ce type a été conduite en Irlande par Trafford et al. (2022) pour déterminer le profil de vitesses de cisaillement dans les 25 premiers

mètres de sédiments dans le cadre d'une étude de site préalable à l'implantation d'un champ d'éoliennes en mer. Le second type d'acquisition est une approche de sismique passive qui consiste à acquérir de longues séries temporelles afin d'enregistrer le bruit sismique généré par l'interaction entre les ondes gravitaires océaniques et le fond marin (Longuet-Higgins, 1950 ; Ardhuin et al., 2011). La corrélation de bruit sismique permet de définir les fonctions de Green des ondes de surface et de réaliser une tomographie en l'absence de source active (Campillo & Shapiro, 2004, Shapiro et al., 2005). Cette approche s'est largement développée depuis vingt ans dans le domaine terrestre et a également été appliquée dans le domaine marin (Mordret et al., 2013). L'analyse des courbes de dispersion des ondes de surface et l'inversion des différents modes permettent d'obtenir la distribution des vitesses de cisaillement en fonction de la profondeur. Cette approche a été mise en œuvre en exploitant des données DAS au cours de ces dernières années (Spica et al., 2020 ; Cheng et al., 2021 ; Williams et al., 2021) démontrant ainsi son potentiel malgré quelques limitations (résolution verticale, inversion 1D, absence de caractérisation de distribution des sources).

Acquisition de sismique active conjointe surface/fond

La technologie DAS offre la possibilité de réaliser des expériences de sismique réflexion active avec une antenne de réception sur le fond de mer en exploitant les infrastructures de télécommunications déjà existantes et des observatoires sous-marins. Un des intérêts de la réception en fond de mer est de pouvoir enregistrer les ondes converties afin de réaliser une imagerie PS du sous-sol marin permettant une caractérisation plus complète de celui-ci. L'imagerie PS s'est montrée notamment très efficace pour l'imagerie des structures renfermant du gaz (Knapp et al., 2001). Une première étude réalisée par Bachrach et al. (2023) a montré le potentiel des données DAS pour l'enregistrement des ondes converties et l'obtention d'une imagerie PS à partir d'un câble. Une imagerie PP de bonne qualité peut également être obtenue, y compris avec des sources hautes fréquences (Taweesintananon et al., 2021) et peut être complémentaire à une imagerie obtenue avec une réception en surface avec un *streamer*. En effet, la configuration géométrique et la réponse instrumentale différente des mesures distribuées permettent une atténuation des multiples associés à la surface libre pour des réflecteurs profonds pour lesquels les angles d'incidence sont proches de la verticale. Afin d'exploiter les techniques de traitement développées pour les données OBN ou de comparer à l'imagerie issue des données streamer, le développement d'une méthode de transformation déformation-vitesse/pression des données DAS mentionnée plus haut est nécessaire.

3.4.3 Projets en cours sur les mesures acquises en fond de mer

Je participe depuis déjà plusieurs années à l'analyse de données issues d'OBS dans le cadre de projets menés à Ifremer et en collaboration avec d'autres instituts de recherche. L'Ifremer dispose d'un parc d'OBS important mais principalement mis en œuvre dans le cadre de mesures de sismiques actives grand angle dont les objectifs ne sont pas la caractérisation haute résolution des sédiments superficiels. L'utilisation de fibre optique est quant à elle une activité nouvelle portée notamment par des projets de recherche européens.

Mesures issues des sismomètres de fond de mer : projet Bruit-FM

Depuis mai 2022, je participe au projet ANR Bruit-FM porté par Wayne Crawford (IPGP) sur l'exploitation des signaux enregistrés par les sismomètres et hydrophones large-bande de fond de mer. La participation à ce projet est motivée par l'acquisition de compétences dans l'analyse des

longues séries temporelles, dans l'étude des caractéristiques du bruit sismique ambiant et de la *compliance*. Ces compétences seront exploitées dans les projets portant sur les mesures réparties sur fibre optique. Plus précisément, je co-anime, avec Wayne Crawford, la thématique de la séparation de signaux enregistrés par les sismomètres de fond de mer. Une des problématiques abordées est l'estimation robuste du signal de *compliance*. Celle-ci a fait l'objet d'un projet de recherche postdoctoral mené par Simon Rebeyrol (2022-2023) à l'Ifremer que j'ai supervisé en collaboration avec Laurent Duval (Université Gustave Eiffel) et Wayne Crawford. La technique classique de la fonction de transfert, permettant de soustraire le signal de *compliance* présent sur la composante verticale du sismomètre, est revisitée avec une estimation plus robuste en respectant l'hypothèse de stationnarité prérequise pour cette approche (figure 4.2). L'étude de la stationnarité est obtenue par une analyse multi-échelle de la déviation (MAD : *median absolute deviation*). La robustesse de la fonction de transfert est obtenue par la sommation de son estimation sur plusieurs jours (Rebeyrol et al., 2024 en révision). L'intérêt de cette approche est de permettre également une estimation plus robuste de la *compliance*.

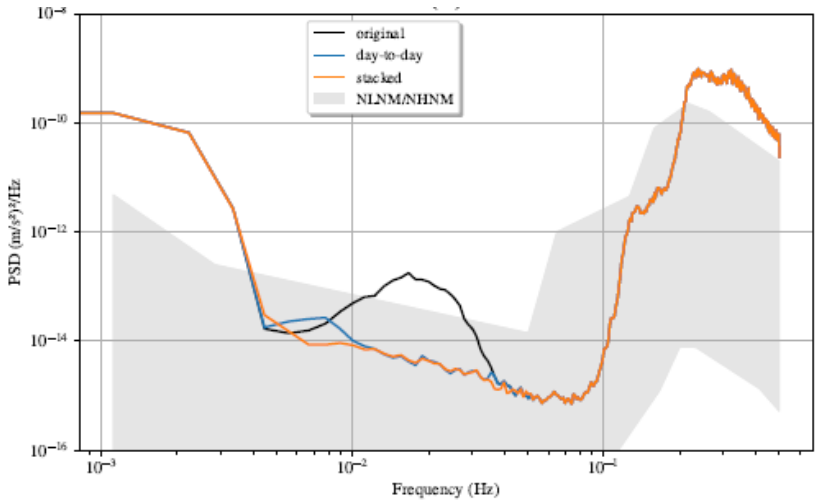

Figure 4.2 : Densités spectrales brutes et corrigées de l'accélération verticale de la station M11B (Cascadia Initiative) pour le printemps 2013. Le modèle de bruit est également indiqué (NHNM and NLNM: New High and Low Noise Model tiré de Peterson, 1993)

Dans la seconde partie de ce projet, nous tenterons également de développer des techniques pour isoler les signaux sismiques et microsismiques d'autres signaux qui peuvent interférer (bruit anthropique, signaux biologiques, etc.). Il est important de noter que dans l'analyse des données réparties sur fibre, il sera nécessaire de s'appuyer sur ce type de données issues des instruments « classiques » tels que les sismomètres et hydrophones, pour des objectifs de calibration et/ou pour la complémentarité des informations décrivant les ondes sismiques.

Projets de mesures distribuées du taux de déformation sur fibre optique

Projet ERC Focus

Le projet ERC Focus porté par Marc-André Gutscher (CNRS-Geo-Ocean) vise à utiliser les câbles sous-marins pour surveiller les déformations du sous-sol et à améliorer le dispositif d'alerte aux séismes et tsunamis. Le projet repose sur l'utilisation de la réflectométrie Brillouin (BOTDR) et sa capacité à mesurer des possibles déformations des fonds marins. Une acquisition continue est opérée depuis mai 2020 en mer Ionienne à l'Ouest de la Sicile. Elle utilise la fibre du câble sous-marin MEOC (Main Electro Optical Cable) de 28 km associé au site de test de la nouvelle génération de télescope à neutrinos opéré par INFN-LNS (Italie). En octobre 2020, un nouveau

câble de 6 km (câble FOCUS) a été déployé et connecté au site de test sud (TSS). Il recoupe 4 fois la faille Alfeo au large de Catane (figure 4.3). Ce câble a été conçu spécialement pour le projet avec Lionel Quetel (IDIL fiber optics) et renferme des fibres libres et serrées pour étudier leurs réponses. Pour ce projet, des réseaux de stations géodésiques et de sismomètres de fond de mer (courte et longue périodes) ont également été déployés. L'analyse de la série temporelle collectée depuis octobre 2020 a révélé des déformations de 2.5 cm générées soit par un glissement lent, soit par l'action de courant (Gutscher et al., 2023).

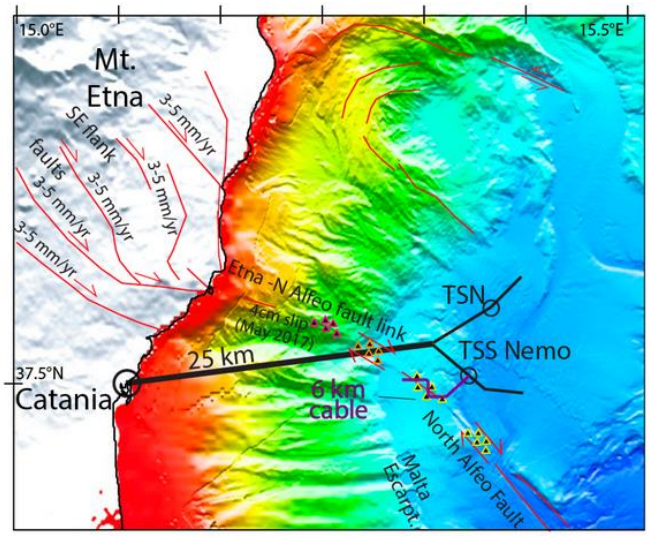

Figure 4.3 : Carte présentant la bathymétrie au large de Catane (Gutscher et al., 2023), la localisation de la faille Alfeo (en rouge) et la localisation du câble sous-marin MEOC (en noir) opéré par INFN-LNS avec ses deux branches nord et sud à laquelle est raccordé le câble FOCUS de 6 km (en violet).

Première campagne d'acquisition DAS en mer Ionienne

A la fin de l'année 2022, avec Shane Murphy responsable Ifremer du projet Focus, nous avons pu procéder à l'achat d'un interrogateur DAS. L'objectif est de travailler sur ce type de mesures en complément des travaux réalisés sur les données BOTDR. L'interrogateur OptoDAS d'ASN a été sélectionné et nous a été livré en mai 2023. Après une période de familiarisation avec l'équipement, nous avons pu procéder à notre première campagne de mesures DAS à Catane et à Capo Passero en novembre 2023 sur plusieurs longueurs de câbles de 30 à 200 km de long en collaboration avec INFN et IDIL. Florian Le Pape, qui a rejoint l'Ifremer en octobre 2023, a pu ainsi participer à ces premières acquisitions DAS.

Travaux sur la réponse instrumentale et la corrélation de bruit

Dans le cadre de la thèse de Giuseppe Cappelli (2023-2025) financée par la société IDIL dans le cadre du projet Focus portant sur « L'analyse des données de réflectométrie laser (BOTDR et DAS) sur des câbles de fibre-optique sous-marins », des travaux seront menés sur la réponse instrumentale de la fibre du câble FOCUS (sensibilité à la déformation, couplage). Nous exploiterons les signaux associés aux séismes pour étudier la différence de sensibilité des fibres libres et serrées (figure 4.1). Les problématiques du positionnement et de l'*overstuffing* du câble Focus seront également investiguées en exploitant les signaux de séismes mais également d'autres types de signaux (navires, bruit …). Le couplage des câbles MEOC et FOCUS avec le sous-sol marin sera étudié en analysant les signaux associés aux ondes sismiques mais également les signaux des ondes gravitaires associées aux vagues pour le câble MEOC. Il sera intéressant de quantifier l'impact de la *compliance* sur les signaux DAS associés aux ondes gravitaires.

L'étude des ondes gravitaires et du mécanisme de génération des ondes de surface induites par l'interaction Océan – Terre solide, menée avec Florian Le Pape, sera un prérequis à l'exploitation du bruit sismique afin de bien caractériser la localisation des sources de bruit pour les deux sites de Catane et Capo Passero (figure 4.4). Pour la détermination du profil des vitesses de cisaillement, je mènerai des travaux sur le conditionnement des données avant corrélation, sur l'obtention des fonctions de Green empiriques et sur l'inversion des courbes de dispersion. La connaissance précise de la position du câble et de la caractérisation de la distribution des sources permettra d'évaluer les possibles biais dans l'analyse des courbes de dispersions et l'estimation des vitesses. L'étude préliminaire des données DAS a mis en évidence l'enregistrement des ondes gravitaires et du bruit microsismique. Le spectre de Fourier à deux dimensions (FK) permet de bien distinguer les ondes gravitaires associées aux vagues se propageant vers la côte et leur réflexion. Les ondes de Scholte présentent un contenu fréquentiel et une vitesse apparente plus élevée (figure 4.4). L'analyse fréquentielle des données acquises à Capo Passero permet également d'identifier les deux types d'onde avec l'illustration de la dispersion des ondes gravitaires qui voient leur amplitude décroitre. Une augmentation de l'amplitude des ondes de Scholte est observable dans la partie profonde du bassin à partir de la distance de câble de 60 km (figure 4.5).

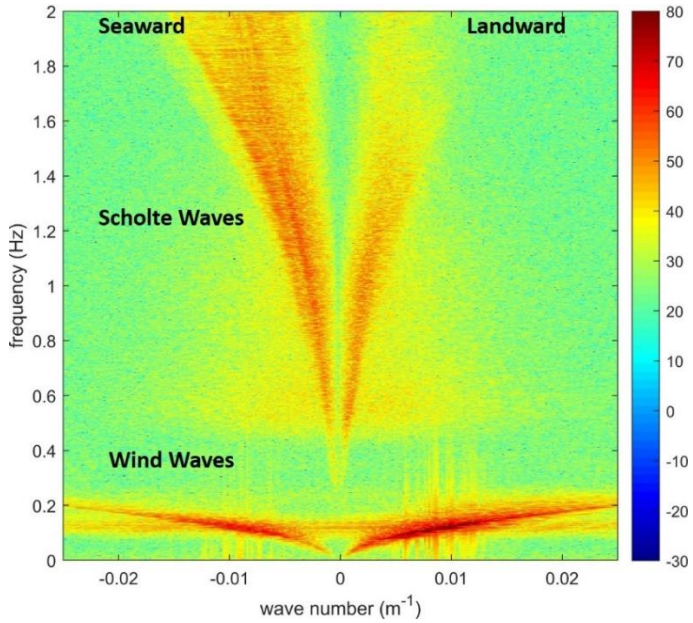

Figure 4.4 : Spectre FK des données DAS enregistrées sur le câble de Catane.

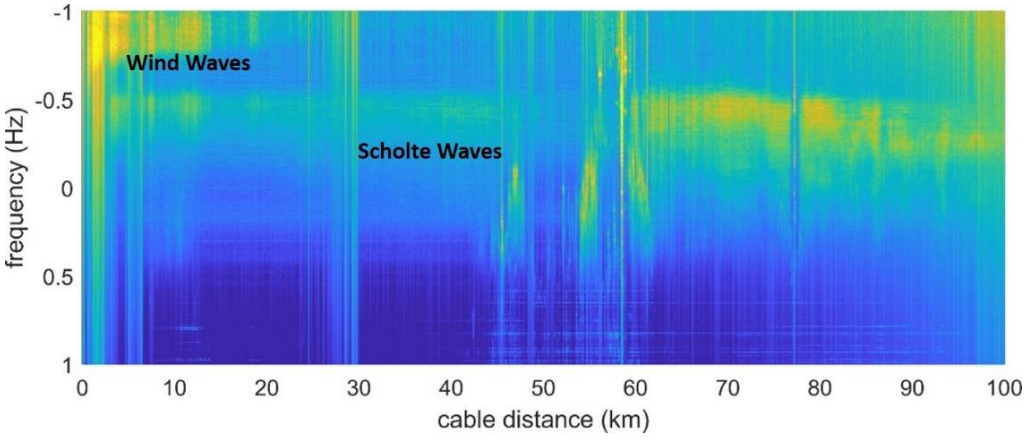

Figure 4.5 : Evolution du spectre des données DAS enregistrées sur le câble de Capo Passero en fonction de la longueur de câble.

Projets Fibescope, TAM-TAM et STORM

- Dans le cadre du projet Fiberscope (2024-2027), financé par la BPI, qui vise à atteindre une portée de l'interrogateur optique de 200 km, nous mènerons une étude sur le couplage du câble sous-marin avec le sous-sol. Ce projet sera mené dans le cadre d'un consortium avec la société FOSINA, fabricant d'interrogateurs optiques, et le groupe de télécommunication ORANGE. Au cours de ce projet nous étudierons tout particulièrement les signaux associés au bruit sismique ambiant observable en domaine côtier (des câbles localisés en Bretagne sont ciblés) et profond. Un point remarquable de ce projet est la possibilité de conserver l'enregistrement des données optiques « brutes ». Nous adapterons la séquence de traitement des données optiques aux signaux d'intérêt avec notamment une optimisation de la distance de jauge.

- Dans le cadre du projet TAM-TAM, en cours de montage pour le programme « Grands fonds marins » de France 2030, un câble sous-marin de télécommunication reliant la Nouvelle-Calédonie au Vanuatu va être muni de quelques nœuds instrumentés (accéléromètres et sismomètres 3 axes, capteurs de pression et température) et d'une fibre dédiée à l'acquisition de mesures DAS. Ce projet pourrait être l'opportunité de calibrer, par grande profondeur d'eau, les mesures ponctuelles et les mesures distribuées en utilisant une source sismique active et de proposer la réalisation d'une acquisition conjointe surface-fond pour l'imagerie de la zone.

- Le projet STORM porté par Geo-Ocean devrait être déposé en mars 2024 sous la coordination de Marc-André Gutscher pour l'appel à projet européen « Smart photonics ». Mon implication dans ce projet porterait sur l'étude de la réponse instrumentale en utilisant des sources actives/passives en complément du projet TAM-TAM.

- Projet d'acquisition de mesures DAS sur un câble côtier avec le déploiement d'une source active de type canon à air

Références

Adam, L., Batzle, M., Lewallen, K.T., van Wikj, K., (2009). Seismic wave attenuation in carbonates. *Journal of Geophysical Research*, 114, B06208.

Al-Yahya, K. (1989). Velocity analysis by iterative profile migration. *Geophysics*, *54*(6), 718–729. doi.org/10.1190/1.1442699

Ardhuin, F., Stutzmann, E., Schimmel, M., Mangeney, A. (2011). Ocean wave sources of seismic noise. *Journal of Geophysical Research,* 116(C9), doi: 10.1029/2011JC006952

Bachrach, R. et al. (2023). New wiggles from old cable: Data processing and imaging. *Geophysics*, 88, no. 6, WC199–WC208, doi.org/10.1190/GEO2023-0115.1

Ballas, G., Garziglia, S., Sultan, N., Pelleter, E., Toucanne, S., Marsset, T., Riboulot, V., Ker, S. (2018). Influence of early diagenesis on geotechnical properties of clay sediments (Romania, Black Sea). *Engineering Geology*, 240, 175-188.

Berryhill, J. R. (1979). Wave-equation datuming. *Geophysics, 44*(8), 1329–1344, doi: 10.1190/1.1441010

Biescas, B., Armi, L., Sallarès, V., Gràcia E. (2010). Seismic imaging of staircase layers below the Mediterranean Undercurrent. *Deep-Sea Research*, Part I, 57, 1345–1353.

Biot, M. A. (1956a). Theory of propagation of elastic waves in fluid-saturated porous solid. I. Low-frequency range. *Journal of the Acoustical Society of America*, 28, 168–178.

Biot, M. A. (1956b). Theory of propagation of elastic waves in a fluid-saturated porous solid. II. Higher frequency range. *Journal of the Acoustical Society of America*, 28, 179–191.

Bourbié, T., Coussy, O., Zinszner, B. (1987). Acoustics of porous media: Technip.

Bourbié, T. & Nur, A. (1984). Effects of attenuation on reflections: Experimental test. *Journal of Geophysical Research*, 89, 6197–6202.

Bryan, G. M. (1979). Basement profiling with a deep-towed hydrophone near Deep Sea Drilling Project Site 417. *Initial Reports of the Deep Sea Drilling Project*, *51*, 52–53.

Calvert, S. E. & Batchelor, C. H. (1978). Major and minor element geochemistry of sediments from Hole 379A, Leg 42B, Deep-Sea Drilling Project, *Initial Reports of the Deep Sea Drilling Project* (Vol. 42, pp. 527–541). Washington, DC: Government Printing Office.

Carcione, J. M. & Picotti, S. (2006). P-wave seismic attenuation by slow wave diffusion: Effects of inhomogeneous rock properties. *Geophysics*, 71(3), O1–O8, doi: 10.1190/1.2194512.

Chapman, N. R., Gettrust, J. F., Walia, R., Hannay, D., Spence, G. D., Wood, W. T., Hyndman, R. D. (2002). High-resolution, deep-towed, multichannel seismic survey of deep-sea gas hydrates off western Canada. *Geophysics*, *67*(4), 1038–1047, doi: 10.1190/1.1500364

Cheng, F., Chi, B., Lindsey, N.J., Dawe, T.C., Ajo-Franklin, J.B. (2021). Utilizing distributed acoustic sensing and ocean bottom fiber optic cables for submarine structural characterization. *Scientific Reports,* 11(1), 1–14.

Colin, F., Ker, S., Riboulot, V., Sultan, N. (2020b). Irregular BSR: Evidence of an ongoing reequilibrium of a gas hydrate system. *Geophysical Research Letters*, 47(20), e2020GL089906 (10p.).

Colin, F., Ker, S., Marsset, B. (2020a). Fine-scale velocity distribution revealed by datuming of VHR deep-towed seismic data: Example of a shallow gas system from the western Black Sea. *Geophysics*, *85*(5), 1–12, doi: 10.1190/geo2019-0686.1

Conn, A. R., Gould, N. I., Toint, P. L. (2000). *Trust region methods*. SIAM.

Daley, T. M., Miller, D. E., Dodds, K., P. Cook, P., Freifeld, B. M. (2016). Field testing of modular borehole monitoring with simultaneous distributed acoustic sensing and geophone vertical seismic profiles at Citronelle, Alabama. *Geophysical Prospecting*, 64, 1318–1334, doi: 10.1111/1365-2478.12324.

Davies, R. J., Morales Maqueda, M. A., Li, A., Ganopolski, A. (2017). Millennial-scale shifts in the methane hydrate stability zone due to Quaternary climate change. *Geology*, *45*(11), 1027–1030, doi: 10.1130/G39611.1

Dickens, G. R. & Quinby-Hunt, M. S. (1997). Methane hydrate stability in pore water; a simple theoretical approach for geophysical applications. *Journal of Geophysical Research*, *102*(B1), 773–783, doi: 10.1029/96JB02941

Dvorkin, J., Prasad, M., Sakai, A., Lavoie, D. (1999). Elasticity of marine sediments. *Geophysical Research Letters*, *26*(12), 1781–1784, doi: 10.1029/1999GL900332

Fagot, M. G. (1986). Development of a Deep-Towed Seismic System A New Capability for Deep-Ocean Acoustic Measurements. In T. Akal & J. M. Berkson (Eds.). *Ocean Seismo-Acoustics* (pp. 853–862). Springer US, doi: 10.1007/978-1-4613-2201-6_80

Futterman, W. I. (1962). Dispersive body waves. *Journal of Geophysical Research,* 67, 5279–5291, doi: 10.1029/JZ067i013p05279.

Gazdag, J., & Sguazzero, P. (1984). Migration of seismic data by phase shift plus interpolation. *Geophysics*, *49*(2), 124–131, doi: 10.1190/1.1441643

Gesret, A., Laigle, M., Diaz, J., Sachpazi, M., Hirn, A. (2010). The oceanic nature of the African slab subducted under Peloponnesus: thin-layer resolution from multiscale analysis of teleseismic P-to-S converted waves. *Geophysical Journal International,* 183**,** 833–849.

Goswami, B. K., Weitemeyer, K. A., Bunz, S., Minshull, T. A., Westbrook, G., Ker, S., Sinha, M. C. (2017). Variations in pockmark composition at the Vestnesa Ridge: Insights from marine controlled source electromagnetic and seismic data. *Geochemistry Geophysics Geosystems*, 18(3), 1111-1125.

Goswami, B. K., Weitemeyer, K. A., Minshull, T. A., Sinha, M. C., Westbrook, G. K., Chabert, A., Henstock, T. J., Ker, S. (2015). A joint electromagnetic and seismic study of an active pockmark

within the hydrate stability field at the Vestnesa Ridge, West Svalbard margin. *Journal of Geophysical Research: Solid Earth*, *120*(10), 6797–6822, doi: 10.1002/2015JB012344

Gurevich, B., Osypov, K., Ciz, R., Makarynska, D. (2008). Modeling elasticwave velocities and attenuation in rocks saturated with heavy oil. *Geophysic*s, 73, E115–E122.

Gutscher et al. (2023). Detecting strain with a fiber optic cable on the seafloor offshore Mount Etna, Southern Italy. *Earth and Planetary Science Letters*, 616, 118230.

Hajnal, Z., & Sereda, I. T. (1981). Maximum uncertainty of interval velocity estimates. *Geophysics*, *46*(11), 1543–1547, doi: 10.1190/1.1441160

Hartog, A.H. (2017). An Introduction To Distributed Optical Fibre Sensors, CRC Press.

He, T., Spence, G. D., Wood, W. T., Riedel, M., Hyndman, R. D. (2009). Imaging a hydrate-related cold vent offshore Vancouver Island from deep-towed multichannel seismic data. *Geophysics*, *74 (2)*, B23–B36, doi: 10.1190/1.3072620

Helgerud, M. B., Dvorkin, J., Nur, A., Sakai, A., Collett, T. S. (1999). Elastic-wave velocity in marine sediments with gas hydrates: Effective medium modeling. *Geophysical Research Letters*, *26*(13), 2021–2024, doi: 10.1029/1999GL900421

Hill, T. M., Kennett, J. P., Valentine, D. L., Yang, Z., Reddy, C. M., Nelson, R. K., et al. (2006). Climatically driven emissions of hydrocarbons from marine sediments during deglaciation. *Proceedings of the National Academy of Sciences*, *103*(37), 13,570–13,574, doi: 10.1073/pnas.0601304103

Hobbs, R. W., Klaeschen, D., Sallarès, V., Vsemirnova, E., Papenberg C. (2009). Effect of seismic source bandwidth on reflection sections to image water structure. *Geophysical Research Letters,* 36, L00D08, doi: 10.1029/2009GL040215.

Holbrook, W. S., Hoskins, H., Wood, W. T., Stephen, R. A., Lizarralde, D. (1996). Methane hydrate and free gas on the Blake ridge from vertical seismic profiling. *Science*, *273*(5283), 1840–1843, doi: 10.1126/science.273.5283.1840

Hovland, M. et al. (1984). Characteristic features of pockmarks on the north sea floor and scotia shelf. *Sedimentology* 31, 471–480.

Holbrook, W. S. & Fer, I. (2005). Ocean internal wave spectra inferred from seismic reflection transects. *Geophysical Research Letters*, 32, L15604, doi: 10.1029/2005GL023733.

Janiszewski, H. A., Eilon, Z., Russell, J. B., Brunsvik, B., Gaherty, J. B., Mosher, S. G., Hawley, W. B., Coats, S. (2022). Broadband ocean bottom seismometer noise properties. *Geophysical Journal International*, 233, Issue 1, April 2023, Pages 297–315, doi: 10.1093/gji/ggac450

Johannessen K., Drakeley B., Farhadiroushan M. (2012). Distributed Acoustic Sensing – a new way of listening to your well/reservoir, SPE Intelligent Energy International held in Utrecht, The Netherlands, 27–29 March 2012, SPE 149602, 9 pp.

Jousset, P. et al. (2018). Dynamic strain determination using fibre-optic cables allows imaging of seismological and structural features. *Nature Communications*, *9*(1), 2509.

Kennett, J. P., Cannariato, K. G., Hendy, I. L., Behl, R. J. (2003). Methane Hydrates in Quaternary Climate Change: The Clathrate Gun Hypothesis, Volume 54. In *Special Publications Series, American Geophysical Union, Washington, DC*.

Ker, S. & Le Gonidec, Y. (2020). Filtering of a Ricker wavelet induced by anelastic seismic wave propagation and reflection. *Journal of Geophysics and Engineering*, 17(5), 838-851.

Ker, S., Thomas, Y., Riboulot, V., Sultan, N., Bernard, C., Scalabrin, C., Ion, G, Marsset, B. (2019). Anomalously deep BSR related to a transient state of the gas hydrate system in the western Black Sea. *Geochemistry Geophysics Geosystems*, 20(1), 442-459.

Ker, S. & Le Gonidec, Y. (2018). Fractional integration of seismic wavelets in anelastic media to recover multiscale properties of impedance discontinuities. *Geophysics*, 83(2), V61-V71.

Ker, S., Le Gonidec, Y., Marié, L. (2016). Multifrequency seismic detectability of seasonal thermoclines assessed from ARGO data. *Journal of Geophysical Research: Oceans*, 121(8), 6035-6060.

Ker, S., Le Gonidec, Y., Marié, L., Thomas, Y., Gibert, D. (2015). Multiscale seismic reflectivity of shallow thermoclines. *Journal of Geophysical Research: Oceans*, 120(3), 1872-1886.

Ker, S., Le Gonidec, Y., Marsset, B., Westbrook, G., Gibert, D., Minshull, T. A. (2014). Fine-scale gas distribution in marine sediments assessed from deep-towed seismic data. *Geophysical Journal International*, 196(3), 1466-1470.

Ker, S., Le Gonidec, Y., Gibert, D. (2013). Multiresolution seismic data fusion with a generalized wavelet-based method to derive subseabed acoustic properties. *Geophysical Journal International*, 195(2), 1370-1383.

Ker, S., Le Gonidec, Y., Gibert, D. (2012). Multiscale seismic attributes: source-corrected wavelet response and application to high-resolution seismic data. *Geophysical Journal International*, 190(3), 1746-1760.

Ker, S., Le Gonidec, Y., Gibert, D., Marsset, B. (2011). Multiscale seismic attributes: A wavelet-based method and its application to high-resolution seismic and ground truth data. *Geophysical Journal International*, 187(2), 1038-1054.

Ker, S., Marsset, B., Garziglia, S., Le Godinec, Y., Gibert, D., Voisset, M., Adamy, J. (2010). Highresolution seismic imaging in deep sea from a joint deep-towed/OBH reflection experiment: Application to a Mass Transport Complex offshore Nigeria. *Geophysical Journal International*, *182*, 1524–1542, doi: 10.1111/j.1365-246X.2010.04700.x

Kjartansson, E. (1979). Constant Q-wave propagation and attenuation. *Journal of Geophysical Research*, 84, 4737–4748.

Klein, G., Bohlen, T., Theilen, F., Kugler, S., Forbriger, T. (2005). Acquisition and inversion of dispersive seismic waves in shallow marine environments. *Marine Geophysical Researches*, *26*(2–4), 287–315, doi: 10.1007/s11001-005-3725-6

Knapp, S., Payne, N., Johns, T. (2001). Imaging through gas clouds: a case history in the Gulf of Mexico. *CSEG Recorder*, 26(3).

Kolsky, H. (1956). The propagation of stress pulses in viscoelastic solids. *Philosophical Magazine*, 1, 693–710, doi: 10.1080/14786435608238144.

Le Gall, Y. (1999). Low-frequency Janus-Helmholtz transducers for great-depth. *Acoustical Oceanography*. *21*.

Le Gonidec, Y., Gibert, D., Proust, J.-N. (2002). Multiscale analysis of waves reflected by complex interfaces: basic principles and experiments. *Journal of Geophysical Research,* 107(B9), 2184.

Lewis, B., Garmany, J., Bond, L. (1979). The University of Washington Deep-Towed Array. *Workshop of Deep-Towed, Low-Frequency Sources and Receivers*, 25–26.

Lindsey, N. J. et al. (2019). Illuminating seafloor faults and ocean dynamics with dark fiber distributed acoustic sensing. *Science,* 366(6469), 1103–1107.

Longuet-Higgins, M.S. (1950). A theory of the origin of microseisms. *Philosophical Transactions of the Royal Society of London, A,* 243**,** 1–35.

Lumens, P. G. E. (2014). Fibre-optic sensing for application in oil and gas wells. Ph.D. thesis, Eindhoven University of Technology.

Mallat, S. & Hwang, W. L. (1992). Singularity detection and processing with wavelets. *IEEE Transactions on Information Theory,* 38**,** 617–643.

Margrave, G. F. (1998). Theory of nonstationary linear filtering in the Fourier domain with application to time-varying filtering. *Geophysics*, 63, 244–259, doi: 10.1190/1.1444318.

Marsset, B., Ker, S., Thomas, Y., Colin, F. (2018). Deep-towed high-resolution seismic imaging II: Determination of P-wave velocity distribution. *Deep-Sea Research Part I*, *132*, 29–36, doi: 10.1016/j.dsr.2017.12.005

Marsset, B., Menut, E., Ker, S., Thomas, Y., Regnault, J.-P., Leon, P., Martinossi, H., Artzner, L., Chenot, D., Dentrecolas, S., Spychalski, B., Mellier, G., Sultan, N. (2014). Deep-towed high-resolution multichannel seismic imaging. *Deep Sea Research Part I*, *93*, 83–90, doi: 10.1016/j.dsr.2014.07.013

Marsset, T., Marsset, B., Ker, S., Thomas, Y., Le Gall, Y. (2010). High and very high-resolution deep-towed seismic system: Performance and examples from deep water Geohazard studies. *Deep Sea Research Part I*, *57*(4), 628–637, doi: 10.1016/j.dsr.2010.01.001

Ménesguen, C., Hua, B., Carton, X., Klingelhoefer, F., Schnurle, P., Reichert C. (2012). Arms winding around a meddy seen in seismic reflection data close to the Morocco coastline. *Geophysical Research Letters*, 39, L05604, doi: 10.1029/2011GL050798.

Merey, S. & Sinayuc, C. (2016). Investigation of gas hydrate potential of the Black Sea and modelling of gas production from a hypothetical class 1 methane hydrate reservoir in the Black Sea conditions. *Journal of Natural Gas Science and Engineering*, *29*, 66–79, doi: 10.1016/j.jngse.2015.12.048

Mordret, A., Landès, M., Shapiro, N., Singh, S. C., Roux, P., Barkved, O. I. (2013). Near-surface study at the Valhall oil field from ambient noise surface tomography, *Geophysical Journal International*, 193, 1627-1643.

Müller, T., Gurevich, B., Lebedev, M. (2010). Seismic wave attenuation and dispersion resulting from wave-induced flow in porous rock —A review. *Geophysics*, *75*(5), 75A147–75A164.

Müller, T. M. & Gurevich, B. (2004). One-dimensional random patchy saturation model for velocity and attenuation in porous rocks. *Geophysics*, 69, 1166–1172.

Nouzé, H., Sibuet, J.-C., Savoye, B., Marsset, B., Thomas, Y. (1997). Pasisar: performance of a high and very high resolution hybrid deep-towed seismic device. *Marine Geophysical Researches*, 19(5), 379-395.

Pei, Y., Wen, M., Wei, Z. *et al.* (2022). Development of a high-resolution deep-towed multi-channel seismic exploration system: Kuiyang-ST2000. *Journal of Applied Geophysics*, 198, 104575.

Pei, Y., Wen, M., Wei, Z. *et al.* (2023). Data processing of the Kuiyang-ST2000 deep-towed high-resolution multichannel seismic system and application to South China Sea data. *Journal of Oceanology and Limnology,* 41, 644–659. doi.org/10.1007/s00343-022-2049-6

Piété, H., Marié, L., Marsset, B., Thomas, Y., Gutscher, M.-A. (2013). Seismic reflection imaging of shallow oceanographic structures. *Journal of Geophysical Research:* Oceans, 118, 2329–2344, doi: 10.1002/jgrc.20156.

Pilcher, R. & Argent, J. (2007). Mega-pockmarks and linear pockmark trains on the West African continental margin. *Marine Geology,* 244, 15–32.

Phrampus, B. J., & Hornbach, M. J. (2012). Recent changes to the Gulf Stream causing widespread gas hydrate destabilization. *Nature*, *490*(7421), 527-530, doi: 10.1038/nature11528

Podvin, P., & Lecomte, I. (1991). Finite difference computation of traveltimes in very contrasted velocity models: A massively parallel approach and its associated tools. *Geophysical Journal International*, *418*, 271–284.

Popescu, I., Lericolais, G., Panin, N., De Batist, M., Gillet, H. (2007). Seismic expression of gas and gas hydrates across the western Black Sea. *Geo-Marine Letters*, *27*(2), 173–183, doi: 10.1007/s00367-007-0068-0

Popescu, I., De Batist, M., Lericolais, G., Nouzé, H., Poort, J., Panin, N., Versteeg, W., Gillet, H. (2006). Multiple bottom-simulating reflections in the Black Sea: Potential proxies of past climate conditions. *Marine Geology*, *227*(3–4), 163–176, doi: 10.1016/j.margeo.2005.12.006

Provenzano, G., Vardy, M. E., Henstock, T. J. (2017). Pre-stack full waveform inversion of ultra-high-frequency marine seismic reflection data. *Geophysical Journal International*, Volume 209, Issue 3, 1593–1611, doi: 10.1093/gji/ggx114

Riboulot, V., Ker, S., Sultan, N., Thomas, Y., Marsset, B., Scalabrin, C., Ruffine, L., Boulart, C., Ion, G. (2018). Freshwater lake to salt-water sea causing widespread hydrate dissociation in the Black Sea. *Nature Communications*, 9(117), 1-8, doi: 10.1038/s41467-017-02271-z

Riboulot, V., Cattaneo, A., Scalabrin, C., Gaillot, A., Jouet, G., Ballas, G., Marsset, T., Garziglia, S., Ker, S. (2017). Control of the geomorphology and gas hydrate extent on widespread gas emissions offshore Romania. *Bulletin de La Société Géologique de France*, *188*(4), 26.

Riboulot, V., Sultan, N., Imbert, P., Ker, S. (2016). Initiation of gas-hydrate pockmark in deep-water Nigeria: Geo-mechanical analysis and modelling. *Earth and Planetary Science Letters*, 434, 252-263.

Riboulot, V., Cattaneo, A., Sultan, N., Garziglia, S., Ker, S., Imbert, P., Voisset, M. (2013). Sea-level change and free gas occurrence influencing a submarine landslide and pockmark formation and distribution in deepwater Nigeria. *Earth and Planetary Science Letters*, 375, 78-91.

Rowe, M. M., & Gettrust, J. F. (1993). Fine structure of methane hydrate-bearing sediments on the Blake Outer Ridge as determined from deep-tow multichannel seismic data. *Journal of Geophysical Research: Solid Earth*, *98*(B1), 463–473, doi: 10.1029/92JB01706

Ruffine, L., Deusner, C., Haeckel, M., Kossel, E., Toucanne, S., Chéron, S., Boissier, A., Schmidt, M., Donval, J-P., Scholz, F., Guyader, V., Ker, S., Riboulot, V. (2021). Effects of postglacial seawater intrusion on sediment geochemical characteristics in the Romanian sector of the Black Sea. *Marine and Petroleum Geology*, 123, 104746.

Ruppel, C. D., & Kessler, J. D. (2017). The interaction of climate change and methane hydrates. *Reviews of Geophysics*, *55*, 126–168, doi: 10.1002/2016RG000534

Sallarès, V., Biescas, B., Buffett, G. Carbonell, R., Dañobeitia, J. J., Pelegri, J. L. (2009). Relative contribution of temperature and salinity to ocean acoustic reflectivity. *Geophysical Research Letters*, 36, L00D06, doi: 10.1029/2009GL040187

Sarkar, S., Berndt, C., Minshull, T. A., Westbrook, G. K., Klaeschen, D., Masson, D., et al. (2012). Seismic evidence for shallow gas-escape features associated with a retreating gas hydrate zone offshore west Svalbard. *Journal of Geophysical Research*, *117*, B09102, doi: 10.1029/2011JB009126

Scholte, J. G. (1947). The range of existence of Rayleigh and Stoneley waves. *Geophysical Journal International*, 5, 120–126, doi: 10.1111/j.1365-246X.1947.tb00347.x.

Shapiro, N. M. & Campillo, M. (2004). Emergence of broadband Rayleigh waves from correlations of the ambient noise. *Geophysical Research Letters*, 31(7), doi:10.1029/2004GL019491.

Shapiro, N. M., Campillo, M., Stehly, L., Ritzwoller, M. H. (2005). High-resolution surface-wave tomography from ambient seismic noise. *Science*, 307, no. 5715, 1615-1618, doi : /10.1126/ science.1108339.

Sladen, A. et al. (2019). Distributed sensing of earthquakes and ocean-solid earth interactions on seafloor telecom cables. *Nature Communications,* 10(1), 1–8.

Sloan E.D. (2003). Fundamental principles and applications of natural gas hydrates. *Nature,* 426: 353–363.

Sloan, E.D., Koh, C.A. (2008). Clathrate Hydrates of Natural Gases, vol.119. Chemical Industries, Boca Raton, Florida.

Soulet, G., Ménot, G., Lericolais, G., Bard, E. (2011). A revised calendar age for the last reconnection of the Black Sea to the global ocean. *Quaternary Science Reviews*, *30*(9-10), 1019–1026, doi: 10.1016/j.quascirev.2011.03.001

Spica, Z.J., Nishida, K., Akuhara, T., Pétrélis, F., Shinohara, M., Yamada, T. (2020). Marine sediment characterized by ocean-bottom fiber-optic seismology. *Geophysical Research Letters,* 47(16), e2020GL088360, doi: 10.1029/2020GL088360

Sultan, N., Bohrmann, G., Ruffine, L., Pape, T., Riboulot, V., Colliat, J. -L., de Prunele, Alexis, Dennielou, B., Garziglia, S., Himmler, Tobias, Marsset, T., Peters, C. A., Rabiu, A., Wei J. (2014). Pockmark formation and evolution in deep water Nigeria: Rapid hydrate growth versus slow hydrate dissolution. *Journal of Geophysical Research: Solid Earth*, 119(4), 2679-2694.

Sultan, N., Marsset, B., Ker, S., Marsset, T., Voisset, M., Vernant, A-M., Bayon, G., Cauquil, E., Adamy, J., Colliat, J. L., Drapeau, D. (2010). Hydrate dissolution as a potential mechanism for pockmark formation in the Niger delta. *Journal of Geophysical Research: Solid Earth*, 115(B08101), 1-33.

Sultan, N. (2007). Excess pore pressure and slope failures resulting from gas-hydrates dissociation and dissolution, *Offshore Technology Conference,* 30 April-3 May 2007, Houston, Texas, U.S.A. ISBN 978-1-55563-254-0. OTC-18532-MS, 1–9.

Takam Takougang, E. & Bouzidi, Y. (2018). Imaging high-resolution velocity and attenuation structures from walkaway vertical seismic profile data in a carbonate reservoir using visco-acoustic inversion. *Geophysics*, 83, B323–B337.

Taweesintananon, K., Landrø, M., Brenne, J. K., Haukanes, A. (2021). Distributed acoustic sensing for near-surface imaging using submarine telecommunication cable: A case study in the Trondheimsfjord, Norway. *Geophysics*, 86(5), B303–B320, doi: 10.1190/geo2020-0834.1.

Terzaghi, K., Peck, R. B., Mesri, G. (1996). Soil mechanics in engineering practice (3rd ed.p. 549). New York: John Wiley.

Théréau, E. & Thomas, Y. (2023). GHASS2 – Traitement des données multitraces. Analyse de vitesse RMS et imagerie avec migration après sommation, *rapport Ifremer* REM/GEOOCEAN/ANTIPOD-21092023-01, archimer.ifremer.fr/doc/00854/96594

Thomas, Y., Ker, S., Thereau, E., Dupont, P. (2021). Mission GHASS2 LEG1 N/O Pourquoi pas ? 16 août au 3 septembre 2021, Mer Noire. Compte rendu d'acquisition sismique multi-trace, *rapport Ifremer* PDG/REM/GM/LAD-24112021-01.

Trabattoni, A. et al. (2023). From strain to displacement: using deformation to enhance distributed acoustic sensing applications. *Geophysical Journal International*, 235, Issue 3, December 2023, Pages 2372–2384, doi: 10.1093/gji/ggad365

Trafford, A., Ellwood, R., Wacquier, L. et al. (2022). Distributed acoustic sensing for active offshore shear wave profiling. *Scientific Reports,* 12, 9691, doi: 10.1038/s41598-022-13962-z

Virieux, J. & Operto, S., 2009. An overview of full waveform inversion in exploration geophysics. *Geophysics*, 74(6), WCC1–WCC26.

Walia, R. & Hannay, D. (1999). Source and receiver geometry corrections for deep towed multichannel seismic data. *Geophysical Research Letters*, *26*(13), 1993–1996, doi: 10.1029/1999GL900402

Wang, Y., (2015). Generalized seismic wavelets. *Geophysical Journal International*, 203, 1172–1178, doi: 10.1093/gji/ggv346.

Wege, S., Legendre, C. P., Chi, W.-C.,Wang, T. K., Kunath, P., Liu, C.-S. (2022). Field and synthetic waveform tests on using large-offset seismic streamer data to derive shallow seabed shear-wave velocity and geotechnical properties. *Earth and Space Science*, *9*, e2021EA002196.

Wei, D., Jinquiang, L., Wei, Z., Zenggui, K., Tong, Z., Yulin, H. (2021). Typical charcateristics of fracture-filling hydrate-charged reservoir caused by heterogeneous fluid flow in the Qiongdongnam Basin, northen south China sea. *Marine and Petroleum Geology*, 124, 10-4810.

Westbrook, G. K., Thatcher, K. E., Rohling, E. J., Piotrowski, A. M., Pälike, H., Osborne, A. H., Nisbet, E. G., Minshull, T. A., Lanoisellé, M., James, R. H., Hühnerbach, V., Green, D., Fisher, R. E., Crocker, A. J., Chabert, A., Bolton, C., Beszczynska-Möller, A., Berndt, C., Aquilina, A. (2009). Escape of methane gas from the seabed along the West Spitsbergen continental margin. *Geophysical Research Letters*, 36(15), doi: 10.1029/2009GL039191

White, J. E., Mikhaylova, N. G., Lyakhovitskiy, F. M. (1975). Low-frequency seismic waves in fluid saturated layered rocks. Izvestija Academy of Sciences USSR. *Physics of the Solid Earth*, *11*, 654–659.

Williams, E.F., Fernandez-Ruiz, M.R., Magalhaes, R., Vanthillo, R., Zhan, Z., Gonzalez-Herraez, M., Martins, H.F. (2021). Scholte wave inversion and passive source imaging with ocean-bottom DAS. *Leading Edge,* 40(8), 576–583.

Williams, E.F., Fernandez-Ruiz, M.R., Magalhaes, R., Vanthillo, R., Zhan, Z., Gonzalez-Herraez, M., Martins, H.F. (2019). Distributed sensing of microseisms and teleseisms with submarine dark fibers. *Nature Communications,* 10(1), 1–11.

Yang, J., Shragge, J., Jin, G. (2022). Filtering strategies for deformation- rate distributed acoustic sensing. *Sensors,* 22 (22), 8777, doi: 10.3390/s22228777.

4 Sélection d'articles

Ker, S., Le Gonidec, Y., Gibert, D. (2013). Multiresolution seismic data fusion with a generalized wavelet-based method to derive subseabed acoustic properties. *Geophysical Journal International*, 195(2), 1370-1383.

Ker, S., Le Gonidec, Y., Marié, L., Thomas, Y., Gibert, D. (2015). Multiscale seismic reflectivity of shallow thermoclines. *Journal of Geophysical Research: Oceans*, 120(3), 1872-1886.

Ker, S. & Le Gonidec, Y. (2018). Fractional integration of seismic wavelets in anelastic media to recover multiscale properties of impedance discontinuities. *Geophysics*, 83(2), V61-V71.

Ker S., Thomas, Y., Riboulot, V., Sultan, N., Bernard, C., Scalabrin, C., Ion, G, Marsset, B. (2019). Anomalously deep BSR related to a transient state of the gas hydrate system in the western Black Sea. *Geochemistry Geophysics Geosystems*, 20(1), 442-459.

Colin, F., Ker, S., Marsset, B. (2020). Fine-scale velocity distribution revealed by datuming of VHR deep-towed seismic data: Example of a shallow gas system from the western Black Sea. *Geophysics*, *85*(5), 1–12.

Geophysical Journal International

Geophys. J. Int. (2013) doi: 10.1093/gji/ggt317

Geophysical Journal International Advance Access published August 30, 2013

Multiresolution seismic data fusion with a generalized wavelet-based method to derive subseabed acoustic properties

S. Ker,[1] Y. Le Gonidec[2] and D. Gibert[3]

[1] *IFREMER, Géosciences marines, Centre de Brest, F-29280 Plouzané, France. E-mail: stephan.ker@ifremer.fr*
[2] *Géosciences Rennes (CNRS UMR 6118), Université Rennes 1, Bât. 15 Campus de Beaulieu, F-35042 Rennes cedex, France*
[3] *Institut de Physique du Globe de Paris (CNRS UMR 7154), Sorbonne Paris Cité, 1 rue Jussieu, F-75238 Paris cedex, France*

Accepted 2013 August 5. Received 2013 June 25; in original form 2013 January 25

SUMMARY

In the context of multiscale seismic analysis of complex reflectors, that takes benefit from broad-band frequency range considerations, we perform a wavelet-based method to merge multiresolution seismic sources based on generalized Lévy-alpha stable functions. The frequency bandwidth limitation of individual seismic sources induces distortions in wavelet responses (WRs), and we show that Gaussian fractional derivative functions are optimal wavelets to fully correct for these distortions in the merged frequency range. The efficiency of the method is also based on a new wavelet parametrization, that is the breadth of the wavelet, where the dominant dilation is adapted to the wavelet formalism. As a first demonstration to merge multiresolution seismic sources, we perform the source-correction with the high and very high resolution seismic sources of the SYSIF deep-towed device and we show that both can now be perfectly merged into an equivalent seismic source with a broad-band frequency bandwidth (220–2200 Hz). Taking advantage of this new multiresolution seismic data fusion, the potential of the generalized wavelet-based method allows reconstructing the acoustic impedance profile of the subseabed, based on the inverse wavelet transform properties extended to the source-corrected WR. We highlight that the fusion of seismic sources improves the resolution of the impedance profile and that the density structure of the subseabed can be assessed assuming spatially homogeneous large scale features of the subseabed physical properties.

Key words: Wavelet transform; Wave propagation; Acoustic properties.

1 INTRODUCTION

In the framework of subseabed characterization, seismic imaging is often jointed to ground truth measurements to improve the data interpretation in terms of both morphological structures and physical properties (Pennington 2001; Fomel 2007). Seismic imaging involves low frequency seismic sources (<2 kHz) and requires signal processing, such as deconvolution, to highlight seismic reflectors (Yilmaz 2001). But obviously, a one-to-one relationship between seismic attributes and petrophysical properties (Chopra & Marfurt 2005) is not straightforward (Partyka *et al.* 2000) and highlights the multiscale structure of seismic reflectors, which characterization requires broad-band sources (Widess 1973; Morlet *et al.* 1982; Le Gonidec *et al.* 2002; Le Gonidec & Gibert 2007; Ker *et al.* 2012).

Recent technological improvements of seismic devices such as the deep-towed seismic system SYSIF (Wood *et al.* 2003; Ker *et al.* 2010; Marsset *et al.* 2010) result in a significant extension of the frequency range towards the high frequencies (up to 2200 Hz). The availability of seismic data spanning several octaves in wavelength motivates new methodological developments of signal analysis relying on the multiscale analysis of seismic traces. In this context, the continuous wavelet transform (CWT) naturally appears as a powerful processing tool (Castagna *et al.* 2003) and in order to consider sound propagation in the analysis, we used the wavelet response (WR) method introduced by Le Gonidec *et al.* (2002). Assuming the validity of the Born approximation (i.e. negligible multiple scattering), both the CWT and WR methods are equivalent and we proposed to extend the use of the ridge functions as a new multiscale seismic attribute (Ker *et al.* 2011), a sparse support of the multiscale information brought by the seismic WR (Mallat & Hwang 1992; Le Gonidec *et al.* 2002). However, the limited frequency bandwidth of seismic sources induce distortions of the ridge functions, as discussed in Ker *et al.* (2012) where we developed a theoretical framework of the source-corrected WR. The method, based on the properties of the Lévy-alpha stable functions, aims at defining a wavelet model for the seismic source with respect to the wavelet formalism, and as a first approach, Gaussian derivative functions with integer derivative orders were considered.

When a single seismic source is involved, the approach is satisfactory and source-corrected multiscale seismic attributes allow characterizing the morphological properties of seismic reflectors (Fig. 1). Note that the characterization is performed in the dilation parametrization of the wavelet formalism, where the relation between dilation and physical properties of the wavelets is not

© The Authors 2013. Published by Oxford University Press on behalf of The Royal Astronomical Society.

Downloaded from http://gji.oxfordjournals.org/ by guest on September 1, 2013

GJI Seismology

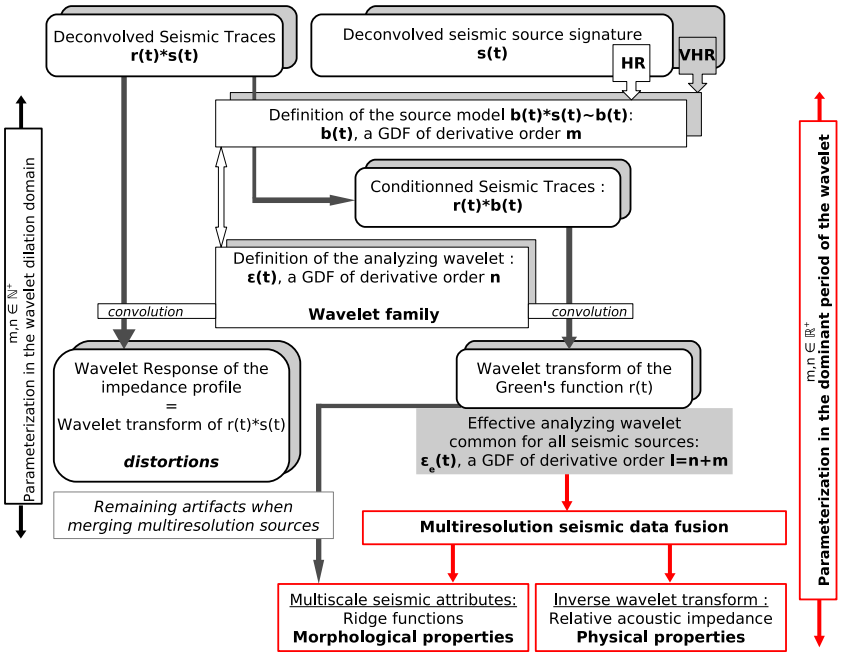

Figure 1. Flow chart of the source-corrected wavelet-based method introduced in Ker *et al.* (2012; GDF, Gaussian derivative functions). In red: the new features proposed in this paper to assess the data fusion from different seismic sources (involving GFDF, i.e. fractional derivative orders: see the text).

straightforward (Ker *et al.* 2012). Moreover, the source-correction suffers from distortions mainly located at large dilations, which limits the method efficiency when merging seismic attributes from multiple sources since artefacts remained in the merged frequency range. Actually, the merged WR that results from the contribution of each seismic source suffered from distortions, located at the junction between individual WRs and the method does not allow working in a continuous source-corrected effective dilation range. As a consequence, methodological developments are necessary to efficiently span the seismic frequency range for multiscale analysis, that is, to perform multiresolution source data fusion (Garguet-Duport *et al.* 1996; Zhou *et al.* 1998; Dong *et al.* 2009). The high resolution and very high resolution seismic sources available with the SYSIF device motivate such new developments and this work fully takes advantage of these multiresolution sources to propose an original approach to both quantify morphological structures of complex reflectors and reconstruct subseabed acoustic properties (Fig. 1).

To make this paper self-consistent, Section 2 recalls the principles of the source-corrected method introduced by Ker *et al.* (2012) and introduce the main definitions of the different terms used throughout the paper. New developments of the wavelet-based method are discussed in Section 3 in order to overcome the limitations encountered in Ker *et al.* (2012). We demonstrate that the optimal Lévy-alpha stable function adapted to the deconvolved seismic source is a Gaussian function and we take advantage of the generalized background of the source-corrected method to develop the method with fractional derivative orders. We also define a new parametrization of the multiscale seismic attributes, based on the breadth of the source model wavelet adapted to the wavelet formalism. Section 4 deals with the optimization of the source model for both high and very high resolution seismic sources, used to perform the source-corrected WR associated to homogeneous thin layers and then to realistic complex subseabed structures. In Section 5, we extend the inverse wavelet transform to the source-corrected WR and we show the capacity of the approach to reconstruct the relative acoustic impedance profile of the subseabed.

2 BACKGROUND OF THE WAVELET-BASED METHOD

In recent works (Ker *et al.* 2011, 2012), we have demonstrated the efficiency of an original wavelet-based approach to characterize multiscale discontinuities of acoustic impedance profiles from seismic data. The method, called the WR introduced by Le Gonidec *et al.* (2002), is a natural extension of the continuous wavelet transform (CWT) where the wavelet family is not convolved with but propagated through the impedance profile $p(z)$ of the medium, that is, the WR is expressed by

$$R\left[\xi, p\right](t,a) \equiv \left(\mathcal{D}_a\xi \otimes p\right)(t) \tag{1a}$$

$$= \mathcal{D}_a\xi(t) * r(t) \tag{1b}$$

$$= W\left[\xi, r\right](t,a)\,, \tag{1c}$$

where $\mathcal{D}_a\xi\,(t) = a^{-1}\xi(t/a)$ is the dilation operator applied on the analysing mother wavelet ξ, with the dilation factor $a \in \mathbb{R}^+$. The operator $\otimes$ stands for the 1-D propagation and $*$ stands for the convolution operator. Note that the wavelet transform W involves the Green's function of the medium $r(t)$; instead, the WR R involves the impedance $p(z)$, that is, R represents the collection of seismic traces obtained by sounding the medium with a set of wavelet source signals defined by $\mathcal{D}_a\xi\,(t)$. In Ker *et al.* (2011), we demonstrate that taking into account a real seismic source $s(t)$ with a limited frequency bandwidth, the WR suffers from distortions: $\tilde{R}\left[\xi, p\right](t,a) = W\left[\xi, r * s\right](t,a)$, that is, the WR does not deal with the Green's function of the medium but with the seismic trace $r(t) * s(t)$. In order to recover the wavelet transform properties for the Green's function $r(t)$, we propose a source-corrected method introduced in Ker *et al.* (2012). An overview of the method is depicted in the flow chart of Fig. 1. A wavelet source model $b(t)$ is estimated such that $b(t) * s(t) \simeq b(t)$, defined in the least square sense, where

Downloaded from http://gji.oxfordjournals.org/ by guest on September 1, 2013

the deconvolved seismic source signal $s(t)$ is the identity element of the convolution in a limited frequency bandwidth. Considering both the source wavelet $b(t)$ and the mother analysing wavelet $\xi(t)$ as derivatives of a Lévy-alpha stable function $L(t)$ (Voit 2003), that is, $b(t) = \frac{\mathrm{d}^m}{\mathrm{d}t^m} L(t)$ and $\xi(t) = \frac{\mathrm{d}^n}{\mathrm{d}t^n} L(t)$ $(m, n \in \mathbb{R}^+)$, we show that:

$$\tilde{R}\,[\xi,\, p]\,(t, a) = [\mathcal{D}_a \xi(t) * b(t)] * r(t) \tag{2a}$$

$$= A \times \mathcal{D}_{a_e} \xi_e(t) * r(t) \tag{2b}$$

$$= A \times W\,[\xi_e, r]\,(t, a_e)\,, \tag{2c}$$

where $\xi_e(t) = \frac{\mathrm{d}^l}{\mathrm{d}t^l} L(t)$ is the effective mother wavelet with the derivative order $l = m + n$. See Ker *et al.* (2012) for a full description of the effective dilation a_e and the amplitude factor A. As a result, the CWT of a seismic trace $r(t) * s(t)$ can be equivalent to the CWT of the Green's function $r(t)$ of the medium according to the amplitude correction A and a representation following the effective dilation a_e. This result is analogous to the one obtained in the multiscale analysis of potential fields performed with wavelets belonging to the Poisson semi-group (Moreau *et al.* 1997, 1999; Sailhac *et al.* 2009).

3 MERGING SEISMIC SOURCES IN A NEW PARAMETRIZATION

3.1 Previous application on the seismic system SYSIF: limitations and new requirements

In Ker *et al.* (2012), we first applied the wavelet-based method to correct the WR of seismic data acquired by the SYSIF, a deep-towed seismic system developed by Ifremer to image the subseabed (Ker *et al.* 2010; Marsset *et al.* 2010). SYSIF is equipped with two seismic sources covering the high resolution (HR: $220 < f < 1050$ Hz) and very high resolution (VHR: $580 < f < 2200$ Hz) frequency bands. The SYSIF streamer is a dual channel antenna, where the first channel is a single hydrophone with an offset of 10 m from the seismic source.

As a straightforward application, the wavelet source model was $b(t) = \frac{\mathrm{d}^m}{\mathrm{d}t^m} e^{-t^2}$, that is, a Gaussian derivative functions (GDF) limited to $m \in \mathbb{N}^+$ as commonly used in seismic imaging (for instance, $m = 2$ is the Ricker wavelet). In this particular context, the minimum derivative order of the analysing mother wavelet $\xi(t)$ was $n = 1$, as required to minimize the complexity of the effective mother wavelet $\xi_e(t)$ (eq. 2c). With an objective of merging different seismic sources, this wavelet $\xi_e(t)$ has to be the same for each source (see Ker *et al.* 2012, for a justification), and we have shown that for the HR and VHR sources of the SYSIF device, the derivative order of $\xi_e(t)$ was $l = 5$, that is, $m = 4$ for both sources.

The first applications of the source-corrected method on both synthetic and field seismic traces demonstrated the potential of the approach, but a lack of efficiency was observed at the transition dilation range between the HR and VHR components. This remaining artefact can be explained by the constraint of both minimizing l in order to reduce the complexity of the multiscale seismic attributes and optimizing the source model. As a consequence, the method limited to $m, n \in \mathbb{N}^+$ does not allow optimizing individual source models and is not fully efficient to perform a source-corrected WR over the whole dilation range composed by several seismic sources. Advanced developments are required in the WR processing to correctly merge seismic sources, a key point of this paper. Actually, the source-corrected method as recalled in Section 2 can be generalized to $m, n \in \mathbb{R}^+$, and we can take benefit from these fractional derivative orders. The introduction of a fractional order in the source model enables both a better control of the frequency bandwidth of the model spectrum and a reduction of the complexity of the effective analysing wavelet $\xi_e(t)$. This complexity is related to the sum of two derivative orders, n for the mother analysing wavelet $\xi(t)$ and m for the source model $b(t)$. This means that the effective derivative order l of $\xi_e(t)$ for the SYSIF sources should be associated to a low derivative order of the analysing wavelet $n \in]0; 1[$ and an optimized source model with $m > 4$.

Furthermore, the method has been developed in Ker *et al.* (2012) with respect to the wavelet formalism, that is, the ridge functions are represented in the dilation domain. In this context, the multiscale seismic attributes depend not only on the reflector topology but also on the effective analysing wavelet, that is, on the derivative order m in particular. To overcome this limitation, which requires a dimensionless proportionality factor between the dimensionless wavelet dilation and the size of the discontinuity, this paper proposes a new parametrization based on the temporal resolution of the source wavelet, that is, based on its dominant period (Gesret *et al.* 2010). For this new approach, we fixed the dilation a_b of the source model $b(t)$ introducing the relation $a_b = 1/(\delta_m B)$, where $1/B$ is the temporal resolution of the seismic source. This is of first importance compare to Ker *et al.* (2012) where a coupling between a_b and m decrease the temporal resolution of the source model when increasing m.

The next two sections address theses new developments applied to the wavelet-based method, required in particular to assess the fusion of different seismic sources. See the flow chart of Fig. 1 to identify the new features and objectives of the generalized method (in red).

3.2 Source model based on optimal Lévy-alpha stable fractional derivative functions

In the general background of the source-corrected method recalled in Section 2, the Lévy-alpha stable function $L(t)$ is not fixed and can be of many kinds, including Lévy, Cauchy and normal distributions, and there is no restriction on the derivative orders m, n, l. We first show that a normal distribution, dealing with Gaussian functions as considered in the wavelet-based method by Ker *et al.* (2012), is actually the optimal distribution to model seismic sources. In a second step, we introduce the fractional derivative orders.

3.2.1 The Gaussian as an optimal Lévy-alpha stable function

In Ker *et al.* (2010), we have shown that the frequency spectrum of a deconvolved seismic source $s(t)$ is characterized by a flat amplitude in a frequency bandwidth limited by a lower frequency and an upper frequency. In the wavelet-based method, $s(t)$ is substituted by a source model $b(t) = \frac{\mathrm{d}^m}{\mathrm{d}t^m} L(t)$ defined as a Lévy-alpha stable function whose Fourier transform is (Brcich 2005):

$$\hat{L}(f) = \exp\left(-|\pi a_b f|^\alpha\right), \tag{3}$$

where the scale parameter a_b is the dilation and $\alpha \in]0; 2]$ is the stability parameter of $L(t)$. The spectrum of $\hat{L}(f)$, symmetric about $f = 0$, controls the bandwidth of $b(t)$ which has an infinite frequency support, unlike $s(t)$. This means that the substitution of $s(t)$ by $b(t)$ can not be perfect but is optimal for a frequency spectrum of $b(t)$ included as much as possible in the frequency bandwidth of $s(t)$,

Downloaded from http://gji.oxfordjournals.org/ by guest on September 1, 20

that is, we search for α associated to the Lévy-alpha stable function with the most compact frequency support. A threshold $\gamma > 1$ is required to define a limited bandwidth for $b(t)$: the spectrum of $\hat{L}(f)$ decreases with f, a behaviour that depends on α, and the upper frequency f_{up} is associated to the minimum amplitude $\hat{L}(0)/\gamma$. We can express the limited frequency support $\Delta f = 2f_{up}$ for the source model $b(t)$ by

$$\Delta f = \frac{2}{\pi a_b} \sqrt[\alpha]{\ln \gamma}. \quad (4)$$

Eq. (4) states that for $\ln \gamma > 1$, the bandwidth Δf decreases with α: the most compact frequency support of $b(t)$ corresponds to the stability parameter $\alpha = 2$, that is, we show that a Gaussian function is the Lévy-alpha stable function of the source model $b(t)$ that optimizes the substitution of the seismic source $s(t)$. As a consequence, we consider the Lévy-alpha stable function $L(t) \equiv e^{-t^2}$ in the remaining of the paper.

3.2.2 Extension to Gaussian fractional derivative functions

In order to take advantage of the general form of the wavelet-based method, we extend the derivative orders m and n to $\mathbb{R}^+$, that is, without the restriction to $\mathbb{N}^+$ as first applied in Ker *et al.* (2012). Such fractional derivatives are common in physics to model diffusion phenomena in acoustic or electromagnetism through the definition of differentiation operators (Miller & Ross 1993; Kilbas *et al.* 2006). To compute the fractional derivative of the Lévy-alpha stable function, we consider the general property of the Fourier transform (Bracewell 1999)

$$\frac{\mathrm{d}^m \hat{L}(f)}{\mathrm{d}f^m} = (2i\pi f)^m \hat{L}(f). \quad (5)$$

Thanks to this extension to fractional derivative orders m and n for the source model $b(t)$ and mother analysing $\xi(t)$ wavelets, respectively, the complexity of the former can be balanced by the simplicity of the latter for a fixed derivative order $l = m + n$ of the effective analysing wavelet $\xi_e(t)$. This new development is of first importance in particular when merging different seismic sources, that requires a common $\xi_e(t)$ analysing wavelet, since it allows optimizing each source model independently: each wavelet model is a Gaussian fractional derivative function, noted GFDF in the following.

Note that in the previous paper (Ker *et al.* 2012), the minimum order for the analysing wavelet was $n = 1$ and the source models were defined by $m = 4$, that is, $l = 5$. In order to highlight the capacity of the methodological developments proposed in this paper, we still consider $l = 5$ which gave satisfactory results for the multiscale seismic attributes, but we search for $n \in]0; 1[$ and $m > 4$ in order to optimize each source model and then to improve the source-correction, in particular at the transition dilation range between seismic sources.

3.3 Source model parametrization based on the dominant period

A deconvolved seismic source $s(t)$ with a frequency bandwidth B can be assimilated, as a first approximation, to a Klauder wavelet defined by a width $T_s = 1/B$ which corresponds to the temporal resolution of the seismic source (Gutowski *et al.* 2002). In the wavelet-based method introduced in a previous section, we discussed about the substitution of $s(t)$ by a source model $b(t)$: as a consequence, $b(t)$ has to share the same temporal resolution T_s. The wavelet $b(t)$, defined as a GFDF with a derivative order m, is characterized by a dilation a_b in the wavelet formalism which can be related to T_s by

$$T_s = \delta_m a_b, \quad (6)$$

where the factor δ_m only depends on m. According to the Rayleigh's criterion (Kallweit & Wood 1982), the temporal resolution T_s is given by the dominant period, or breadth, of the wavelet: for instance, the authors defined the dominant period of a Ricker wavelet ($m = 2$) by the trough-trough time. In Ker *et al.* (2012), we extended the definition of the dominant period to any kind of wavelets, that is, not only the Ricker wavelet but also to asymmetrical wavelets defined by odd m values: we define the dominant period as twice the time between two primary extrema of the wavelet. It is important to note that this definition is valid also for a fractional derivative order, that is, for $m \in \mathbb{R}^+$, as illustrated in Fig. 2 for an even ($m = 2$, Ricker wavelet), an odd ($m = 3$) and a Gaussian fractional derivative ($m = 2.5$) functions.

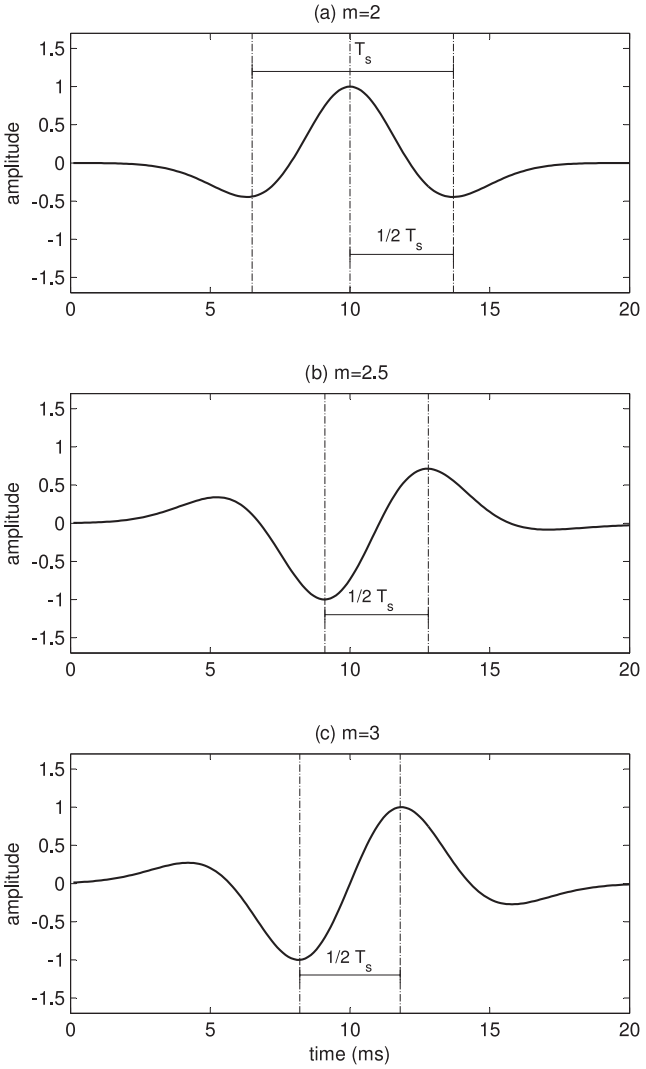

Figure 2. The dominant period T_s, that is, the breadth of the source wavelet, is defined as twice the time between two primary extrema: (a and c) illustrate the case of an even ($m = 2$, the dominant period is also the trough-trough time) and an odd ($m = 3$) Gaussian derivative function (GDF), respectively, and (c) illustrates a Gaussian fractional derivative function (GFDF with $m = 2.5$). Note that all wavelets have the same dominant period.

Downloaded from http://gji.oxfordjournals.org/ by guest on September 1, 2013

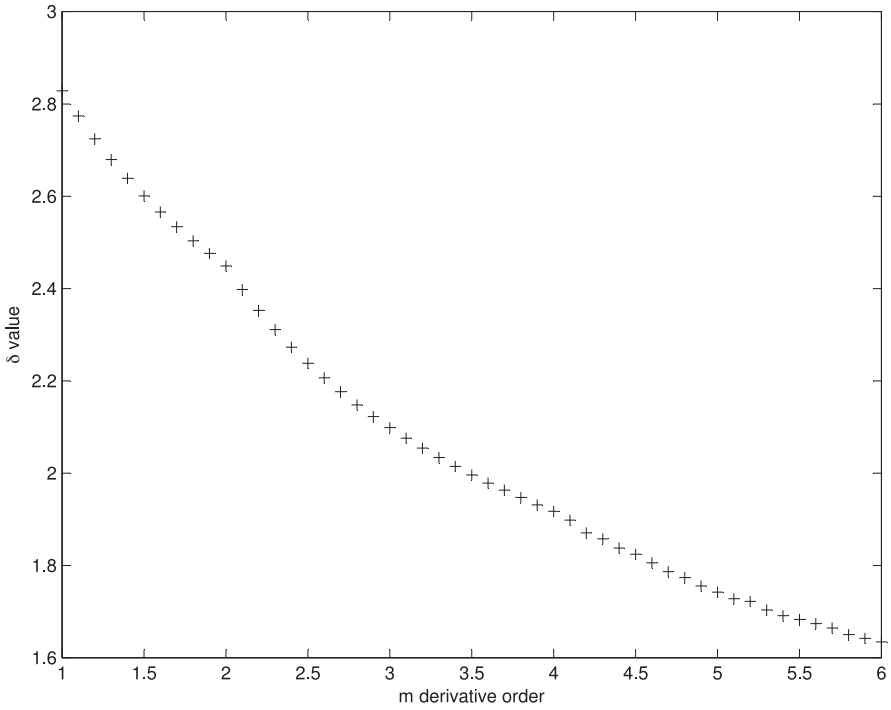

Figure 3. Numerical computation of the δ_m factor as a function of the fractional derivative order m of the GFDF. δ_m enables to relate the dilation a_b of a source model $b(t)$ defined in the wavelet formalism with the temporal resolution of the source $s(t)$.

In most cases, including fractional derivative orders m, numerical computations are required to determine δ_m but analytical expressions exist for $m = 1, 2, 3, 4$ and we can show that $\delta_1 = 2\sqrt{2}, \delta_2 = \sqrt{6}, \delta_3 = 2\sqrt{(6-2\sqrt{6})}$, and $\delta_4 = \sqrt{(10-2\sqrt{10})}$. In Fig. 3, we plot δ_m versus the derivative order $m \in \mathbb{R}^+$ up to $m = 6$.

4 WR OF MERGED SYSIF SOURCES: MULTISCALE SEISMIC ATTRIBUTES

In this section, we apply the new methodological results to both the HR and the VHR seismic sources of the SYSIF system so as to obtain a unique wavelet response WR_e in a wide dilation range. We define two GFDF source models, one for each SYSIF source. We also present the effective analysing wavelet $\xi_e(t)$ associated to the merged SYSIF sources: we illustrate the efficiency of the new developments by performing the WR_e of synthetic thin layers. Then, we perform the WR_e of synthetic seismic data: actually based on *in situ* measurements, such data sets allow working with both HR and VHR data at exactly the same subseabed location, which is difficult to perform at sea as the precision in positioning of a deep-towed vehicle is ≈20 m in 1700 m water depth.

4.1 Fractional Gaussian derivative models for SYSIF sources

In the wavelet-based method, the criteria to determine the source model wavelet $b(t)$ of a seismic source $s(t)$ is based on both a low wavelet complexity, that is, a low value of the derivative order m and a low quadratic misfit between both sides of $b(t) * s(t) \simeq b(t)$ which is minimized with high values of m. In our previous study (Ker *et al.* 2012), the optimal trade-off was reached for $m = 4$ for each SYSIF sources, associated to a common effective wavelet $\xi_e(t)$ of order $l = 5$ and a maximum misfit of 20 per cent. In this work, GFDF with $m \in \mathbb{R}^+$ allow adapting the model for each SYSIF sources and reduce the misfit to 10 per cent. The following shows that the source-correction with $l = 5$ is fully satisfactory, that is, an optimization of l is not required in this work where we still consider a derivative order $l = 5$ for the effective wavelet $\xi_e(t)$ in order to highlight the comparison of efficiency between the new developments and the initial approach. Note that the morphological structure of a complex reflector is based on multiscale seismic attributes that require l values as lows as possible to reduce the effective wavelet complexity, that is, searching for $l > 5$ is out of interest.

We determine the relative error in $b(t) * s(t) \simeq b(t)$ for different values of the derivative order m in the extended range [1; 6], for both SYSIF sources (Fig. 4a). At low derivatives orders, the efficiency of the substitution strongly decreases, with relative errors larger than 5 per cent. The error stabilizes at $m = 3$ for the HR source and $m = 5$ for the VHR source, with relative errors less than 2 per cent, that is, the range $3 < m < 5$ includes the best GFDF source models for the two SYSIF sources.

According to eq. (1a), the effective wavelet family is related to the analysing wavelet family $\mathcal{D}_a\xi(t)$. As a consequence, we search for the pair of derivative orders n of $\xi(t)$ and m of $b(t)$ which minimizes, in average, the misfit between the effective wavelet family and the reference wavelets, that is, we search for $m = 5 - n$ in the range [3; 5[which minimizes this error (Fig. 4b): $m = 4.6$ ($n = 0.4$) for the VHR source, and $m = 4.9$ ($n = 0.1$) for the HR source. It is important to observe that with fractional derivative orders, we can improve independently the two source models for each SYSIF seismic source while the complexity of the effective analysing wavelet is kept unchanged, that is, the complexities of $b(t)$ and $\xi(t)$ balance.

Downloaded from http://gji.oxfordjournals.org/ by guest on September 1, 20

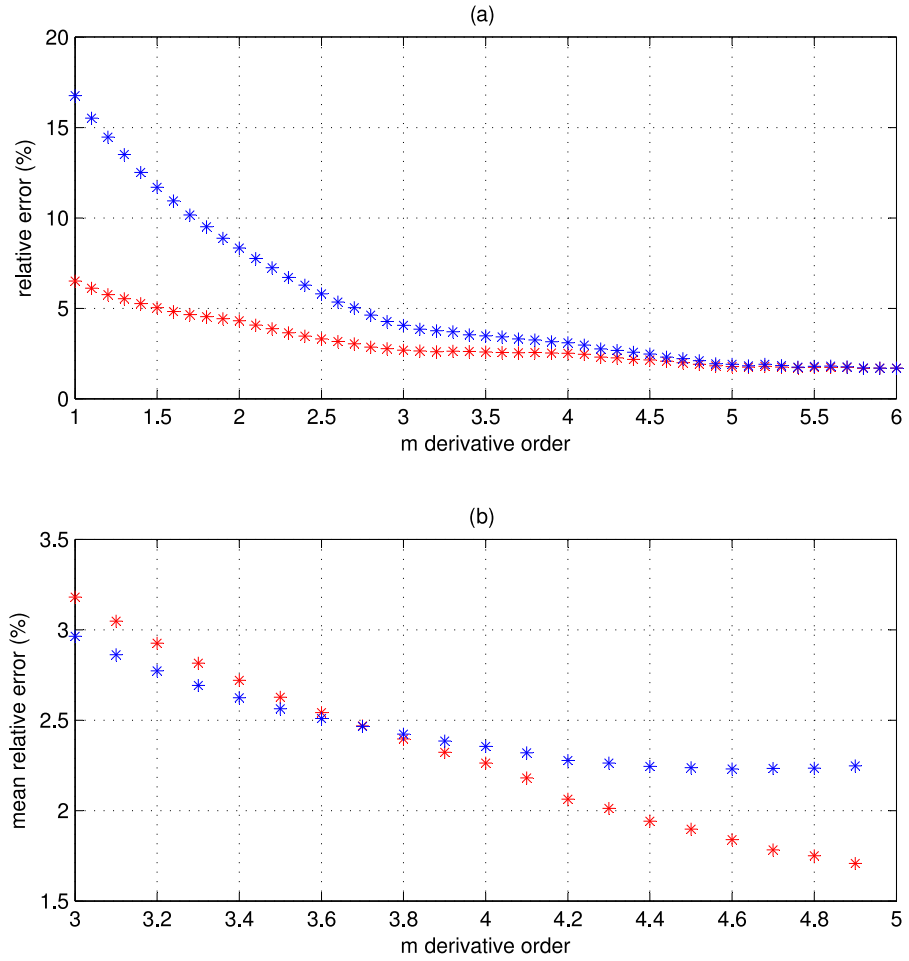

Figure 4. (a) Relative error between $b(t)$ and $b(t) * s(t)$ as a function of the derivative order m: for the HR (red) and VHR (blue) sources of the seismic SYSIF device. (b) Average of the relative errors between the reference wavelets of the fifth derivative order and the effective wavelets $\xi_e(t)$ with the derivative order $l = 5 = m + n$ and $3.9 < m < 4.9$.

4.2 Dominant period of the effective analysing wavelet from merged SYSIF sources

According to the frequency bandwidths B of the HR and VHR sources of the SYSIF device, the dominant periods are $T_{\mathrm{HR}} = 1200$ µs and $T_{\mathrm{VHR}} = 620$ µs, respectively. Moreover, the former is associated to the source model $m = 4.9$ and the latter to $m = 4.6$, that is, their factors δ_m are $\delta_{\mathrm{HR}} = 1.76$ and $\delta_{\mathrm{VHR}} = 1.81$, respectively (Fig. 3). Following eq. (6), it is straightforward to define the associated dilations a_b: 682 and 342 µs, respectively.

Similarly, it is possible to represent the effective analysing wavelet $\xi_e(t)$ versus the dominant dilation a_d instead of the effective dilation a_e as proposed in Ker *et al.* (2012). Actually, a_d corresponds to the dominant period T_d of the effective wavelet and represents the temporal resolution of $\xi_e(t)$

$$a_d \equiv T_d = \delta_l a_e = \delta_l \sqrt{a^2 + a_b^2}, \tag{7}$$

where a, a_b and a_e are the dilations of the analysing, source model and effective wavelets, which derivative orders are m, n and $l = m + n$, respectively. Working with the dilation $\delta_l a_e$ instead of a_e allows considering directly the temporal resolution of the wavelet, that is, a physical more than a geometrical property of the wavelet. Note that the dominant dilation $a_d = \delta_l a_e$ is thus a quantitative parametrization which defines the dilation of the wavelet according to the wavelet formalism.

The dominant dilation a_d depends on the dilation a_b of the source filter, that is, it spans a dilation range that depends on the seismic source frequency content. In the case of the SYSIF seismic sources, this leads to two different dilation ranges, noted $\mathcal{R}_{a_d}^{\mathrm{HR}}$ and $\mathcal{R}_{a_d}^{\mathrm{VHR}}$ for the HR and VHR components, respectively. The lower bound $a_{d,\min}$ of each seismic source dilation range corresponds to the limit $a \to 0$:

$$a_{d,min} = \delta_l a_b = \frac{\delta_l}{\delta_m} T_s. \tag{8}$$

The upper bound is constrained by the lack of low frequency content of $b(t) * s(t)$ which introduces more and more distortions as the dilation increases (see Ker *et al.* 2012), that is, $a_{d,\max}$ is defined by a threshold on the mean relative error. When both the HR and VHR contributions are merged, the dominant dilation range of the merged effective wavelets is thus $\mathcal{R}_{a_d} = \mathcal{R}_{a_d}^{\mathrm{HR}} \cup \mathcal{R}_{a_d}^{\mathrm{VHR}}$ and we define the threshold in order to make $\mathcal{R}_{a_d}$ continuous, that is, to join the upper and lower bounds of $\mathcal{R}_{a_d}^{\mathrm{VHR}}$ and $\mathcal{R}_{a_d}^{\mathrm{HR}}$, respectively. The lower and upper bounds of $\mathcal{R}_{a_d}$ are then fixed by $a_{d,\min}^{\mathrm{VHR}}$ and $a_{d,\max}^{\mathrm{HR}}$, respectively. In this work, we define a threshold of 10 per cent and the dominant dilation ranges for the SYSIF sources are $\mathcal{R}_{a_d}^{\mathrm{VHR}} = [620; 1200$ µs] and $\mathcal{R}_{a_d}^{\mathrm{HR}} = [1200; 3260$ µs]. In Fig. 5, we show the relative error of the effective wavelet family in the global range $\mathcal{R}_{a_d} = [620; 3260$ µs] associated to a virtual broad-band seismic source resulting from the fusion of both sources of the SYSIF

Downloaded from http://gji.oxfordjournals.org/ by guest on September 1, 2013

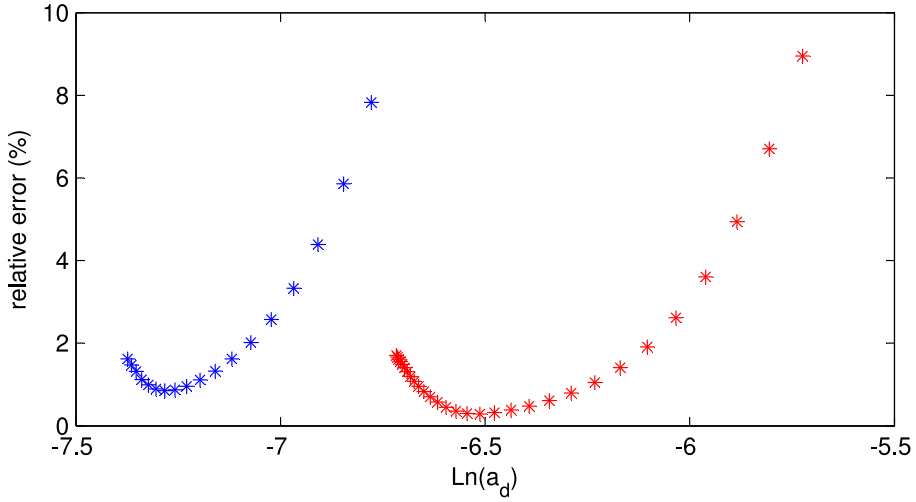

Figure 5. Relative errors between the reference wavelet and the source-corrected analysing wavelet ($l = 5$) as a function of the dominant dilation a_d: for the HR (red) and VHR (blue) sources of the seismic SYSIF device.

device. As expected, the relative error does not exceed 10 per cent in the whole dilation range, and in particular at the transition between the HR and VHR components, which illustrates the efficiency of the new approach based on GFDF.

4.3 Source-corrected multiscale seismic attributes of a homogeneous thin layer

A canonical model to illustrate the source-corrected WR method is a homogeneous layer of thickness Δz sounded by the wavelet family based on $\xi_e(t)$ as defined in the previous section for the SYSIF device. We perform the WR_e associated to the HR and VHR sources for different thickness values $\Delta z = 22, 45$ and 130 cm. The synthetic data set associated to the impedance profile of the layer is based on a forward modelling as described in Ker *et al.* (2011). We extract the multiscale seismic attributes defined by the ridge functions plotted versus the dominant dilation range $a_d \in \mathcal{R}_{a_d}$. The result can be compared to the ridge functions performed with a reference wavelet family without source effects ($a_d \in \mathbb{R}^+$; Figs 6a–c) and the misfit is studied as a relative error in per cent (Figs 6d–f).

For the three thicknesses, the HR and VHR ridge functions are in very good agreement with the reference lines and both components perfectly merged, that is, no discontinuity appears between them (details on the analysis of the ridge functions can be found in Ker *et al.* 2011, 2012). The relative errors are very weak, mainly less than 1 per cent and no more than 3 per cent in the whole dilation range. Since the ridge function is not a linear process, the errors appear lower than the relative errors observed in the effective wavelet family (Fig. 5). Note that in the linear parts of the HR and VHR components, the errors mimic the ones affecting the effective wavelet family.

For the homogeneous layers of thickness $\Delta z = 45$ cm and $\Delta z = 130$ cm, the dominant dilation $a_d^{\max}$ associated to the maximum of the ridge function (Figs 6b and c) is included in the dilation range of the SYSIF device, that is, $a_d^{\max} \in \mathcal{R}_{a_d}$. This means that the maximum is sampled by the SYSIF sources and we can determine the thickness of the layer according to the relation $\Delta z = \lambda/4$ based on the Rayleigh criterion (Kallweit & Wood 1982), where λ is the wavelength associated to the dominant dilation $a_d^{\max}$

$$\Delta z = \frac{a_d^{\max} V_p}{4}, \tag{9}$$

where V_p is the *P*-wave velocity. Note that eq. (9) is valid for all effective wavelets that share the same dominant period range. From Fig. 6(b) for instance, we measure $a_d^{\max} = 1200$ µs which perfectly corresponds to the layer thickness $\Delta z = 45$ cm ($V_p = 1500\,\mathrm{m\,s^{-1}}$).

4.4 Source-corrected multiscale seismic attributes of a complex subsurface ground truth data

A more realistic application deals with an *in situ* acoustic impedance profile of a subseabed, which can show complex structures such as multiscale discontinuities (see Fig. 8 discussed in the following section). The seismic source is the SYSIF device used to compute a synthetic data set with the impedance profile obtained from *in situ* and core measurements described in Ker *et al.* (2011). The interest in using such synthetic seismic traces rather than real seismic traces is to sound exactly the same subseabed with both the HR and VHR, which were not experimentally acquired at the same location as a mean distance of ≈50 m separates both profiles (Ker *et al.* 2012).

Similarly to the previous section, we perform the effective wavelet response WR_e of the impedance profile with the source-corrected method based on GFDF (with $m = 4.6$ and $n = 0.4$ for the VHR source, and with $m = 4.9$ and $n = 0.1$ for the HR source), and compare the results with the reference WR performed without the source limitation. We also compare the results with the previous method described in Ker *et al.* (2012) and based on GDF with the same derivative order $l = 5$ for both the VHR and HR seismic sources.

The results are plotted in Fig. 7, where the absolute amplitude of the WR performed without source limitation represents the reference WR in the merged dilation range of the HR and VHR seismic sources (Fig. 7a). A strong discontinuity between both source dilation ranges exists in the source-corrected WR_e performed with the previous approach of GDF (HR and VHR: $m = 4, n = 1$), that is, the source merging can not be achieved (Fig. 7b). When applying the new developments based on GFDF (HR $m = 4.9, n = 0.1$; VHR $m = 4.6, n = 0.4$), the source-corrected WR_e is in perfect agreement with the reference WR with fully removed arteficats between HR and VHR components, that is, multiresolution seismic data fusion can clearly be achieved in the merged dilation range (Fig. 7c). A subset of these multiscale seismic attributes also takes advantage of the new method accuracy to characterize morphological structures

Downloaded from http://gji.oxfordjournals.org/ by guest on September 1, 20

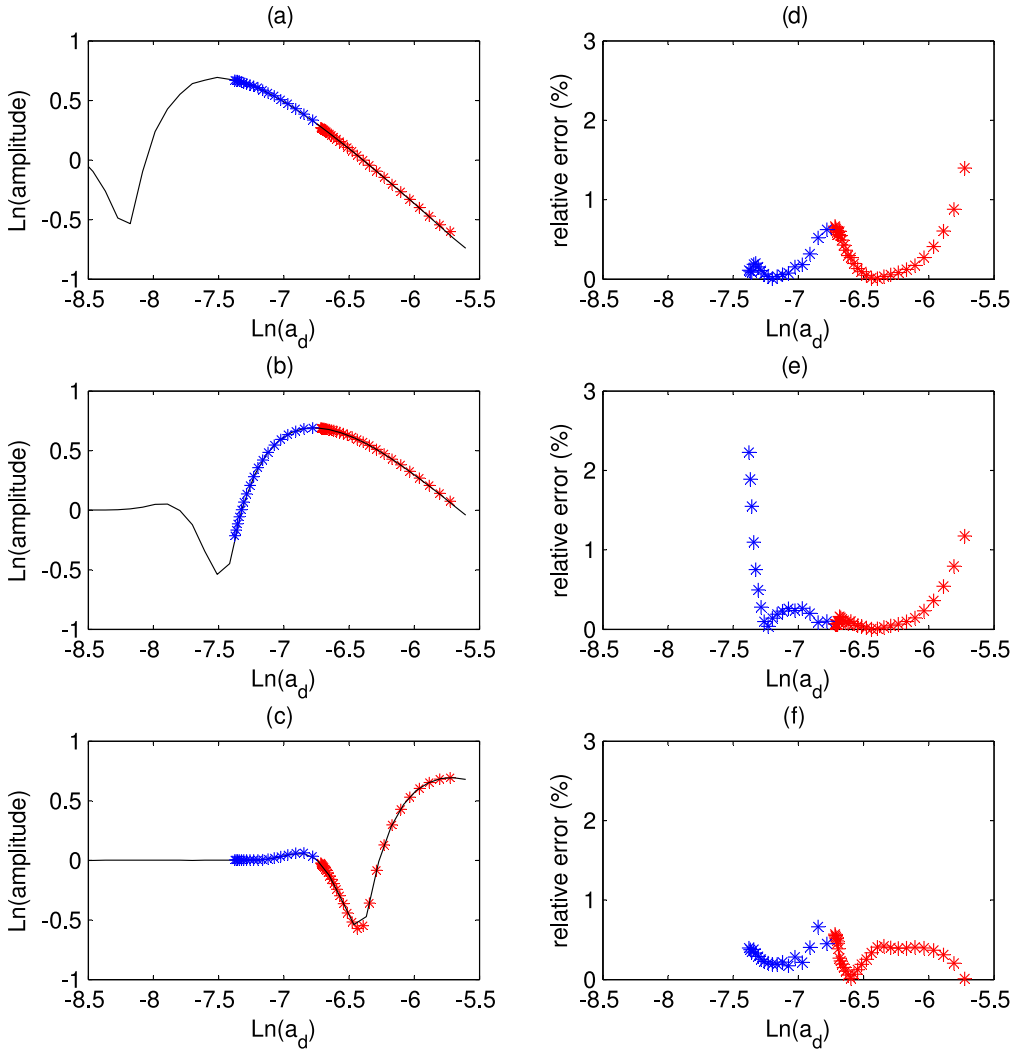

Figure 6. (a–c) Ridge functions extracted from the source-corrected WR_e of homogeneous layers of thicknesses $\Delta z = 22, 45$ and 130 cm, respectively: for the HR (red: $a_d \in \mathcal{R}_{a_d}^{\mathrm{HR}}$) and VHR (blue: $a_d \in \mathcal{R}_{a_d}^{\mathrm{VHR}}$) sources of the seismic SYSIF device. The solid black line stands for the reference ridge function performed with $a_d \in \mathbb{R}^+$. (d–f) Associated relative errors between the source-corrected and reference ridge functions.

of complex seismic reflectors. For instance, the ridge functions of two particular seismic reflectors A and B (Ker *et al.* 2011, 2012) extracted from the WR_e of Fig. 7(c) are plotted as a function of the dominant dilation a_d (Figs 7d and e) and compared with the reference ridge functions: as expected, the results put in evidence a very good agreement, even at the transition between the HR and VHR components. Thanks to the new parametrization, thicknesses of reflectors A and B can be directly defined from $\ln(a_d^{\max}) = -6.08$ and $\ln(a_d^{\max}) = -5.9$, respectively: according to eq. (9), $\Delta z^A = 85$ cm and $\Delta z^B = 100$ cm.

As a conclusion on the new developments proposed in this work, we put in evidence that the source-corrected method based on GFDF in the dominant dilation parametrization allows removing artefacts in the multiscale seismic attributes, and in particular in the determination of morphological structures of complex reflectors. Above all, we show that the method is highly powerful to correctly span the frequency range in the WR multiscale analysis, that is, we are now able to perform multiresolution seismic data fusion by merging different seismic sources. This new approach in seismic topics is promising for future works, as we illustrate in the following with a first application to reconstruct *in situ* high resolution subseabed physical properties.

5 WR OF MERGED SYSIF SOURCES: INVERSE TRANSFORM TO RETRIEVE THE SUBSURFACE IMPEDANCE

The new developments based on both Gaussian fractional derivative functions and a new representation in the dominant dilation domain a_d, are very efficient to merge the WRs of multiple real seismic sources, that is, to span over a large dilation range from. With the equivalence between the WR and the CWT (Le Gonidec *et al.* 2002), the inverse wavelet transform properties can be extended to the source-corrected WR in order to obtain the Green's function of the subsurface.

5.1 Inverse transform of the source-corrected WR

The wavelet transform of a signal $p(z)$ performed with the analysing wavelet $\xi(t)$ is expressed by (Mallat 2008)

$$W[\xi, p](z, a) = \frac{1}{a} \int_{-\infty}^{\infty} \xi^* \left(\frac{z - \tau}{a} \right) p(z)\, \mathrm{d}z, \tag{10}$$

where $a > 0$ is the dilation factor and τ is a translational value. From these wavelet coefficients, the signal $p(z)$ can be

Downloaded from http://gji.oxfordjournals.org/ by guest on September 1, 2013

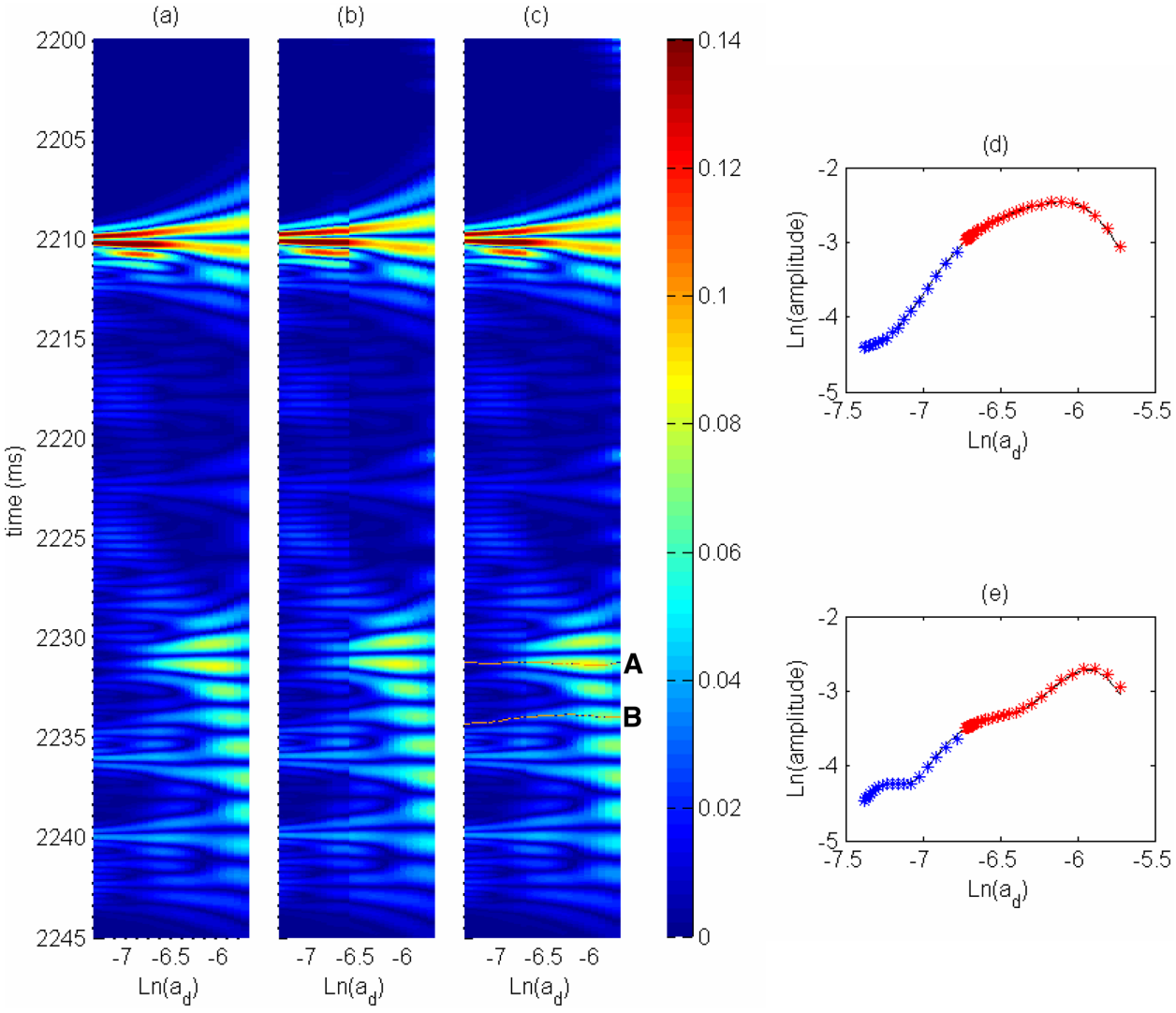

Figure 7. Wavelet responses of the *in situ* impedance log obtained from ground truth measurements with different methods: (a) the reference WR with $a_d \in \mathbb{R}^+$, (b) the previous GDF source-correction method ($m = 4$ for both the HR and VHR sources and $l = 5$) introduced in Ker *et al.* (2012) and (c) the GFDF method developed in this paper ($m = 4.9$ for the HR and $m = 4.6$ for the VHR, and $l = 5$). (d, e) Ridge functions associated to reflectors *A* and *B*, respectively: the HR (red) and VHR (blue) sources of the seismic SYSIF device from the panel (c) and the reference from the panel (a) in solid line.

reconstructed according to the inverse wavelet transform (Mallat 2008)

$$p(z) = \frac{1}{C_\xi} \int_0^\infty \int_{-\infty}^\infty W\,[\xi,\, p]\,(z,\, a)\,\xi\left(\frac{z-\tau}{a}\right)\frac{\mathrm{d}\tau\,\mathrm{d}a}{a^2}, \qquad (11)$$

C_ξ is a constant associated to the admissibility condition (Mallat 2008): $C_\xi = \int_0^\infty \frac{|\hat{\xi}(\omega)|^2}{|\omega|}\mathrm{d}\omega$, with $\hat{\xi}$ the Fourier transform of ξ.

In the framework of the propagation of plane waves in a non-dispersive 1-D medium and assuming the Born approximation valid, the wavelet response WR is the CWT of the Green's function of the medium (eq. 1c). Thus, it is possible to reconstruct the Green's function $r(t)$ of the medium from the coefficients of the WR (eq. 11):

$$r(t) = \frac{1}{C_\xi} \int_0^\infty \int_{-\infty}^\infty W\,[\xi, r]\,(t, a)\,\xi\left(\frac{t-\tau}{a}\right)\frac{\mathrm{d}\tau\ \mathrm{d}a}{a^2} \qquad (12a)$$

$$= \frac{1}{C_\xi} \int_0^\infty \int_{-\infty}^\infty R\,[\xi,\, p]\,(t, a)\,\xi\left(\frac{t-\tau}{a}\right)\frac{\mathrm{d}\tau\ \mathrm{d}a}{a^2}, \qquad (12b)$$

and the impedance profile $p(t)$ can be obtained by integrating the Green's function $r(t)$ over t. Actually, it is a relative impedance profile because the impedance component which contains the mean value of the impedance (i.e. the continuous component) cannot be retrieved.

In order to illustrate the efficiency of this approach, we show here that we can reconstruct the impedance profile of a complex subseabed by using the associated WR coefficients. The impedance profile to retrieve, plotted in Fig. 8(a) versus depth, corresponds to the *in situ* acoustic impedance log determined from ground truth data, already used in Section 4.3 and described in previous works (Ker *et al.* 2011, 2012). When this impedance profile is sounded with a reference wavelet family without any source limitation, we can determine the WR coefficients for a dilation range extended to $a \in \mathbb{R}^+$: using the integration form of eq. (12b), we reconstruct the impedance profile plotted in Fig. 8(b). The high frequency variations are in very good accordance with the initial impedance profile which continuous component has been removed, that is, the reconstructed impedance profile shows positive and negative values (Fig. 8b).

Downloaded from http://gji.oxfordjournals.org/ by guest on September 1, 20

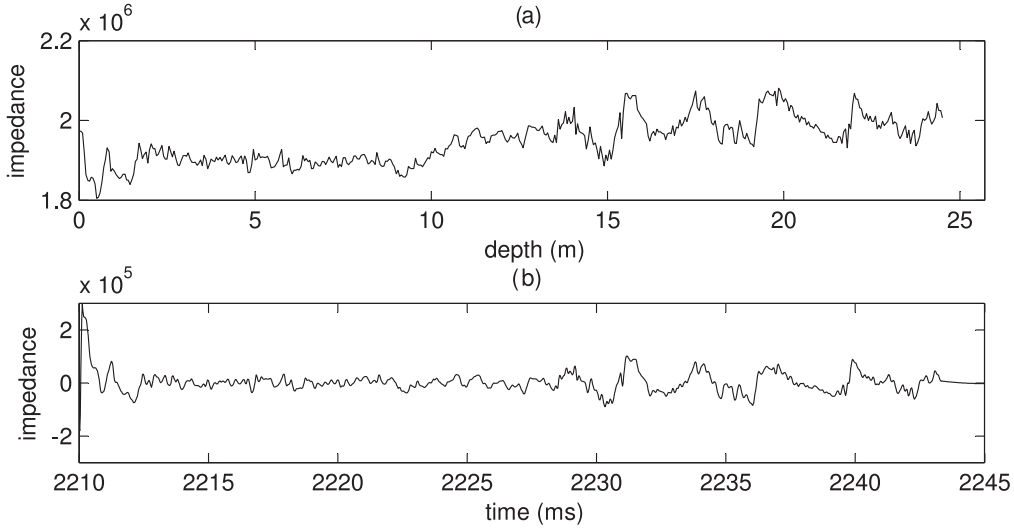

Figure 8. (a) Acoustic impedance profile (unit: Pa.s m^{-1}) obtained from density and sound velocity measurements on ground truth data as a function of depth. (b) Relative acoustic impedance profile reconstructed with the inverse wavelet transform of the reference WR ($a \in \mathbb{R}^+$) as a function of the two way traveltime.

When the WR of the impedance profile involves a seismic source, the dilation range is limited to $a_d \in \mathcal{R}_{a_d}$ according to the WR$_e$ analysis developed in the previous sections: the effect is to partially reconstruct the impedance profile, noted $\tilde{p}(t)$, with the partial Green's function defined by

$$\tilde{r}(t) = \frac{1}{C_{\xi_e}} \int_{\mathcal{R}_{a_d}} \int_t \tilde{R}\,[\xi_e, p]\,(t, a_d)\,\xi_e\left(\frac{t-\tau}{a_d}\right)\frac{\mathrm{d}\tau\ \mathrm{d}a_d}{a_d^2}. \qquad (13)$$

According to these new developments, we are able to perform the inverse wavelet transform obtained from both the HR and VHR SYSIF sources used to compute synthetic seismic data for the *in situ* impedance profile plotted in Fig. 8(a). The results are plotted in Figs 9(a) and (b) for the HR and VHR sources, respectively, that is, for $\mathcal{R}_{a_d}^{\mathrm{HR}}$ and $\mathcal{R}_{a_d}^{\mathrm{VHR}}$. Even if both results involve the same initial impedance profile, they differ because of different limited dilation ranges. This highlights the effect of partially reconstructed profiles when a reduced dominant dilation range is involved, that is, the efficiency of the inverse wavelet transform obviously derives some benefit from merged seismic sources. Actually, we show in Fig. 9(c) the result $\tilde{p}(t)$ reconstructed when we merge the HR and VHR components: the result is in very good agreement with the reference inverse transform performed with $a_d \in \mathbb{R}^+$ (Fig. 8b) when no limited frequency bandwidth seismic source is involved. In that case, we increase the dominant dilation range to $\mathcal{R}_{a_d} = \mathcal{R}_{a_d}^{\mathrm{HR}} \cup \mathcal{R}_{a_d}^{\mathrm{VHR}}$, which is continuous thanks to the source-corrected method developed in this work, that is, the reconstruction of the impedance profile is improved when the HR and VHR seismic sources are merged. Note that $\tilde{p}(t)$ is a smooth version of the reference inverse transform (red curve) and clearly puts in evidence the efficiency of the optimal source-corrected method to quantify the main multiscale acoustic contrasts in complex subseabed structures.

It is interesting to discuss about the vertical resolution of the impedance profile. For a seismic source of frequency bandwidth B, the vertical resolution is given by $Vp/2B$ (Gutowski *et al.* 2002), where $Vp \simeq 1485\,\mathrm{m\,s^{-1}}$: the resolutions are 45 and 90 cm for the VHR and HR sources, respectively. When both sources are merged into a virtual broad-band seismic source, the vertical resolution increases to 38 cm: if not accessible directly with the individual seismic data sets, this improved vertical resolution can be expected in $\tilde{p}(t)$ when the inverse wavelet transform is performed in the merged dominant dilation range $\mathcal{R}_{a_d}^{\mathrm{HR}} \cup \mathcal{R}_{a_d}^{\mathrm{VHR}}$.

5.2 Impedance profiles extracted from seismic SYSIF data

The previous section deals with HR and VHR synthetic seismic traces associated to a common *in situ* acoustic impedance profile which can be reconstructed from the merged source-corrected WR. In this section, we work on field seismic traces acquired by the SYSIF deep-towed seismic system in the close vicinity (110 m) of the location site of the *in situ* acoustic impedance profile: it is important to remember that the HR seismic acquisition, the VHR seismic acquisition and the subseabed samples do not correspond exactly to the same location (the distance between both traces is $\approx$50 m). As shown below, a consequence is a difference between impedance profiles related to *in situ* measurements and seismic data, mainly due to the acquisition conditions rather than the method itself.

Similarly to the previous approach, we perform the source-corrected WR of both the HR and VHR seismic traces and reconstruct the relative impedance profile $\tilde{p}$ from the inverse wavelet transform. Results are plotted in Fig. 10(a) for $a_d \in \mathcal{R}_{a_d}^{\mathrm{HR}}$, in Fig. 10(b) for $a_d \in \mathcal{R}_{a_d}^{\mathrm{VHR}}$ and in Fig. 10(c) for the merged dilation range $a_d \in \mathcal{R}_{a_d}$. In each case, we also plot the impedance profile obtained from the *in situ* measurements in the same dilation range ($\mathcal{R}_{a_d}^{\mathrm{HR}}$, $\mathcal{R}_{a_d}^{\mathrm{VHR}}$ and $\mathcal{R}_{a_d}$). We observe good agreements, in particular in the recovering of the main structures located at $t > 2230$ ms which slight temporal shift is attributed to the difference in the spatial locations of the different data sets. At earlier times, low acoustic impedance contrasts induce low signal-to-noise ratio, that is, we focus the comparison for $t > 2230$ ms. The HR data are more sensitive to the large scale structures, clearly identified with $a_d \in \mathcal{R}_{a_d}^{\mathrm{HR}}$. The small scale features require the higher seismic frequencies of the VHR data. These new results put in evidence the efficiency of the source-corrected method which merges the HR and VHR sources, that is, we are now able to define the relative impedance profile $\tilde{p}(t)$ of the subseabed from broad-band seismic traces acquired with the SYSIF device.

In future works, HR and VHR acquisitions should be performed at the same location in order to improve the combination of the

Downloaded from http://gji.oxfordjournals.org/ by guest on September 1, 2013

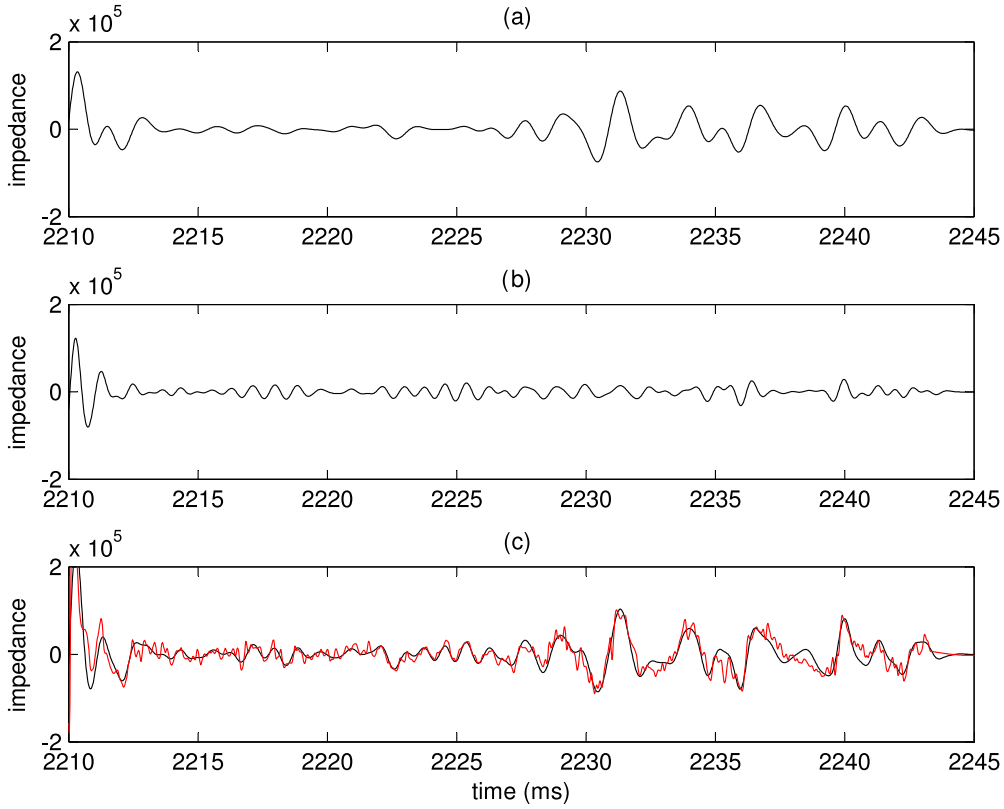

Figure 9. Relative acoustic impedance profiles reconstructed with the inverse wavelet transform applied on the WR of the *in situ* acoustic impedance profile of Fig. 8(a) for (a) the source-corrected WR of the HR component, (b) the source-corrected WR of the VHR component and (c) the source-corrected WR when both the HR and VHR sources are merged (black line) and the reference WR with $a \in \mathbb{R}^+$ (red line, similar to Fig. 8b).

two seismic data sets. But already, we present here what we can get when working with a HR and a VHR seismic data sets, each composed by 450 seismic traces in the vicinity of the *in situ* subseabed samples (Fig. 11). When we process the fusion of both data sets, the reconstruction of the impedance profile is improved as shown in the previous section, that is, the vertical resolution is better than what can be expected with the HR and VHR seismic sources: the subseabed imaging of the impedance profiles is plotted in Fig. 12(a). The strong contrast at $t \simeq 2210$ ms is due the partial reconstruction process of the relative profile which dominates at the seafloor interface. Geological layers can be clearly identified in the subsurface, with a vertical resolution of 38 cm: we are now able to follow and quantify spatial variations of the subseabed acoustic impedance. We remember that we do not have access to the low frequency content of the impedance profile, removed by the integration of the Green's function. But it is interesting to highlight that if the large scale physical properties measured at the core sample location can be extended to the seismic imaging area, the absolute impedance profile can be determined with high confidence. Moreover, we have shown in Ker *et al.* (2011) that the acoustic impedance of the core sample is mainly controlled by density variations, that is, the sound velocity $Vp = 1485\,\mathrm{m\,s^{-1}}$ is roughly constant. With these realistic assumptions, we are able to propose a quantitative information of the seabed physical properties and we can image the density structure of the subseabed with respect to the depth (Fig. 12b).

Another point to highlight is the low computational cost of the present method to quantify the subseabed structure from the inverse wavelet transform of the source-corrected WR_e (eq. 13). The potential of this approach is obvious in order to get a quick preview of the subseabed impedance profile but also to process very large seismic data sets.

6 CONCLUSION

The potential of the new wavelet-based developments, which involve the theoretical properties of both the wavelet transform and Lévy-alpha stable functions, is of particular interest when merging multiresolution data from different seismic sources. Actually, we show that fractional derivative orders allow adapting a source model for each seismic source and we are now able to merge such data, an original fusion processing that spans the analysis frequency range required for multiscale seismic imaging of complex subseabeds. Moreover, we develop the source-corrected WR of seismic reflectors with respect to a new parametrization based on the dominant period, or breadth of the wavelet, in accordance with both the wavelet formalism and the temporal resolution of the seismic sources.

Applied on a homogeneous thin layer, we illustrate the efficiency of the method to correct complex reflectors WR performed by merging the high resolution and very high resolution seismic sources of the SYSIF deep-towed device. The corrected ridge functions, proposed as multiscale seismic attributes, are in perfect agreement with the reference ridge functions and the transition between the both contributions does not suffer from discontinuity anymore, allowing working in the continuous dominant dilation range covered by the merged multiresolution seismic sources. We also show the efficiency of the method with complex impedance structures defined from ground truth data where seismic reflectors can be identified: their multiscale seismic attributes are fully corrected over the whole frequency broadband of the SYSIF device.

Downloaded from http://gji.oxfordjournals.org/ by guest on September 1, 20

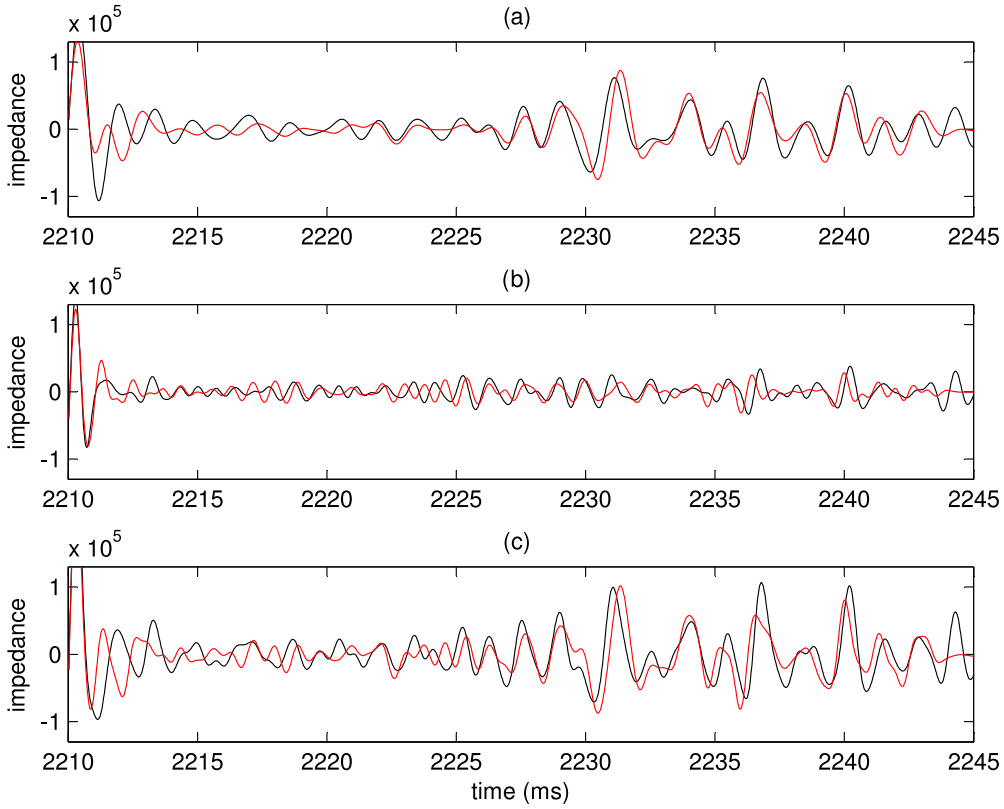

Figure 10. Relative acoustic impedance profiles reconstructed with the inverse wavelet transform applied on the WR of the seismic data (black lines) and *in situ* acoustic impedance profile (in red) for (a) the source-corrected WR of the HR component, (b) the source-corrected WR of the VHR component and (c) the source-corrected WR when both the HR and VHR sources are merged.

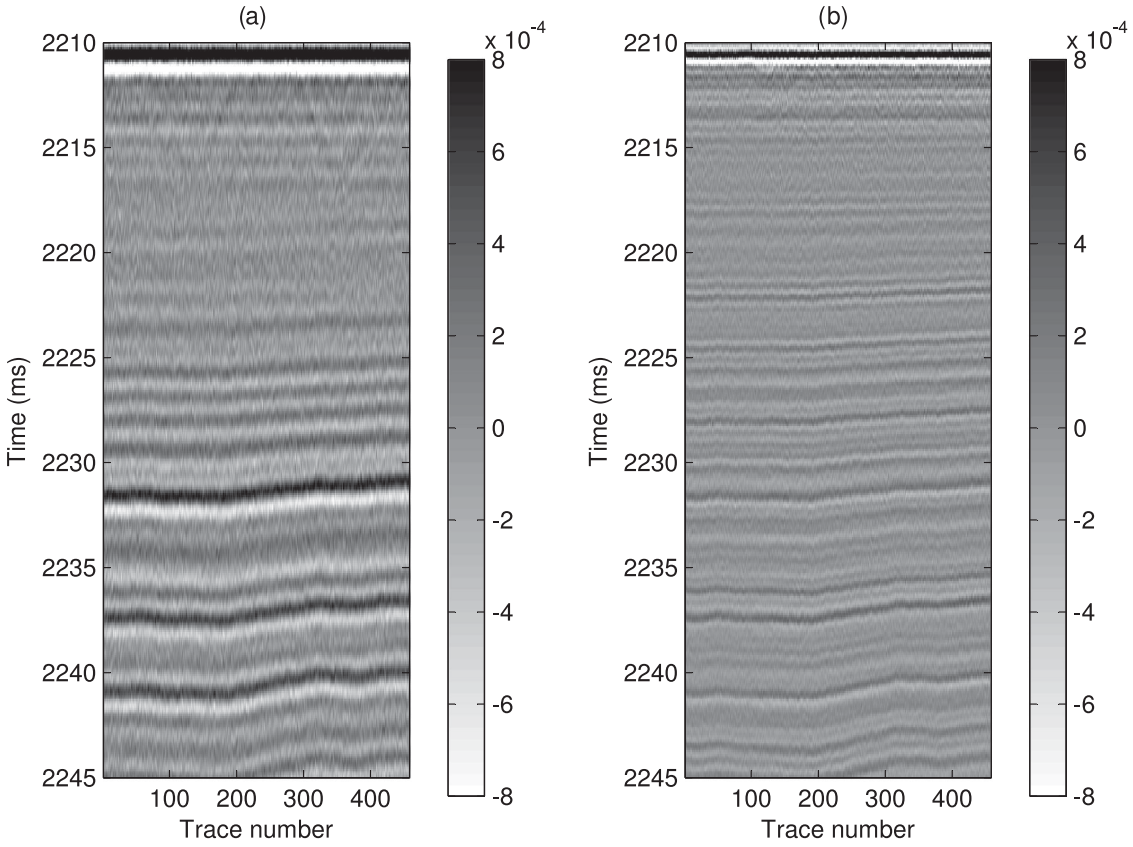

Figure 11. (a) HR seismic profile. (b) VHR seismic profile. The *in situ* impedance profile is located close to trace number 273.

Downloaded from http://gji.oxfordjournals.org/ by guest on September 1, 2013

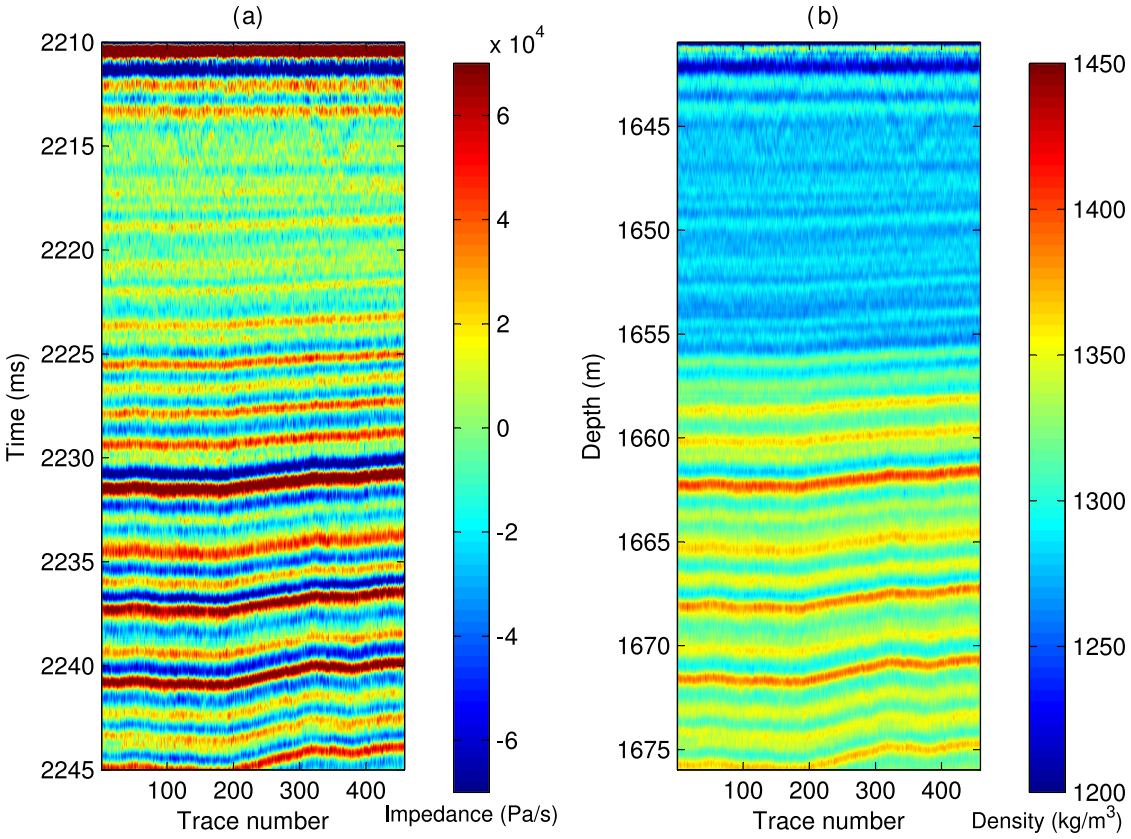

Figure 12. (a) Subseabed imaging of the relative acoustic impedance profiles reconstructed with the inverse wavelet transform of the source-corrected WR of seismic data when both the HR and VHR sources are merged. (b) Associated subseabed density imaging with the assumption of a lateral extension for the low frequency content of the local *in situ* impedance profile.

Thanks to the wavelet-based method to remove the seismic source filtering effects, we also take advantage of the inverse wavelet transform properties extended to the source-corrected WR (Fig. 1). With a first application to reconstruct the acoustic impedance profile of the subseabed, we illustrate that merging both the HR and VHR sources of the SYSIF device allows working with a very broad-band seismic source that improves the vertical resolution of the relative impedance profile. We note that the method benefits from a low computation cost which efficiency can be increased by implementing the simplified reconstruction formula of the inverse wavelet transform (Farge 1992), in particular when assessing physical properties of the subseabed over large seismic data sets. Promising for future works in subseabed geophysical imaging, the source-corrected WR is a powerful method to merge multiresolution seismic sources and can be extended to more general acoustic source signals in the context of multisensor fusion.

ACKNOWLEDGEMENTS

We would like to thank the Editor Pr Jean Virieux and anonymous reviewers for their constructive suggestions. We wish also to thank Alexandrine Gesret for interesting discussion about dominant period. This is IPGP contribution number 3417.

REFERENCES

Bracewell, R.N., 1999. *The Fourier Transform and its Applications,* 3d edn, McGraw-Hill Science/Engineering/Math, 640 pp.

Brcich, R.R., Iskander, D.R. & Zoubir, A.M., 2005. The stability test for symmetric alpha-stable distributions, *IEEE Trans. Signal Process.,* **53,** 977–981.

Castagna, J., Sun, S. & Siegfried, R.W., 2003. Instantaneous spectral analysis: detection of low-frequency shadows associated with hydrocarbons, *Leading Edge,* **22,** 120–127.

Chopra, S. & Marfurt, K., 2005. Seismic attributes—a historical perspective, *Geophysics,* **70,** 3SO–28SO.

Dong, J., Zhuang, D., Huang, Y. & Fu, J., 2009. Advances in multi-sensor data fusion: algorithms and applications, *Sensors,* **9,** 7771–7784.

Farge, M., 1992. Wavelet transforms and their applications to turbulence, *Annu. Rev. Fluid Mech.,* **24,** 395–457.

Fomel, S., 2007. Local seismic attributes, *Geophysics,* **72,** A29–A33.

Garguet-Duport, B., Girel, J., Chassery, J.-M. & Pautou, G., 1996. The use of multiresolution analysis and wavelets transform for merging SPOT panchromatic and multispectral image data, *Photogramm. Eng. Remote Sens.,* **62**(9),1057–1066.

Gesret, A., Laigle, M., Diaz, J., Sachpazi, M. & Hirn, A., 2010. The oceanic nature of the African slab subducted under Peloponnesus: thin-layer resolution from multiscale analysis of teleseismic P-to-S converted waves, *Geophys. J. Int.,* **183,** 833–849.

Gutowski, M., Bull, J., Henstock, T., Dix, J., Hogarth, P., Leighton, T. & White, P., 2002. Chirp sub-bottom source signature design and field testing, *Mar. Geophys. Res.,* **23,** 481–492.

Kallweit, R.S. & Wood, L.C., 1982. The limits of resolution of zero-phase wavelets, *Geophysics,* **47,** 1035–1046.

Kilbas, A., Srivastava, H. & Trujillo, J., 2006. *Theory and Applications of Fractional Differential Equations,* Elsevier.

Ker, S., Marsset, B., Garziglia, S., Le Gonidec, Y., Gibert, D., Voisset, M. & Adamy, J., 2010. High-resolution seismic imaging in deep sea from a joint deep-towed/OBH reflection experiment: application to a Mass Transport Complex offshore Nigeria, *Geophys. J. Int.,* **182,** 1524–1542.

Downloaded from http://gji.oxfordjournals.org/ by guest on September 1, 20

Ker, S., Le Gonidec, Y., Gibert, D. & Marsset, B., 2011. Multiscale seismic attributes: a wavelet-based method and its application to high-resolution seismic and ground truth data, *Geophys. J. Int.,* **187,** 1038–1054.

Ker, S., Le Gonidec, Y. & Gibert, D., 2012. Multiscale seismic attributes: source-corrected wavelet response and its application to high-resolution seismic data, *Geophys. J. Int.,* **190,** 1746–1760.

Le Gonidec, Y. & Gibert, D., 2007. Multiscale analysis of waves reflected by granular media: acoustic experiments on glass beads and effective medium theories, *J. geophys. Res.,* **112**(B05103), doi:10.1029/2006JB004518.

Le Gonidec, Y., Gibert, D. & Proust, J.-N., 2002. Multiscale analysis of waves reflected by complex interfaces: basic principles and experiments, *J. geophys. Res.,* **107**(B9), 2184.

Le Gonidec, Y., Conil, F. & Gibert, D., 2003. The wavelet response as a multiscale NDT method, *Ultrasonics,* **41,** 487–497.

Mallat, S., 1998, *A Wavelet Tour of Signal Processing,* 2nd edn, Academic Press.

Mallat, S. & Hwang, W. L., 1992. Singularity detection and processing with wavelets, *IEEE Trans. Inf. Theory,* **38,** 617–643.

Marsset, T., Marsset, B., Ker, S., Thomas, Y. & Le Gall, Y., 2010. High and very high resolution deep-towed seismic system: performance and examples from deepwater Geohazard studies, *Deep-Sea Res. I,* **57,** doi:10.1016/j.dsr.2010.01.001.

Miller, K.S. & Ross, B., 1993. *An Introduction to the Fractional Calculus and Fractional Differential Equations,* John Wiley and Sons.

Moreau, F., Gibert, D., Holschneider, M. & Saracco, G., 1997. Wavelet analysis of potential fields, *Inverse Probl.,* **13,** 165–178.

Moreau, F., Gibert, D., Holschneider, M. & Saracco, G., 1999. Identification of sources of potential fields with the continuous wavelet transform: basic theory, *J. geophys. Res.,* **104,** 5003–5013.

Morlet, J., Arens, G., Forgeau, I. & Giard, D.1982. Wave propagation and sampling theory—part I: complex signal and scattering in multilayered media, *Geophysics,* **47,** 203, doi:10.1190/1.1441328.

Partyka, G., Thomas, J., Turco, K. & Hartmann, D., 2000. Upscaling petrophysical properties to the seismic scale, *in Proceedings of the 70th Annual International Meeting,* Calgary, SEG Expanded Abstracts.

Pennington, W.D., 2001. Reservoir geophysics, *Geophysics,* **66,** 25–30.

Sailhac, P., Gibert, D. & Boukerbout, H., 2009. The theory of the continuous wavelet transform in the interpretation of potential fields: a review, *Geophys. Prospect.,* **57,** 517–525.

Voit, J., 2003. *The Statistical Mechanics of Financial Markets (Texts and Monographs in Physics),* Springer-Verlag.

Widess, M.A., 1973. How thin is a thin bed?, *Geophysics,* **38,** 1176–1180.

Wood, W., Gettrust, J.F. & Spychalski, S., 2003, A new deep-towed, multichannel seismic system, *Sea Technol.,* **44,** 44–49.

Yilmaz, O., 2001, *Seismic Data Processing,* Society of Exploration Geophysicists.

Zhou, J., Civco, D.L. & Silander, J.A., 1998. A wavelet transform method to merge Landsat TM and SPOT panchromatic data, *Int. J. Remote Sens.,* **19,** 743–757.

Downloaded from http://gji.oxfordjournals.org/ by guest on September 1, 2013

AGU PUBLICATIONS

JGR

Journal of Geophysical Research: Oceans

RESEARCH ARTICLE

10.1002/2014JC010478

Multiscale seismic reflectivity of shallow thermoclines

S. Ker[1], Y. Le Gonidec[2], L. Marié[3], Y. Thomas[1], and D. Gibert[2]

[1]IFREMER, Géosciences Marines, Centre de Brest, F-29280 Plouzané, France, [2]Géosciences Rennes (CNRS UMR 6118), Université Rennes 1, Rennes, France, [3]Laboratoire de Physique des Océans, UMR 6523 CNRS/IFREMER/IRD/UBO, Plouzané, France

Key Points:
- A wavelet-based seismic method is extended to thermocline-related reflectors
- An analytical seismic reflectivity is developed for a simple thermocline model
- Recommendations are suggested to improve thermocline seismic detection

Correspondence to:
S. Ker,
stephan.ker@ifremer.fr

Citation:
Ker, S., Y. Le Gonidec, L. Marié, Y. Thomas, and D. Gibert (2015), Multiscale seismic reflectivity of shallow thermoclines, *J. Geophys. Res. Oceans*, *120*, 1872–1886, doi:10.1002/2014JC010478.

Received 30 SEP 2014
Accepted 9 FEB 2015
Accepted article online 14 FEB 2015
Published online 20 MAR 2015

Abstract Seismic oceanography is coming of age as an established technique of observation of the thermohaline structure of the ocean. The present paper deals with the seismic reflectivity of the Armorican Shelf seasonal thermocline, west of France, based on two seismic experiments performed with a sparker source. The peak frequency was 500 Hz for the ASPEX experiment, where the thermocline was located at 27 m water depth, and reduced to 400 Hz associated to a higher source level for the IFOSISMO experiment, where the thermocline was 12 m deeper. Despite these settings, only the first experiment could clearly highlight the thermocline reflector, providing the first seismic observation of a shallow oceanic structure. To better understand the limitation of high-resolution seismic devices in detecting weak oceanic features, we develop a wavelet-based seismic analysis and consider, as a first approximation, a simple thermocline modeled by a Gauss error function, allowing an analytical expression for the associated seismic reflectivity. We show that the acoustic impedance profile of the thermocline is mainly controlled by a sound velocity proportional to the temperature. We show that the seismic reflectivity is controlled by the reflection coefficient of the large-scale structure of the thermocline and by an attenuation factor which depends on the ratio between the seismic wavelength and the characteristic size of the thermocline. Depending on this ratio, the strength of the thermocline-related reflection may be too weak to be detected by seismic measurement.

1. Introduction

The Ocean Surface Boundary Layer (OSBL) controls the exchange of heat, momentum, and gases between the atmosphere and ocean. As such, it is a key component of the climate system, and developing a thorough understanding of its dynamics, though experimentally very challenging, is a pressing scientific issue. Even harder to observe are actually the so-called "entrainment" processes occurring at the base of the mixed layer [*Johnston and Rudnick*, 2009; *Grant and Belcher*, 2011], out of grasp of satellite observation, and which in turn control the exchanges of the OSBL with the bulk of the water column.

Ship-borne acoustic Doppler current profilers can provide measurements of current velocity at resolutions adequate for the study of these entrainment processes, but their accuracy is still marginal, and the interpretation is hampered by the lack of corresponding observations of density structure. In situ towed instruments [see, e.g., *Brown et al.*, 1996], which provide direct measurements of thermohaline properties, are currently limited to spatial resolutions on the order of one to two profiles per kilometer, which are insufficient to represent small-scale processes such as internal waves and the decameter-scale coherent structures they energize on the mixed-layer base. Microstructure measurements [see, e.g., *Soloviev et al.*, 1988; *Moum et al.*, 1995] can provide profiles of turbulent kinetic energy across the mixed-layer base, as well as indirect estimates of the turbulent diffusivities of heat, momentum, and tracers, but this information lacks horizontal context, and the influence of coherent structures, such as Langmuir circulations or Kelvin-Helmholtz billows, can be missed.

Broadband acoustic backscatter measurements are a very promising technique and have permitted spectacular advances, for instance in the study of nonlinear internal waves and their role as a source of turbulent mixing and entrainment on the seasonal thermoclines of shelf seas [*Moum et al.*, 2003]. The mechanism by which high-frequency acoustic energy is backscattered is however complicated, and untangling the contributions of turbulent microstructure and suspended particles (zooplankton, notably) from the backscattered signal remains a subject of active research [*Lavery et al.*, 2010].

During the past decade, seismic reflection techniques have been successfully applied to study the thermohaline structure of the deep ocean, including small-scale thermohaline structures like thermohaline

© 2015. American Geophysical Union. All Rights Reserved.

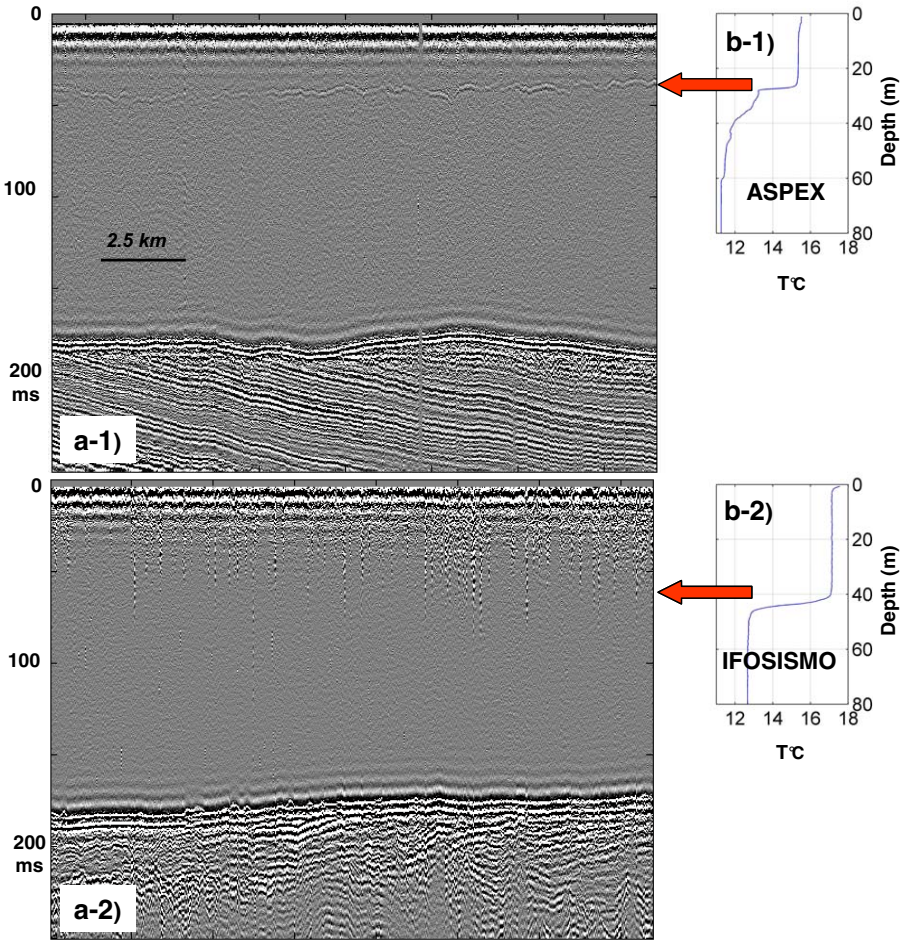

Figure 1. (a-1) Seismic profile acquired during the ASPEX cruise and (b-1) associated temperature CTD measurement [*Piété et al*., 2013]. A strong seismic reflector is clearly correlated with the main contrast of the thermocline, as pointed by the red arrow. (a-2) Seismic profile acquired during the IFOSISMO cruise and (b-2) associated temperature CTD measurement [*Thomas et al*., 2013]. In that case, even performed with the same HR seismic device, no seismic reflector associated to the significant thermocline interface is observed. It has to be noted that the salinity shows a value of 35.5 ± 0.1 (pss-78) for both cases and has no influence in the seismic response of the thermocline.

intrusions [*Holbrook et al*., 2003], thermohaline staircases [*Biescas et al*., 2010; *Fer et al*., 2010], internal gravity waves [*Holbrook and Fer*, 2005; *Holbrook et al*., 2009], and mesoscale structures like eddies [*Biescas et al*., 2008; *Ménesguen et al*., 2012] and current flows [*Mirshak et al*., 2010]. The acoustic reflectivity is essentially governed by the vertical variations of acoustic impedance, a quantity which varies with thermohaline properties according to the seawater equation of state, with temperature usually playing a dominant role [*Sallarès et al*., 2009; *Ruddick et al*., 2009]. As a first approximation, seismic sections can thus be considered to represent maps of the vertical temperature gradient. So far, however, seismic oceanography has mainly been used to study deep ocean structures, and studies of the shallowest levels of the water column (<150 m) remain rare [*Phillips and Dean*, 1991; *Carniel et al*., 2012]. This paper addresses the question of the detectability of thermohaline structures by seismic methods, and is a follow-up of the previous study by *Piété et al*. [2013].

The work of *Piété et al*. [2013] mainly focused on the specific challenges of the use of seismic methods in the shallow water column and succeeded in providing the first seismic observations of a shallow (∼30 m deep) oceanic structure, the seasonal thermocline of the Armorican Shelf, west of France (Figure 1a-1). This previous work, however, should deserve additional investigations as 3 months later another cruise performed on the same shelf, at less than 200 km distance and using the same seismic device, failed to observe the same water mass structure [*Thomas et al*., 2013] (Figure 1a-2).

Seismic reflection coefficients associated to seasonal thermoclines have not been extensively studied yet, but according to *Piété et al*. [2013], they present a high variability, ranging from −60 down to −90 dB and

© 2015. American Geophysical Union. All Rights Reserved.

are very weak compared to those found for solid Earth reflectors (typically around −40 dB). Thus, seismic detectability of such weak thermocline-related reflectors is sensitive to the noise level present in the seismic data, introduced by the electronics of the seismic apparatus itself, by mechanical noise at the sensing elements, and by the prevailing meteorological conditions. Moreover, as already observed for deeper oceanic structures [*Hobbs et al*., 2009], the seismic reflectivity of a given property interface depends sensitively on the frequency content generated by the source device [*Piété et al*., 2013]. The aim of this article is to present a systematic study of these observations and to provide a rationalization of the relationship between the physical structure of water mass interfaces and their seismic reflectivity.

In section 2, we present the two seismic surveys and associated thermocline structures. In section 3, seismic reflectivity is introduced in relation with a thermocline interface and we present a simple yet enlightening analytical model of such interface. In section 4, we present the two main multiscale wavelet-based analysis tools, the continuous wavelet transform and the wavelet response method, which we apply to the analytical thermocline profile. The insight gained is used in section 5, where the parameters controlling the seismic reflection of a given interface are quantitatively discussed, and the separate roles played by the acoustic impedance contrast, interface thickness, and seismic source peak frequency are made clear. Section 6 then provides a discussion of the contrasting results of the two seismic acquisitions at hand and provides design guidelines to improve seismic devices devoted to thermohaline structures. We finally draw some conclusions in section 7.

2. Data Sets: The Elusive Seasonal Thermocline of the Armorican Shelf

Seismic waves reflect on acoustic impedance contrasts which can be induced by sound velocity and/or density variations. In the case of ocean water masses, the cause of these variations, i.e., the origin of seismic reflections, can be temperature and/or salinity contrasts. On the western Brittany continental shelf, two seismic reflection surveys (ASPEX and IFOSISMO) were performed in 2012 to observe the structure of the seasonal thermocline.

2.1. Description of the ASPEX Case

During the ASPEX cruise aboard the French R/V Gwen Drez in June 2012, an experimental seismic device, involving a sparker source, was tested close to the island of Belle Ile. The seismic data acquisition was performed shortly after a period of intense surface-induced mixing and a satisfactory image of the mixed-layer base could be obtained, providing the first seismic image of a shallow structure (Figure 1a-1), the seasonal thermocline [*Piété et al*., 2013].

The seasonal thermocline, observed in situ with CTD measurements with a depth sampling of 20 cm, indicates a salinity S = 35.5 (pss-78) with small variations of ±0.1. The temperature profile (Figure 1b-1) is characterized by a top layer with a constant temperature $T_0 = 15.3°C$ followed by a sharp decrease of $\Delta T = 2.1°C$ in a water layer of thickness $\Delta z = 2.4$m located at 26 m water depth. Deeper, between the bottom of the thermocline and 60 m water depth, a gentle temperature decrease by 2°C occurs. On the associated seismic profile (Figure 1a-1), strong reflection at the seafloor is observed and, close to the sea surface, a weak reflector is observed in perfect agreement with the location of the thermocline: this is the seismic signature of the main thermocline discontinuity. The sparker source signal was set with a central frequency $f_p = 500$ Hz and an emission level of 205 dB re 1μ Pa at 1 m. The fold of the stacking was 100 in order to increase the signal-to-noise ratio. Note that the acquisition conditions were very good during the cruise, i.e., the sea conditions induced a low level of ambient noise.

2.2. Description of the IFOSISMO Case

During the IFOSISMO cruise aboard the French R/V Côtes de la Manche in September 2012, the same seismic device was deployed around the island of Ushant with the same objective: image the seasonal thermocline and provide a high-resolution view of the structure of the Ushant tidal front [*Le Boyer et al*., 2009]. However, in the seismic data (Figure 1a-2), the acquisition of which followed a long period of mild weather, no acoustic reflector could be observed in correspondence with the thermocline highlighted with the CTD measurements (Figure 1b-2).

The CTD data, which also indicate a salinity S = 35.5 (pss-78) with small variations of ±0.1, reveal a top layer temperature $T_0 = 17.1°C$ and a strong temperature contrast $\Delta T = 4.5°C$ in a layer thickness $\Delta z = 8.2$m located

© 2015. American Geophysical Union. All Rights Reserved.

Table 1. Parameters of the Seasonal Thermocline Measured During the ASPEX and IFOSISMO Cruises

	ΔT (°C)	T_0 (°C)	Δz (m)	z (m)	Freq (Hz)	Source Level (dB re 1μ Pa at 1 m)
ASPEX	2.1	15.3	2.4	27	500	205
IFOSISMO	4.5	17.1	8.2	39	400	208

at the water depth 39 m. As an empirical approach to improve this seasonal thermocline detection with seismic experiments, new acquisition parameters of the sparker source were set to compensate for the attenuation of the seismic wave with depth: this includes a frequency as low as $f_p = 400$ Hz and a higher emission level of 208 dB re 1μ Pa at 1 m. The fold of the stacking was set as the one of the previous case in order to insure the same sensitivity of the system as described in *Piété et al*. [2013]. But despite these settings, the seismic detection of the thermocline interface did not succeed: the thermocline reflector was too weak to be highlighted with the seismic measurements.

2.3. Rationale of the Study

These observations show that detecting a seasonal thermocline with seismic measurements is not straightforward and requires optimizing seismic acquisition settings (Table 1 sums up the different physical parameters introduced above for the IFOSISMO and ASPEX seismic cruises). On one hand, ambient and electronic noise cannot be ignored and increasing seismic source level is not a practical option because of specific technological limitations of the source devices. All these factors are detrimental to the sensitivity of the seismic device to weak reflection on thermohaline interfaces. On the other hand, it is well known that the interaction between a seismic wave and a complex seismic reflector depends on the frequency of the source signal, as introduced in the next section. To better understand seismic detectability, which represents a key point in designing seismic experiments deployed at sea to observe oceanic features, we also introduce a simple model to approximate a thermocline-related reflector used to both develop and discuss the multiscale analysis described in section 4.

3. Seismic Wave Reflected by a Thermocline Interface

3.1. Seismic Reflectivity

As a general introduction, we consider acoustic waves propagating in a fluid characterized by a vertical acoustic impedance profile $\gamma(z)=v(z)\rho(z)$, z being the depth, v the sound velocity, and ρ the density. A contrast between $\gamma(z)$ and $\gamma(z+dz)$ induces an acoustic reflectivity profile expressed by $\eta(z)=\frac{1}{2\gamma(z)}\frac{d\gamma(z)}{dz}$. Seismic reflection is thus a sonography technique that provides an image of acoustic impedance contrasts [*Yilmaz*, 1987]. In the time domain of seismic reflection, the two-way travel time for a seismic source-receiver located at the sea surface is $t(z)=2\int_0^z v^{-1}(\xi)\mathrm{d}\xi$, and the expression of the acoustic reflectivity in the single scattering approximation is $\eta(t)=\frac{1}{2}\frac{d\ln\gamma(t)}{dt}$ [*Gray and Bleistein*, 1986]. In the case of water columns in oceans, sound velocity and density, and thus γ, are both related to the temperature T, salinity S, and water depth z, through the equation of state of seawater [*Millero et al*., 1980]. If the influence of density changes can be neglected with respect to sound velocity changes in $\gamma(z)$, the reflectivity can be expressed as a spatial derivative of the sound velocity profile: $\eta(t)=\frac{1}{4}\frac{\mathrm{d}}{\mathrm{dz}}v[z(t)]$. If we further assume S contrasts are negligible in the case of thermoclines, the acoustic reflectivity only depends on the temperature gradient $dT(z)/dz$ of the thermocline.

Another parameter which controls the seismic reflectivity is the wavelength λ of the acoustic wave. Indeed, considering the simple case of two successive interfaces, the respective reflected waves can interact constructively or destructively depending on λ relative to the distance between the interfaces which is the characteristic size of the reflector. As a consequence, the reflective properties of a thermocline have to be analyzed both in time and frequency, to be able to distinguish the signatures of the different seismic impedance interfaces and the responses at the different frequencies contained in the probing signal, respectively.

© 2015. American Geophysical Union. All Rights Reserved.

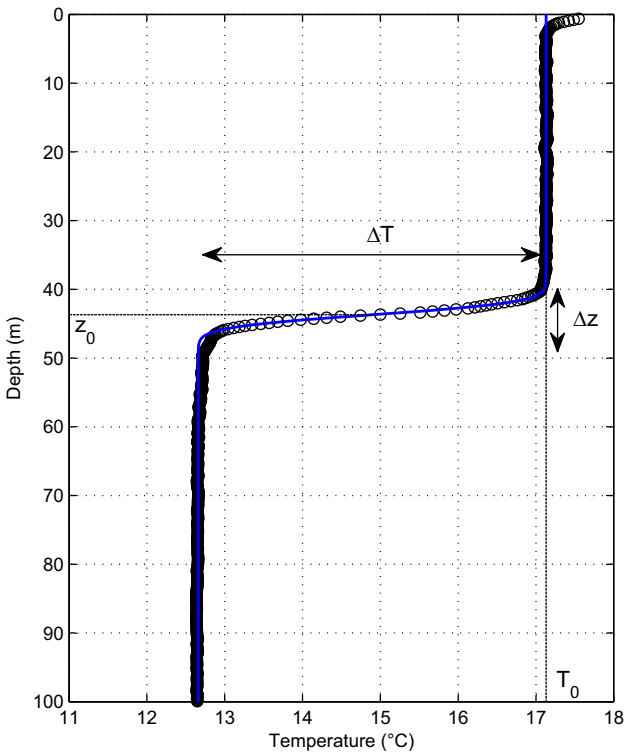

Figure 2. Seasonal thermocline measured during the IFOSISMO cruise (black circles) and the analytical GEF thermocline (blue line) based on a Gauss error function. The thermocline's parameters are shown: top layer temperature T_0, temperature contrast ΔT, thermocline thickness Δz, and depth z_0 of the thermocline's barycenter.

3.2. Analytical Thermocline Model

An analytical model to approximate a thermocline morphology, simple enough to permit an exact and illustrative analysis, can be constructed as follows. As a first approximation, a thermocline is an oceanic interface located between two water layers of different temperatures, T_0 and $T_0-\Delta T$, where the temperature contrast $\Delta T > 0$. If the discontinuity is a step-like function located at the water depth z_0, the temperature profile is expressed by:

$$T(z)=\begin{cases} T_0 & \text{if } z \le z_0 \\ T_0-\Delta T & \text{if } z > z_0 \end{cases}. \quad (1)$$

A slightly more elaborate model which still allows analytical computations and involves a measure of thermocline thickness can be formulated using a Gauss error function [*Crank*, 1980], written GEF in the remainder of the paper:

$$T(z)=T_0-\frac{\Delta T}{2}\left(1+erf\left(\frac{z-z_0}{\Delta z/4}\right)\right). \quad (2)$$

In that case, z_0 becomes the barycenter of the interface, whose characteristic size is Δz, the scale over which 90% of the total temperature variation occurs. To illustrate the morphology of such a simple analytical GEF thermocline, we use the main physical parameters of the in situ IFOSISMO thermocline summarized in Table 1. In this particular case, it is important to observe the very good agreement between the analytical GEF and the actual IFOSISMO thermoclines (Figure 2, solid line and black circles, respectively). Actually, limitations of the GEF thermocline exist at fine scales: the effects of such fine structures, which cannot easily be included in the analytical approach of the multiscale method described below, are discussed in section 6.

As recalled above, contrasts in the temperature profile $T(z)$, defined by the temperature gradient $dT(z)/dz$, induce acoustic impedance contrasts which are responsible for seismic reflections. According to the analytical GEF thermocline presented above, this gradient is expressed by

$$\frac{dT(z)}{dz}=\frac{-\Delta T}{\sqrt{2\pi}}\frac{1}{\kappa\Delta z}\exp\left(\frac{-(z-z_0)^2}{2(\kappa\Delta z)^2}\right), \quad (3)$$

and defines an analytical thermocline-related seismic reflector. Note that the temperature gradient tends to $-\Delta T\delta(z-z_0)$ when $\Delta z \to 0$: in this asymptotic case, no length scale is involved, i.e., the interface is homogeneous. The general expression of the temperature gradient (equation (3)) is a Gaussian function defined by the standard deviation $\kappa\Delta z$, where $\kappa=1/(4\sqrt{2})$ and Δz is the thermocline thickness, and by the expected value z_0 which corresponds to the thermocline depth location. The existence of the characteristic size $\Delta z \neq 0$ means the analytical GEF interface is complex.

4. Multiscale Wavelet-Based Method

When the temperature profile $T(z)$ is available, with CTD measurements for instance, we can analyze its morphology at different scales of observation through the use of the generic multiscale continuous wavelet

© 2015. American Geophysical Union. All Rights Reserved.

transform, which allows describing internal (small scale) and global (large scale) structures: this is the aim of section 4.1 where we show the specific results when the $T(z)$ morphology is characterized by a Gauss error function (equation (2)). When $T(z)$ is not a priori known, we extend the approach with the wavelet response method specifically devoted to the study of acoustic reflectivity of multiscale seismic reflectors: this is the aim of section 4.2 where we highlight the relation between the seismic reflectivity and the parameters of the GEF thermocline morphology.

4.1. Continuous Wavelet Transform of the Analytical Thermocline Model

To assess the multiscale features of the analytical GEF thermocline, the Continuous Wavelet Transform (CWT) method offers a depth-scale representation of the temperature profile $T(z)$ with good depth and frequency localization [*Mallat*, 1998]. The CWT can be expressed as the convolution between $T(z)$ and a family of wavelets that enables to decompose the profile at different observation scales [*Mallat*, 1998; *Alexandrescu et al.*, 1995]:

$$W[\psi,T](z,a)=\frac{1}{a}\psi\left(\frac{z}{a}\right)*T(z), \tag{4}$$

where a is the dilation, or scale parameter, of the analyzing wavelet ψ. The wavelet is an oscillating function with vanishing moments, such as the Gaussian derivative functions, i.e., $\psi=\psi_n(z)=\frac{\mathrm{d}^n}{\mathrm{d}z^n}\exp(-z^2)$, where n is the derivative order. In that case, we can write:

$$W[\psi_n,T](z,a)=\frac{1}{a}\frac{\mathrm{d}^n}{\mathrm{d}(z/a)^n}\exp\left(-\frac{z^2}{a^2}\right)*T(z), \tag{5a}$$

$$=\frac{\mathrm{d}^{n-1}}{\mathrm{d}(z/a)^{n-1}}\exp\left(-\frac{z^2}{a^2}\right)*\frac{d}{dz}T(z), \tag{5b}$$

$$=-\Delta T\left(\frac{a}{a'}\right)^n\psi_{n-1}\left(\frac{z-z_0}{a'}\right), \tag{5c}$$

with the new dilation $a'=\sqrt{a^2+2(\kappa\Delta z)^2}$. The passage from equation (5a) to equation (5b) is a general property of convolutions, while the passage from equation (5b) to equation (5c) is due to the stability over convolution of Gaussian functions.

In the framework of the wavelet transform, a ridge function is defined as the absolute value of $W[\psi_n,T](z,a)$ along a given line of maxima and constitutes a sparse support of the multiscale analysis [*Mallat*, 1998; *Alexandrescu et al.*, 1995]. For a step-like thermocline interface $\Delta z=0$ (Figure 3a-1), $W[\psi,T](z,a)=-\Delta T\psi_{n-1}\left(\frac{z-z_0}{a}\right)$: the ridge function does not depend on a and the CWT components are all Gaussian derivative functions with the order $n-1$, i.e., the integral of the analyzing wavelet ψ_n. We illustrate this result by performing the CWT with $n=3$: the CWT presents a cone-like structure with three extrema pointing onto the singularity location [*Mallat and Hwang*, 1992] (Figure 3a-2) and the ridge function plotted in a *log−log* diagram (Figure 3a-3) is a straight line with a slope $\alpha=0$ in accordance with the homogeneity degree of a step-like discontinuity [*Holschneider*, 1995].

For a finite-thickness interface $\Delta z\neq 0$ (Figure 3b-1), the CWT amplitude depends on both a and ΔT, according to equation (5c), i.e., the thermocline is a complex interface whose multiscale analysis depends nontrivially on the seismic frequency. The CWT of the GEF interface performed with $n=3$ shows a cone-like structure pointing toward the center of the discontinuity (Figure 3b-2) but the ridge function is more complex, with an absolute amplitude given by $\Delta T\left(1+2\left(\frac{\kappa\Delta z}{a}\right)^2\right)^{-\frac{3}{2}}$ (Figure 3b-3). At large dilations a, the curve is characterized by a straight line with $\alpha=0$, i.e., the GEF interface is equivalent to a step-like interface at large scales of observation. At small scales of observation, the ridge function decreases as a^3, i.e., the amplitude is strongly sensitive to the wavelet dilation.

4.2. Extension to the Seismic Reflectivity With the Wavelet Response Method

4.2.1. Introduction of the Method

Le Gonidec et al. [2002] have shown experimentally that the acoustic response of a complex interface to wavelet-shaped source signals could be well predicted by the Wavelet Response (WR) method, an

© 2015. American Geophysical Union. All Rights Reserved.

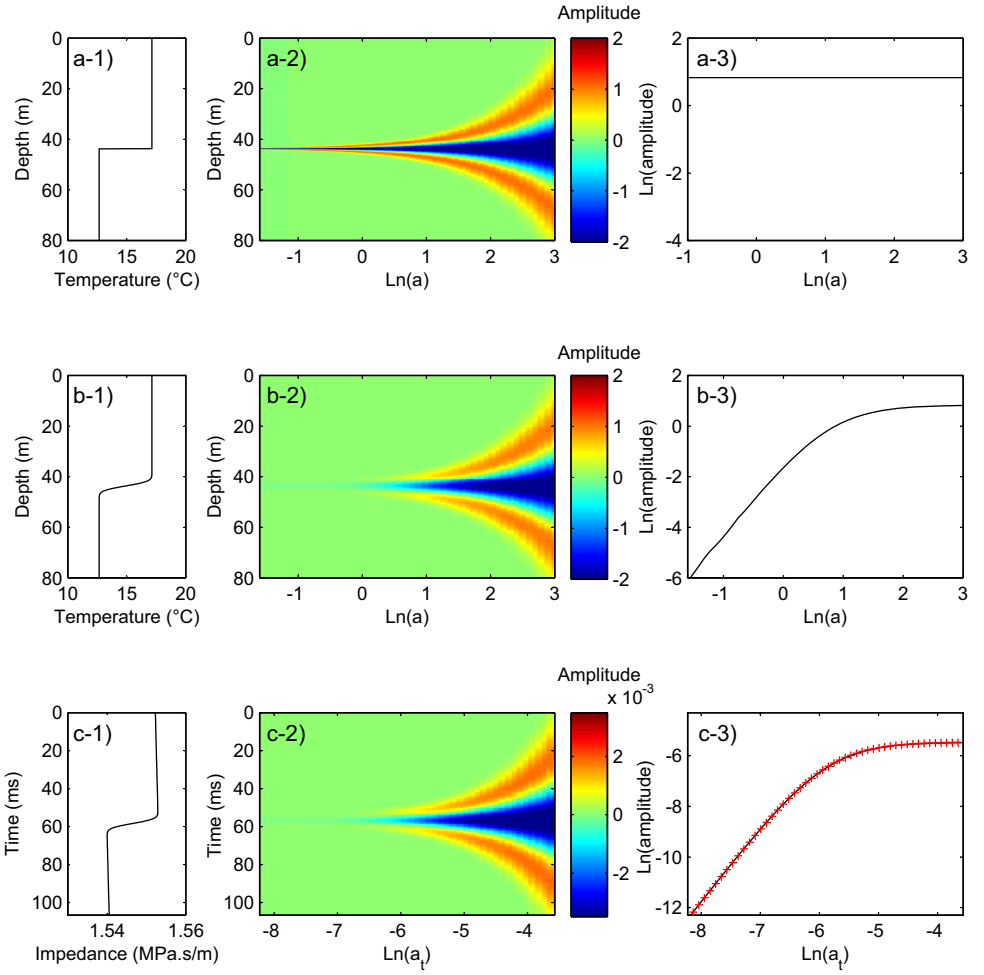

Figure 3. Step-like thermocline: (a-1) temperature profile, (a-2) CWT, and (a-3) ridge function. Analytical GEF thermocline (Gauss error function with $T_0 = 17.1°C$, $\Delta = 4.5°C$, $\Delta z = 8.2$ m, and $z_0 = 39$ m): (b-1) temperature profile, (b-2) CWT, and (b-3) ridge function. Acoustic impedance of the GEF thermocline: (c-1) profile in the TWT domain, (c-2) synthetic WR, and (c-3) ridge functions that provide the seismic reflectivity, extracted from the WR (solid line), and from the analytical solution of equation (12) (red crosses).

extension of the CWT where the convolution operator is replaced by a propagation operator $\otimes$ according to:

$$R[\psi_n, v](t, a_t) = \frac{1}{a_t}\psi_n\left(\frac{t}{a_t}\right) \otimes v(t). \tag{6}$$

The dilation a_t in the time domain controls the frequency content of the dilated wavelets: the associated wavelet peak frequency is $f_p = 1/\pi a_t$ [*Ker et al.*, 2012].

In the special case where ρ can be assumed constant and multiple scattering can be neglected, *Le Gonidec et al.* [2002] demonstrate that the WR of the sound velocity profile is equivalent to the CWT of the seismic reflectivity profile $\eta(z)$, i.e.,

$$R[\psi_n, v](t, a_t) \equiv W[\psi_n, \eta](z, a). \tag{7}$$

A perfect equivalence between both methods to analyze a sound velocity profile v is expressed by $a_t R[\psi_{n-1}, v](t, a_t) \iff W[\psi_n, v](z, a)$, where $\iff$ emphasizes that the WR and the CWT share the same multiscale properties although they belong to different physical spaces, i.e., time t and space z, respectively.

Currently available seismic sources cannot perform full WR measurements. Rather, each available technology can only generate a subset of the wavelets used by *Le Gonidec et al.* [2002] and *Le Gonidec and Gibert*

© 2015. American Geophysical Union. All Rights Reserved.

[2007]. In *Ker et al*. [2011], the authors extend the approach to seismic data, performing synthetic WRs based on the Goupillaud's modeling approach [*Goupillaud*, 1961] which can thus provide a full description of the acoustic response of water column interfaces at seismic wavelengths, against which available technology can be benchmarked.

4.2.2. Correspondence Between Seismic Reflectivity and Thermocline Parameters

In both our study cases, S contrasts are negligible, and the influence of density changes is negligible with respect to sound velocity changes in the acoustic impedance profile [*Piété et al*., 2013]. Linearizing the relation between v and T within the thermocline, we can establish a direct equivalence between the WR of v and the CWT of T:

$$a_t R[\psi_{n-1}, v](t, a_t) \Longleftrightarrow W[\psi_n, T](z, a). \tag{8}$$

This original result shows that the multiscale structure of a thermocline temperature profile T could be directly assessed by performing a seismic survey with source signals designed as dilated wavelets ψ_{n-1} and taking benefits of the CWT properties. According to equation (5c) and relation (8), we show that the analytical expression of the seismic WR of a GEF thermocline (equation (2)) is expressed by:

$$R[\psi_{n-1}, v](t, a_t) = r_0 \left(\frac{a_t}{a'_t}\right)^n \frac{1}{a'_t} \psi_{n-1}\left(\frac{t-t_0}{a'_t}\right). \tag{9}$$

The seismic signal reflected by the GEF thermocline insonified by a seismic wavelet ψ_{n-1} with a peak frequency $f_p = 1/\pi a_t$ is thus a similar wavelet ψ_{n-1} with modified peak frequency $1/\pi a'_t$ and dilation $a'_t = \sqrt{a_t^2 + 2\left(\frac{\kappa \Delta z}{v_{rms}}\right)^2}$, which depends on the thermocline thickness Δz and $v_{rms} = \sqrt{\frac{\sum_i v_i^2 \Delta t_i}{\sum_i \Delta t_i}}$, the root mean square sound velocity.

For a step-like thermocline $\Delta z = 0$, the ridge function of the WR (equation (9)) does not depend on the source dilation a_t as expected for this homogeneous interface [*Le Gonidec et al*., 2002]. Thus, r_0 corresponds to the reflection coefficient of the step-like thermocline-related reflector located at the two-way travel time $t_0 = 2z_0/v_{rms}$:

$$r_0 = \frac{v(T_0 - \Delta T) - v(T_0)}{v(T_0 - \Delta T) + v(T_0)}. \tag{10}$$

For a finite-thickness interface $\Delta z \neq 0$, the ridge function depends on a_t, as expected for a complex reflector, and we note

$$r = r_0 \left(\frac{a_t}{a'_t}\right)^n, \tag{11}$$

the multiscale seismic reflection coefficient of the reflector, called seismic reflectivity for the sake of simplicity in the remainder of the paper.

4.2.3. Comparison Between the Analytical Seismic Reflectivity and the Synthetic Wavelet Response

In exploration seismology, it is common to approximate the seismic source signal ψ_{n-1} of equation (9) as a Ricker signal, defined by $\frac{d^2}{dt^2} \exp(-t^2)$. For this particular application where $n = 3$, the analytical expression of the thermocline seismic reflectivity established from equation (11) is given by:

$$r = r_0 \left(1 + 2\left(\frac{\pi \kappa \Delta z}{\lambda}\right)^2\right)^{-\frac{3}{2}}, \tag{12}$$

where $\lambda = v_{rms}/f_p$ is the wavelength of the seismic source wavelet of peak frequency $f_p = 1/\pi a_t$.

We remember that the analytical expression of r given by equation (12) is based on four main approximations: a constant seawater salinity S, a constant fluid density ρ, a sound velocity $v \propto T$, and the Born approximation. The first approximation is validated by in situ CTD measurements as mentioned in section 2. To discuss the last three approximations, we now compare the analytical expression of r, based on a GEF thermocline, with the seismic reflectivity computed with a direct synthetic WR [*Ker et al*., 2011], which consists in propagating seismic wavelets ψ_2 through the acoustic impedance profile γ. This synthetic WR method allows

© 2015. American Geophysical Union. All Rights Reserved.

taking into account the full polynomial expansion of the seawater sound velocity [*Millero et al.*, 1980] (with T and z but also S for general purposes) as well as the seawater density, to define the impedance profile as a function of the exact two-way travel time (Figure 3c-1). As a first observation, the global shape of γ is similar to the temperature profile (Figure 3b-1), i.e., the acoustic impedance is actually dominated by the temperature contrasts within the thermocline structure: the slight increase of γ in the top and underlying layers is due to both surrounding pressure variations with depth and residual temperatures induced by the Gauss error function model (equation (2)). A second observation deals with the synthetic WR (Figure 3c-2) which shows a cone-like structure pointing toward the center of the discontinuity in perfect agreement with the CWT analysis (Figure 3b-2): the WR of the acoustic impedance profile performed with an analyzing wavelet ψ_2 is equivalent to the CWT of the temperature profile performed with ψ_3 as expected by the equivalence expressed by equation (8). The main ridge function extracted from the WR is plotted in a *log−log* diagram where we also plot the analytical seismic reflectivity (equation (12)) of the associated GEF thermocline (Figure 3c-3, solid line and red crosses, respectively). It is obvious that both curves perfectly match, without discrepancy, showing identical asymptotic behavior at large dilations and linear decrease at small dilations.

Three main conclusions can be drawn from these quantitative results about the multiscale characterization of a thermocline morphology from seismic measurements. First, the assumptions required to consider the analytical expression of the seismic reflectivity are satisfied in the context of thermocline interfaces: the multiple scattering of seismic waves by the thermocline features and the nonlinearity of the seawater sound velocity with T and z can actually be neglected. Second, the analytical expression of the seismic reflectivity of a thermocline based on a Gauss error function shape can be used to analyze the relationship between the thermocline physical parameters and the seismic reflectivity, as discussed now in section 5. Third, we highlight that the wavelet response is an efficient multiscale method to analyze general in situ thermoclines with complex morphologies, as discussed in section 6.

5. Physical Parameters Controlling the Seismic Thermocline Detectability

The seismic reflectivity given by equation (12) can be expressed in decibel (dB) as $r^{dB}=r_0^{dB}+\Lambda^{dB}$ with:

$$r_0^{dB}=20\ \log_{10}(r_0), \tag{13}$$

$$\Lambda^{dB}=-30\ \log_{10}\left(1+\left(\frac{4}{\pi}\frac{\lambda}{\Delta z}\right)^{-2}\right). \tag{14}$$

The term r_0^{dB} corresponds to the seismic reflection coefficient of a step-like interface (equation (10)) and depends on ΔT and T_0 only, not on the seismic wavelength λ. The negative term Λ^{dB} is an attenuation factor controlled by the ratio between λ and the thermocline thickness Δz, not on the thermocline temperatures.

5.1. Large-Scale Seismic Reflectivity: $r_0^{dB}(T_0, \Delta T)$

As discussed in the previous sections, the thermocline interface is equivalent to a step-like reflector at large scales of observation, i.e., when the seismic wavelength is much larger than the thermocline thickness. In that case, the asymptotic seismic reflectivity is r_0^{dB} (equation (13)) and we now discuss its sensitivity to the top layer temperature T_0 and to the temperature contrast ΔT. To do so, we consider typical temperatures of midlatitude seasonal thermoclines, i.e., the large-scale seismic reflectivity is determined for T_0 ranging between 14°C and 20°C, and for ΔT between 1°C and 6°C (Figure 4). We observe that r_0^{dB} slightly decreases with T_0 for a given ΔT and strongly increases with ΔT for a given T_0, i.e., variations of the reflection coefficient is dominated by variations of ΔT. For example with $\Delta T=1$°C, a decrease of 1 dB only is observed between $T_0=14$ and 20°C, and an increase as high as 24 dB is observed between $\Delta T=1$ and 6°C for $T_0=14$°C. Note that similar values of r_0^{dB} can be associated to different values of $(T_0, \Delta T)$, i.e., a single measurement of the large-scale seismic reflectivity is not sufficient to isolate ΔT and T_0.

5.2. Multiscale Attenuation: $\Lambda^{dB}(\lambda, \Delta z)$

At smaller scales of observations, the seismic reflectivity decreases with the seismic frequency according to the attenuation factor Λ^{dB} (equation (14)) related to the complex morphology of the thermocline-related reflector. Actually, the relevant parameter is the ratio $\lambda/\Delta z$, as already discussed in previous works with solid

© 2015. American Geophysical Union. All Rights Reserved.

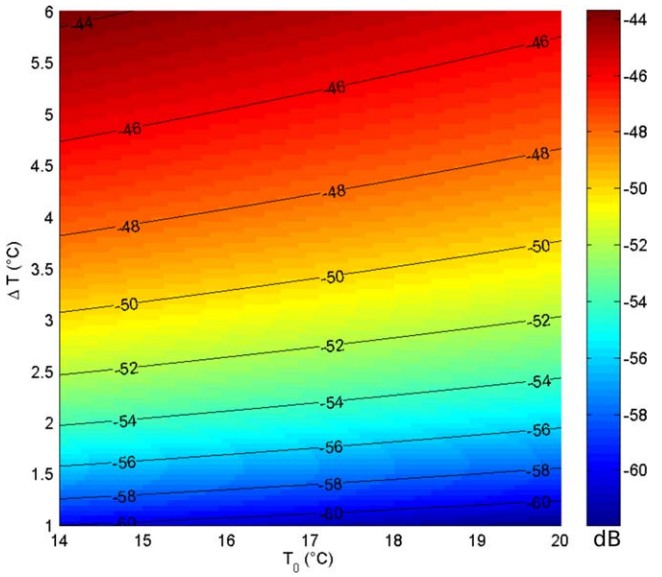

Figure 4. Large-scale reflection coefficient r_0^{dB} of an analytical GEF thermocline with a top layer temperature T_0 ranging between 14°C and 20°C and a temperature contrast ΔT between 1°C and 6°C.

Earth reflectors [*Le Gonidec et al.*, 2002; *Ker et al.*, 2012, 2014]. Thus, we determine the attenuation Λ^{dB} for typical $\lambda/\Delta z$ ranging between 0.1 up to 50 (Figure 5). As expected, the shape of the curve is equivalent to the one of the ridge function plotted as a function of a_t (Figure 3c-3), with two asymptotic behaviors: $\Lambda^{dB} \simeq 0$ dB at low frequencies where the seismic reflectivity is thus the constant large-scale reflection coefficient r_0^{dB}, and $\Lambda^{dB} \propto -60\log_{10}(\lambda/\Delta z)$ at high frequencies.

As a consequence, we can define three characteristic domains of the seismic reflectivity which depend on the nondimensional parameter $\lambda/\Delta z$. Domain I stands for the large scales of observation and is defined for $\lambda/\Delta z > 10$ where $r^{dB} = r_0^{dB}$ does not depend on the thermocline thickness. Note that this is in favor of the thermocline detectability but no information can be recovered about the multiscale structure of the thermocline. Domain III stands for the small scales of observation and is defined for $\lambda/\Delta z < 0.5$, where the seismic reflectivity strongly decreases as the cube of the seismic frequency: such very weak reflections require sensitive seismic devices and are directly related to thermocline thicknesses. Domain II, the transition zone between these two domains is defined as the mesoscales of observation where the seismic reflectivity does not depend linearly on the frequency in a *log*−*log* diagram.

5.3. Application to the Thermocline Detectability Problem

To specifically investigate the thermocline detectability problem, we perform the multiscale seismic analysis of GEF thermoclines of varying thicknesses, for which we have derived the analytical expression of the seismic reflectivity (equation (12)). The parameters of the analytical GEF thermocline are chosen to fit the IFO-SISMO thermocline (whose thickness is $\Delta z = 8.2$ m) (Figure 2), i.e., the optimized parameters are the following: a barycenter located at the water depth $z_0 = 43.7$ m, a top layer temperature $T_0 = 17.13$°C, and a temperature contrast $\Delta T = 4.47$°C. In order to study the impact of λ and Δz on the seismic reflectivity, we perform the analysis for several thicknesses ranging between 0 and 20 m and for typical seismic source peak frequencies f_p between 50 and 1000 Hz (Figure 6). Note that larger thicknesses are usually not observed for midlatitude seasonal thermoclines, lower f_p relative to z_0 have to be avoided because of interferences between the strong direct signal and the weak reflection on the thermocline (see Figure 1a), and higher frequencies usually do not insure good signal-to-noise ratio. We observe a general decreasing trend of r^{dB} with both Δz and f_p. For a given Δz, a strong variation of r^{dB} with f_p is related to a large thermocline, whereas narrow thermoclines are weakly frequency-dependent and highly reflective. Similarly, the seismic reflectivity of a wide range of thermocline thicknesses is high and nearly stable for a fixed low seismic frequency, whereas a high frequency shows a strong attenuation of the seismic reflectivity with large Δz. This highlights the seismic detectability of a thermocline: for instance, considering a sensitivity of the seismic device typically limited to -70 dB, a seismic device with $f_p = 400$ Hz is theoretically not able to detect thermoclines larger than 5 m.

6. Seismic Detection of Shallow Thermoclines in the Western Brittany Continental Shelf

The seismic multiscale analysis based on the WR approach provides a quantitative description of the seismic reflectivity associated to an analytical GEF thermocline (equation (2)). Now we extend the analysis to the

© 2015. American Geophysical Union. All Rights Reserved.

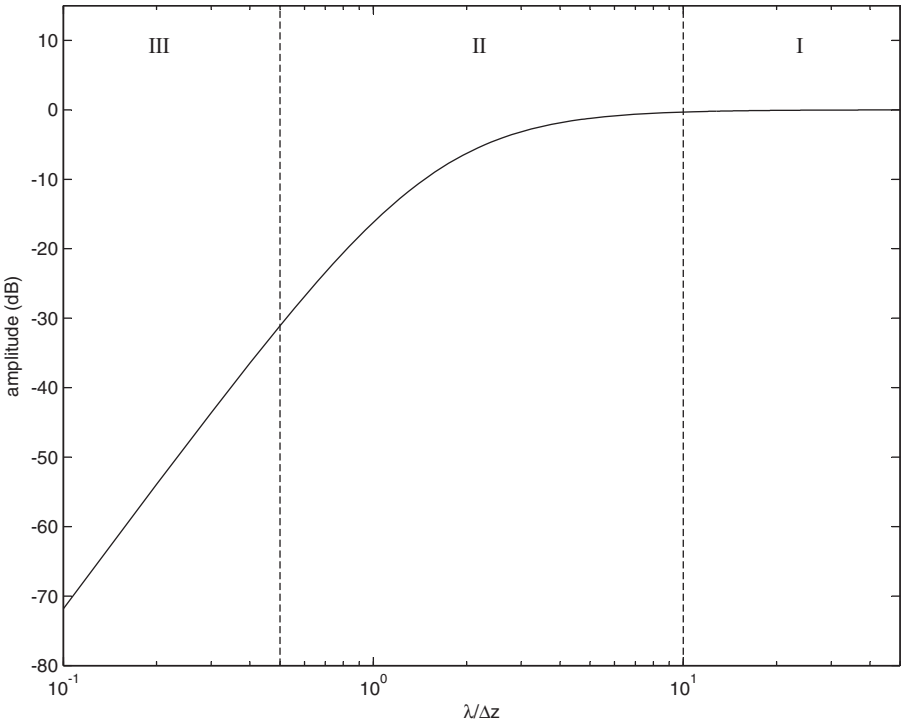

Figure 5. Multiscale attenuation Λ^{dB} as a function of the ratio between the seismic wavelength λ and the thermocline thickness Δz. Identification of three scales of observation: (I) large scales $\lambda/\Delta z > 10$, (II) mesoscales, and (III) fine scales $\lambda/\Delta z < 0.5$.

actual in situ ASPEX and IFOSISMO thermoclines, respectively, in order to better explain and discuss the seismic observations introduced in section 2.

6.1. Multiscale Analysis of the ASPEX Thermocline Observed in the Seismic Data

We consider the main physical parameters of the in situ ASPEX thermocline summarized in Table 1 to define the associated analytical GEF thermocline (Figure 7a, black and blue lines, respectively): both thermoclines are similar down to the water depth 27 m and then disagree, with a difference increasing with depth. However, the synthetic WR of the actual ASPEX thermocline displayed in Figure 7b shows a main cone-like structure pointing toward the main discontinuity, i.e., the thermocline location. Located after this dominant structure, additional weak features can be observed in the WR (see, for instance, the low-frequency content located around 60 ms) but, nevertheless, the actual thermocline looks locally equivalent to an analytical thermocline based on the Gauss error function. Accordingly, the ridge function (white dashed line) is in good agreement with the analytical seismic reflectivity r^{dB} of the associated GEF thermocline when plotted as a function of the seismic frequency (Figure 7c, black and blue lines, respectively). This

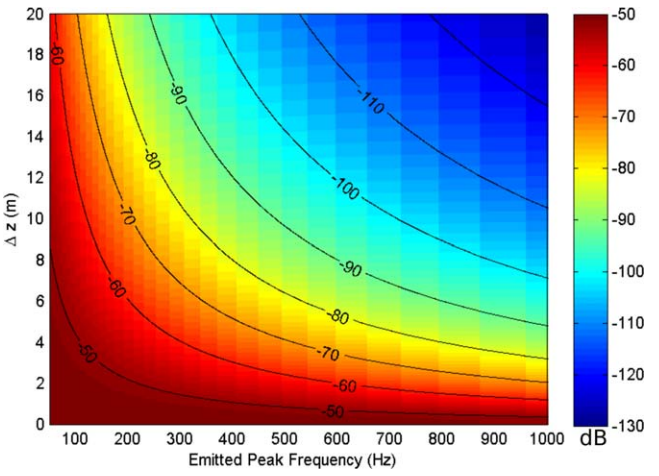

Figure 6. Seismic reflectivity r^{dB} of an analytical GEF thermocline (Gauss error function with $T_0 = 17.1°C$, $\Delta = 4.5°C$) as a function of the thermocline thickness Δz ranging between 0 and 20 m and the seismic peak frequency f_p ranging between 50 and 1000 Hz.

© 2015. American Geophysical Union. All Rights Reserved.

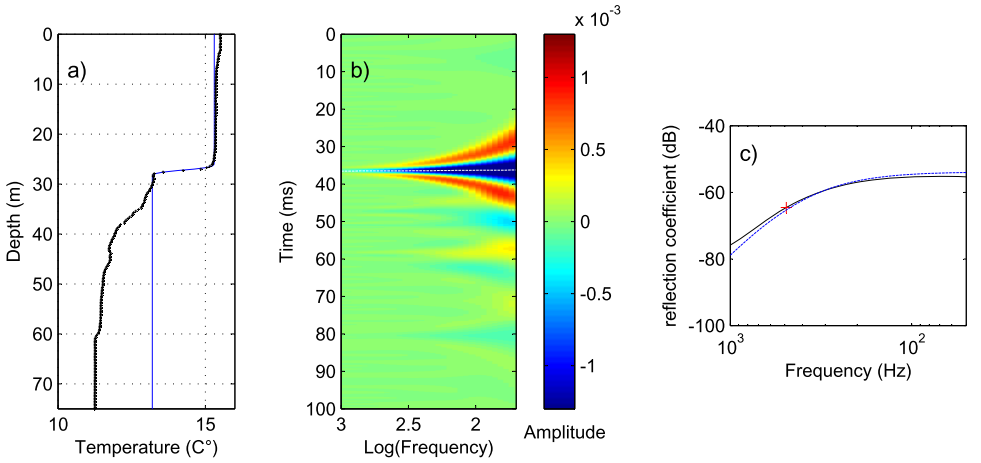

Figure 7. (a) Temperature profile of the actual thermocline measured from a CTD probe during the ASPEX cruise (black line) and associated analytical GEF thermocline (blue line). (b) Synthetic WR of the actual thermocline. (c) Seismic reflectivity of the actual thermocline extracted from the WR ridge function (black line) and analytical seismic reflectivity from the GEF thermocline (blue line). The red cross indicates the reflection coefficient at the central frequency of the ASPEX seismic device.

agreement highlights that even if the actual and GEF thermoclines do not agree at all scales of observation, the seismic reflectivity is dominated by the sharp temperature contrast of the thermocline. At low frequencies, both curves tend to an asymptotic value around −55.2 dB which corresponds to the reflection coefficient of an equivalent step-like interface. At higher frequencies, both curves similarly decrease down to −78 dB at 1000 Hz. In particular at the sparker source frequency $f_p = 500$ Hz, the reflection coefficient of the thermocline is about −64.5 dB, as predicted by the GEF thermocline. Since the ASPEX thermocline was clearly observed in the seismic data, this actual reflection coefficient is obviously above the detection limit of the seismic device, i.e., the detectability conditions were satisfied for this first seismic observation of a shallow oceanic structure. Note that in the present case characterized by a low background noise associated with good sea conditions, the detectability limit of the seismic device is thus lower than −64.5 dB.

6.2. Multiscale Analysis of the IFOSISMO Thermocline Not Observed in the Seismic Data

The plots of both the actual IFOSISMO and associated analytical GEF thermoclines are recalled in Figure 8a (black and blue lines, respectively). As already discussed in section 3.2, both curves match closely, with weak disagreements at small scales of observations. The synthetic WR of the actual thermocline is displayed in Figure 8b: a main cone-like structure points toward the center of the thermocline in accordance with the synthetic WR of the analytical GEF thermocline described in section 4.2 (Figure 3c-2). Actually, additional weak features can be observed: they are related to the fine-scale structures of the actual IFOSISMO temperature profile which are not considered in the associated GEF thermocline. The synthetic ridge function (white dashed line) is plotted as a function of the seismic frequency in Figure 8c (black line) superimposed with the analytical seismic reflectivity r^{dB} of the associated GEF thermocline (blue line). At low frequencies (<150 Hz), both curves are in good agreement, with a similar asymptotic trend, suggesting the thermocline is equivalent to a step-like interface characterized by a seismic reflection coefficient r_0^{dB} of −48.7 dB, at least. At higher frequencies, the two curves do not agree: the analytical GEF seismic reflectivity underestimates the ridge function of the IFOSISMO thermocline. This disagreement highlights that even if the actual IFOSISMO thermocline and the analytical GEF thermocline look very similar (Figure 8a), the fine-scale structures of the actual thermocline have a strong impact on the ridge function morphology, i.e., on the seismic reflectivity. In particular at the sparker source frequency $f_p = 400$ Hz, the amplitude −71.3 dB of the ridge function is 10 dB higher than the reflection coefficient predicted with a GEF thermocline. This low reflectivity of the IFOSISMO thermocline at $f_p = 400$ Hz explains the weakness of the signal reflected on the thermocline interface, a conclusion supported by the present work. But since sea conditions were not as good as in the ASPEX case, ambient noise cannot be neglected and can also contribute to the thermocline undetectability.

© 2015. American Geophysical Union. All Rights Reserved.

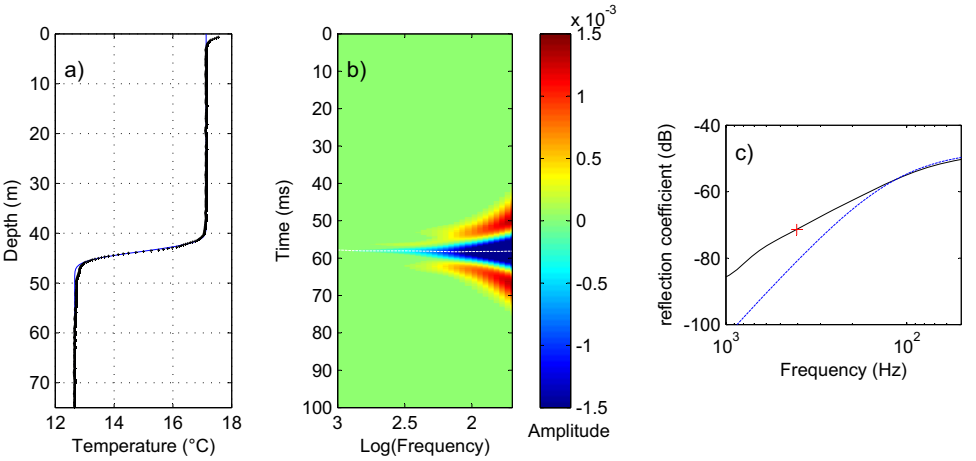

Figure 8. (a) Temperature profile of the actual thermocline measured from a CTD probe during the IFOSISMO cruise (black line) and associated analytical GEF thermocline (blue line). (b) Synthetic WR of the actual thermocline. (c) Seismic reflectivity of the actual thermocline extracted from the WR ridge function (black line) and analytical seismic reflectivity defined from the GEF thermocline (blue line). The red cross indicates the reflection coefficient at the central frequency of the IFOSISMO seismic device.

6.3. Recommendations About the Seismic Frequency

The present analysis helps to better understand why a seismic survey is able to detect a thermocline or not, as was the case for the ASPEX and IFOSISMO cruises, respectively. For the ASPEX seismic data, the acquisition conditions were optimal (see section 2.1) to detect the thermocline-related reflector, comprising a source emission level and frequency adapted to the thermocline reflective properties. For the IFOSISMO seismic data, in addition to bad sea conditions (see section 2.2) which deteriorate the signal-to-noise ratio, the thermocline reflection coefficient is two times weaker than the one of ASPEX. As a consequence, even with a higher source level which compensates for the spherical divergence of the seismic signal, the detection limit of the seismic device was not satisfied. According to the present work, the seismic source frequency appears not adapted to the thermocline morphology and explains why the thermocline-related reflector does not emerge from the noise level of the IFOSISMO seismic profile. Which recommendations about the seismic device could have been done to optimize the thermocline detection?

Taking benefits of the multiscale seismic analysis, the seismic reflectivity $r^{dB} = r_0^{dB} + \Lambda^{dB}$ of a seasonal thermocline can be determined for a wide range of seismic frequencies. At low frequencies, both the ASPEX and the IFOSISMO thermoclines are characterized by nearly similar asymptotic behaviors of the ridge functions: at large scales, r^{dB} tends to the reflection coefficient r_0^{dB} of an equivalent step-like thermocline. Note that r_0^{dB}, which mainly depends on ΔT (see section 5.1), is at least 6 dB higher for the IFOSISMO thermocline than for the ASPEX thermocline (Table 2). This suggests that low seismic frequencies are recommended to detect thermoclines, keeping in mind three main limitations: low frequencies cannot be used for superficial thermoclines because of wave interferences with the direct source signal, the lateral resolution of seismic imaging decreases at low frequencies, and last but not least, low frequencies do not inform about the thermocline morphology.

At high frequencies, r^{dB} is controlled by the ratio $\lambda/\Delta z$ following the attenuation Λ^{dB} described in section 5.2. Removing r_0^{dB} from the seismic reflectivity r^{dB}, the ridge functions of both actual thermoclines are plotted as a function of $\lambda/\Delta z$ in Figure 9 (blue diamonds and red circles, respectively). Note that considering the frequency of the seismic source signal and the thermocline thickness given in Table 1, $\lambda/\Delta z = 0.45$ for IFOSISMO and 1.25 for ASPEX, associated to an attenuation 12 dB higher for the former (Table 2). The thermocline attenuation curve (Figure 9, blue diamonds) shows a good agreement with the simple analytical model for $1 < \lambda/\Delta z < 7$: at higher frequencies, a disagreement is explained by the fine-scale features of the thermocline. This highlights the strong sensitivity of the seismic reflectivity with the seismic wavelength relative to the thermocline thickness, explaining the weak seismic signals reflected by the IFOSISMO thermocline. High frequencies inform about the thermocline morphology, but the associated attenuation might make the thermocline undetectable by the seismic measurements. If we consider the ASPEX seismic

© 2015. American Geophysical Union. All Rights Reserved.

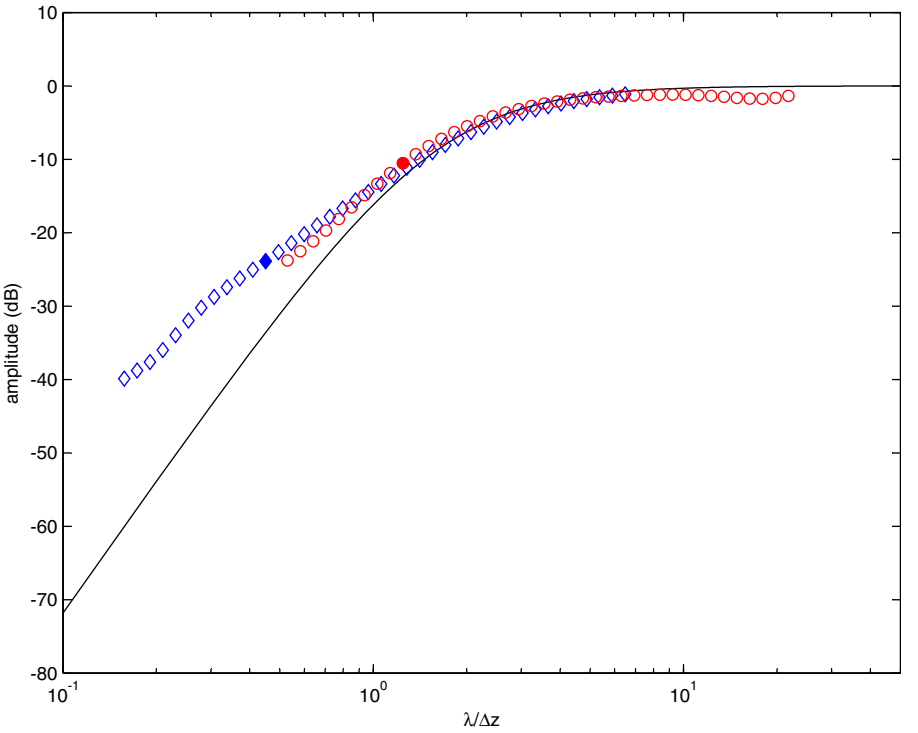

Figure 9. Seismic reflectivity as a function of the ratio between the seismic wavelength λ and the thermocline thickness Δz for the actual thermoclines of IFOSISMO (blue diamonds) and ASPEX (red circles) cruises. Note that the large-scale seismic reflectivity value has been removed. Filled symbols correspond to the ratio associated to the seismic source central frequency for both cruises. The solid line shows the multiscale attenuation Λ^{dB} of the analytical result of the GEF thermocline (equivalent to Figure 3).

reflectivity as a reference for a thermocline detectability, a seismic frequency around 180 Hz would have been in favor of the seismic observation of the IFOSISMO thermocline, i.e., the selected frequency $f_p = 400$ Hz was far too high. Note that when talking about thermocline detectability, the ambient noise level is superimposed to the weakness of the reflector described in the present paper and contributes to a poor signal-to-noise ratio.

7. Concluding Remarks

The multiscale seismic analysis based on the WR approach is an effective tool to assess the frequency-dependent reflection coefficient of shallow seasonal thermoclines. Considering a simple model of a thermocline based on both a Gauss error function and a linear relation between the sound velocity and temperature in the water column, we derive an analytical expression of the seismic reflectivity which consists in two terms: an asymptotic value at low frequencies, where the seismic reflectivity is maximum, constant, and controlled by the temperature parameters, and a frequency-dependent attenuation factor controlled by the ratio between the seismic source wavelength and the size of the thermocline.

This work allows us quantifying the influence of the thermocline morphology on the seismic reflection coefficient, i.e., a better understanding of the interaction between a seismic wave and a thermocline-like reflector. But an additional effect controls the detectability of weak reflectors: indeed, ambient noise including sea conditions limits the signal-to-noise ratio and thus the thermocline detection. To overcome this limitation, a first attempt is to increase the fold of the stacking or/and the seismic source level according to the ambient noise level mainly controlled by the wind speed [*Wenz*, 1962]. Finally, we are able to make some recommendations about seismic devices designed for seasonal thermocline detection, including

Table 2. Parameters of the Seismic Reflectivity Associated to the ASPEX and IFOSISMO Thermoclines

	r^{dB} (dB)	r_0^{dB} (dB)	Λ^{dB} (dB)	$\lambda/\Delta z$
ASPEX	−64.5	−55.2	−9.3	1.25
IFOSISMO	−71.3	−48.7	−22.6	0.45

© 2015. American Geophysical Union. All Rights Reserved.

seismic source frequency, and the present work should contribute to a better knowledge of the spatial distribution and circulation of water masses in the ocean.

Acknowledgments
It is a pleasure to thank the captains and crews of R/V Gwen Drez and R/V Côte de la Manche, who made the data collection possible. The authors thank B. Marsset for the acquisition of IFOSISMO and ASPEX seismic data sets. We also thank C. Ménesguen for constructive discussions. Please note that CTD and seismic data used in this article still belong exclusively to IFREMER and are not available at the present time.

References

Alexandrescu, M., D. Gibert, G. Hulot, J.-L. L. Mouël, and G. Saracco (1995), Detection of geomagnetic jerks using wavelet analysis, *J. Geophys. Res.*, *100*, 12,557–12,572.
Biescas, B., V. Sallarès, J.-L. Pelegrí, F. Machín, R. Carbonell, G. Buffett, J.-J. D. Nobeitia, and A. Calahorrano (2008), Imaging meddy finestructure using multichannel seismic reflection data, *Geophys. Res. Lett.*, *35*, L11609, doi:10.1029/2008GL033971.
Biescas, B., L. Armi, V. Sallarès, and E. Gràcia (2010), Seismic imaging of staircase layers below the Mediterranean Undercurrent, *Deep Sea Res., Part I*, *57*, 1345–1353.
Brown, J., K. Brander, L. Fernand, and A. E. Hill (1996), Scanfish: High performance towed undulator, *Sea Technol.*, *37*, 23–27.
Carniel, S., A. Bergamasco, J. W. Book, R. W. Hobbs, M. Sclavo, and W. T. Wood (2012), Tracking bottom waters in the Southern Adriatic Sea applying seismic oceanography techniques, *Cont. Shelf Res.*, *44*, 30–38.
Crank, J. (1980), *The Mathematics of Diffusion*, Oxford Univ. Press. Oxford, U. K.
Fer, I., P. Nandi, W. Holbrook, R. Schmitt, and P. Pàramo (2010), Seismic imaging of a thermohaline staircase in the western tropical North Atlantic, *Ocean Sci.*, *6*, 621–631.
Goupillaud, P. (1961), An approach to inverse filtering of near-surface layer effects from seismic records, *Geophysics*, *26*, 754–760.
Grant, A. L. M., and S. E. Belcher (2011), Wind-driven mixing below the oceanic mixed layer, *J. Phys. Oceanogr.*, *41*, 1556–1575.
Gray, S. H., and N. Bleistein (1986), Imaging and inversion of zero-offset seismic data, *Proc. IEEE*, *74*, 440–456.
Hobbs, R. W., D. Klaeschen, V. Sallarès, E. Vsemirnova, and C. Papenberg (2009), Effect of seismic source bandwidth on reflection sections to image water structure, *Geophys. Res. Lett.*, *36*, L00D08, doi:10.1029/2009GL040215.
Holbrook, W. S., and I. Fer (2005), Ocean internal wave spectra inferred from seismic reflection transects, *Geophys. Res. Lett.*, *32*, L15604, doi:10.1029/2005GL023733.
Holbrook, W. S., P. Pàramo, S. Pearse, and R. Schmitt (2003), Thermohaline fine structure in an oceanographic front from seismic reflection profiling, *Science*, *301*, 821–824.
Holbrook, W. S., I. Fer, and R. Schmitt (2009), Images of internal tides near the Norwegian continental slope, *Geophys. Res. Lett.*, *36*, L00D10, doi:10.1029/2009GL038909.
Holschneider, M. (1995), *Wavelets: An Analysis Tool*, Clarendon, Oxford, U. K.
Johnston, T. M. S., and D. L. Rudnick (2009), Observations of the transition layer, *J. Phys. Oceanogr*, *39*, 780–797.
Ker, S., Y. Le Gonidec, D. Gibert, and B. Marsset (2011), Multiscale seismic attributes: A wavelet-based method and its application to high-resolution seismic and ground truth data, *Geophys. J. Int.*, *187*, 1038–1054.
Ker, S., Y. Le Gonidec, and D. Gibert (2012), Multiscale seismic attributes: Source-corrected wavelet response and its application to high-resolution seismic data, *Geophys. J. Int.*, *190*, 1746–1760.
Ker, S., Y. Le Gonidec, B. Marsset, G. Westbrook, D. Gibert, and T. A. Minshull (2014), Fine-scale gas distribution in marine sediments assessed from deep-towed seismic data, *Geophys. J. Int.*, *196*, 1466–1470.
Lavery, A., D. Chu, and J. N. Moum (2010), Observations of broadband acoustic backscattering from nonlinear internal waves: Assessing the contribution from microstructure, *IEEE J. Oceanic Eng.*, *35*(4), 695–709.
Le Boyer, A., G. Cambon, N. Daniault, S. Herbette, B. L. Cann, L. Marié, and P. Morin (2009), Observations of the Ushant tidal front in September 2007, *Cont. Shelf Res.*, *29*, 1026–1037.
Le Gonidec, Y., and D. Gibert (2007), Multiscale analysis of waves reflected by granular media: Acoustic experiments on glass beads and effective medium theories, *J. Geophys. Res.*, *112*, B05103, doi:10.1029/2006JB004518.
Le Gonidec, Y., D. Gibert, and J.-N. Proust (2002), Multiscale analysis of waves reflected by complex interfaces: Basic principles and experiments, *J. Geophys. Res.*, *107*(B9), 2184, doi:10.1029/2001JB000558.
Mallat, S. (1998), *A Wavelet Tour of Signal Processing*, 2nd ed., Academic, Burlington, Vermont.
Mallat, S., and W. L. Hwang (1992), Singularity detection and processing with wavelets, *IEEE Trans. Inf. Theory*, *38*, 617–643.
Ménesguen, C., B. Hua, X. Carton, F. Klingelhoefer, P. Schnurle, and C. Reichert (2012), Arms winding around a meddy seen in seismic reflection data close to the Morocco coastline, *Geophys. Res. Lett.*, *39*, L05604, doi:10.1029/2011GL050798.
Millero, F. J., C. Chen, A. Bradshaw, and K. Schleicher (1980), A new high pressure equation of state for seawater, *Deep Sea Res., Part A*, *27*, 255–264.
Mirshak, R., M. R. Nedimovic, B. J. W. Greenan, B. Ruddick, and K. Louden (2010), Coincident reflection images of the gulf stream from seismic and hydrographic data, *Geophys. Res. Lett.*, *37*, L05602, doi:10.1029/2009GL042359.
Moum, J. N., M. C. Gregg, R. C. Lien, and M. E. Carr (1995), Comparison of turbulence kinetic energy dissipation rate estimates from two ocean microstructure profilers, *J. Atmos. Oceanic Technol.*, *12*, 346–366.
Moum, J. N., D. M. Farmer, W. D. Smyth, L. Armi, and S. Vagle (2003), Structure and generation of turbulence at interfaces strained by internal solitary waves propagating shoreward over the continental shelf, *J. Phys. Oceanogr.*, *33*, 2093–2112.
Phillips, J. D., and D. Dean (1991), Multichannel acoustic reflection profiling of ocean watermass temperature/salinity interfaces, in *Ocean Variability and Acoustic Propagation*, edited by J. Potter and A. Warn-Varnas, pp. 199–214, Kluwer Acad., Dordrecht, Netherlands.
Piété, H., L. Marié, B. Marsset, Y. Thomas, and M.-A. Gutscher (2013), Seismic reflection imaging of shallow oceanographic structures, *J. Geophys. Res. Oceans*, *118*, 2329–2344, doi:10.1002/jgrc.20156.
Ruddick, B., H. B. Song, C. Z. Dong, and L. Pinheiro (2009), Water column seismic images as maps of temperature gradient, *Oceanography*, *22*, 192–205.
Sallarès, V., B. Biescas, G. Buffett, R. Carbonell, J. J. Dañobeitia, and J. L. Pelegrí (2009), Relative contribution of temperature and salinity to ocean acoustic reflectivity, *Geophys. Res. Lett.*, *36*, L00D06, doi:10.1029/2009GL040187.
Soloviev, A. V., N. V. Vershinsky, and V. A. Bezverchnii (1988), Small-scale turbulence measurements in the thin surface layer of the ocean, *Deep Sea Res., Part A*, *35*(N12A), 1859–1874.
Thomas, Y., B. Marsset, L. Marié, S. Ker, and H. Piété (2013), Compte rendu de mission: Mission ifosismo, n/o le côtes de la manche 20–23 septembre 2012. Adéquation de la source sismique sparker à l'imagerie de la thermocline en mer d'iroise, technical report, PDG/REM/GM/EIS-08022013-01, IFREMER, Brest.
Wenz, G. M. (1962), Acoustic ambient noise in the Ocean: Spectra and sources, *J. Acoust. Soc. Am.*, *34*(12), 1936–1956.
Yilmaz, O. (1987), *Seismic Data Processing*, Soc. of Explor. Geophys., Tulsa, Okla.

© 2015. American Geophysical Union. All Rights Reserved.

GEOPHYSICS, VOL. 83, NO. 2 (MARCH-APRIL 2018); P. V61–V71, 9 FIGS.
10.1190/GEO2017-0527.1

Check for updates

Downloaded 12/31/17 to 134.246.166.26. Redistribution subject to SEG license or copyright; see Terms of Use at http://library.seg.org/

Fractional integration of seismic wavelets in anelastic media to recover multiscale properties of impedance discontinuities

Stephan Ker[1] and Yves Le Gonidec[2]

ABSTRACT

Multiscale seismic attributes based on wavelet transform properties have recently been introduced and successfully applied to identify the geometry of a complex seismic reflector in an elastic medium. We extend this quantitative approach to anelastic media where intrinsic attenuation modifies the seismic attributes and thus requires a specific processing to retrieve them properly. The method assumes an attenuation linearly dependent with the seismic wave frequency and a seismic source wavelet approximated with a Gaussian derivative function (GDF). We highlight a quasi-conservation of the Gaussian character of the wavelet during its propagation. We found that this shape can be accurately modeled by a GDF characterized by a fractional integration and a frequency shift of the seismic source, and we establish the relationship between these wavelet parameters and Q. Based on this seismic wavelet modeling, we design a time-varying shaping filter that enables making constant the shape of the wavelet allowing retrieval of the wavelet transform properties. Introduced with a homogeneous step-like reflector, the method is first applied on a thin-bed reflector and then on a more realistic synthetic data set based on an in situ acoustic impedance sequence and a high-resolution seismic source. The results clearly highlight the efficiency of the method in accurately restoring the multiscale seismic attributes of complex seismic reflectors in anelastic media by the use of broadband seismic sources.

INTRODUCTION

In the framework of seismic analysis aiming at quantifying physical properties of seismic reflectors, recent methodologies have been developed using multiscale decomposition of seismic traces (Castagna et al., 2003), in particular, based on multifrequency wavelet analyses (Ker et al., 2013). The interest and scientific issue of such developments have been motivated by a significant increase of the seismic data frequency bandwidth related to recent improvements in seismic acquisition: broadband seismic acquisition (Soubaras and Dowle, 2010) and source design (Marsset et al., 2010) now allow assessing seismic information over several octaves, a prerequisite when imaging complex seismic structures. The potential of multifrequency quantitative characterization of various kinds of seismic reflectors has been extensively demonstrated, including subsurface thin beds (Ker et al., 2011), gas-charged layers (Ker et al., 2014), and more recently thermocline-related oceanographic structures (Ker et al., 2015). The method is the so-called wavelet response (WR) introduced by Le Gonidec et al. (2002) that considers wavelet propagation as a natural extension of continuous wavelet transform (CWT) signal processing. In the WR method, the seismic sources consist of wavelet signals that are dilated versions of a common analyzing wavelet defined in the theoretical framework of the CWT: This wavelet family is used to probe the medium to perform a multiscale analysis of its acoustic impedance profile. Assuming the validity of the Born approximation, the seismic WR method is equivalent to computing the CWT of the in situ impedance profile (Le Gonidec et al., 2002). In particular, this allowed (1) extending the use of the CWT ridge functions as new multiscale seismic attributes (Ker et al., 2011), (2) providing an original processing sequence to correct the WR from the seismic source signature (Ker et al., 2012), and (3) merging seismic sources in the wavelet domain to improve seismic resolution capability (Ker et al., 2013).

But, the capacity of the WR in characterizing reflector geometry could be altered. For instance, Le Gonidec and Gibert (2006) highlight the impact of viscoelastic properties in the ridge function associated to a complex reflector. A similar effect is observed by Ker et al. (2014) with the WR associated to a half-space gas-charged medium. This suggests that the WR can be strongly affected by

Manuscript received by the Editor 9 August 2017; revised manuscript received 28 September 2017; published ahead of production 11 November 2017; published online 26 December 2017.
[1]IFREMER, Géosciences Marines, Plouzané, France. E-mail: stephan.ker@ifremer.fr.
[2]Université Rennes 1, Géosciences Rennes, Rennes Cedex, France. E-mail: yves.legonidec@univ-rennes1.fr.
© 2018 Society of Exploration Geophysicists. All rights reserved.

Downloaded 12/31/17 to 134.246.166.26. Redistribution subject to SEG license or copyright; see Terms of Use at http://library.seg.org/

seismic attenuation, a physical phenomenon that may affect seismic waves during their propagation and constitutes two main research topics. The first topic deals with attenuation as a quantitative parameter, i.e., the so-called quality factor Q, related to the physical properties of the medium, for instance, in seismology and in exploration seismology, in which attenuation can be related to fault density (Worthington and Hudson, 2000) or gas saturation (Morgan et al., 2012). The second topic deals with the impact of attenuation on the resolution of seismic images, i.e., so-called Q inverse filtering, which aims at correcting this effect to improve imaging of oil and gas reservoirs (Wang, 2008). To better address these issues, seismic attenuation mechanisms have to be identified, with a distinction between extrinsic and intrinsic phenomena. The former refers to attenuation generated by geometric spreading of the seismic wave and to scattering effects related to the presence of heterogeneities in the medium. The latter is related to the viscoelastic properties of the medium, in which the elastic energy of a seismic wave is gradually converted into heat and then dissipated (Toksöz and Johnston, 1981). This attenuation is inversely proportional to the quality factor Q defined as the wave energy divided by the energy loss per cycle. Seismic attenuation is a frequency-dependent phenomenon, and its effect during wave propagation is to modify the amplitude and the shape of the seismic waveform, related to dispersion (frequency-dependent wave velocity). As a consequence, anelasticity may make the WR different from the CWT of the acoustic impedance properties, preventing the use of ridge functions as accurate attributes to assess the geometry of seismic reflectors. The present paper deals with extended developments of the WR method to the case of anelastic media for which we establish an original framework to analyze seismic reflectors by the use of broadband seismic sources.

After a brief overview of the WR method established for elastic media, we introduce the modification of the WR when dealing with anelastic media characterized by an attenuation factor and a dispersive phase velocity. We consider seismic source wavelets defined as Gaussian derivative functions (GDFs), commonly used in seismic analysis. We show that the Gaussian character of such sources is preserved by integration during propagation in a Kolsky-Futterman (K-F) attenuating medium (Kolsky, 1956; Futterman, 1962). A description of a K-F medium, characterized by a linear dependency of the attenuation with the seismic frequency, is provided in this paper to briefly recall the key properties of such an anelastic medium. By introducing a dimensionless parameter, it is possible to establish the expression of the quality factor Q of the anelastic medium as a function of the GDF properties. Then, we consider a seismic propagation medium characterized by a Q factor constant with depth and an acoustic reflectivity sequence defined by either step-like or thin-bed discontinuities, and we illustrate how attenuation affects the WR analysis. Finally, we take advantage of the quasi-conservation of the Gaussian character of a GDF to design a time-varying shaping filter, an original approach used to compensate the WR for attenuation effects. We illustrate the approach on a synthetic data set involving an in situ acoustic reflectivity sequence embedded in an anelastic medium and a broadband seismic source signature.

WAVELET RESPONSE OF AN ANELASTIC MEDIUM

The WR is a multiscale seismic probing of a medium based on the properties of the wavelet transform (Le Gonidec et al., 2002). Instead of using a single seismic source, the WR method uses a family of source wavelets that are dilated or contracted versions of the same signal called the mother analyzing wavelet ψ. The WR is thus a collection of seismic traces obtained by a set of seismic sources forming a wavelet family that enables a time-scale decomposition of the acoustic impedance p of the medium. The expression of the WR related to a plane-wave propagation in 1D medium is given by

$$R[\psi, p](t, a) = \mathcal{D}_a \psi(t) * r(t), \tag{1}$$

where $*$ stands for the convolution operator, $r(t)$ is the reflectivity sequence in the time domain, and $\mathcal{D}_a$ is the dilation operator controlled by the dilation a that enables to contract or dilate the mother wavelet $\psi(t)$ according to $\mathcal{D}_a\psi(t) = (1/a)\psi(t/a)$. When dealing with one element of this wavelet family, we will consider the reference wavelet $\psi(t)$ for the sake of simplicity. The function R is the wavelet transform of the reflectivity $r(t)$, and Le Gonidec et al. (2002) show that it is strictly equivalent to the wavelet transform of p performed in the traveltime domain t when the Born approximation is valid. The mother wavelet $\psi(t)$ has to satisfy some necessary conditions, i.e., an oscillating differentiable function with compact support and zero-mean value (Mallat, 1998). In the present work, $\psi(t)$ is a GDF, such as the Ricker wavelet commonly used in seismic imaging and discussed in the next section. The potential of GDF properties has been used by Ker et al. (2012) to design a multiscale processing of high-resolution seismic data, and it is now extended to study the propagation of multiscale seismic waves in anelastic media.

In an elastic homogeneous medium, the shape of a wavelet source signal $\psi(t)$ generated by a seismic emitter remains unchanged and the wavelet conserves the same features during its propagation at depth z, where the seismic wave is $\phi_0(z, t) \equiv \psi(t)$. When the medium is anelastic, the seismic wave experiences some changes, including amplitude decrease, dispersion, and phase rotation. As a consequence, the seismic wavelet becomes a time-depth-varying wave defined as

$$\phi(z, t) = \frac{1}{2\pi} \int_{-\infty}^{\infty} \hat{\psi}(\omega) \hat{u}(z, \omega, t) d\omega, \tag{2}$$

where $\hat{\psi}(\omega)$ is the Fourier transform of $\psi(t)$ and ω is the angular frequency. The term $\hat{u}(z, \omega, t)$ is the Fourier transform of the displacement or the pressure (i.e., the waveform) which can be, in the framework of plane-wave propagation in 1D anelastic media, expressed as

$$\hat{u}(z, \omega, t) = \exp(-\beta z) \exp\left[i\omega \left(t - \frac{z}{\gamma} \right) \right], \tag{3}$$

where β is the attenuation of the wave amplitude and γ is the phase velocity, which describes the velocity dispersion and the phase rotation of the wave. The WR is thus modified and, noted $\tilde{R}$, it can be described as a nonstationary process (Margrave, 1998), which can be expressed, based on the superposition principle, as

$$\tilde{R}[\psi, p](t, a) = \int_0^{\infty} \mathcal{D}_a \phi(z, t) r(z) dz. \tag{4}$$

In the following, $\phi(z, t)$ is noted $\phi_\tau(t)$, where τ stands for the time of propagation in the anelastic medium, and we are reminded that $\phi_0(t)$ corresponds to the elastic case.

Downloaded 12/31/17 to 134.246.166.26. Redistribution subject to SEG license or copyright; see Terms of Use at http://library.seg.org/

As a result, attenuation effects preclude the use of the properties of the WR to study acoustic impedance discontinuities from multiscale seismic attributes. The aim of the present paper is to develop a method to recover reliable properties of multiscale seismic attributes allowing quantitative description of the geometry of reflectors. The approach is based on few assumptions described below.

QUASI-CONSERVATION OF THE GAUSSIAN CHARACTER OF A SEISMIC WAVELET IN ANELASTIC MEDIA

Kolsky-Futterman anelastic medium

A first assumption deals with the modeling of the anelastic propagation medium. In numerous attenuation models, the attenuation parameter β introduced in equation 3 may be expressed as a power law of the frequency $\beta \propto \omega^{\delta}$ (Wang, 2008). In particular, $\delta = 1$ corresponds to the Kolsky-Futterman model, which describes a linear frequency dependency (Kolsky, 1956; Futterman, 1962). This model is intensively used for attenuation analysis (Xintao et al., 2014) or designing an inverse Q filter (Wang, 2008) because it has a high degree of similarity to several Q models (Ursin and Toverud, 2002; Wang, 2008). In the K-F model, the attenuation β and phase velocity γ are defined by

$$\beta = \frac{\omega}{2cQ}, \tag{5a}$$

$$\frac{1}{\gamma} = \frac{1}{c}\left(1 - \frac{1}{\pi Q}\ln\frac{\omega}{\omega_h}\right), \tag{5b}$$

where c is the reference phase velocity and ω_h is a tuning parameter corresponding to the highest possible seismic frequency and ensuring compliance with the Kramers-Kröning dispersion relation (Wang and Guo, 2004).

When Q tends to infinity, the attenuation β tends to zero and the phase velocity γ tends to the reference velocity; i.e., the medium is equivalent to an elastic medium: This is the reference case used in the present work. In the following, a value of $Q = 50$ is selected for numerical simulation purposes.

Gaussian derivative seismic source signal

A second assumption is to assimilate a seismic source signal with a wavelet defined as a GDF, i.e., a derivative of order α of a Gaussian function (Ker et al., 2012). This assumption is commonly used in seismic analysis: The first ($\alpha = 1$) and second ($\alpha = 2$) derivatives of a Gaussian function correspond to the wavelet erroneously called minimum-phase Ricker (Hosken, 1988) used in seismic modeling, for instance, and to the so-called Ricker wavelet (Ricker, 1953), respectively. This second wavelet is a symmetric wavelet widely used to model seismic source signals in seismic imaging, attenuation estimation, and Q inverse filtering (Wang, 2008, 2015a). Higher derivative orders α are used in acoustic logging to model sources with a high number of cycles (Heigl, 2007); we note that fractional derivative orders, which correspond to asymmetric GDF, have been recently used to better represent seismic signals, such as vertical seismic profile (VSP) data waveforms (Wang, 2015b) or to process large frequency bandwidth seismic data (Ker et al., 2013).

The general expression of a reference wavelet ψ defined by a GDF to model a seismic source signal in the time domain is given by

$$\psi(t) = \Omega\frac{d^{\alpha}}{dt^{\alpha}}\exp\left(-\frac{\omega_0^2 t^2}{4}\right). \tag{6}$$

The parameter Ω is the amplitude, the derivative order α can either be an integer or be fractional, and the angular frequency ω_0 is the reciprocal of the reference dilation defined by $a_0 = 2/\omega_0$. Note that a GDF can be written as the product of a Hermite polynomial and a Gaussian potential (Heigl, 2007; Ker et al., 2012); i.e., the amplitude spectrum $\hat{\psi}$ of the GDF ψ is always derived from the Gaussian function and is expressed in the frequency domain by (Wang, 2015b)

$$\hat{\psi}(\omega) = \Omega\frac{\omega^{\alpha}}{\omega_0^{\alpha}}\exp\left(-\frac{\omega^2}{\omega_0^2}\right). \tag{7}$$

In seismic analysis, a seismic wavelet is commonly characterized by its peak frequency f_p, which is the frequency associated with the maximum of the amplitude spectrum; i.e., $f_p = \omega_p/2\pi$, where the peak angular frequency ω_p is defined by $(\partial\hat{\psi}/\partial\omega)|_{\omega_p} = 0$. For a GDF wavelet, $\omega_p = \omega_0\sqrt{\alpha/2}$ (Ker et al., 2012; Wang, 2015b), which means that f_p depends on the derivative order α and the natural angular frequency ω_0. In the following, α and f_p will be the quantified wavelet parameters.

Attenuated wavelet modeled by a GDF

In this section, we consider a Ricker seismic source, a GDF wavelet ψ defined by a derivative order $\alpha = 2$ and a peak frequency $f_p = 180$ Hz typical of a small airgun source (Piété et al., 2013). We model the attenuated wavelet signal $\phi_\tau(t)$ according to equation 2, based on the K-F model with $Q = 50$ and measured at different times of propagation $\tau = [0; 25; 50; 75; 100]$ ms, where $\tau = 0$ s corresponds to $\phi_0(t) = \psi(t)$. The results, plotted in solid red lines in the time domain (Figure 1a1–1a5) and in the frequency domain (Figure 1b1–1b5), clearly highlight the dispersive character of the seismic wave during its propagation in an anelastic medium; the wavelet symmetry is broken and the frequency content is shifted to lower frequencies, which means that there is no conservation of α and f_p when a seismic signal propagates in an anelastic medium. Note that recently, Wang (2015b) observes a similar behavior on VSP data and suggests attenuation as a plausible mechanism, without exploring the possible relationship with the wavelet-shape parameters.

The decrease of α and f_p with τ suggests that the attenuated wavelet signal $\phi_\tau(t)$ may be an integrated version of the wavelet $\psi(t)$: This means that we may approximate $\phi_\tau(t)$ with an equivalent GDF wavelet $\phi'_\tau(t)$ defined by a derivative order α', a natural angular frequency ω'_0 associated with a peak frequency f'_p, and an amplitude Ω'. This approach is expressed by assuming

$$\phi_\tau(t) \sim \phi'_\tau(t) = \Omega'\frac{d^{\alpha'}}{dt^{\alpha'}}\exp\left(-\frac{1}{4}\omega_0'^2 t^2\right). \tag{8}$$

To evaluate this assumption, we apply the method developed by Wang (2015b) to determine the $\phi'_\tau(t)$ parameters from the centroid frequency ω_m and the standard deviation ω_σ evaluated from the power spectrum of $\phi_\tau(t)$

$$\left(\frac{1}{2\alpha'}+1\right)\left(\frac{\Gamma(\alpha'+1/2)}{\sqrt{\alpha'}\Gamma(\alpha')}\right)^2=\frac{\omega_\sigma^2}{\omega_m^2}, \tag{9a}$$

$$\omega_0'=2\sqrt{\frac{\omega_m^2+\omega_\sigma^2}{1+2\alpha'}}, \tag{9b}$$

where Γ is the gamma function (Abramowitz and Stegun, 1972). For each $\phi_\tau(t)$ seismic wavelet plotted in solid red lines in Figure 1, we determine the associated GDF approximation $\phi'_\tau(t)$ according to this method: The results, plotted in dashed black lines in Figure 1, show a very good agreement between $\phi_\tau(t)$ and $\phi'_\tau(t)$.

Because the derivative order α is a key parameter to model the shape of seismic source signatures (Heigl, 2007; Wang, 2015b) and to analyze complex discontinuities (Le Gonidec et al., 2002), it is of critical importance to evaluate the accuracy of the GDF approximation as a function of α. We study how different GDF wavelet sources $\psi(t)$ with a similar peak frequency $f_p = 180$ Hz, but different integer derivative orders $\alpha = [1;2;3;4;5]$ (Figure 2a1–2a5, solid black curves) are modified after a propagation of $\tau = 100$ ms, corresponding to a depth of 150 m for a sound velocity of 1500 m/s. We model the nonattenuated wavelet $\phi_0(t)$, which is equivalent to $\psi(t)$ and used as a reference; the attenuated wavelet signal $\phi_\tau(t)$ according to equation 2; and the approximated attenuated wavelet signal $\phi'_\tau(t)$ defined as a GDF with the parameters given in equation 9a and 9b. The results are plotted in the time domain in Figure 2b1–2b5 and in the frequency domain in Figure 2c1–2c5: The normalized solid black, dashed black, and solid red curves correspond to $\phi_0(t)$, $\phi_\tau(t)$, and $\phi'_\tau(t)$, respectively.

As a key result, we show that a GDF seismic wavelet affected by a K-F attenuation model is an attenuated wavelet signal, which can be modeled by a specifically designed GDF $\phi'_\tau(t)$. The quasi-conservation of the Gaussian character means that attenuation effects can be approximated by a filter $F_\tau(t)$, which has Lévy alpha-stable properties (Ker et al., 2012) according to

$$\phi'_\tau(t)=\psi(t)*F_\tau(t), \tag{10}$$

where the wavelet source $\psi(t)$ depends on the parameters (Ω, α, ω_0) according to equation 6 and the filter $F_\tau(t)$ depends on the anelastic medium quality factor Q and is function of the time of propagation τ. The attenuated GDF wavelet $\phi'_\tau(t)$ depends on the parameters (Ω', α', ω'_0), and the aim of the next section is to establish the explicit relationship between the physical parameter Q, the propagation time τ, and the wavelet parameters ω_0, α, ω'_0, and α'.

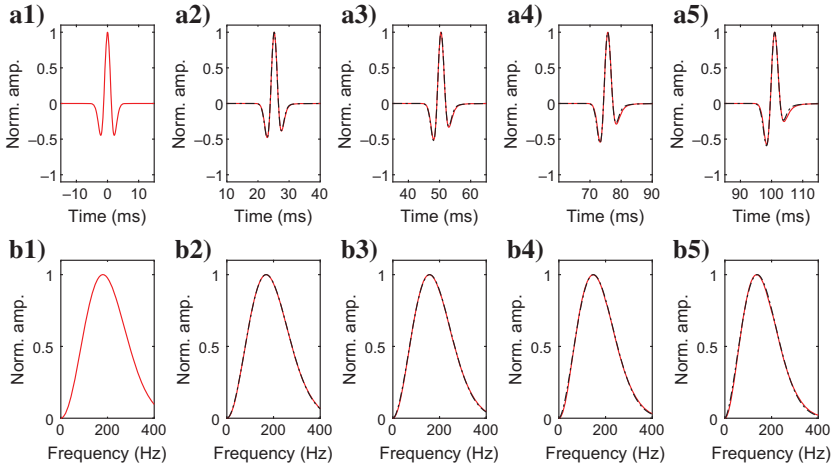

Figure 1. Normalized attenuated seismic wavelets $\phi_\tau(t)$, associated to a Ricker seismic source (GDF derivative order $\alpha = 2$ and peak frequency $f_p = 180$ Hz), based on the Kolsky-Futterman model with $Q = 50$ and for $\tau = [0;25;50;75;100]$ ms, respectively (solid red lines) and associated GDF models $\phi'_\tau(t)$ (dashed black line): representation in the time domain (a1-a5) and in the frequency domain (b1-b5).

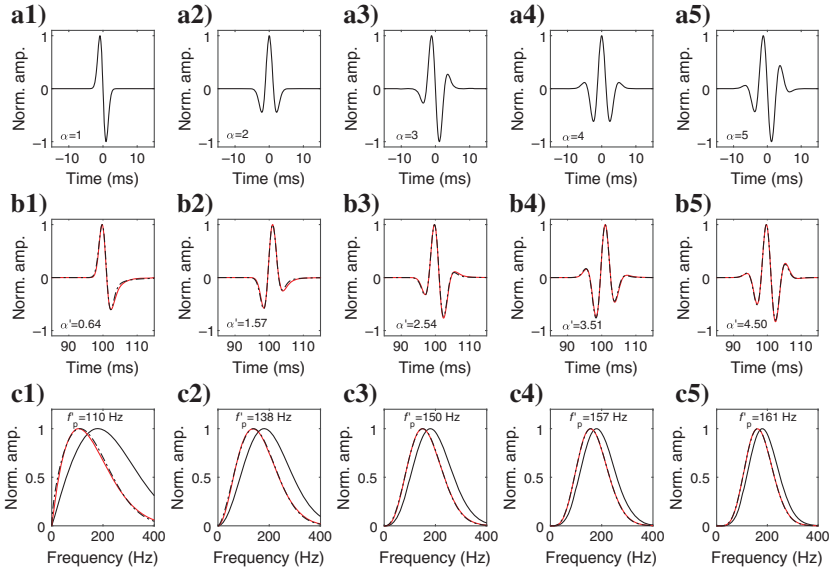

Figure 2. (a1-a5) Normalized GDF wavelet sources $\psi(t)$ associated to derivative orders $\alpha = [1;2;3;4;5]$ and peak frequency $f_p = 180$ Hz, respectively. (b1-b5) Normalized attenuated seismic wavelets $\phi_\tau(t)$ based on the Kolsky-Futterman model with $Q = 50$ and $\tau = 100$ ms (solid red curves) and associated GDF models $\phi'_\tau(t)$ (dashed black curves) in the time domain, and (c1-c5) in the frequency domain, in which the normalized solid black curve correspond to the nonattenuated wavelet $\phi_0(t)$ (equivalent to $\psi(t)$). Derivative order α' and peak frequency f'_p stand for the GDF wavelet model.

QUANTITATIVE RELATIONSHIP BETWEEN GDF PARAMETERS AND ATTENUATION

Attenuation-dependent wavelet parameters

The WR method involves a wavelet family $\mathcal{D}_a\psi(t)$ for which each member is defined by the initial set of parameters (Ω, α, ω_0), and it is modified during propagation within an anelastic medium characterized by a quality factor Q. To characterize how each member of the wavelet family is modified, we perform a quantitative

Downloaded 12/31/17 to 134.246.166.26. Redistribution subject to SEG license or copyright; see Terms of Use at http://library.seg.org/

Downloaded 12/31/17 to 134.246.166.26. Redistribution subject to SEG license or copyright; see Terms of Use at http://library.seg.org/

analysis of the variation of the set of parameters (Ω', α', ω_0') associated with the GDF that models the attenuated wavelet signal. We assess the range of these attenuation-related parameters for a seismic propagation in an anelastic medium taking into account the wavelet family source signals. To do so, we introduce the dimensionless parameter $\Upsilon = \tau f_p Q^{-1}$. For a range of Υ as wide as $[10^{-3} - 30]$ describing nonattenuating to highly attenuated seismic signals, we determine (Ω', α', ω_0') according to equation 9a and 9b for the five GDF analyzing wavelets introduced in Figure 2, i.e., for $\alpha = [1; 2; 3; 4; 5]$. The variations of the amplitude ratio (Figure 3a, in dB) are weak for $\Upsilon < 10^{-1}$, with a decreasing trend when Υ increases: For $\Upsilon > 1$, the amplitude drops are more pronounced for high derivative orders α. The derivative order α' (Figure 3b) exhibits a hysteresis behavior: At low Υ values, which corresponds in particular to short time of propagation and/or low attenuation, the attenuation effects can be neglected and $\alpha' \sim \alpha$ as expected. At high Υ values, α' tends toward much lower and fractional orders: For $\alpha = [1; 2; 3; 4; 5]$, we obtain $\alpha' \sim [0.2; 0.8; 1.3; 1.9; 2.4]$, i.e., $\alpha' \sim \alpha/2$ as a rough estimate, which shows the significant integrating effects. The ratio ω_0'/ω_0 (Figure 3c) also exhibits a hysteresis behavior: The curve starts with a value close to one at low Υ values, followed by a steep decrease and trend toward zero at high Υ values.

For a practical applicability of the method, the asymptotic behavior of the derivative order and the frequency shift of a seismic wave that propagates in a highly attenuating medium ($\Upsilon \gg 0.1$) is sensitive to noise conditions, as suggested by the strong decrease of the amplitude (Figure 3a). As a consequence, even if signal-to-noise ratio (S/N) issues affect not only this method but also many conventional geophysical processing methods, it may be unlikely to observe this asymptotic behavior if the S/N is not high enough.

General Q expression from fractional integrated wavelet parameters

We now demonstrate how the quality factor can be evaluated from the parameters of the attenuated wavelet signal $\phi_\tau(t)$. The associated amplitude spectrum $\hat{\phi}_\tau(\omega)$ is first defined following equations 2 and 7 for a time of propagation τ, which gives, based on a K-F attenuating medium:

$$\hat{\phi}_\tau(\omega) \equiv \Omega \frac{\omega^\alpha}{\omega_0^\alpha} \exp\left(-\frac{\omega^2}{\omega_0^2}\right) \exp\left(-\frac{\tau\omega}{2Q}\right). \tag{11}$$

By definition, the peak angular frequency ω_τ of the attenuated seismic wavelet $\phi_\tau(t)$ can be obtained by solving $(\partial\hat{\phi}_\tau/\partial\omega) = 0$. As a result, the expression of Q is given by

$$Q = \frac{\tau\omega_\tau\omega_0^2}{2(\alpha\omega_0^2 - 2\omega_\tau^2)}, \tag{12}$$

which is a generalization to any fractional GDF wavelet source of the result given by Zhang and Ulrych (2002) for a Ricker wavelet. This highlights the usefulness of approximating a seismic signal, the amplitude spectrum of which may be defined by several solutions of $(\partial\hat{\phi}_\tau/\partial\omega) = 0$, by a GDF wavelet characterized by a unique solution ω_τ. As shown in the previous section, the approach based on the centroid frequency and standard deviation of the seismic signal $\phi_\tau(t)$ makes this assessment more robust compared with peak-frequency detection (Tary et al., 2017). According to the approximation of ϕ_τ by a GDF wavelet ϕ_τ', ω_τ can be assimilated to $\omega_p' = \omega_0'\sqrt{\alpha'/2}$, resulting in the following approximation:

$$Q \sim Q' = \frac{\tau\omega_0'\sqrt{\frac{\alpha'}{2}}\omega_0^2}{2(\alpha\omega_0^2 - \alpha'\omega_0'^2)}. \tag{13}$$

Interestingly, this can be rewritten $Q' = (\tau\pi f_p' f_p^2)/\alpha(f_p^2 - f_p'^2)$, which means that the quality factor can actually be assessed by only determining the peak frequency f_p' of the attenuated seismic wavelet.

The accuracy of the quality factor estimated from equation 13 is now assessed by modeling the attenuation of seismic wavelets previously presented for typical Q values in the range [5–250] and a seismic source wavelet peak frequency f_p in the range [50–1000 Hz] to consider the propagation of low to very high resolution seismic sources in strongly to weakly attenuating media. In this f_p-Q domain, we determine the error $|Q - Q'|/Q$ (in %) for five derivative orders $\alpha = [1; 2; 3; 4; 5]$ of the GDF source wavelet (Figure 4). As a first observation, the distribution of errors shifts toward the minimum error value as α increases and on average, the error decreases with α: Its highest value is larger than 11% for $\alpha = 1$, approximately 8.5% for $\alpha = 2$ (Ricker wavelet) and less than 4% for $\alpha = 5$. The decreasing tendency of the mean error with α is not linear, and a preliminary estimate suggests an exponential behavior. At low frequencies ($f_p < 100$ Hz), the error slightly increases with Q but remains very small; i.e., estimating Q from the GDF parameters is accurate at low frequencies for any Q values. Note that for $\alpha = 1$, the error is minimum for $Q < 50$, when it is maximum for $\alpha > 1$. However, a general trend shows that the error increases with f_p and decreases with Q, remaining in a range lim-

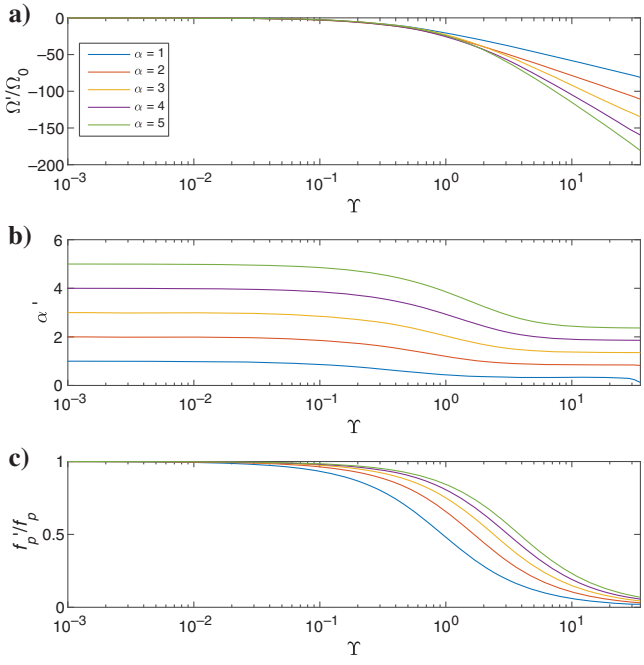

Figure 3. Variations of the attenuated seismic wavelet parameters as a function of the adimensional parameter Υ for source wavelets defined by $\alpha = [1; 2; 3; 4; 5]$, respectively: (a) amplitude Ω' normalized by the reference source amplitude Ω_0, (b) derivative order α', and (c) peak frequency f_p' normalized by the reference source peak frequency f_p.

Downloaded 12/31/17 to 134.246.166.26. Redistribution subject to SEG license or copyright; see Terms of Use at http://library.seg.org/

ited to approximately 2% independently of α. This means that the error is mainly controlled by α and f_p, and by Q to a lesser extent. These results highlight the potential of the present approach in quantifying the quality factor from a GDF approximation: The efficiency is particularly improved by considering a seismic source wavelet defined by a high derivative order.

SEISMIC ATTENUATION AFFECTING MULTISCALE REFLECTORS: QUANTITATIVE INTERPRETATION BASED ON THE WAVELET RESPONSE

Preliminary considerations

We now consider seismic reflection propagation in an anelastic medium characterized by a homogeneous quality factor Q, using the K-F model, and an acoustic impedance profile. In a first approximation, we consider seismic reflections induced by density contrasts.

The analyzing wavelet $\psi(t)$ is an antisymmetric GDF of order $\alpha = 5$ composed of six extrema: As introduced in previous papers, this wavelet has been used to model high-resolution seismic sources (Ker et al., 2013). The wavelet family is composed of 48 elements, the peak frequency of which f_p ranges between 100 and 1000 Hz. The WR is thus a collection of seismic wavelets of different peak frequencies, i.e., different dilations, acquired in normal incidence: The WR corresponds to a time-dilation representation of the wavelet amplitude. Following Ker et al. (2013), we consider the dilation

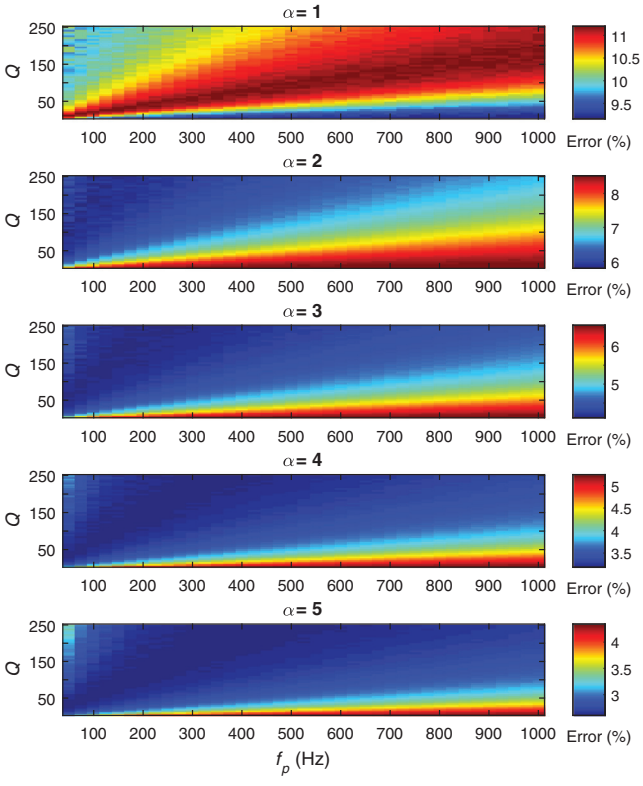

Figure 4. Error on the evaluation of the quality factor (equation 13) for anelastic media characterized by Q in the range [5–250] and for seismic peak frequencies in the range [50–1000 Hz], for different shapes of the seismic source defined by a derivative order α.

defined by the wavelet-dominant period (Gesret et al., 2010), called the dominant dilation $a_d = \sqrt{\alpha/2}(\delta/\pi f_p)$, where $\delta \sim 1.75$ for $\alpha = 5$ (Ker et al., 2013). A ridge function is a multiscale seismic attribute, which represents the evolution of an extremum amplitude as a function of the dilation plotted in a log–log diagram: It is a sparse support of the wavelet decomposition of the seismic reflectivity, and that is why it has been proposed in seismic analysis as a multiscale seismic attribute (Ker et al., 2011).

To assess the effect of attenuation on multiscale seismic attributes, we compute R (equation 1) and $\tilde{R}$ (equation 4 and associated equations 2 and 3), respectively, by setting $Q = \infty$ (elastic case) and 50 (anelastic case), respectively. According to the previous sections, we then approximate $\tilde{R}$ by R' for which each element is modeled by a GDF wavelet. Two seismic reflectors are considered below as preliminary case studies, i.e., a step-like reflector and a thin bed.

Step-like density contrast in an anelastic medium

The acoustic impedance profile of the medium is described by a step-like density contrast located at the time of 37.5 ms, i.e., a homogeneous Heaviside-like reflector geometry Figure 5a. For an elastic medium, R is the WR of a homogeneous reflector already described by Le Gonidec et al. (2002). The WR is equivalent to the wavelet family, scaled by the reflection coefficient and normalized in Figure 5b, which points toward the position of the discontinuity. In that case, the number of ridge functions is equal to the number of extrema of the analyzing wavelet: As illustrated with the third extremum, the ridge function (Figure 5b, blue line) of the Heaviside discontinuity is a flat straight line (Figure 5d, blue line).

For an anelastic medium, the global structure of the WR $\tilde{R}$ looks at a first glance barely changed, still being a cone-like structure pointing toward the discontinuity (Figure 5c), but the third ridge function (Figure 5c, red curve) now differs from a simple straight line (Figure 5d, red curve). In addition, the last ridge function tends to disappear at small dilations, as highlighted when plotting the derivative order α' as a function of the dilation a_d (Figure 5e, red line). At large dilations, α' tends to $\alpha = 5$, which characterizes the elastic case (Figure 5e, blue line), and decreases to four at small dilations, which means a symmetric wavelet with five extrema only. The dilation a_0' is very similar to the reference dilation a_0 of the elastic case (Figure 5f, red and blue lines, respectively), with a weak divergence when a_d decreases. Based on equation 13 expressed in the wavelet-transform formalism, we use the wavelet parameters extracted from R' (Figure 5e and 5f) to assess Q, which gives a mean value of 51.7 ± 0.5 in very good agreement with the expected value of 50. It has to be noted that the error of 3.4% in Q determination is in perfect agreement with results obtained in Figure 4 for $\alpha = 5$.

This simple case study illustrates the method to assess the quality factor of an anelastic medium by the use of the WR method, but also the misinterpretation of a seismic reflector geometry if only one source signal is considered, and reciprocally. This is even worse for complex seismic reflectors for which characteristic size quantification is not straightforward when it is embedded in an attenuating medium, as discussed in the following section.

Thin bed in an anelastic medium

The geometry of a thin bed is a window function defined as two successive step-like discontinuities: The distance between them

Downloaded 12/31/17 to 134.246.166.26. Redistribution subject to SEG license or copyright; see Terms of Use at http://library.seg.org/

corresponds to the window aperture, which is the characteristic size of the thin bed (Figure 6a). In the elastic case, the structure of the WR R is symmetric (Figure 6b) (for a full description, see Le Gonidec et al., 2002). At large dilations compared with the window aperture, the WR has a cone-like structure pointing toward the center of the discontinuity and is composed of five ridge functions: Note that the second and fourth ridge functions (Figure 6b, the solid and dashed blue lines, respectively) are similar in a log–log diagram (Figure 6d) and are characterized by a slope -1 at large dilations, where the window function is equivalent to a Dirac-like reflector. At small dilations, the WR is composed of two subconical structures: Each one points toward a step-like discontinuity composing the window function and is characterized by six ridge functions as discussed in the previous section. At intermediate dilations, the WR is characterized by a coalescence structure with an amplitude extremum related to seismic wave interferences between the edges of the internal structure of the reflector: The associated characteristic dilation is related to the characteristic size of the reflector.

In the anelastic case, the global symmetry of the WR is lost (Figure 6c), as shown by the two selected ridge functions (the solid and dashed red lines, respectively) which strongly differ from each other when plotted in a log–log diagram (Figure 6e) and cannot be used to properly characterize the reflector geometry. Actually, the slope of the ridge function analysis is not -1 at large dilations, which would mean a reflector not equivalent to a Dirac-like discontinuity as expected. At small dilations, the slope is not zero, which would not allow us to conclude to internal step-like structures of the complex reflector. And more critically, the characteristic dimension of the reflector, which should be identified at intermediate dilations, cannot be assessed with confidence.

These analyses clearly highlight that a quantitative characterization of a seismic reflector embedded in an anelastic medium is not straightforward when the reflector has a complex structure. Reciprocally, assessing the quality factor of a complex seismic reflector is not straightforward because of the multifrequency dependency of the seismic wavelets reflected by the multiscale discontinuities of the propagating medium, including layering effects and interference patterns that may induce apparent attenuation and frequency tuning effects (Tary et al., 2017).

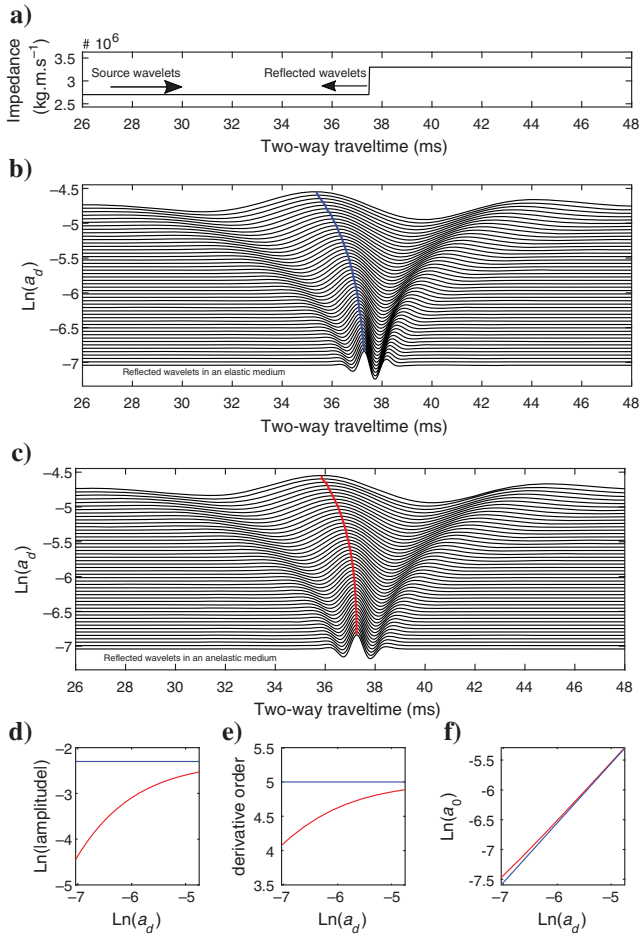

Figure 5. (a) The WR associated to a step-like reflector in an (b) elastic and (c) anelastic medium: The blue and red lines, respectively, stand for the ridge functions plotted in (d) as a function of the dominant dilation a_d. The variations of the derivative orders α and α', and the variations of the dilations a_0 and a_0' of the WR wavelets as a function of a_d are plotted in (e and f), respectively.

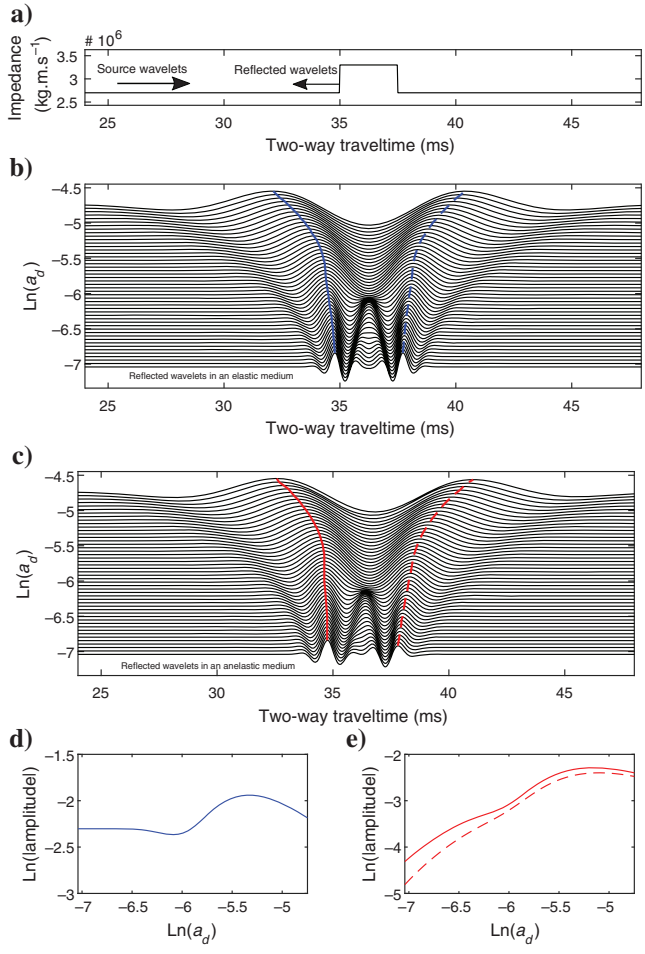

Figure 6. (a) The WR associated to a thin-bed reflector in an (b) elastic and (c) anelastic medium: the blue and red lines, respectively, stand for ridge functions plotted in (d and e), respectively, as a function of the dominant dilation a_d. Note that for the elastic case (d), the two ridge functions (solid and dashed lines) are identical, but they differ for the anelastic case (e).

Downloaded 12/31/17 to 134.246.166.26. Redistribution subject to SEG license or copyright; see Terms of Use at http://library.seg.org/

TIME-VARYING SHAPE FILTERING TO RECOVER MULTISCALE SEISMIC ATTRIBUTES

Principles of the method

When embedded in an elastic medium, a seismic reflector can be identified in terms of morphology and characteristic dimensions by quantitative analyses of its multiscale seismic attributes based on the WR R properties. This can no longer be achieved when the medium is anelastic, as illustrated in the previous section in which the attenuated WR $\tilde{R}$ is obtained with $Q = 50$: Actually, each time-varying seismic wavelet related to $\tilde{R}$ can be accurately approximated by a GDF wavelet $\phi'_\tau(t)$ with a particular shape (defined by α'), which deviates more from the shape of the source wavelet $\psi(t)$ the greater ω'_0 and/or τ are (see Figure 3). We introduce a new method to compensate for this deviation to restore the properties of the WR analysis: The aim is to define a compensated WR $\bar{R}$ for which each element $\bar{\phi}_\tau(t)$ is a dilated version of a common GDF wavelet $\bar{\psi}(t)$ defined by a derivation order $\bar{\alpha}$ and a natural frequency $\bar{\omega}_0$, associated to a peak frequency $\bar{f}_p$ as previously discussed. The approach consists of a time-varying filtering method that enables the transformation of a time-varying seismic wavelet $\phi'_\tau(t)$ into a wavelet $\bar{\phi}_\tau(t)$ of constant shape (given by $\bar{\alpha}$), taking advantage of the mathematical properties of the GDF. The choice of the reference constant shape is based on the attenuated wavelet most affected by seismic attenuation, i.e., which corresponds to the smallest dilation of the wavelet source family and the largest propagation time $\bar{\tau}$. Note that $\bar{\tau}$ controls not only the derivative order but also the natural angular frequency $\bar{\omega}_0$, i.e., the peak frequency $\bar{f}_p$ of the wavelet $\bar{\phi}_\tau(t)$. With this method, we do not aim at recovering the frequency content lost or reduced by seismic attenuation, such as Q inverse filtering or other resolution enhancement techniques would do (Wang, 2008; van der Baan, 2012), but rather at obtaining a constant shaping of wavelets, regardless of the global frequency content reduction of the seismic wavelets. In practice, considering $\bar{\alpha}$ as an integer value facilitates the ridge functions analysis, but this is not mandatory.

We now define the so-called time-varying shape-filtering method. For each dilation and propagation time, the attenuated seismic wavelet has to be transformed into a dilated version of the analyzing wavelet $\bar{\psi}$ involving (1) an amplitude correction term κ; (2) a fractional integration of order η to remove the variations of the seismic wave derivative order; (3) a Gaussian term, where ω_s compensates for the frequency shift of the seismic wave; and (4) an exponential term, where τ_s compensates for the time shift. In the Fourier domain, the expression of the shaping filter is thus given by

$$\hat{h}(\omega) = \kappa(i\omega)^{-\eta} \exp\left(-\frac{\omega^2}{\omega_s^2}\right) \exp(-i\omega\tau_s), \tag{14}$$

with

$$\eta = \alpha' - \bar{\alpha}, \tag{15a}$$

$$\omega_s = \sqrt{\bar{\omega}_0^2 - \omega_0'^2}. \tag{15b}$$

We perform the shape filtering by using a nonstationary convolution approach: To do so, we define the impulse response of the filter by using the definition of the fractional derivation of a Gaussian function in the time domain (Caputo, 1967) and the Laplace convolution of causal functions Wang (2015b). According to this approach, we can express the impulse response in the time domain by

$$h(t) = \begin{cases} 0 & \text{if } t < 0, \\ \kappa \frac{t^{\eta-1}}{\Gamma(\eta)} * \exp\left(-\frac{1}{4}\omega_s^2 (t-\tau_s)^2\right) & \text{if } t \geq 0. \end{cases} \tag{16}$$

The numerical implementation of the shape filtering relies on the multiplication of (1) a matrix, in which each row contains the time-varying filter computed for each traveltime sample, by (2) a row vector containing the seismic trace.

In practice, the parameters $\bar{\alpha}$ and $\bar{f}_p$ of the constant-shape wavelet are defined for the attenuated seismic wavelet associated with the smallest dilation for a reference propagation time $\bar{\tau}$ related to the depth position of the seismic reflector. This is done by performing on the attenuated seismic wavelets the fractional integration operation expressed in equation 15a. The parameters of the shaping filter are obtained from the relationships governing the wavelet parameters variation and the relationship describing the attenuation-induced time-shift variations.

Application to the step-like and thin-bed seismic reflectors embedded in an anelastic medium

The WR analysis of the step-like reflector has been developed above (Figure 5b): The WR of the anelastic case is characterized by a frequency-dependent α', which tends to four at small dilations (Figure 5d, red line). According to the principles of the method described above, we determine the time-varying shape-filtered WR $\bar{R}$ by considering an analyzing wavelet $\bar{\psi}$ defined by $\bar{\alpha} = 4$. Note that this arbitrary integer value corresponds to the less dilated wavelet ($\bar{f}_p \sim 550$ Hz) for a reference time $\tau = 41.5$ms larger than the two-way traveltime of the seismic reflector. As a result, the method allows the recovery of the symmetric cone-like structure of the WR for the anelastic case, which is now defined by dilated wavelets with a constant-shape $\bar{\alpha}$, in very good agreement with the WR performed with the same analyzing wavelet in the elastic case (Figure 7a, black and green curves, respectively): We then retrieve the correct morphology of the seismic reflector from the ridge function (Figure 7a, magenta line), which is now properly defined by a flat, straight line (Figure 7c, magenta line).

The efficiency of the time-varying shape filter is clearly demonstrated when assessing the characteristic dimension of a complex reflector in an anelastic medium, such as the thin bed. Similarly to the previous analysis performed on a step-like reflector, we determine the same time-varying filtering with $\bar{\alpha} = 4$. The compensated WR $\bar{R}$ has a global complex structure (Figure 7b, black curves) in very good agreement with the characteristic WR R of a window discontinuity (Figure 7b, green curves): In particular, the compensated ridge function (Figure 7b, black line) now allows an accurate estimation of the window aperture from the dilation associated with the maximum amplitude (Figure 7d). The compensation of the attenuation-induced shape effects enables the recovery of the shape of the ridge functions but involves a GDF derivative order $\bar{\alpha} = 4$, which differs from $\alpha = 5$ of the seismic source wavelet: This explains the slight difference between the thin-layer ridge functions plotted in Figures 7d (magenta and black lines) and 6d (blue line), respectively. It has to be noted that until the GDF wavelet has several vanishing moments (which is related to the derivative order)

Downloaded 12/31/17 to 134.246.166.26. Redistribution subject to SEG license or copyright; see Terms of Use at http://library.seg.org/

greater than the regularity of the reflector discontinuity, this has no consequence on the quantitative descriptions based on the multiscale seismic attributes.

Extended application to seismic data reflected by complex geologic reflectors in an anelastic medium

To extend the analysis to a more realistic seismic data set, we now consider the complex reflectivity sequence defined from the in situ impedance log introduced in Ker et al. (2011), embedded in a K-F anelastic medium defined by a quality factor Q. We model the synthetic data set by using (1) a real seismic source signature related to the deep-towed seismic device SYstème SIsmique Fond de mer/Deep-towed Seismic System (SYSIF) (Marsset et al., 2010) and (2) the nonstationary convolution of the Green's function. The SYSIF source signature consists in a broadband chirp signal (220–1050 Hz). Applying the source-correction developed by Ker et al. (2013) to compute a WR from a broadband seismic source signature, we associated GDF wavelets of derivative order $\alpha = 5$ for the SYSIF seismic source in the dilation range (logarithm values) $[-6.6; -5.7]$, equivalent to a peak-frequency range [315–830 Hz].

As a first step, we perform R and $\tilde{R}$, which stand for the WR of the complex acoustic impedance profile embedded in an elastic medium (Figure 8a) and in an anelastic medium (Figure 8b), respectively. The two particular reflectors extensively studied by Ker et al. (2013) are identified by a solid (A) and a dashed (B) line, respectively. The associated ridge functions are plotted in a log–log diagram (Figure 8c and 8d, respectively, where the blue and red curves correspond to the elastic and anelastic cases, respectively). As introduced in the section presenting the WR background, the aim is not to describe these multiscale seismic attributes, but to highlight the efficiency of the time-varying shape filtering compensation in recovering the WR properties required to assess the geometry of the realistic complex seismic reflectors.

In a second step, we apply the time-varying shape filtering compensation to the realistic seismic data set associated with $\tilde{R}$. We still consider the derivative order $\bar{\alpha} = 4$ for the sake of simplicity in the interpretation of the ridge function and the time $\bar{\tau} = 41.5$ ms, which is larger than the two-way traveltimes of the analyzed reflectors A and B. The less dilated SYSIF wavelet corresponds to a reference

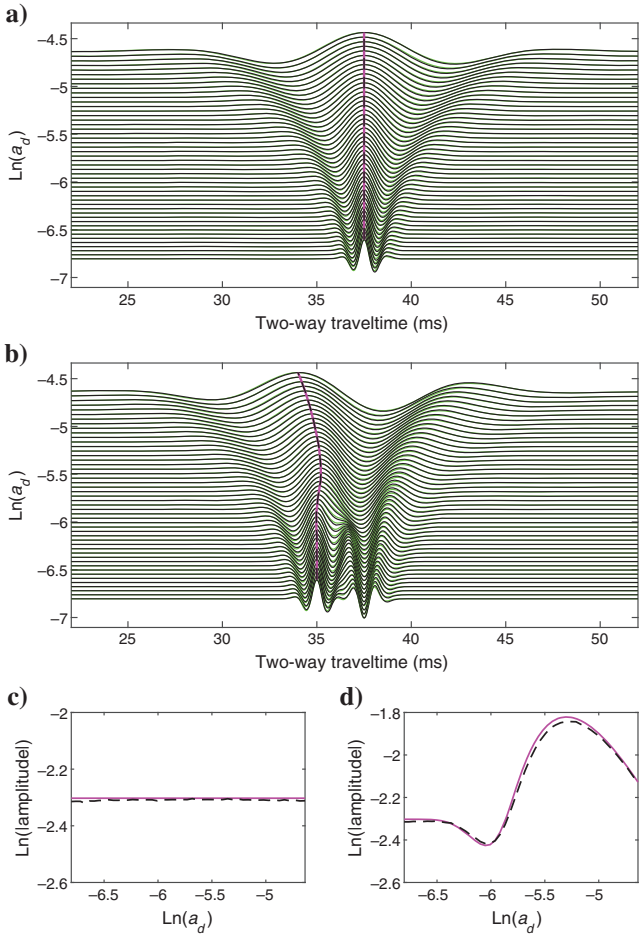

Figure 7. The WR of (a) a step-like and (b) a thin-bed reflectors embedded in an anelastic medium, processed by the time-varying shaping filter (black curves), in comparison with the WR performed for an elastic medium (green curves). The black and magenta lines stand for the ridge functions extracted from the corrected WR and the elastic WR respectively plotted in (c and d) for the step-like and thin-bed reflectors.

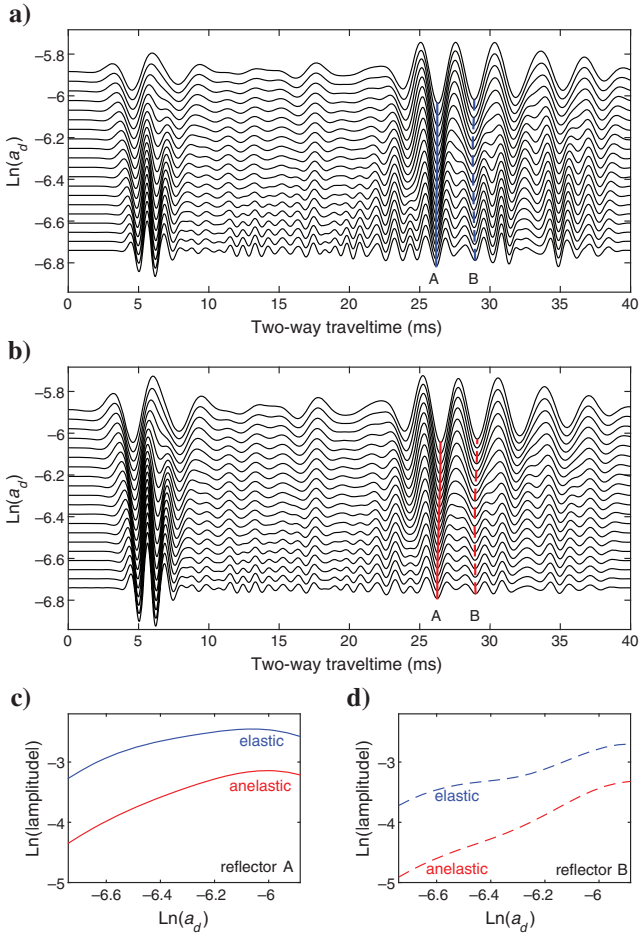

Figure 8. The WR of a synthetic seismic data, involving a seismic source and an in situ reflectivity sequence embedded in (a) an elastic and (b) an anelastic medium, in which the blue and red lines stand for the ridge functions of reflectors A (solid line) and B (dashed line), plotted in (c and d), respectively.

Downloaded 12/31/17 to 134.246.166.26. Redistribution subject to SEG license or copyright; see Terms of Use at http://library.seg.org/

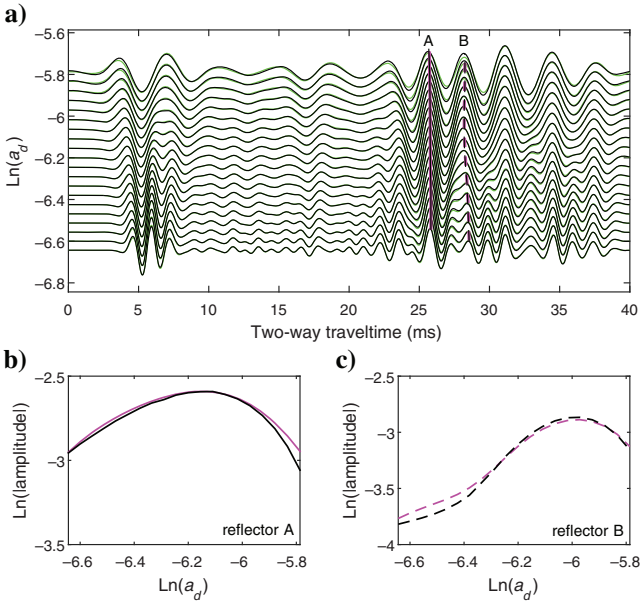

Figure 9. (a) The WR of a synthetic seismic data processed by the time-varying shaping filter (black curves), in comparison with the WR performed for an elastic medium (green curves) for which ridge functions (black and magenta lines, respectively) of reflectors A and B are plotted in (b and c), solid and dashed lines, respectively.

peak frequency $\bar{f}_p = 468$ Hz. Based on these parameters, the result is the compensated WR $\bar{R}$, which is in very good agreement with the WR R related to the reference case with $\alpha = 4$ (Figure 9a, the black and green curves, respectively). The agreement is particularly highlighted when plotting the ridge functions in a log–log diagram (Figure 9a, black and magenta lines, respectively) with an error in the reconstruction lower than 5% for reflector A (solid lines) and 10% for reflector B (dashed lines): The time-varying shape filtering approach is thus very accurate to allow further quantitative analyses of broadband SYSIF data of complex reflectors in anelastic media.

CONCLUSION

We have studied the effects of the intrinsic attenuation on a seismic source signal during its propagation into an anelastic medium. The analysis considers a seismic source signal defined as a GDF wavelet of derivative order α and peak frequency f_p, and a K-F anelastic medium, whose attenuation is $\beta \propto \omega^{\delta}$, with $\delta = 1$ and the proportionality factor is related to the reciprocal of the quality factor Q, considered constant with depth in the present study. We have shown that a GDF source wavelet that propagates into this anelastic medium is modified according to a fractional integration operation and a frequency shift; i.e., the attenuated signal is equivalent to another GDF. We have also demonstrated the dependency between the wavelet parameters and Q, by establishing an expression of their relationship.

As a consequence of these attenuation-related effects, the multiscale seismic attributes analysis based on the WR of a seismic reflector embedded in an anelastic medium is not straightforward. In particular, the ridge functions cannot be used to characterize the geometry of the reflector. To go further into this study, in which a complex acoustic reflectivity induces tunning effects, for instance, and attenuation also modifies the shape of the seismic source wavelet, we took advantage of the quasi-conservation of the Gaussian character of a GDF to compensate for these effects and to recover properly the quantitative properties of the multiscale seismic attributes. We designed a time-varying shaping filter based on fractional integration that enables to substitute the time-varying wavelet by a constant-shape wavelet. We demonstrated this approach first on a step-like and a thin-bed related reflectors, widely analyzed in the framework of the WR in elastic media, and then on realistic synthetic data modeled by using a deep-towed SYSIF source signature and in situ acoustic-impedance log. The multiscale seismic attributes are accurately corrected from their attenuation-related distortions, while spanning in a smaller dilation range. The proposed approach allows extending the use of multiscale seismic attributes to anelastic media enabling us to properly analyze the geometry of the seismic reflector.

These results have been performed for an anelastic medium characterized by $\delta = 1$ and Q homogeneous in space. It is interesting to note that similar developments should be extended to other models, such as power-law attenuation model with $1 < \delta < 2$. The potential of the approach in developing attenuation analysis methods such as Q estimation has been introduced in the present work from the variations of the GDF parameters and deserves to be tested with in situ seismic transmission measurements, such as VSP data. The interest also deals with seismic source signature deconvolution, by providing a simple model for the seismic wavelet based on only three parameters that describe the time-varying shape of the seismic wavelet and can be used to extend the ongoing work dedicated to seismic wavelet modeling.

ACKNOWLEDGMENTS

The authors would like to thank A. Gesret and two anonymous reviewers for their valuable suggestions that contributed to improving the manuscript.

REFERENCES

Abramowitz, M., and I. A. Stegun, 1972, Handbook of mathematical functions: U.S. Department of Commerce, National Bureau of Standards, US Government Printing.

Caputo, M., 1967, Linear models of dissipation whose Q is almost frequency independent. Part II: Geophysical Journal of the Royal Astronomical Society, **13**, 529–539, doi: 10.1111/j.1365-246X.1967.tb02303.x.

Castagna, J., S. Sun, and R. W. Siegfried, 2003, Instantaneous spectral analysis: Detection of low-frequency shadows associated with hydrocarbons: The Leading Edge, **22**, 120–127, doi: 10.1190/1.1559038.

Futterman, W. I., 1962, Dispersive body waves: Journal of Geophysical Research, **67**, 5279–5291, doi: 10.1029/JZ067i013p05279.

Gesret, A., M. Laigle, J. Diaz, M. Sachpazi, and A. Hirn, 2010, The oceanic nature of the African slab subducted under Peloponnesus: Thin-layer resolution from multiscale analysis of teleseismic P-to-S converted waves: Geophysical Journal International, **183**, 833–849, doi: 10.1111/j.1365-246X.2010.04738.x.

Heigl, W. M., 2007, Computing Gaussian derivative waveforms of any order: Geophysics, **72**, no. 4, H39–H42, doi: 10.1190/1.2716624.

Hosken, J. W. J., 1988, Ricker wavelets in their various guises: First Break, **6**, 24–33, doi: 10.3997/1365-2397.1988002.

Ker, S., Y. Le Gonidec, and D. Gibert, 2012, Multiscale seismic attributes: Source-corrected wavelet response and application to high-resolution seismic data: Geophysical Journal International, **190**, 1746–1760, doi: 10.1111/j.1365-246X.2012.05601.x.

Ker, S., Y. Le Gonidec, and D. Gibert, 2013, Multiresolution seismic data fusion with a generalized wavelet-based method to derive subseabed acoustic properties: Geophysical Journal International, **195**, 1370–1383, doi: 10.1093/gji/ggt317.

Ker, S., Y. Le Gonidec, D. Gibert, and B. Marsset, 2011, Multiscale seismic attributes: A wavelet-based method and its application to high-resolution seismic and ground truth data: Geophysical Journal International, **187**, 1038–1054, doi: 10.1111/j.1365-246X.2011.05207.x.

Ker, S., Y. Le Gonidec, L. Marié, Y. Thomas, and D. Gibert, 2015, Multiscale seismic reflectivity of shallow thermoclines: Journal of Geophysical Research, **120**, 1872–1886, doi: 10.1002/2014JC010478.
Ker, S., Y. Le Gonidec, B. Marsset, G. Westbrook, D. Gibert, and T. A. Minshull, 2014, Fine-scale gas distribution in marine sediments assessed from deep-towed seismic data: Geophysical Journal International, **196**, 1466–1470, doi: 10.1093/gji/ggt497.
Kolsky, H., 1956, The propagation of stress pulses in viscoelastic solids: Philosophical Magazine, **1**, 693–710, doi: 10.1080/14786435608238144.
Le Gonidec, Y., and D. Gibert, 2006, The wavelet response as a multiscale characterization of scattering processes at granular interfaces: Ultrasonics, **44**, 381–390, doi: 10.1016/j.ultras.2006.05.212.
Le Gonidec, Y., D. Gibert, and J.-N. Proust, 2002, Multiscale analysis of waves reflected by complex interfaces: Basic principles and experiments: Journal of Geophysical Research, **107**, 2184, doi: 10.1029/2001JB000558.
Mallat, S., 1998, A wavelet tour of signal processing, 2nd ed.: Academic Press Inc.
Margrave, G. F., 1998, Theory of nonstationary linear filtering in the Fourier domain with application to time-varying filtering: Geophysics, **63**, 244–259, doi: 10.1190/1.1444318.
Marsset, T., B. Marsset, S. Ker, Y. Thomas, and Y. Le Gall, 2010, High and very high resolution deep-towed seismic system: Performance and examples from deepwater geohazard studies: Deep-Sea Research I, **57**, 628–637, doi: 10.1016/j.dsr.2010.01.001.
Morgan, E. C., M. Vanneste, I. Lecomte, L. G. Baise, O. Longva, and B. McAdoo, 2012, Estimation of free gas saturation from seismic reflection surveys by the genetic algorithm inversion of P-wave attenuation model: Geophysics, **77**, no. 4, R175–R187, doi: 10.1190/geo2011-0291.1.
Müller, G., 1983, Rheological properties and velocity dispersion of a medium with power-law dependence of *Q* on frequency: Journal of Geophysics, **54**, 20–29.
Piété, H., L. Marié, B. Marsset, Y. Thomas, and M.-A. Gutscher, 2013, Seismic reflection imaging of shallow oceanographic structures: Journal of Geophysical Research, **118**, 2329–2344, doi: 10.1002/jgrc.20156.
Ricker, N., 1953, The form and laws of propagation of seismic wavelets: Geophysics, **18**, 10–40, doi: 10.1190/1.1437843.
Skauvold, J., J. Eidsvik, and U. Theune, 2016, A parametric model for seismic wavelets — With estimation and uncertainty quantification: Geophysical Journal International, **205**, 796–809, doi: 10.1093/gji/ggw029.
Soubaras, R., and R. Dowle, 2010, Variable-depth streamer: A broadband marine solution: First Break, **28**, 89–96.
Tary, J. B., M. van der Baan, and R. H. Herrera, 2017, Applications of high-resolution time-frequency transforms to attenuation estimation: Geophysics, **82**, no. 1, V7–V20, doi: 10.1190/geo2016-0022.1.
Toksöz, M. N., and D. H. Johnston, 1981, Seismic wave attenuation: SEG, 45.
Ursin, B., and T. Toverud, 2002, Comparison of seismic dispersion and attenuation models: Studia Geophysica et Geodaetica, **46**, 293–320, doi: 10.1023/A:1019810305074.
van der Baan, M., 2012, Bandwidth enhancement: Inverse *Q* filtering or time-varying Wiener deconvolution?: Geophysics, **77**, no. 4, V133–V142, doi: 10.1190/geo2011-0500.1.
Wang, Y., 2008, Seismic inverse *Q* filtering: Blackwell, Oxford.
Wang, Y., 2015a, The Ricker wavelet and the Lambert W function: Geophysical Journal International, **200**, 111–115, doi: 10.1093/gji/ggu384.
Wang, Y., 2015b, Generalized seismic wavelets: Geophysical Journal International, **203**, 1172–1178, doi: 10.1093/gji/ggv346.
Wang, Y., and J. Guo, 2004, Modified Kolsky model for seismic attenuation and dispersion: Journal of Geophysics and Engineering, **1**, 187–196.
Worthington, M. H., and J. A. Hudson, 2000, Fault properties from seismic *Q*: Geophysical Journal International, **143**, 937–944, doi: 10.1046/j.1365-246X.2000.00315.x.
Xintao, C., S. Wang, S. Yuan, J. Zhao, L. Sun, and X. Wei, 2014, Sparse reflectivity inversion for nonstationary seismic data: Geophysics, **79**, no. 3, V93–V105, doi: 10.1190/geo2013-0313.1.
Zhang, C., and T. J. Ulrych, 2002, Estimation of quality factors from CMP records: Geophysics, **67**, 1542–1547, doi: 10.1190/1.1512799.

Downloaded 12/31/17 to 134.246.166.26. Redistribution subject to SEG license or copyright; see Terms of Use at http://library.seg.org/

Geochemistry, Geophysics, Geosystems

RESEARCH ARTICLE
10.1029/2018GC007861

Anomalously Deep BSR Related to a Transient State of the Gas Hydrate System in the Western Black Sea

S. Ker[1], Y. Thomas[1], V. Riboulot[1], N. Sultan[1], C. Bernard[1,2], C. Scalabrin[1], G. Ion[3], and B. Marsset[1]

[1]Ifremer, REM-GM, Plouzané, France, [2]ENSTA Bretagne, Brest, France, [3]GeoEcoMar, Bucharest, Romania

Key Points:
- There is a discrepancy between observed BSR depth and theoretical steady state base of gas hydrate stability zone
- The transient state of the hydrate system is due to excess pore pressure related to hydrate dissociation
- BSR depth is used to derive maximum excess pore pressure at the base of the gas hydrate stability zone

Correspondence to:
S. Ker,
stephan.ker@ifremer.fr

Citation:
Ker, S., Thomas, Y., Riboulot, V., Sultan, N., Bernard, C., Scalabrin, C., Ion, G., & Marsset, B. (2019). Anomalously deep BSR related to a transient state of the gas hydrate system in the western Black Sea. *Geochemistry, Geophysics, Geosystems*, *20*. https://doi.org/10.1029/2018GC007861

Received 26 JUL 2018
Accepted 27 DEC 2018
Accepted article online 3 JAN 2019

©2019. American Geophysical Union. All Rights Reserved.

Abstract A comprehensive characterization of gas hydrate system offshore the western Black Sea was performed through an integrated analysis of geophysical data. We detected the bottom-simulating reflector (BSR), which marks, in this area, the base of gas hydrate stability. The observed BSR depth does not fit the theoretical steady state base of gas hydrate stability zone (BGHSZ). We show that the disparity between the BSR and predicted BGHSZ is the result of a transient state of the hydrate system due to the ongoing reequilibrium since the Last Glacial Maximum. When gas hydrates are brought outside the stability zone due to changes in temperature and sea level, their dissociation generates an increase in interstitial pore pressure. This process is favorable to the recrystallization of gas hydrates and delays the upward migration of the hydrate stability zone explaining the anomalously deep BSR. The BSR depth, which is commonly used to derive geothermal gradient values by assuming steady state conditions, is used here to derive the maximum excess pore pressure at the BGHSZ. Derived excess pore pressure values of 1–2 MPa are probably the result of the low permeability of hydrate-bearing sediments. Higher pore pressure values derived at the location of a fault system could cause hydrofracturing enabling the free gas to cross the gas hydrate stability zone and emerge at the seafloor, forming the flares observed in close vicinity to where the shallow gas hydrates were sampled.

1. Introduction

Since the first recovery of gas hydrates within marine sediments at the beginning of the 1970s and decades of scientific investigations (Ginsburg, 1998; Yefremova & Zhizhchenko, 1974), the Black Sea is nowadays considered to contain large amounts of hydrate deposits (Merey & Sinayuc, 2016). The presence of gas hydrates in the Danube fan, located in the western part of the Black Sea, is inferred from the identification of a hydrate-related seismic reflector called the bottom-simulating reflector (BSR). The BSR corresponds to a decrease in the seismic impedance between a hydrate-bearing sediment characterized by a high *P* wave velocity and a gas-charged layer characterized by a low *P* wave velocity. The BSR occurs at the limit of gas hydrate stability, which depends on the pressure, temperature, salinity conditions, and gas composition (Holbrook et al., 1996; Shipley et al., 1979). BSRs may present various forms such as a reverse polarity, they may be semicontinuous, or show aligned terminations of high amplitudes (Davies et al., 2017). The BSR has been mapped out in the western Black Sea by Popescu et al. (2007) who also indicate the presence of multiple BSRs in the Danube deep-sea fan (Popescu et al., 2006) that could be related to past stability conditions (Zander et al., 2017).

In addition to BSR identification, gas seeps and gas-related seismic evidences have been also reported in the Danube fan (Popescu et al., 2007). Methane seepages are widespread on the shelf and on the slope of the Black Sea especially along the Ukrainian (Greinert et al., 2010; Naudts et al., 2006, 2009) and Romanian margins (Popescu et al., 2007). More recently, Riboulot et al. (2017) identified more than 1,400 gas seeps in the Romanian sector of the Black Sea based on water column acoustic records. Gas emissions in the water column seem to be controlled by the geomorphology and gas hydrates extent as 98% of the gas seeps are located in a water depth where gas hydrates are thermodynamically unstable. Consequently, the presence of hydrate seems to prevent any free gas migration into the sediments and the water column. It has to be highlighted that a large number of seeps observed by Riboulot et al. (2018) are located close to the predicted landward termination of the gas hydrate stability zone (GHSZ) and where hydrates could be currently under destabilization related to the salt diffusion within the sediment (Riboulot et al., 2018).

The present study aims at providing a comprehensive understanding of the gas hydrate system of the Romanian margin (Figure 1) by assessing the following questions: (1) how hydrate deposits are

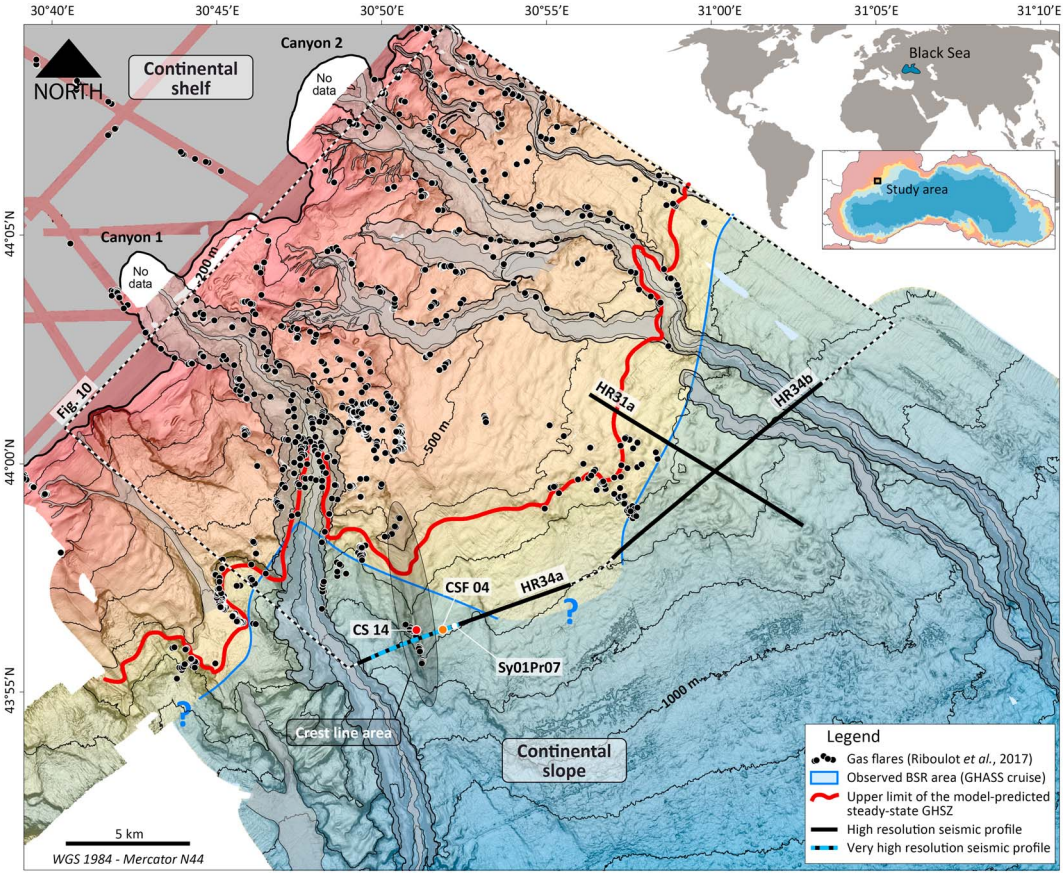

Figure 1. Bathymetric map of the study area with location of the high-resolution (HR) and very high resolution (Sy01Pr07) seismic profiles and with superposed BSR area (modified from Popescu et al., 2007 using the results obtained in this study). The BSR is not ubiquitous in the study area, but the extension of the area without BSR is unknown. The upper limit of the predicted base of the gas hydrate stability zone (BGHSZ) is indicated by the thick red line. Acoustic gas flares (black dots) are mostly located outside the gas hydrate stability zone (GHSZ) but can also be found at the landward termination of the GHSZ and within the GHSZ in the crest line area. CSF04: geothermal gradient measurement. CS14: core with gas hydrate. BSR = bottom-simulating reflector.

distributed within the GHSZ? (2) where hydrate deposits impede the vertical migration of free gas and how to explain the presence of gas flares within the GHSZ? and (3) what is the current dynamics of the hydrate system? Characterization of the gas hydrate system is performed using an integrated analysis of geophysical data acquired during the 2015 Gas Hydrates, fluid Activities and Sediment deformations in the western Black Sea (GHASS) cruise (doi:10.17600/15000500) on board the R/V *Pourquoi Pas?*. The acquired data set includes multibeam bathymetric and water column data, 2D high-resolution and very high-resolution seismic reflection profiles, high-resolution *P* wave velocity fields, and modeling of the base of GHSZ (BGHSZ). We use the BSR to define the BGHSZ as it marks a sharp border between hydrate deposit and free gas. The vertical extent of hydrate-bearing sediments is revealed by positive *P* wave velocity anomalies. Gas-related seismic signatures and low velocity enable to identify the distribution of free gas within Black Sea marine sediments. To complete the quantitative characterization of the hydrate system, we estimate methane and hydrate concentrations from *P* wave velocity inversion using first-principle-based effective models. Observed BSR depths are compared to predicted depths of the BGHS at present and during the Last Glacial Maximum (LGM) in steady state conditions by using well-constrained parameters from in situ measurements and literature.

2. The Study Area

The study area is located in the Romanian margin northward and close to the Danube canyon between 150- and 1,000-m water depth (Figure 1). The margin is characterized by a shelf edge occurring at 190-m water

depth and a continental slope with a mean value of 2° (Riboulot et al., 2017). The outer shelf and the slope are incised by two canyons and are affected by seafloor instabilities identified through headwall scarps. Water column acoustic records acquired during the GHASS cruise enable to map the distribution of 1,409 gas seeps (Riboulot et al., 2017). Ninety-eight percent of gas flares are located between 200- and 700-m water depth. Gas flare locations can be associated to canyons, headwall scarps, pockmarks, or the landward termination of the current predicted GHSZ indicated by the thick red line in Figure 1. The 2% remaining gas flares are localized within the GHSZ, along a crest line that could be related to a fault system similar to what has been observed at the Blake ridge crest by Gorman et al. (2002).

3. Data and Methods

3.1. High-Resolution Surface Seismic Data

To undertake a comprehensive study of the free gas/gas hydrate system, several HR seismic profiles were acquired perpendicular to the slope in order to investigate the transition between the domain outside the GHSZ from the upper slope (550- to 650-m water depth) down to the deeper slope within the GHSZ (800–900 m of water depth). Two additional HR seismic profiles (HR34a and HR34b) were acquired within the GHSZ. The profile H34a was localized perpendicular to the crest line area where acoustic flares occurred with the aim to understand the mechanism controlling the presence of free gas within the GHSZ. The joint analysis of high-resolution velocity analysis and prestack depth migration seismic data realized on these profiles provides an effective tool for characterizing hydrate systems (Crutchley et al., 2015; Sarkar et al., 2012) or defining the internal structure of hydrate-related chimney (Plaza-Faverola et al., 2010).

Two-dimensional high-resolution seismic profiles were acquired using a 96-channel streamer (Sentinel® solid technology) of 6.25-m group intervals and a maximum source-receiver offset of 650 m. The seismic source consisted of a single small air gun (min-GI© 24 cubic inches) providing a short repeatable signature. The streamer was towed at a depth of 2 m, while the air gun was deployed at 1.5 m. The resulting source signal has a 40–170 Hz frequency bandwidth with a central frequency of 110 Hz.

For the whole seismic data set (including profile H34b presented in Figure 2b), we applied a conventional poststack processing sequence. Detailed Root Mean Square (RMS) velocity analyses were performed on super gathers every 150 m (5 combined Common Mid Point (CMP) every 24 CMPs) corresponding to the lateral resolution of the resulting velocity field. The picking of RMS velocities was performed on semblance panels using a horizon consistent approach. Interval velocities were computed using Dix's law. The 2D velocity model was then smoothed in order to compute Green's functions used to perform the poststack depth Kirchhoff migration.

For two profiles of particular interest (HR31a and HR34a presented in Figures 2a and 2c), we processed the seismic data by using a prestack depth imaging sequence. The first step of the sequence involves the determination of the velocity field. We use a migration velocity analysis (MVA) procedure that is based on iterative prestack Kirchhoff depth migration using a layer-stripping method (Al-Yahya, 1989; Marsset et al., 2012). The principle of this seismic imaging procedure is to compare migration results obtained for a range of velocities at given locations called common image gathers (CIG). The determination of the velocity is driven by focalizing, at the same depth of reflection, amplitudes associated with a different range of offsets. Detailed velocity analyses were performed on CIG every 32 m corresponding to the lateral resolution on the velocity field. The depth interval 2D velocity model is built using a layer stripping approach. For a given layer, the updated velocity is the one that best focused the bottom reflector. Velocity within a layer is vertically constant but varies laterally. In order to avoid unrealistic lateral variations, the velocity is edited and smoothed along the layer by giving higher weight to CIG of clear focalization and by maintaining trends. To allow sharp velocity contrast at the BSR, layers with pinch-outs are allowed. The selection of horizons/layers is driven both by geophysical and geological constraints. Green's functions used to perform the Kirchhoff prestack depth migration are obtained with the Eikonal equation solver (Podvin & Lecomte, 1991). The second step of the sequence is to perform the prestack depth migration by using the velocity model obtained by the velocity analysis procedure. Seismic resolutions after migration are in the order of 3.5 m vertically and 15 m horizontally (mean seismic wavelength). Related to the sensitivity in the velocity picking and to the edition step, uncertainties on *P* wave velocity are estimated to be ±50 m/s up to the depth of 1,000 m and increase to ±100 m/s at 1,200 m using MVA approach. The conventional analysis provides *P*

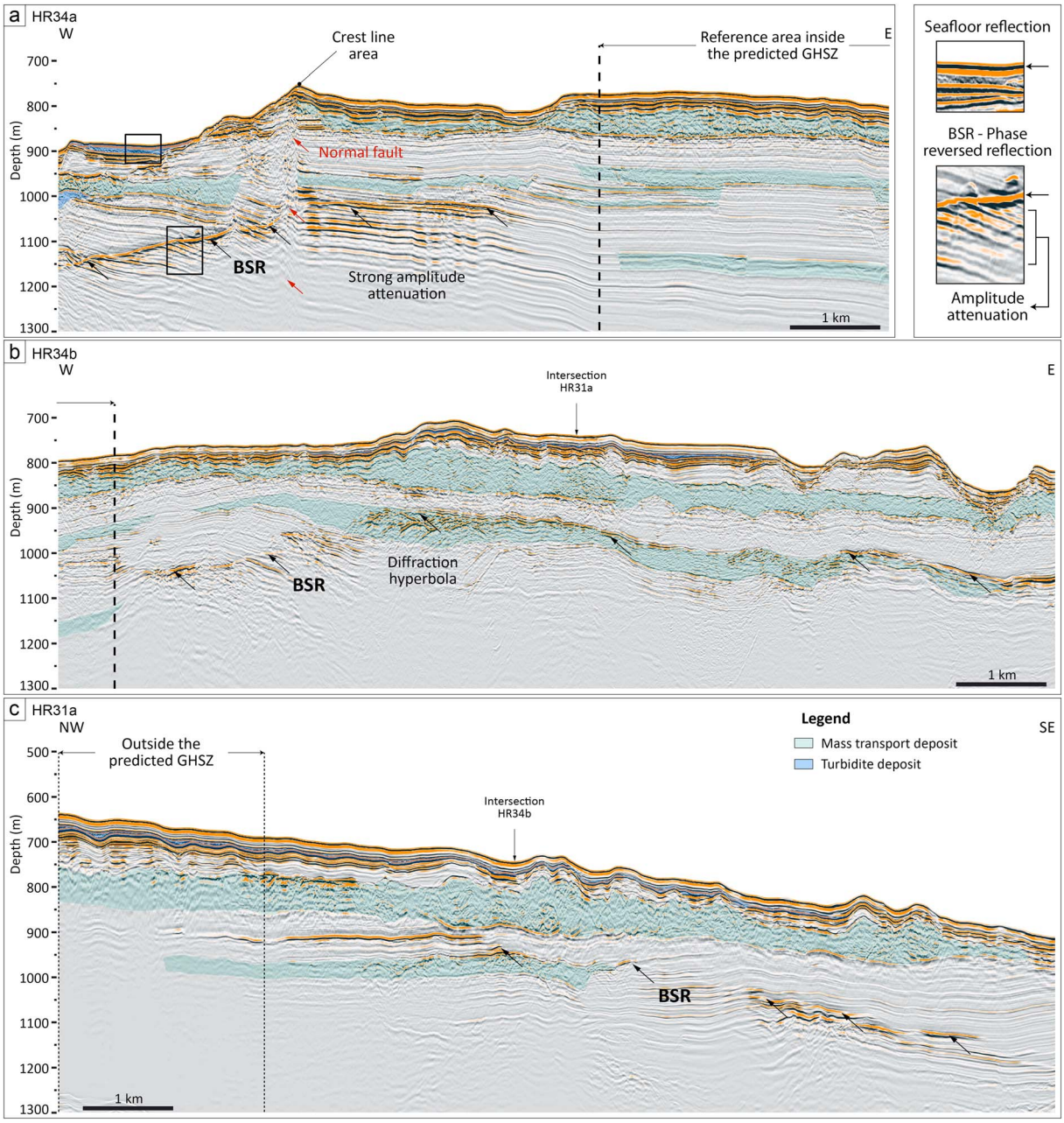

Figure 2. High-resolution seismic profiles: (a) HR34a, (b) HR34b both located within the GHSZ, and (c) HR31a that crosses the landward termination of the GHSZ. BSR (thick black dashed line) is ubiquitous within the GHSZ except in the so-called *reference area* located at the eastern part of profile HR34a. The onset indicates the reverse polarity of the BSR related to the seafloor reflection and the amplitude attenuation right under the BSR due to the presence of free gas. Mainly three seismic facies can be identified: (1) low-amplitude subparallel seismic reflectors related to hemipelagic sediments, (2) low-amplitude seismic facies related to turbidites (in blue), and (3) chaotic facies associated with mass transport deposit (in green). BSR = bottom-simulating reflector; GHSZ = gas hydrate stability zone.

wave velocity values with greater uncertainties, which are estimated to be twice those of the MVA analysis. Data penetration is limited to 500 mbsf (meter below sea floor) related to the presence of gas and the high-frequency content of seismic data.

3.2. Deep-Towed Seismic Data

Two-dimensional very high resolution deep-towed seismic profiles were acquired with the Ifremer SYstème SIsmique Fond system (Marsset et al., 2014). SYstème SIsmique Fond is a deep-towed seismic device hosting a Janus-Helmholtz transducer emitting a linear chirp signal in the frequency bandwidth (220–1050 Hz) and

a 52-channel seismic streamer with a hydrophone spacing of 2 m, both towed between 50 and 100 m above the seafloor. After careful processing of the positioning, seismic signature deconvolution enables to obtain a 1-m vertical resolution while the prestack depth imaging procedure specifically developed for the particular geometry of the deep-towed acquisition (Marsset et al., 2014, 2018) allows to reach a 2-m lateral resolution.

3.3. In Situ Measurements and Cores

During the GHASS cruise, in situ measurements and cores were collected. Geochemical measurements performed on gas hydrate samples, which were collected for the first time in the Romanian sector of the Black Sea, confirmed that the gas entrapped is biogenic methane with a concentration of 99.6% (Riboulot et al., 2018), and the remaining 0.4% is mainly N_2. Pore water analyses performed on eight cores revealed a gradual fall in salinity from 22 psu at the seafloor level to near 2 psu at around 25 mbsf. A mineralogy analysis performed on eight cores up to 30-m deep below the seafloor indicated that the average composition of these soft sediments is made of 60% clay, 35% quartz, and 5% calcite (Ballas et al., 2018).

3.4. Estimates of Gas Hydrate and Methane Concentration

Regarding the lack of borehole data to precisely define an effective medium model taking into account gas hydrate morphology and free gas distribution, we used first principle-based effective medium models to obtain rough estimates of gas hydrate and methane concentrations. For gas hydrate, we used the upper and lower bounds of the Helgerud et al. (1999) effective medium model, which either consider hydrate as part of the pore space or part of the sediment frame. For methane, we used the model of White et al. (1975) as it accounts for the attenuation of the high frequencies clearly observed on the seismic data. This model considers a patchy distribution of free gas using a periodic layered system composed of porous media; the attenuation comes from wave-induced fluid flow (WIFF). This phenomenon, which cannot exist in the case of a homogeneous gas distribution, occurs at a mesoscopic scale where the size of the gas pocket is much larger than the pore size but lower than the seismic wavelength (Müller et al., 2010). Using attenuation-related quantities as the Q value in addition to P wave velocity enables to derive (1) the gas concentration in the range defined by the Gassmann-Wood and Gassmann-Hill bounds (Carcione & Picotti, 2006) and (2) the mean size of gas patches. This joint inversion of Q and P wave velocity was conducted where robust Q measurements (i.e., not affected by scattering attenuation due to complex wave propagation) were derived from HR data using the centroïd frequency shift method (Ker & Le, 2018; Quan & Harris, 1997).

3.5. Base of Gas Hydrate Stability Zone Modeling

The BGHSZ has been computed in steady state conditions. We consider a pure s-I methane hydrate as the main component of gas from the Black Sea hydrates is biogenic methane (99.6% from our geochemical measurements and 93.3–99.7% for the whole Black Sea from Vassilev & Dimitrov, 2003). The stability of methane hydrate is controlled by the following parameters: (1) pore pressure that is given by the hydrostatic condition with a gradient of 10 kPa/m, (2) temperature that is 8.9 °C at the seafloor and increases with depth with a geothermal gradient of 24.5 °C/km (CSF04, Figure 1; Riboulot et al., 2018), (3) salinity is derived from the measured chloride profile over 25 m below the seafloor (mbsf) that decreases from 22 psu at the seafloor to 2 psu at 25 mbsf (Riboulot et al., 2018) and then remains constant down to 400 mbsf (Calvert & Batchelor, 1978).

We also computed the predicted BGHSZ for past conditions during the LGM period (Constantinescu et al., 2015). The sea level reached a low value down to −100/−150 m (Demirbağ et al., 1999; Winguth et al., 2000), and the seawater temperature at the seafloor was estimated to be 4 °C by Soulet et al. (2011). As the Black Sea was a lake, the salinity of the sediment pore water was constant with a value of 2 psu down to 400 mbsf. The GHSZ was simulated using the two-dimensional GH stability model developed by Sultan et al. (2010), in order to take into account the bathymetry profile.

4. Results

4.1. Seismic Observations: Stratigraphy, BSR, and Gas-Related Reflections

4.1.1. Stratigraphy

Three main kinds of seismic facies can be identified on seismic profiles presented in Figure 2: (1) low-amplitude subparallel seismic reflectors related to hemipelagic layers, (2) low-amplitude/transparent seismic facies (in gray) related to small turbidity deposits less than 20-m thick. and (3) low-amplitude chaotic

seismic facies with distinctive internal high amplitude associated with mass transport deposits (in light green). A buried mass transport deposit (MTD) is identified on all seismic profiles acquired to the east of Canyon 1 (Figure 2). The extension of this MTD is limited to the north by the shelf edge and to the east by the crest line. The top of this MTD is found at various depths below the seafloor from 50 to 100 m, and its thickness varies from 20 to 120 m and has an increasing trend seaward and in its eastward extension. Several other MTDs are present on the study area at larger depth below the seafloor but with a lower lateral extension.

Below the crest line area (Figure 2a), a splay of faults can be observed separating subparallel layers and affecting the imaged sedimentary column. Faults termination could not be identified due to a lack of penetration of the seismic signal. At the location of the crest and in its vicinity, large gas flares up to 400-m high rising from the seafloor were detected through water column acoustics. Acoustic signatures of gas flares are superimposed on a deep-towed seismic profile acquired along the same track as profile HR34a in Figure 3. Hydrate samples were collected near the gas flares indicating the coexistence of free gas and gas hydrates within sediments close to the seafloor.

4.1.2. BSR Distribution

Indirect evidence of gas hydrate is related to BSR observation. The BSR identified on HR seismic profiles is mainly characterized by a reversal of the wave polarity compared to the reflection at the seafloor as presented in the close-up of Figure 2a. The BSR can also present aligned terminations of high amplitudes (HR31a and HR34b). The BSR is ubiquitous over the study area except in the eastern part of HR34a. The BSR is indicated by dashed thick lines on the three profiles of Figure 2, and the BSR spatial extent is shown by the blue line in Figure 1. The new acquired seismic data have enabled to update the Popescu et al. (2007) map of the BSR distribution with a more accurate depth location (related to the depth imaging procedure that has been performed). The seaward extension of the area without BSR was not identified.

4.1.3. Gas-Related Reflections

Below the BSR, the presence of free gas is revealed by high-amplitude reflections and high attenuation of the frequency content (close-up of Figure 2). In shallow water depth, outside the GHSZ (Figure 2c), gas-related seismic signatures such as bright spot or velocity pull-down artifact can be observed above the main MTD. In the eastern part of HR34a inside the GHSZ (Figure 2a), no anomalous seismic signature associated with free gas has been identified in the whole sedimentary column.

4.2. Velocity Anomalies as Proxies of Hydrate and Gas Occurrence

4.2.1. Profile HR34a

The eastside of the profile (i.e. the *reference area* in Figure 4a that shows neither evidence of BSR nor gas) exhibits a gentle increase of velocity with depth. The westside of the profile shows a different distribution of the velocity with depth as a velocity inversion (i.e., a sharp decrease of velocity) can be observed precisely at the location of the BSR: high interval velocity (1,700–2,050 m/s) above the BSR and low interval velocity (1,200–1,500 m/s) below the BSR. Consequently, compared to the velocity values measured in the absence of BSR (reference area), positive and negative velocity anomalies exist on either side of the BSR. As the BSR corresponds to the limit of stability of gas hydrates, it can be assessed with high confidence that the high interval velocity (1,700–2,050 m/s) is related to the presence of gas hydrate-bearing sediments and the low interval velocity (1,200–1,500 m/s) is related to free gas-bearing sediments. The highest velocity (2,050 m/s) is observed at the west side of the crest. East of the crest, the positive velocity anomalies, although characterized by lower values, also indicate that the presence of gas hydrate is very likely. The vertical extension of a positive anomaly layer related to hydrate deposit could reach a thickness of 200 m west of the crest, whereas it is limited to a maximum of 100 m to the east.

Low-velocity anomalies observed below the BSR correlated with the decrease in frequency content strongly indicate the presence of free gas. A 30-m thick layer below the shallowest BSR is characterized by the lowest velocity of ~1,200 m/s**.** The maximum offset of the seismic data is too short to constrain through velocity analysis the base of the free gas zone under the BSR.

4.2.2. Profile HR31a

Likewise the seismic profile HR34a, a strong velocity inversion is associated with the presence of the BSR that is located in the southern side of profile HR31a (Figure 4c). A zone of high velocity (1,900–2,050 m/s)

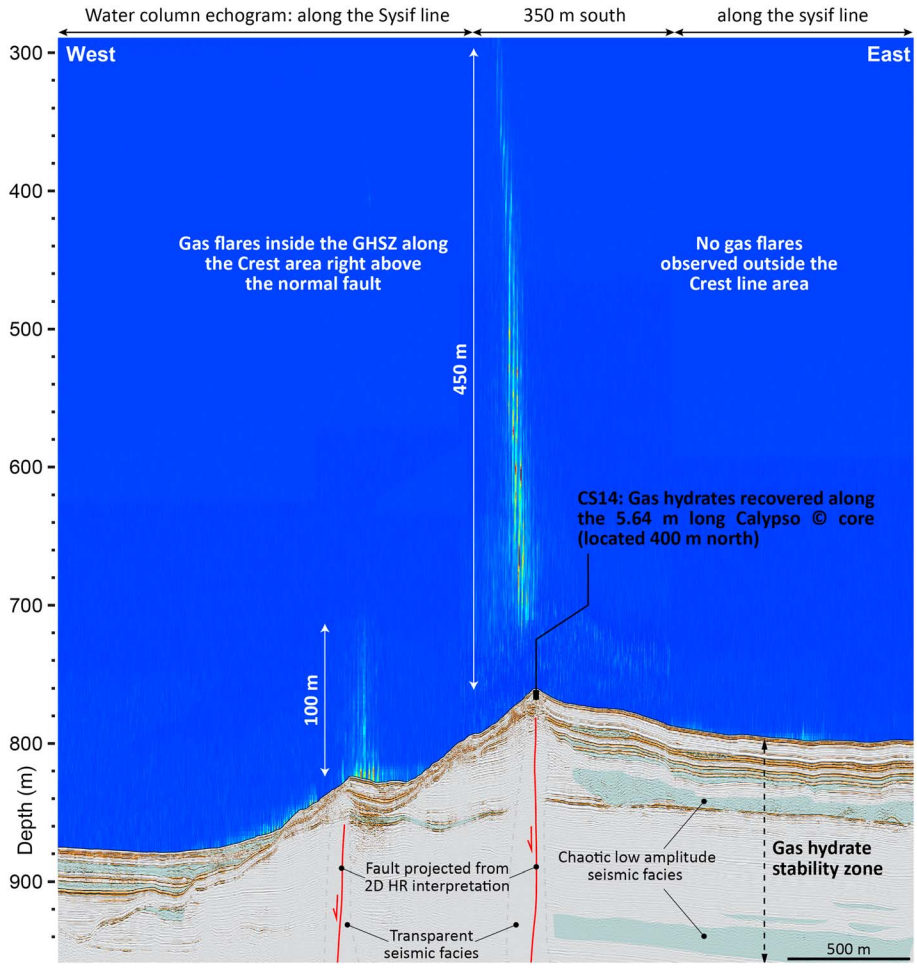

Figure 3. The processed water column echogram along the Sysif line PL01PR07 shows the location of two gas flares above the two vertical discontinuities in the crest line area inside the GHSZ. The acoustic signature of the gas flare has a height of ~400 m. The hydrate samples collected in the vicinity of the crest line area (core CS14) indicate the nature of the gas that is mostly methane (99.6%). Presence of hydrate in the superficial sediment and of free gas in the water column in this area shows the coexistence of free gas and hydrate in the GHSZ. GHSZ = gas hydrate stability zone.

is localized just above the BSR and under a MTD characterized by a *P* wave velocity of about 1,750 m/s. This high-velocity zone is associated with the presence of GH within sediments. Under the BSR, the velocity is low and highly variable laterally with *P* wave velocities ranging from 1,200 to 1,600 m/s. The trend of the velocity is to decrease as the BSR goes deeper toward the southern part of the profile. Outside the GHSZ, in the northern part of the profile, a succession of velocity inversions can be observed related to the obvious presence of free gas (Figure 2c, e.g., bright spots above the MTD).

4.2.3. Profile HR34b

High-resolution velocity analysis cannot be undertaken on the HR34b profile due to the strong 3D nature of the subseafloor, responsible for diffractions and out of plane reflections, and a lack of coherent seismic horizons necessary to perform the MVA approach. We thus applied a conventional approach with a lower resolution and a higher uncertainty but sufficient to detect the main trend of the *P* wave velocity. Dots on the velocity field of the HR34b profile (Figure 4b) indicate the reflection points picked for the semblance analysis that is not fully horizon consistent. A velocity inversion is visible on the whole profile except at the western border, which belongs to the reference area. The thickness of the high-velocity layer above the BSR is about 50 to 100 m. It should be noted that the discrepancy in velocity values at the intersection of profile HR31a is mainly related to the lack of resolution of the conventional approach and to a higher uncertainty related to the high structural complexity of the subseafloor, especially related to the MTD.

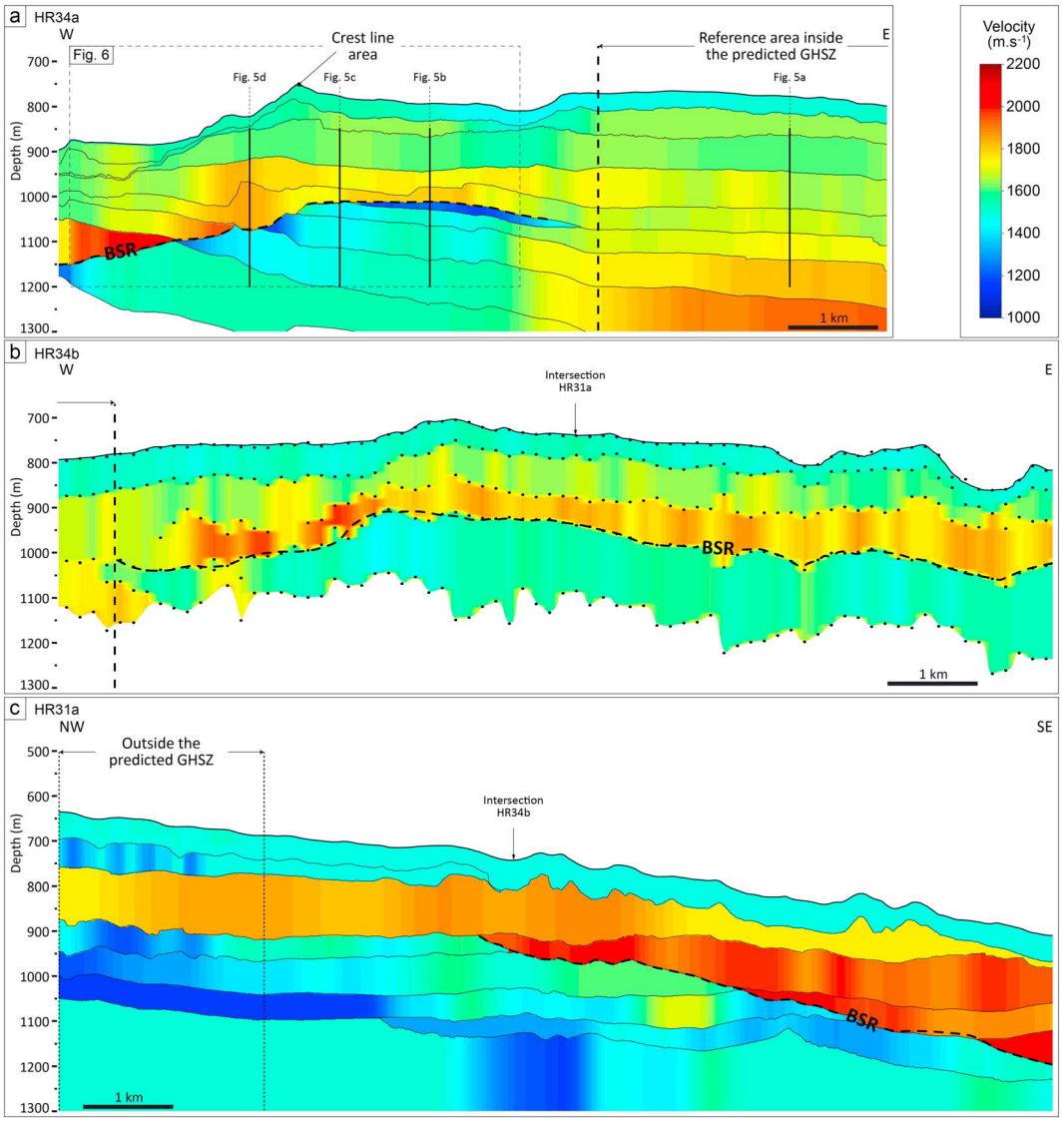

Figure 4. Interval *P* wave velocity field inferred from high-resolution seismic profiles: (a) HR34a, (b) HR34b, and (c) HR 31a. The velocity analysis was performed using a migration velocity analysis for profiles HR34a and HR31a and a conventional NMO approach for profile HR34b. High velocity associated with gas hydrates can be observed just above the BSR with a vertical extension of ~50 to 200 m. Low velocity located under the BSR relates the presence of free gas. The locations of four vertical velocity profiles are indicated on profile HR34a (a): one profile within the reference area, three profiles crossing the velocity inversion related to the BSR (b–d).

4.3. Hydrate and Gas Volumetric Concentration

Estimating hydrate and free gas concentration from effective medium theory requires first to determine a background velocity model for the marine sediments within the studied area. As the reference area presented in Figure 2 appears to be free of gas and gas hydrates, it is a suitable location to determine the reference *P* wave background velocity by calibrating an effective medium model for normally consolidated marine sediments. Mineralogy analyses realized on cores (Ballas et al., 2018) and borehole data available from DSP Leg 42 at site 380 (Calvert & Batchelor, 1978) show that the upper sediments of the Black Sea are mainly composed of clay (60–65%) and quartz (30–35%) and in a smaller proportion calcite (5–10%). In the reference area, the *P* wave velocity derived from seismic data is characterized by a linear gradient of 0.68 s^{-1} that is controlled by the decrease in porosity with depth (Figure 5a dashed blue curve). The inversion of the observed velocity gradient, based on the effective medium model from Dvorkin et al. (1999) and

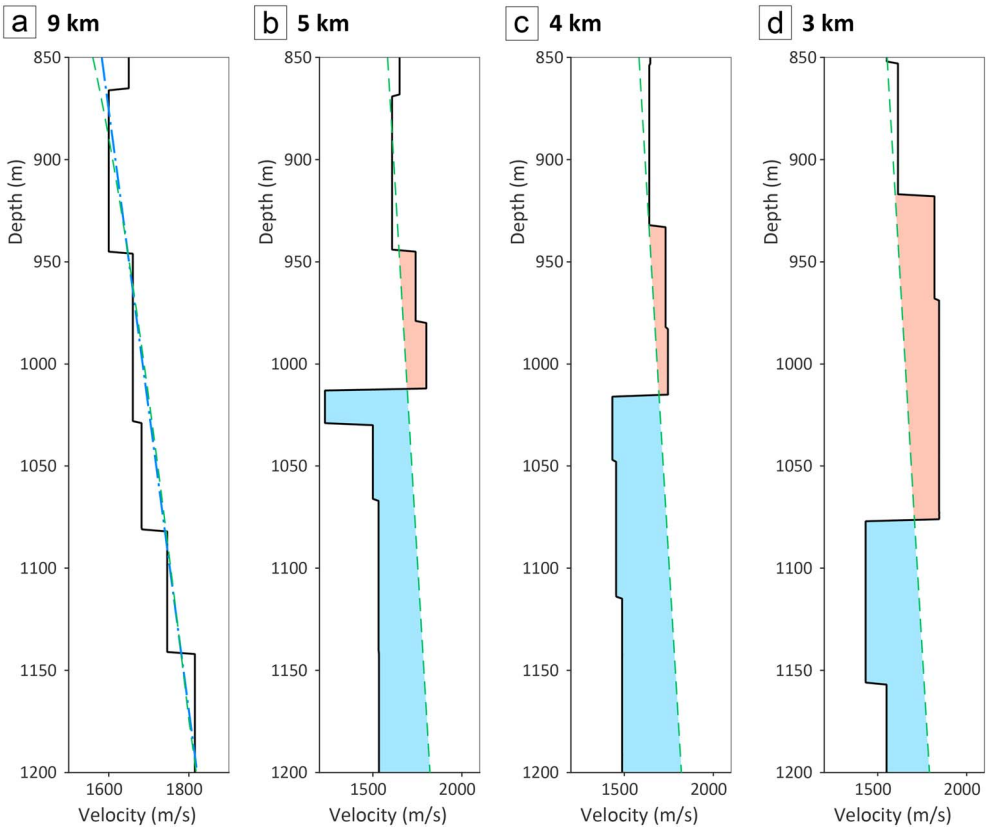

Figure 5. Vertical *P* wave velocity profiles extracted from the velocity field of the HR34a profile. (a) A profile within the reference area (black line), linear velocity gradient representative of the velocity behavior of the reference area (dash-dotted blue line), (b) background velocity (green dashed line) best fitting the linear gradient using effective medium model-based inversion enabling to determine the depth porosity variation. (c and d) Velocity profiles showing positive velocity anomalies (in red) compared to background velocity related to gas hydrates and negative velocity anomalies (in blue) related to free gas.

on the mineralogy defined above, enables to determine the initial void ratio ($e_0 = 4.4$) and the compression index ($C_c = 0.58$) that control the evolution of porosity with the effective stress (or depth) in agreement with Terzaghi's theory (Terzaghi et al., 1996). Based on the deviation to the background velocity (green curves in Figures 5a–5d), we determine positive (red filled area) and negative (blue filled area) velocity anomalies that are used to determine gas hydrate and gas concentration, respectively. Figures 6a and 6b present hydrate volumetric concentrations related to load-bearing and pore-filling hydrate models (Helgerud et al., 1999) inferred from the velocity field of the western part of the profile HR34a. Figure 6c presents the gas volumetric concentration obtained by inversion of *P* wave velocity using the WIFF model from White et al. (1975). A mean size of gas patches of 2 m for the WIFF model was determined by a joint inversion of *P* wave velocity and *Q* value in the area at the eastside of the crest where attenuation could be confidently measured ($Q = 35 \pm 5$). Uncertainties, related to *P* wave velocity, *Q* factor estimates, and poroelastic parameters, were used to quantify a relative error of 30% on gas hydrate and methane volumetric concentrations.

Significant positive velocity anomalies are limited to layers lying just above the BSR. The hydrate concentration has an average value of 5% or 10% considering either the load-bearing or the pore-filling hydrate models. Maximum hydrate concentration is located on the western side of the profile HR34a (15%–22%, Figures 6a and 6b). Negative velocity anomalies under the BSR are related to gas volumetric concentrations of 4–6% except for the upper gas layer where the concentration may reach 12% (Figure 6c). As the uncertainty is about 30%, lateral variation of hydrate or gas concentration has to be cautiously interpreted.

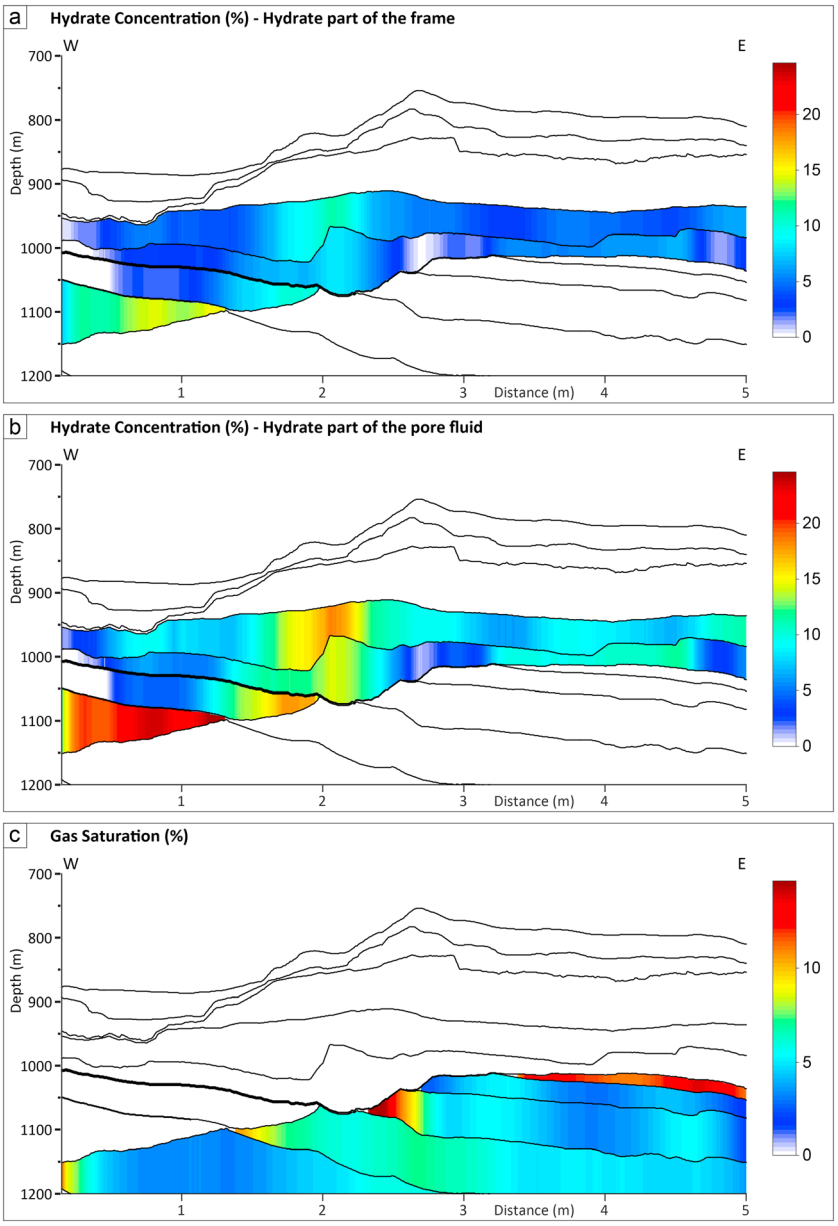

Figure 6. Hydrate volumetric concentration inferred from positive *P* wave velocity anomalies of profile HR34a using effective medium theory (Helgerud et al., 1999): Hydrate considered as part of the frame (a) or as part of the pore fluid (b). (c) Gas volumetric concentration obtained from negative *P* wave velocity anomalies and attenuation quantity (*Q*) using the White et al. (1975) model.

4.4. Results of BGHSZ Modeling

Figure 7 presents the predicted steady state BGHSZ associated with past (LGM) and present conditions for seismic profiles HR34a and HR31a (Figures 7a and 7c, and 7b and 7d respectively). The predicted steady state paleo-BGHSZ related to the LGM is deeper than the current one for both considered LGM conditions of −150 and −100 m for the sea level and a seafloor temperature of 4 °C. The depth of the paleo-BGHSZ associated with the LGM reveals that the thickness of the GHSZ could have been substantially higher than the current one (Figures 7a and 7b). The predicted steady state BGHSZ at present differs from the observed BSR location for both profiles HR34a and HR31a (Figures 7c and 7d, respectively). The BSR depth is located between the deeper-predicted paleo-BGHS and the shallower-predicted BGHS although closer to the present BGHS.

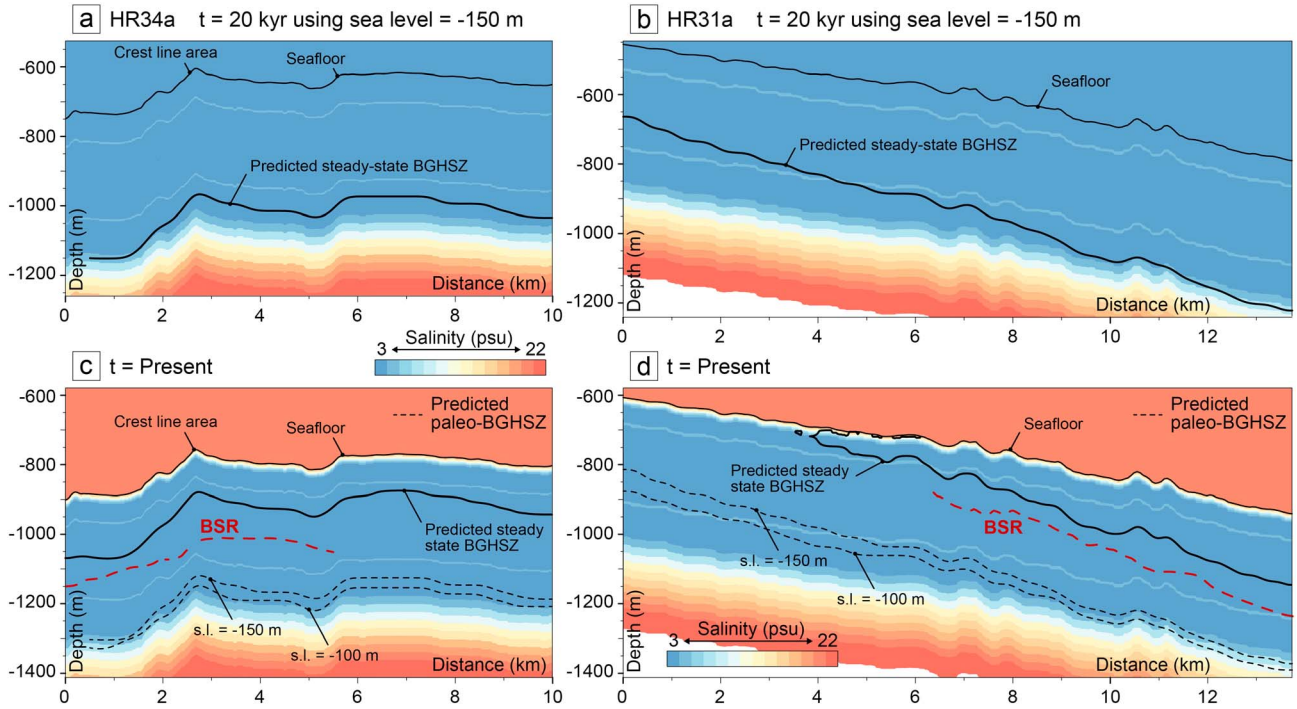

Figure 7. (a and b) Model-predicted steady state BGHS for seismic profiles HR34a and HR31a during the LGM assuming a sea level 150 m below the present sea level. Salinity of sediment pore water is derived from cores for the subsurface and from DSDP hole 379A for the deeper section. Temperature at the seafloor is 8.9 °C at present time and was 4 °C during the LGM; geothermal gradient is 24.5 °C/km. The GHSZ was thicker than at present. (c and d) Predicted BGHS at present (thick black line) and during LGM (dashed line) and observed BSR depths for both HR34a and HR31a profiles. A discrepancy between observed BSR and current predicted BGHSZ is observed. The observed BSR is located between the past and current predicted BGHSZ. GHSZ = gas hydrate stability zone; BGHSZ = base of the gas hydrate stability zone; LGM = Last Glacial Maximum; DSDP = Deep Sea Drilling Project; BSR = bottom-simulating reflector.

5. Discussion

5.1. Hydrates as a Barrier for Gas Migration

The BSR marks the BGHSZ as it corresponds to the interface between high-velocity hydrate-bearing sediments and low-velocity free gas-bearing sediments. The high velocity layer above the BSR is related to the presence of hydrate with a significant volumetric concentration (5–10%). The location of these hydrate deposits is limited to the lower part of the GHSZ close to the BSR with a variable thickness that does not exceed 50–100 m at the landward termination and increases seaward (200 m for the deepest water depth of seismic profile HR31a). Gas hydrates could be present in the upper part of the GHSZ but with a very low concentration (< 2%) as no significant increase in velocity was observed.

Free gas occurrence is ubiquitous below the BSR as indicated by the drop in *P* wave velocity and outside the GHSZ where it can be observed close to the seafloor from gas-related signatures and low-velocity zones (Figure 8c). Outside the GHSZ, the free gas can migrate up to the seafloor and escapes into the water column and generates gas flares (Riboulot et al., 2017). Within the GHSZ, gas flux from deeper sources is converted to hydrates, which impede the upward vertical gas migration by reducing the permeability of marine sediments. This result is in accordance with theoretical (Nimblett & Ruppel, 2003) and experimental investigations (Chuan-Hui et al., 2014; Johnson et al., 2011) attesting a permeability reduction by 1 to 2 orders of magnitude related to the presence of hydrates.

It has to be highlighted that within the reference area where no BSR is observed, neither positive nor negative velocity anomalies were detected as well as no gas-related seismic signatures. In this area, the lack of gas migration path prevents the gas reaching the upper part of the sedimentary column and forming gas hydrates.

The fact that the GHSZ acts as a permeability barrier for gas migrating from deeper sediments into the water column is a well-known process (Ginsburg & Soloviev, 1997; Naudts et al., 2006). However, this study

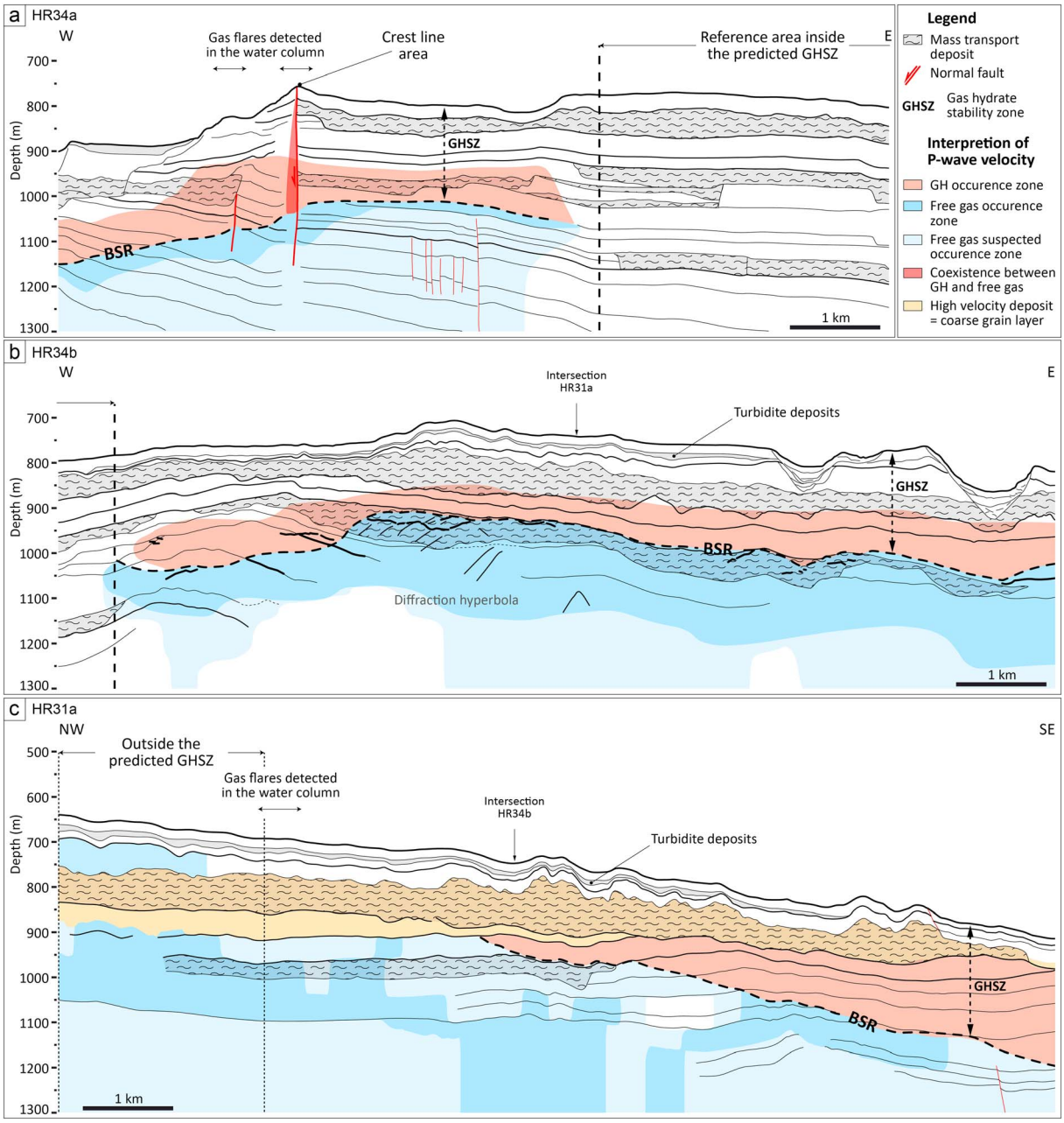

Figure 8. Interpreted seismic profiles (a) HR 34a, (b) HR34b, and (c) HR31a showing hydrate deposits (in red) and the free gas occurrence zone (in blue). Hydrate deposits are located close to the BSR with a vertical extension up to 50–200 m. BSR (bold dash line) is located between model-predicted steady state BGHS at present and during the LGM. On profile HR34a (Figure 8a), the BSR is only located in the western part of the profile. The fault system above the crest line is characterized by the coexistence between gas hydrates and free gas. BSR = bottom-simulating reflector; GHSZ = gas hydrate stability zone; LGM = Last Glacial Maximum.

enables to establish that an ~50- to 100-m thick deposit of hydrate located close to the BSR with a volumetric concentration of 5–10% is sufficient to clog the system and prevent upward free-gas migration.

5.2. Transient State of the Gas Hydrate System

We note a discrepancy between computed BGHSZ and observed BSR depth with a misfit up to 100 m (Figures 7c and 7d). Previous studies focused on investigating the cause of BGHSZ/BSR mismatch on different margins (Flemings et al., 2003; Hornbach et al., 2004; Plaza-Faverola et al., 2017; Xu & Ruppel, 1999).

Phrampus et al. (2014), for instance, observed a similar phenomenon on the upper U.S. Beaufort margin, and the discrepancy was mainly attributed to significant warming of intermediate ocean temperatures.

For the case of the Western Black Sea, we explore four main hypotheses that may explain that the observed BSRs is deeper than the predicted steady state BGHSZ:

1. different composition of gas or water than the ones measured in situ and used in the calculation of the thermodynamic stability of gas hydrates (Dickens & Quinby-Hunt, 1997; Plaza-Faverola et al., 2017; Popescu et al., 2006),
2. inaccurate geothermal gradient values and possible spatial variation (Grevemeyer & Villinger, 2001; Minshull & Keddie, 2010; Yamano et al., 1982),
3. a transient state of the hydrate system related to the nonequilibrium of the thermal regime (Phrampus et al., 2014), and
4. a transient state of the hydrate system related to the excess pore pressure generated by hydrate dissociation.

Phrampus et al. (2014) investigated other phenomena to explain anomalously deep BSR observed on the upper U.S. Beaufort margin as erosion/sedimentation effects and uplift, but these processes are not relevant to our study area of the Romanian margin. Indeed, the sediment rate in the studied zone presented here is 14 cm/kyr, so the most recent unit since the end of the LGM is about 2-m thick (forthcoming publication). This sedimentation rate is in agreement with the one of Soulet et al. (2011) calculated on a core 20 km northeast of our zone by 350-m water depth. The mass transport complexes detected on seismic data are older than the LGM. The sedimentation has no effect on the evolution of the GHSZ since the LGM.

1. *Difference in gas or water composition*. The gas composition was obtained by analysis of gas hydrate samples from the upper part of the hydrate stability zone in the vicinity of a fault system (crest line area, Figure 1), allowing the migration of free gas through the GHSZ. The hydrates formed in the first 6 m of sediment below the seafloor entrapped biogenic methane accumulated under the BGHS. We consider that the gas entrapped in recovered hydrates is representative of the gas composition related to this sector of the Black Sea. The pore water composition is freshwater 25 m below the seafloor down to 400 m (Deep Sea Drilling Project hole 379A). Consequently, difference in gas or water composition is unlikely to be responsible for the discrepancy between observed BSR and computed BGHSZ.
2. *The nonequilibrium of the thermal regime*. Poort et al. (2005) show a transient state of the thermal regime in the whole Black Sea following the LGM. In order to assess if the thermal regime is in a transient state or at equilibrium in the study area, we perform 1D modeling based on the resolution of the differential equation governing the temperature variation down to 350 m below the seafloor. The initial temperature is set at 4 °C at the seafloor at the moment of the connection between the Black and the Mediterranean Seas (9 kyr before present; Soulet et al., 2011). The present temperature of the water is 8.9 °C. We use a range of values for the thermal diffusivity of marine sediments from $1 \cdot 10^{-7}$ to $5 \cdot 10^{-7}$ m^2/s. We do not consider the presence of gas hydrates in our modeling. The evolution of the temperature with depth computed for a seafloor at 800-m water depth is shown in Figure 9. The thermal modeling shows that the temperature equilibrium has been reached since 2 or 3 kyr before present for the lowest thermal diffusivity. Despite seafloor temperature changes since the LGM or 9 kyr ago, we consider that the thermal readjustment is complete and does not impact on the current GHSZ.
3. *The value of the geothermal gradient and its possible spatial variability*. We perform the inversion of the geothermal gradient for the seismic profiles HR34a and HR31a by matching the modeled BGHSZ and observed BSR depth. Figures 10a and 10b present the derived spatial variations of the geothermal gradient inverted along both seismic profiles. We take into account uncertainties on depth locations (due to *P* wave velocity uncertainties) to evaluate the uncertainty on the geothermal gradient (gray area) that can reach 0.5 °C/km. Figures 10c and 10d present the statistical distribution of inverted geothermal gradients. For the seismic profile HR34a, the range of variations is very large (16–24 °C/km) with an occurrence peak at 19.5 °C/km. The lowest value at 16 °C/km occurs at the location of the fault system right above the crest area. For the seismic profile HR31a, the range of variation is narrower (17.5–21.5 °C/km) with an occurrence peak at 20.5 °C/km. These inversion results indicate that a geothermal gradient value of ~20 °C/km could enable a better fit with the current depth of the observed BSR compared to the one of 24.5 ± 0.2 °C/km used for the modeling and derived from in situ

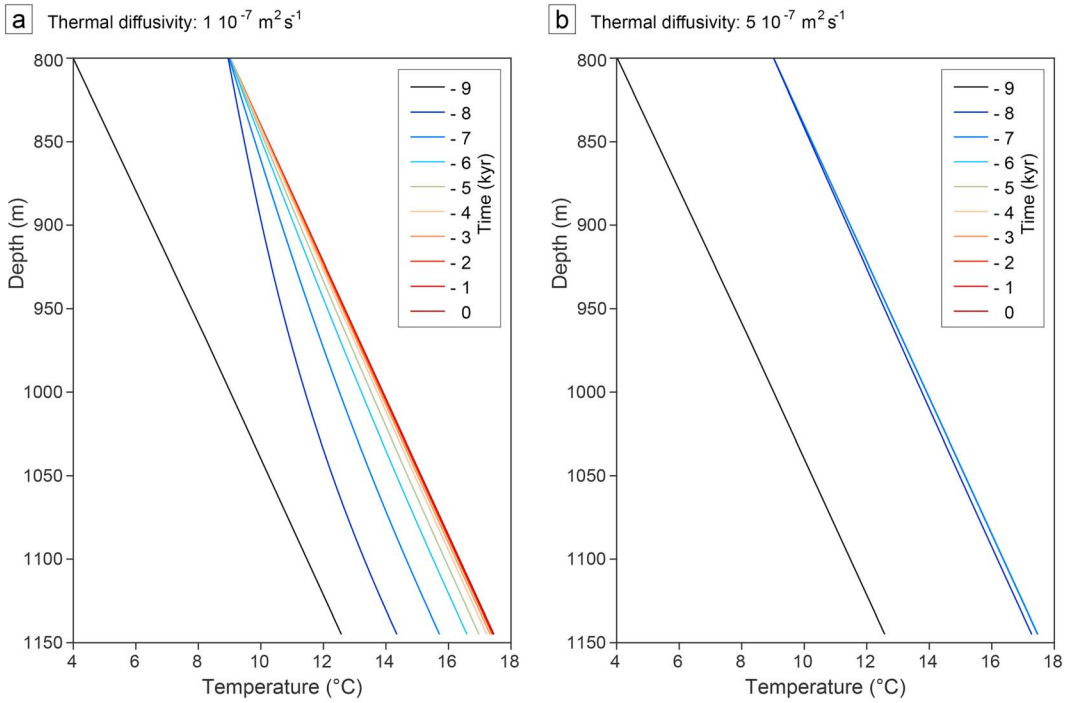

Figure 9. One-dimensional modeling of the temperature variation below the seafloor (800-m water depth) during the last 9 kyr. The initial temperature is 4 °C at the seafloor at the moment of the connection between the Black and the Mediterranean Seas (9 kyr before present). The present temperature of the water is 8.9 °C. The modeling was performed using two values for the thermal diffusivity of marine sediments: $1 \cdot 10^{-7}$ (a) and $5 \cdot 10^{-7}$ m^2/s (b).

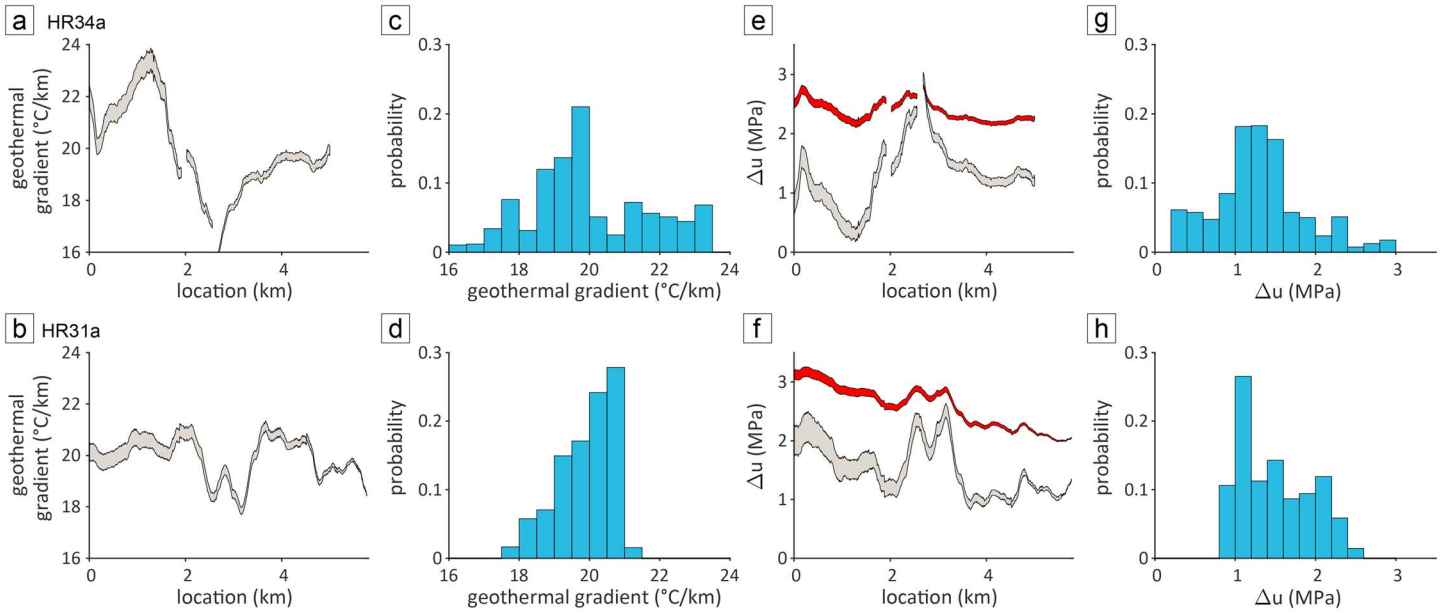

Figure 10. Lateral variation (a, b, e, and f) and statistical (c, d, g, and h) distribution of inferred geothermal gradient (°C/km) and maximum excess pore pressure Δu (MPa) from BSR depth for seismic profiles HR34a and HR31a, respectively. The gray area represents the uncertainty in geothermal gradient and Δu estimates associated with the uncertainty in BSR depth. The red area in Figures 10e and 10f represents the effective stress with its uncertainty. BSR = bottom-simulating reflector.

measurements (Riboulot et al., 2018). However, a geothermal gradient of 20 °C/km would make the observed BSR above the predicted steady state BGHS in numerous locations on both seismic profiles. A possible mechanism responsible for such BSR depth anomalies is difficult to argue. The very large range of variations (up to 8 °C/km) appears to be very unlikely in such a short distance of 2 km. Indeed, the nature of the subseafloor allows to exclude rapid lateral variation of marine sediment thermal conductivity. Furthermore, the presence of methane hydrate can be neglected when considering first-order thermal conductivity (Waite et al., 2009). Lastly, the geothermal gradient might be affected by rising warm fluid at the crest location connected to the deeper part of the basin by a fault system, but instead of high geothermal gradient values, the lowest values of profile HR34a are obtained.

4. Excess pore pressure due to the migration of the BGHS over recent geological history. Overpressure conditions in the free-gas zone right under the BGHS could lead to form hydrate below the theoretical thermodynamic conditions (Tinivella & Giustiniani, 2013). But, as the observed BSR depth is located between the current and the LGM predicted steady state BGHS, we suppose that the gas hydrate layer formed right above the BGHS during the LGM is brought outside the stability conditions when sea level and seafloor temperature rise. The modification of the general gas hydrate thermodynamic conditions generates gas hydrate dissociation producing a free gas/water mixture that will increase pore pressure. Sultan (2007a, 2007ab) showed that before reaching a reequilibrium, the hydrate system is in a transient regime in which excess pore pressure generated by hydrate dissociation enables the recrystallization of part of the hydrate and delays the hydrate dissociation process. This phenomenon produces a metastable thermodynamic state where gas and gas hydrates coexist. The upper bound of excess pore pressure Δu can be estimated from the difference between the hydrate equilibrium pressure corresponding to the temperature at the current BSR depth and the pressure at the current BSR depth (Sultan, 2007b). We use this approach to derive Δu for both seismic profiles by using a constant geothermal gradient of 24.5 °C/km and by taking into account uncertainty in BSR depths. The spatial variation is displayed in Figures 10e and 10f. The statistical distribution of Δu is presented in Figures 10g and 10h. As the inverted Δu depends on BSR depth, its spatial distribution is anticorrelated with the one of the inverted geothermal gradient. The uncertainty in Δu can reach up to 0.5 MPa, but the mean uncertainty is 0.2 MPa. For HR34a, the maximum pore pressure varies in the range (0.26–3 MPa) with a peak occurrence at 1.2 MPa. The highest values of Δu (2–3 MPa) are located above the crest line area and are close to the effective stress values (in red). For HR31a, the maximum pore pressure varies in the range (0.8–2.5 MPa) with a peak occurrence at 1.1 MPa. Δu values are almost everywhere lower than 80% of the effective stress values (in red).

The lateral variation of inverted excess pore pressure could be related to variation in hydrate-bearing sediment permeability. High hydrate concentration may imply low permeability of sediments and high Δu values. Δu values of ~3 MPa at the crest line area could generate the required hydrofracturing process allowing to break hydrates located inside the fault and permitting the upward fluid migration emerging at the seafloor. This high excess pressure may not be only related to hydrate dissociation but also to free-gas accumulation coming from deeper reservoirs.

An Δu value of about 1–2 MPa may indicate the efficiency of gas hydrates to lower the fluid circulation capacity of the system. Such high Δu values may explain why the current state of the hydrate system has not yet reached a steady state as the pressure reequilibrium is a long term process (as an example, a dissipation of 0.5 MPa takes about 10 kyr at 200 bsf and a permeability of 10^{-9} m^2). This phenomenon appears to be a self-preserving behavior of gas hydrates that impedes the hydrate system dissociation. The impact of this high excess pore pressure exceeding at the same locations as 70% of the vertical effective stress is expected to drastically reduce sediment stability and could be the source of some of the observed landslides in the area.

5.3. Main Mechanisms Controlling the Evolution of the Hydrate System

In Figure 11, we propose a schematic hydrate system view to represent the main observed features offshore the western Black Sea and the mechanisms controlling its evolution.

1. The hydrate system is characterized by a dynamic transient regime at the top of the GHSZ related to change in salinity of sediment pore water since the reconnection between the Mediterranean and Black Seas, which generates a migration of the landward termination of the GHSZ (Riboulot et al., 2018). The GHSZ also migrates upward in response to past temperature and sea level changes since

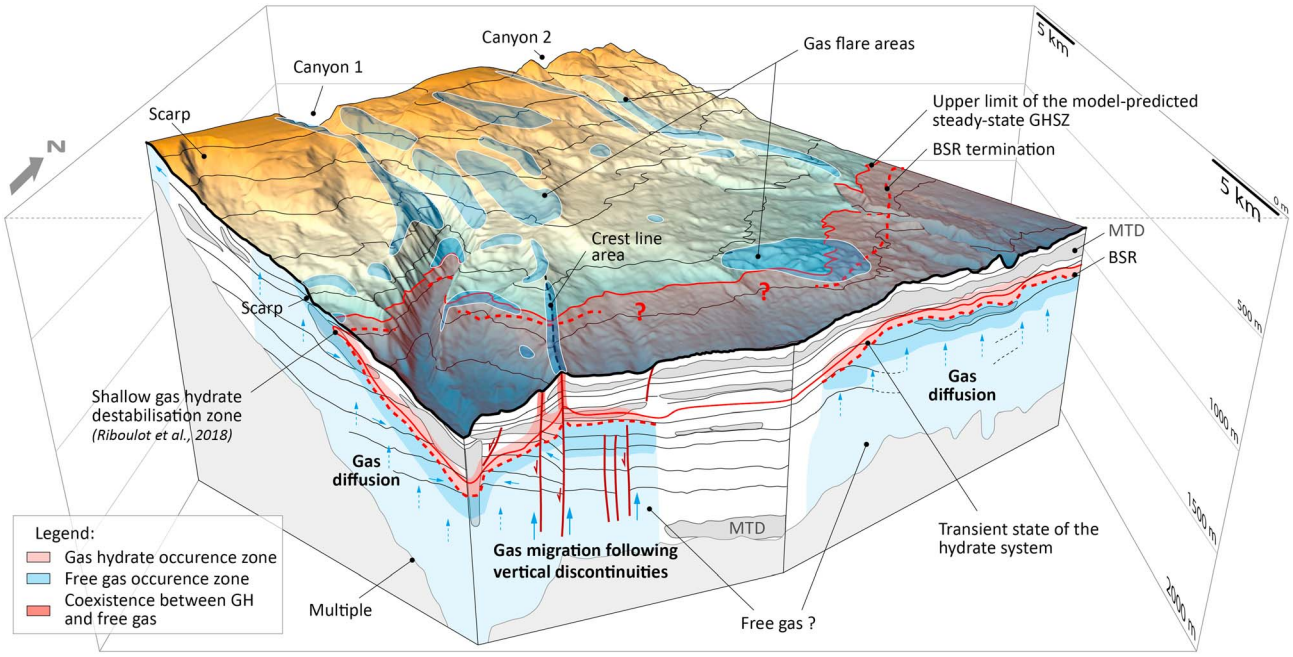

Figure 11. Three-dimensional interpretative view of the hydrate system of the Romanian margin. Gas hydrate deposits with significant concentrations (5–10%) are located in the lower part of the GHSZ with a vertical extension of 50–200 m. Hydrate deposits impede the upward migration of free gas coming from a deeper part of the margin. Gas flares observed at the seafloor inside the GHSZ are located at the crest line connected to a fault system enabling gas migration and the coexistence with gas hydrates. The hydrate system is currently in transient state associated with (1) a migration of the BGHS related to a reequilibrium in response to the evolution of controlling factors of gas hydrate stability since the Last Glacial Maximum (this study) and (2) a migration of the landward termination related to the salinization of sediments (Riboulot et al., 2018). GHSZ = gas hydrate stability zone.

the LGM (Figure 7), a mechanism highlighted by Ruppel and Kessler (2017). This upward migration could be slowed down by excess pore pressure associated with hydrate dissociation explaining an anomalously deep BSR.

2. The hydrate-bearing sediment system is dominated by a concentration of 5–10% (light red, Figure 11) that clogs the upward gas migration. Outside the GHSZ, the free gas reaches the seafloor producing a large number of gas flares in the water column (dashed blue arrows). In the GHSZ, under the BGHSZ, sedimentary layers are characterized by the absence of discontinuities and vertical gas migration pathways although locally disturbed in the crest area by a fault system. The accumulation of free gas under the BGHS is interpreted as the result of a long lasting process dominated by gas diffusion.
3. Locally, hydrofracturing produced by excess pore pressure associated with hydrate dissociation and free-gas supply from deeper reservoirs enables a significant flux of free gas to cross the GHSZ by using preexisting faults in the crest area and reach the seafloor producing free-gas seepages within the hydrate stability zone. In the crest line area, hydrate nodules were sampled at shallow depths (< 10 m) below the seafloor. The fault system is thus characterized by the coexistence of free gas and gas hydrates (dark red area, Figure 11).

6. Conclusion

Based on the integrated analysis of geophysical data and modeling of GHSZ, we show the following.

1. The occurrence of hydrate deposits with a volumetric concentration of 5–10% limited to the lower part of the GHSZ with a mean thickness of 50–100 m reduces sediment permeability and prevents upward free-gas migration by clogging the fluid system in the GHSZ.
2. The observed leakages escaping from the gas hydrate barrier are related to excess pore pressure enabling the free gas to cross the GHSZ and reach the seafloor at the crest line area by using a preexisting fault system. This fault system is characterized by the coexistence of free gas and hydrates.

3. A discrepancy exists between observed BSR and model-predicted steady state BGHSZ. The observed BSR depth is located between the depths of both present and past predicted steady state BGHSZ. The shift in BSR depth could be mainly the result of a current transient state of the hydrate system related to excess pore pressure localized at the BGHSZ due to gas hydrate dissociation as thermodynamic conditions have changed since the LGM. This excess pore pressure enables the recrystallization of hydrate delaying the system in reaching equilibrium and is expected to drastically reduce sediment stability and could be the source of some of the observed landslides in the area.
4. The BSR, which is commonly used as a proxy to derive geothermal gradient values in steady state conditions, could be used to derive maximum excess pore pressure of 1–2 MPa at the BGHSZ when it is in transient state.

While gas hydrate systems have been recognized and described worldwide, we show through this multidisciplinary study the complexity of having a comprehensive view of hydrate dynamics over time without considering all the intrinsic parameters involved in the formation and evolution of gas hydrates.

Acknowledgments
The support by officers and crew during the GHASS cruise on board R/V *Pourquoi Pas?* (2015) is greatly appreciated, as is the dedication of the Genavir and Ifremer technical staff during the cruise. We thank Andreia Plaza Faverola and an anonymous reviewer for their comments that help us to improve this paper. We thank sincerely Alison Chalm and Shane Murphy for the revision of the English language. We thank L. Ruffine for insightful discussion. Data sets used in the current study are acquired during the GHASS expedition (10.17600/15000500), and data set information are available in the GHASS cruise report (http://archimer.ifremer.fr/doc/00300/41141). Data are available from the SISMER website (http://data.ifremer.fr).

References

Al-Yahya, K. (1989). Velocity analysis by iterative profile migration. *Geophysics*, *54*(6), 718–729. https://doi.org/10.1190/1.1442699

Ballas, G., Garziglia, S., Sultan, N., Pelleter, E., Toucanne, S., Marsset, T., et al. (2018). Influence of early diagenesis on geotechnical properties of clay sediments (Romania, Black Sea). *Engineering Geology*, *240*, 175–188. https://doi.org/10.1016/j.enggeo.2018.04.019

Calvert, S. E., & Batchelor, C. H. (1978). *Major and minor element geochemistry of sediments from Hole 379A, Leg 42B, Deep-Sea Drilling Project, Initial Reports of the Deep Sea Drilling Project* (Vol. 42, pp. 527–541). Washington, DC: Government Printing Office.

Carcione, J. M., & Picotti, S. (2006). P-wave seismic attenuation by slow-wave diffusion: Effects of inhomogeneous rock properties. *Geophysics*, *71*(3), O1–O8. https://doi.org/10.1190/1.2194512

Chuan-Hui, L., Qian, Z., Hong-Jun, X., Kai, F., & Xue-Wei, L. (2014). Relation between relative permeability and hydrate saturation in Shenhu area, South China Sea. *Applied Geophysics*, *11*, 207–214.

Constantinescu, A. M., Toucanne, S., Dennielou, B., Jorry, S. J., Mulder, T., & Lericolais, G. (2015). Evolution of the Danube deep-sea fan since the Last Glacial Maximum: New insights into Black Sea water-level fluctuations. *Marine Geology*, *367*, 50–68. https://doi.org/10.1016/j.margeo.2015.05.007

Crutchley, G. J., Fraser, D. R. A., Pecher, I. A., Gorman, A. R., Maslen, G., & Henrys, S. A. (2015). Gas migration into gas hydrate-bearing sediments on the southern Hikurangi margin of New Zealand. *Journal of Geophysical Research: Solid Earth*, *120*, 725–743. https://doi.org/10.1002/2014JB011503

Davies, R. J., Morales Maqueda, M. A., Li, A., & Ganopolski, A. (2017). Millennial-scale shifts in the methane hydrate stability zone due to Quaternary climate change. *Geology*, *45*(11), 1027–1030. https://doi.org/10.1130/G39611.1

Demirbağ, E., Gökaşan, E., Oktay, F. Y., Simsek, M., & Yüce, H. (1999). The last sea level changes in the Black Sea: Evidence from seismic data. *Marine Geology*, *157*(3-4), 249–265. https://doi.org/10.1016/S0025-3227(98)00158-3

Dickens, G. R., & Quinby-Hunt, M. S. (1997). Methane hydrate stability in pore water; a simple theoretical approach for geophysical applications. *Journal of Geophysical Research*, *102*(B1), 773–783. https://doi.org/10.1029/96JB02941

Dvorkin, J., Prasad, M., Sakai, A., & Lavoie, D. (1999). Elasticity of marine sediments. *Geophysical Research Letters*, *26*(12), 1781–1784. https://doi.org/10.1029/1999GL900332

Flemings, P. B., Liu, X., & Winters, W. J. (2003). Critical pressure and multiphase flow in Blake ridge gas hydrates. *Geology*, *31*(12), 1057–1060. https://doi.org/10.1130/G19863.1

Ginsburg, G. D. (1998). Gas hydrate accumulation in deep-water marine sediments. *Geological Society, London, Special Publications*, *137*(1), 51–62. https://doi.org/10.1144/GSL.SP.1998.137.01.04

Ginsburg, G. D., & Soloviev, V. A. (1997). Methane migration within the submarine gas-hydrate stability zone under deep-water conditions. *Marine Geology*, *137*(1-2), 49–57. https://doi.org/10.1016/S0025-3227(96)00078-3

Gorman, A. R., Holbrook, W. S., Hornbach, M. J., Hackwith, K. L., Lizarralde, D., & Pecher, I. (2002). Migration of methane gas through the hydrate stability zone in a low-flux hydrate province. *Geology*, *30*(4), 327–330. https://doi.org/10.1130/0091-7613(2002)030<0327:MOMGTT>2.0.CO;2

Greinert, J., McGinnis, D. F., Naudts, L., Linke, P., & De Batist, M. (2010). Atmospheric methane flux from bubbling seeps: Spatially extrapolated quantification from a Black Sea shelf area. *Journal of Geophysical Research*, *115*, C01002. https://doi.org/10.1029/2009JC005381

Grevemeyer, I., & Villinger, H. (2001). Gas hydrate stability and the assessment of heat flow through continental margins. *Geophysical Journal International*, *145*(3), 647–660. https://doi.org/10.1046/j.0956-540x.2001.01404.x

Helgerud, M. B., Dvorkin, J., Nur, A., Sakai, A., & Collett, T. (1999). Elastic-wave velocity in marine sediments with gas hydrates—Effective medium modeling. *Geophysical Research Letters*, *26*(13), 2021–2024. https://doi.org/10.1029/1999GL900421

Holbrook, W. S., Hoskins, H., Wood, W. T., Stephen, R. A., & Lizarralde, D. (1996). Methane hydrate and free gas on the Blake ridge from vertical seismic profiling. *Science*, *273*(5283), 1840–1843. https://doi.org/10.1126/science.273.5283.1840

Hornbach, M. J., Saffer, D. M., & Holbrook, W. S. (2004). Critically pressured free-gas reservoirs below gas-hydrate provinces. *Nature*, *427*(6970), 142–144. https://doi.org/10.1038/nature02172

Johnson, A., Patil, S., & Dandekar, A. (2011). Experimental investigation of gas-water relative permeability for gas-hydrate bearing sediments from the Mount Elbert gas hydrate stratigraphic test well, Alaska north slope. *Marine and Petroleum Geology*, *28*(2), 419–426. https://doi.org/10.1016/j.marpetgeo.2009.10.013

Ker, S., & Le Gonidec, Y. (2018). Fractional integration of seismic wavelets in anelastic media to recover multiscale properties of impedance discontinuities. *Geophysics*, *83*(2), V61–V71. https://doi.org/10.1190/geo2017-0527.1

Marsset, B., Ker, S., Thomas, Y., & Colin, F. (2018). Deep-towed high resolution seismic imaging II: Determination of P-wave velocity distribution. *Deep Sea Research: Part I-Oceanographic Research Paper*, *132*, 29–36.

Marsset, B., Menut, E., Ker, S., Thomas, Y., Regnault, J. -P., Leon, P., et al. (2014). Deep-towed high resolution multichannel seismic imaging. *Deep Sea Research Part I: Oceanographic Research Paper*, *93*, 83–90.

Marsset, B., Thomas, Y., Sultan, N., Gaillot, A., & Stephan, Y. (2012). A multi-disciplinary approach to marine shallow geohazard assessment. *Near Surface Geophysics*, *10*(4), 279–288. https://doi.org/10.3997/1873-0604.2012012

Merey, S., & Sinayuc, C. (2016). Investigation of gas hydrate potential of the Black Sea and modelling of gas production from a hypothetical class 1 methane hydrate reservoir in the Black Sea conditions. *Journal of Natural Gas Science and Engineering*, *29*, 66–79. https://doi.org/10.1016/j.jngse.2015.12.048

Minshull, T. A., & Keddie, A. (2010). Measuring the geotherm with gas hydrate bottom-simulating reflectors: A novel approach using three dimensional seismic data from the eastern Black Sea. *Terra Nova*, *22*(2), 131–136. https://doi.org/10.1111/j.1365-3121.2010.00926.x

Müller, T., Gurevich, B., & Lebedev, M. (2010). Seismic wave attenuation and dispersion resulting from wave-induced flow in porous rock—A review. *Geophysics*, *75*(5), 75A147–75A164.

Naudts, L., De Batist, M., Greinert, J., & Artemov, Y. (2009). Geo-and hydroacoustic manifestations of shallow gas and gas seeps in the Dnepr paleodelta, northwestern Black Sea. *The Leading Edge*, *28*(9), 1030–1040. https://doi.org/10.1190/1.3236372

Naudts, L., Greinert, J., Artemov, Y., Staelens, P., Poort, J., Van Rensbergen, P., & De Batist, M. (2006). Geological and morphological setting of 2778 methane seeps in the Dnepr paleo-delta, northwestern Black Sea. *Marine Geology*, *227*, 177–199.

Nimblett, J., & Ruppel, C. (2003). Permeability evolution during the formation of gas hydrates in marine sediments. *Journal of Geophysical Research*, *108*(B9), 2420. https://doi.org/10.1029/2001JB001650

Phrampus, B. J., Hornbach, M. J., Ruppel, C. D., & Hart, P. E. (2014). Widespread gas hydrate instability on the upper U.S. Beaufort margin. *Journal of Geophysical Research: Solid Earth*, *119*, 8594–8609. https://doi.org/10.1002/2014JB011290

Plaza-Faverola, A., Vadakkepuliyambatta, S., Hong, W.-L., Mienert, J., Bünz, S., Chand, S., & Greinert, J. (2017). Bottom simulating reflector dynamics at Arctic thermogenic gas provinces: An example from Vestnesa ridge, offshore west Svalbard. *Journal of Geophysical Research: Solid Earth*, *122*, 4089–4105. https://doi.org/10.1002/2016JB013761

Plaza-Faverola, A., Westbrook, G. K., Ker, S., Exley, J. K., Gailler, A. R., Minshull, T. A., & Broto, K. (2010). Evidence from three-dimensional seismic tomography for a substantial accumulation of gas hydrate in a fluid-escape chimney in the Nyegga pockmark field, offshore Norway. *Journal of Geophysical Research*, *115*, B08104. https://doi.org/10.1029/2009JB007078

Podvin, P., & Lecomte, I. (1991). Finite difference computation of traveltimes in very contrasted velocity models. A massively parallel approach and its associated tools. *Geophysical Journal International*, *105*(1), 271–284. https://doi.org/10.1111/j.1365-246X.1991.tb03461.x

Poort, J., Vassilev, A., & Dimitrov, L. (2005). Did postglacial catastrophic flooding trigger massive changes in the Black Sea gas hydrate reservoir? *Terra Nova*, *17*(2), 135–140. https://doi.org/10.1111/j.1365-3121.2005.00599.x

Popescu, I., De Batist, M., Lericolais, G., Nouzé, H., Poort, J., Panin, N., et al. (2006). Multiple bottom-simulating reflections in the Black Sea: Potential proxies of past climate conditions. *Marine Geology*, *227*(3-4), 163–176. https://doi.org/10.1016/j.margeo.2005.12.006

Popescu, I., Lericolais, G., Panin, N., De Batist, M., & Gillet, H. (2007). Seismic expression of gas and gas hydrates across the western Black Sea. *Geo-Marine Letters*, *27*(2-4), 173–183. https://doi.org/10.1007/s00367-007-0068-0

Quan, Y., & Harris, J. M. (1997). Seismic attenuation tomography using the frequency shift method. *Geophysics*, *62*(3), 895–905. https://doi.org/10.1190/1.1444197

Riboulot, V., Cattaneo, A., Scalabrin, C., Gaillot, A., Jouet, G., Ballas, G., et al. (2017). Control of the geomorphology and gas hydrate extent on widespread gas emissions offshore Romania. *Bulletin de la Societe Geologique de France*, *188*(26).

Riboulot, V., Ker, S., Sultan, N., Thomas, Y., Marsset, B., Scalabrin, C., et al. (2018). Freshwater lake to salt-water sea causing widespread hydrate dissociation in the Black Sea. *Nature Communications*, *9*(1). https://doi.org/10.1038/s41467-017-02271-z

Ruppel, C. D., & Kessler, J. D. (2017). The interaction of climate change and methane hydrates. *Reviews of Geophysics*, *55*, 126–168. https://doi.org/10.1002/2016RG000534

Sarkar, S., Berndt, C., Minshull, T. A., Westbrook, G. K., Klaeschen, D., Masson, D., et al. (2012). Seismic evidence for shallow gas-escape features associated with a retreating gas hydrate zone offshore west Svalbard. *Journal of Geophysical Research*, *117*, B09102. https://doi.org/10.1029/2011JB009126

Shipley, T. H., Houston, M. H., Buffler, R. T., Shaub, F. J., McMillen, K. J., Ladd, J. W., & Lamar Worzel, J. (1979). Seismic evidence for widespread possible gas hydrate horizons on continental slopes and rises. *AAPG Bulletin*, *63*, 2204–2213.

Soulet, G., Ménot, G., Lericolais, G., & Bard, E. (2011). A revised calendar age for the last reconnection of the Black Sea to the global ocean. *Quaternary Science Reviews*, *30*(9-10), 1019–1026. https://doi.org/10.1016/j.quascirev.2011.03.001

Sultan, N. (2007a). Excess pore pressure and slope failures resulting from gas-hydrates dissociation and dissolution, Offshore Technology Conference, 30 April-3 May 2007, Houston, Texas, U.S.A. ISBN 978-1-55563-254-0. OTC-18532-MS, 1–9.

Sultan, N. (2007b). Comment on "Excess pore pressure resulting from methane hydrate dissociation in marine sediments: A theoretical approach" by Wenyue Xu and Leonid N. Germanovich. *Journal of Geophysical Research*, *112*, B02103. https://doi.org/10.1029/2006JB004527

Sultan, N., Marsset, B., Ker, S., Marsset, T., Voisset, M., Vernant, A.-M., et al. (2010). Hydrate dissolution as a potential mechanism for pockmark formation in the Niger delta. *Journal of Geophysical Research*, *115*, B08101. https://doi.org/10.1029/2010JB007453

Terzaghi, K., Peck, R. B., & Mesri, G. (1996). *Soil mechanics in engineering practice* (3rd ed.p. 549). New York: John Wiley.

Tinivella, U., & Giustiniani, M. (2013). Variations in BSR depth due to gas hydrate stability versus pore pressure. *Global and Planetary Change*, *100*, 119–128. https://doi.org/10.1016/j.gloplacha.2012.10.012

Vassilev, A., & Dimitrov, L. (2003). Model evaluation of the Black Sea gas hydrates. *Annals of Bulgarian Academy of Sciences*, *56*, 3–15.

Waite, W. F., Santamarina, J. C., Cortes, D. D., Dugan, B., Espinoza, D. N., Germaine, J., et al. (2009). Physical properties of hydrate-bearing sediments. *Reviews of Geophysics*, *47*, RG4003. https://doi.org/10.1029/2008RG000279

White, J. E., Mikhaylova, N. G., & Lyakhovitskiy, F. M. (1975). Low-frequency seismic waves in fluid saturated layered rocks. Izvestija Academy of Sciences USSR. *Physics of the Solid Earth*, *11*, 654–659.

Winguth, C., Wong, H. K., Panin, N., Dinu, C., Georgescu, P., Ungureanu, G., et al. (2000). Upper Quaternary water level history and sedimentation in the northwestern Black Sea. *Marine Geology*, *167*(1-2), 127–146. https://doi.org/10.1016/S0025-3227(00)00024-4

Xu, W., & Ruppel, C. (1999). Predicting the occurrence, distribution, and evolution of methane gas hydrate in porous marine sediments. *Journal of Geophysical Research*, *104*(B3), 5081–5095. https://doi.org/10.1029/1998JB900092

Yamano, M., Uyeda, S., Aoki, Y., & Shipley, T. H. (1982). Estimates of heat flow derived from gas hydrates. *Geology*, *10*(7), 339–343. https://doi.org/10.1130/0091-7613(1982)10<339:EOHFDF>2.0.CO;2

Yefremova, A. G., & Zhizhchenko, B. P. (1974). Gas hydrate occurrences in offshore deposits. *DAN SSSR (Proceedings of the USSR Academy of Sciences)*, *214*, 1179–1181.

Zander, T., Haeckel, M., Berndt, C., Chi, W.-C., Klaucke, I., Bialas, J., et al. (2017). On the origin of multiple BSRs in the Danube deep-sea fan, Black Sea. *Earth and Planetary Science Letters*, *462*, 15–25. https://doi.org/10.1016/j.epsl.2017.01.006

GEOPHYSICS, VOL. 85, NO. 5 (SEPTEMBER-OCTOBER 2020); P. B161–B172, 12 FIGS.
10.1190/GEO2019-0686.1

Check for updates

Downloaded 08/01/20 to 134.246.166.26. Redistribution subject to SEG license or copyright; see Terms of Use at https://library.seg.org/page/policies/terms
DOI:10.1190/geo2019-0686.1

Case History

Fine-scale velocity distribution revealed by datuming of very-high-resolution deep-towed seismic data: Example of a shallow-gas system from the western Black Sea

Florent Colin[1], Stéphan Ker[1], and Bruno Marsset[1]

ABSTRACT

Very-high-resolution (VHR) marine seismic reflection helps to identify and characterize potential geohazards occurring in the upper part (300 m) of the subseafloor. Although the lateral and vertical resolutions achieved in shallow water depths (< 200 m) using conventional surface-towed technology are adequate, these resolutions quickly deteriorate at greater water depths. The SYstème SIsmique de Fond (SYSIF), a multichannel deep-towed seismic system, has been designed to acquire VHR data (frequency bandwidth [220–1050 Hz] and vertical resolution of 0.6 m) at great water depths. However, the processing of deep-towed multichannel data is challenging because the source and the receivers are constantly moving with respect to each other according to the towing configuration. We have introduced a new workflow that allows the application of conventional processing algorithms to extended deep-towed seismic data sets. First, a relocation of the source and receivers is necessary to obtain a sufficiently accurate acquisition geometry. Variations along the profile in the depth of the deep-towed system result in a complex geometry in which the source and receiver depth vary separately and do not share the same acquisition datum. We have designed a dedicated datuming algorithm to shift the source and receivers to the same datum. Thus, the procedure allows the application of conventional processing algorithms to perform velocity analysis and depth imaging and therefore allows access to the full potential of the seismic system. We have successfully applied this methodology to deep-towed multichannel data from the western Black Sea. In particular, the derived velocity model highlights shallow gas charged anticline structures with unrivaled resolution.

INTRODUCTION

Quantitative characterization of shallow marine sediments combining in situ geotechnical measurements and very high resolution (VHR, frequencies > 200 Hz) seismic data is of first interest for assessing marine geohazards such as slope stability, shallow gas, or gas hydrates (Kvalstad, 2007; Vanneste et al., 2014; Clare et al., 2017; Badhani et al., 2020a). In deep-water environments, 2D VHR seismic acquisitions performed at the sea surface suffer from major limitations such as the recording of out-of-plane reflections due to a large first Fresnel zone and a lack of penetration (Chapman et al., 2002; Ker et al., 2010). To overcome these limitations, deep-towed seismic systems have been developed since the 1990s allowing seismic acquisitions close to the seafloor in water depths up to a few kilometers (Ward et al., 2004; Badhani et al., 2020b). The first multichannel deep-towed seismic system, the Deep-Towed Acoustics/Geophysics System (DTAGS) developed by the U.S. Naval Research Laboratory (Gettrust et al., 1988), successfully investigated gas-hydrate systems (Rowe and Gettrust, 1993; Wood et al., 2002). More recently, a second multichannel deep-towed seismic system, called SYstème SIsmique de Fond (SYSIF), was developed by Ifremer (Marsset et al., 2014) enabling the acquisition of seismic data with submetric vertical resolution. The efficiency of joint analysis of SYSIF data with in situ measurements (i.e., from core

Manuscript received by the Editor 18 October 2019; revised manuscript received 2 May 2020; published ahead of production 14 June 2020; published online 28 July 2020.
[1]Ifremer, REM-GM, Centre de Brest, BP 70, Plouzané 29280, France. E-mail: florent.colin@ifremer.fr (corresponding author); stephan.ker@ifremer.fr; bruno.marsset@ifremer.fr.
© 2020 Society of Exploration Geophysicists. All rights reserved.

Downloaded 08/01/20 to 134.246.166.26. Redistribution subject to SEG license or copyright; see Terms of Use at https://library.seg.org/page/policies/terms
DOI:10.1190/geo2019-0686.1

analysis and penetrometer tests) has been demonstrated for thin layer quantification (Ker et al., 2011), slope failures (Ker et al., 2010), pockmarks characterization (Sultan et al., 2010; de Prunelé et al., 2017), and hydrate-systems assessment (Sultan et al., 2011).

An effective approach to the quantitative characterization of gas-charged layers or hydrate bearing sediments lies in detecting compressional-wave (P-wave) velocity anomalies (Tóth et al., 2014). However, processing deep-towed seismic data to perform velocity analysis is challenging due to the particular acquisition geometry (Walia and Hannay, 1999; Marsset et al., 2014). Towing a seismic system at a given altitude over the sea bottom requires constant depth adjustments. Such acquisition at variable depths results in a strong variability in the multichannel streamer's shape, unlike VHR surface acquisitions performed on a constant datum (i.e., 1–2 m below the sea surface).

Alternative processing approaches have been developed for DTAGS and SYSIF to build a fine-scale velocity model of the subsurface. For DTAGS, the shape of the streamer is retrieved through a combination of depth measurements and traveltimes using a genetic algorithm (He et al., 2009). Then, the seismic data are propagated to a flat datum by applying static corrections via a sliding window accounting for the change of raypaths with increasing depth. The process thus allows the application of conventional processing algorithms based on normal moveout (NMO) corrections for velocity analysis (Walia and Hannay, 1999; He et al., 2009). However, the use of static corrections can affect the coherency of acoustic data, especially in a VHR context and, thus, acoustic velocity estimations. For SYSIF, a different strategy based on local pitch measurements along the streamer was developed to reconstruct its shape and access the positions of the receivers (Marsset et al., 2014). Then, a migration velocity analysis (MVA) using a Kirchhoff-migration technique was implemented to build a velocity model (Marsset et al., 2018). The MVA technique is based on layer stripping and thus requires a large amount of time and computational effort to process a single profile. The algorithm requires computing traveltime maps using an eikonal solver (Podvin and Lecomte, 1990) to update the velocity model for each source/receivers position and each investigated velocity value. Finally, prestack depth migrations (PSDMs) are performed to form common image gathers (CIGs). Consequently, the NMO technique appears more suited, as a first step, to perform an initial comprehensive velocity characterization of an extended survey. Such large data set is acquired by SYSIF in the western Black Sea in 650 m water depth during the Gas Hydrates, fluid Activities and Sediment deformations in the western Black Sea (GHASS) cruise (Ker and Riboulot, 2015) with 30 deep-towed seismic profiles.

To enable the use of an NMO analysis, the seismic data have to be corrected to simulate an acquisition at a constant datum. For this purpose and to avoid the approximations involved in the use of static corrections, we propose a new procedure that applies a wave-equation datuming (Berryhill, 1979) to deep-towed seismic data. This technique provides an improvement in deep-towed seismic data processing because it does not require any assumption regarding the sediment velocity and also preserves the wavefield characteristics. The main difficulties in adapting standard seismic techniques for deep-towed seismic imaging lie in reconstructing very accurately the streamer's shape, which varies along the profile, and dealing with the asymmetry of the acquisition geometry where source and receivers do not share the same datum. The first part of this paper addresses the positioning processing and datuming of the data. Once the source and receivers' depth variations have been corrected to a common datum, the seismic data can then be sorted in common-midpoint (CMPs) gathers, enabling an NMO-based velocity analysis. In the second part, we present the fine-scale velocity distribution obtained by applying a semblance analysis on a seismic line of the data set. We assess the velocity uncertainty, and we quantify the impact of the altitude on the analysis. These results enable us to delineate and characterize gas-charged layers and free gas migration paths in the shallow subseafloor (<50 m) with a resolution impossible to obtain from surface-towed seismic systems.

SYSIF ACQUISITION

System description

SYSIF is a deep-towed multichannel VHR seismic acquisition system specifically developed by Ifremer to operate down to water depths of 6000 m. The embedded JH220-6000 source is an open-cavity Janus-Helmholtz transducer producing a 100 ms linear frequency-modulated signal [220–1050 Hz] with an output level of 196 dB reference 1 μPa at 1 m (Le Gall and Marsset, 2007; Ker et al., 2010). The tow fish is equipped with a pressure sensor for depth measurement and an altimeter for altitude measurement; its location relative to the ship is provided by an acoustic ultrashort baseline (USBL) (Marsset et al., 2014).

A 110 m multichannel streamer developed for deepwater acquisitions is towed behind the source. It is composed of 52 digital hydrophones with a 2 m spacing (first offset 10.1 m). Each receiver is coupled to a microelectromechanical system (MEMS) to measure its orientation (pitch, roll, and yaw angles) during the acquisition. In addition to orientation measurements, the electronic boards embedded in the hydrophones perform the digital conversion of the seismic data (10 kHz) after band-pass filtering [150–3000 Hz]. The data are transmitted to the ship through an optical cable using the Ethernet protocol. For design consideration, the streamer is composed of four independent sections including 13 receivers and two Ethernet switches each.

During seismic acquisition, the source is towed at a constant altitude above the seafloor between 50 and 130 m. The altitude choice is a trade-off between the safety of the system (i.e., a safe altitude above large variations in the bathymetry) and the imaging aperture (i.e., proximity to the target). The source is towed at 1 m/s and fired every 2–3 s. The time interval between two shots is chosen carefully before the acquisition to ensure that no multiple reflection from the previous recording window is present in the active one (Marsset et al., 2014).

Absolute source location

The altitude of the tow fish is measured by a Kongsberg 1007 altimeter, with a resolution of 0.15 m. A Digiquartz 8CB7000 depth sensor provides the immersion of the tow fish; its accuracy is 0.01% full scale, or 0.7 m. The altitude and immersion values are combined to produce a bathymetric profile of the acquisition.

The water velocity is obtained from several expendable conductivity-temperature-depth (xCTD) vertical profiles down to the maximum depth of the study area (approximately 1000 m) with a maximum uncertainty of 0.15 m/s. No lateral variation of the seawater velocity has been observed from the three xCTD profiles acquired in the area. The absolute location of the system is validated

Downloaded 08/01/20 to 134.246.166.26. Redistribution subject to SEG license or copyright; see Terms of Use at https://library.seg.org/page/policies/terms
DOI:10.1190/geo2019-0686.1

by comparing the tow-fish bathymetry and the one acquired by the ship multibeam echosounder extracted at the USBL positions.

Signal processing

Due to the proximity of the system to the seafloor, the 100 ms length of the sweep causes overlapping of the direct and reflected wave signals. A specific processing step based on a short-term Fourier transform is applied to isolate the two signals and to mute the direct wave (Marsset et al., 2018).

The acoustic sweep source signal requires further processing such as deconvolving to produce a narrow wavelet, consistent with the VHR approach of the system. The far-field source signature was recorded during a previous cruise, which allows the deconvolution of the data to obtain a narrow, zero-phase wavelet (Ker et al., 2010).

Acquisition parameters of the GHASS survey

Data acquired during the GHASS cruise in the Romanian sector of the Black Sea in 2015 are used as a case study to demonstrate these new techniques. SYSIF was deployed during the cruise to record more than 300 km of deep-towed VHR seismic lines. Profile PL03PR06 was selected to illustrate the proposed processing workflow. The profile is composed of 1863 shots for a total length of approximatively 5000 m; the shot spacing is 2.7 m on average. The water depth averages 660 m, and the source was towed 50 m above the seafloor. Two subprofiles are presented: PL03PR06α (shotpoints 667 to 917) and PL03PR06β (shotpoints 667 to 1863). The average water velocity is $c = 1482$ m/s at the depth of the subprofiles and shows no evidence of lateral variation.

VARIABLE ARRAY SHAPE

Excellent knowledge of the acquisition geometry is essential for the processing of VHR data because inaccuracies will cause destructive summation and dramatically reduce the resolution. This loss in resolution is first evaluated; a relocation procedure is then presented to retrieve the variable array geometry.

Impact of the geometry on imaging performance

We first quantify the resolution capacity of the VHR deep-towed system. This quantification is achieved by assessing the size of the focusing pattern related to the migration of a diffraction point. Vertical and lateral resolutions are obtained by measuring the trough-to-trough vertical width (Kallweit and Wood, 1982) and the horizontal full width at half-maximum (de Souza, 2014) of the migration pattern. It should be noted that the horizontal resolution value represents the maximum resolution as the horizontal resolution decreases with depth.

We simulate the acquisition of a diffraction point embedded in a homogeneous medium using the far-field signature of the Janus-Helmholtz transducer (220–1050 Hz). We model the acquisition of a single shot gather in which the diffraction point is located 50 m below the source and at a lateral position of 56 m behind the source. The streamer's shape is defined as being horizontal. Kirchhoff migration is applied to the shot gather using the exact velocity and a 10 cm bin size. Using the exact geometry, this results in a horizontal resolution of 1.5 m and a vertical resolution of 0.6 m.

To define the resolution loss associated to the receivers' position errors, constant Gaussian noise is added to the receivers' position with a standard deviation σ_{noise}, multiple values are used from 0.05 to 0.8 m. We perform the forward modeling and the migration of the shot gather for 2000 simulations of the Gaussian process to evaluate the degradation of both resolutions for each σ_{noise}. The progressive loss of resolution with increasing σ_{noise} is presented in Figure 1. These results allowed us to estimate the expected loss of resolution after determining the accuracy of the relocation algorithm.

Navigation data processing

The depth variations of the tow fish propagate along the streamer similar to an elastic wave. This fluctuating geometry causes changes in the source-receiver's offsets. MEMS sensors located inside each hydrophone record the pitch and heading angles to determine the streamer's shape and thus the receiver's location (Marsset et al., 2014, 2018). In the acquisition area, deep sea currents are expected to reach on average 0.05 m/s and no more than 0.20 m/s (Korotaev et al., 2006; Markova, 2016). Given that the acquisition is conducted much faster, at 1 m/s on average, no significant feathering is expected to affect the streamer. Therefore, the shape of the streamer is reconstructed only by using pitch measurements.

The raw pitch values are corrected from sensor bias, filtered and integrated along the streamer to obtain the vertical and horizontal offsets x_r^i and z_r^i of each receiver ("the MEMS geometry") as follows:

$$\begin{cases} x_r^i = x_0 + \int_0^{r^i} \cos[\alpha(r)]dr \\ z_r^i = \int_0^{r^i} \sin[\alpha(r)]dr, \end{cases} \tag{1}$$

where r^i is the curvilinear abscissa of the ith receiver from the head of the streamer and α is the pitch angle at position r down the streamer. The curvilinear distance between two receivers is 2 m. The curvilinear distances between the head of the streamer and the 1st and 52nd receivers are 8 and 110 m, respectively. The additional $x_0 = 2.1$ m in horizontal offset corresponds to the distance between the acoustic barycenter of the transducer and the towing point of the streamer (Figure 2).

The accuracy of this reconstruction is evaluated by comparing traveltimes of the direct wave arrivals and the acoustic wave reflected at the seafloor picked on seismic data t_{obs}^i with the computed values $t_{\text{calc}}^i(\alpha)$ expressed as

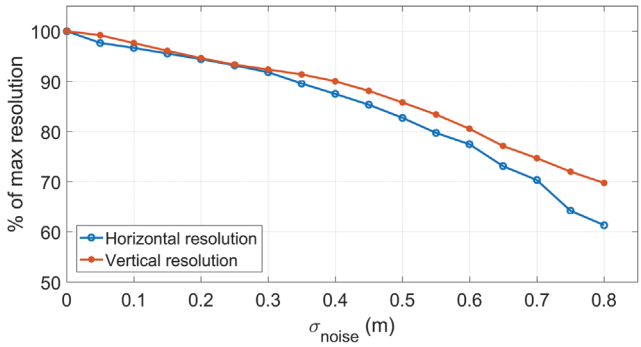

Figure 1. Loss of horizontal and vertical resolutions as a function of σ_{noise}. In total, there are 2000 runs per σ_{noise} value.

Downloaded 08/01/20 to 134.246.166.26. Redistribution subject to SEG license or copyright; see Terms of Use at https://library.seg.org/page/policies/terms
DOI:10.1190/geo2019-0686.1

$$t^i_{\text{calc}}(\alpha) = \begin{cases} t^i_{\text{dir}} = d^i_{\text{dir}} \cdot c^{-1} \\ t^i_{\text{floor}} = d^i_{\text{floor}} \cdot c^{-1}, \end{cases} \quad (2)$$

with

$$d^i_{\text{dir}} = \sqrt{(x^i_r)^2 + (z^i_r)^2}, \quad (3)$$

and

$$d^i_{\text{floor}} = \sqrt{(x^i_{\text{floor}})^2 + (z^i_{\text{floor}})^2} + \sqrt{(x^i_r - x^i_{\text{floor}})^2 + (z^i_r + z^i_{\text{floor}})^2}, \quad (4)$$

where d^i_{dir} and t^i_{dir} are the direct distance and traveltime from the source to the ith receiver, d^i_{floor} and t^i_{floor} are the distance and traveltime of the seafloor reflected wave to the ith receiver, x^i_{floor} is the horizontal distance between the ith receiver and the reflection point on the seafloor for the reflected wave reaching the ith receiver, and z^i_{floor} is the vertical distance between the ith receiver and the seafloor at the reflection point. Note that x^i_{floor} and z^i_{floor} vary with the known bathymetry of the area, the vertical and horizontal offsets of the receiver, and the altitude of the source. Figure 2 presents the different parameters of equations 2–4.

Values of picked and computed traveltimes and their differences are presented in Figure 3 for a given shot record. The average error of approximately 0.8 ms corresponds to an error of 1.2 m in the position of the receivers (for a constant water velocity of 1482 m/s, measured by xCTD probes). Marsset et al. (2018) apply a static shift to reduce this discrepancy and obtain time misfits ranging from 0.1 to 0.7 ms. If this correction improves the quality of the data summation, it also introduces errors in retrieving the P-wave velocity values. We propose a new approach to avoid the former issue and reduce the positioning uncertainties. The method aims to retrieve an accurate acquisition geometry based on the inversion of the seismic arrival times to refine pitch angle values used in the streamer shape reconstruction.

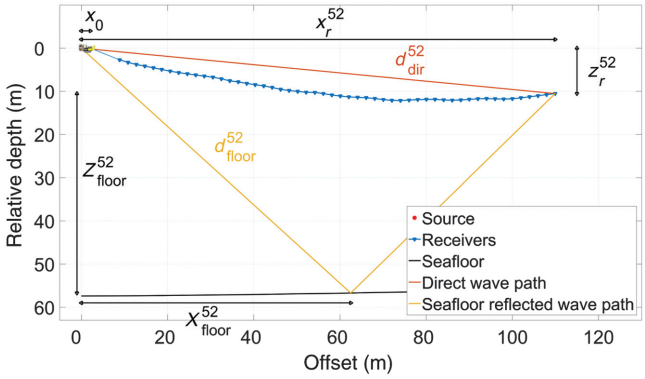

Figure 2. Description of an average acquisition configuration for the deep-towed multichannel seismic acquisition SYSIF. The tow fish is not to scale with the streamer. The distances d^i_{floor}, z^i_{floor}, and x^i_{floor} depend on the depth of the source and receiver as well as the slope of the seafloor.

Array shape reconstruction

To retrieve the streamer shape, the traveltime misfits between the observed and computed values using equation 2 are computed using the least-squares method. The cost function for the relocation inverse problem is defined as

$$S = \min_{\alpha(r)} \sum_i \{t^i_{\text{calc}}[\alpha(r^i)] - t^i_{\text{obs}}\}^2. \quad (5)$$

The relocation inverse problem consists in finding 53 pitch angles values (i.e., one value per receiver and an additional one at the connection between the tow fish and the lead-in cable) from 104 traveltime observations. The curvilinear spacing of 2 m between two consecutive receivers and the smooth shape variation of the streamer also constrain the inversion. We use a local optimization method (the trust region approach; Byrd et al., 1988) to solve this inverse problem, and we use the MEMS pitch angles as initial values to start the search for the minimum value of S.

While preserving the general trend of the pitch values measured by the MEMS (Figure 4a), the inversion retrieves a sine-like event in the streamer shape with a series of peaks and troughs (Figure 4b). The troughs correspond to the positions of the Ethernet switches, which are embedded in titanium containers and have a mass of 1.3 kg. The streamer is neutrally buoyant as a whole, but these denser components (the black dots in Figure 4b) cause the streamer to be locally denser than seawater, which causes local deformations of the streamer.

The mean time misfit for the direct wave and the seafloor reflected wave are approximately 0.18 and 0.10 ms, respectively (the green curves in Figure 5). An increased time misfit toward the tail of the streamer can be observed on both traveltimes in Figure 5a and 5b. The average time misfit for the seafloor reflected wave increases to 0.25 ms for the last 10 receivers in comparison to less than 0.1 ms for the first 30. This increasing misfit can be related to several factors such as a larger uncertainty in picked arrival times, a less constrained streamer tail or an unaccounted-for streamer feathering.

These results translate to positioning uncertainties of 0.27 and 0.15 m, respectively, which correspond to a maximum loss of resolution of approximately 8% (Figure 1). This loss in resolution decreases the theoretical vertical resolution to 0.65 m and the maximum horizontal resolution to 1.62 m for a homogeneous medium and an exact velocity model.

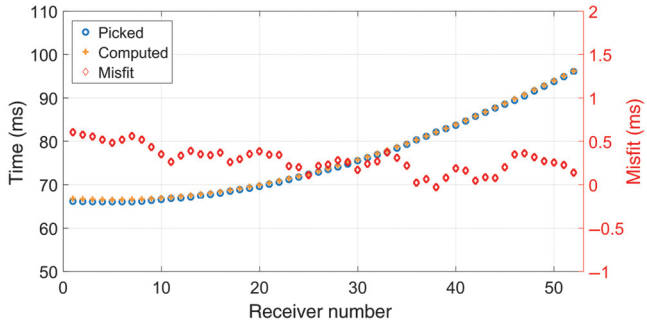

Figure 3. Seafloor-reflected wave traveltimes picked on the seismic data and computed using the MEMS streamer's geometry for shot 823. Differences in traveltimes between the picked values and the one computed using the MEMS geometry (the red diamonds).

Downloaded 08/01/20 to 134.246.166.26. Redistribution subject to SEG license or copyright; see Terms of Use at https://library.seg.org/page/policies/terms
DOI:10.1190/geo2019-0686.1

The results of the relocation procedure are evaluated with the comparison of the profile PL03PR06α, from the GHASS cruise, processed using the initial MEMS geometry and the one obtained after correction. Figure 6 displays both images obtained after a Kirchhoff PSDM using a constant velocity model of 1482 m/s.

WAVE-EQUATION DATUMING

Complex acquisition geometries can be found in UHR shallow-towed seismic acquisitions where the swell can affect the positions of the sources and receivers. However, swell-related motions are limited to a couple of meters and can be corrected with the application of statics corrections (Duarte et al., 2017; Reiche et al., 2020). In the case of deep-towed multichannel acquisitions, the vertical offsets can vary up to several tens of meters and the horizontal offset up to several meters. These large variations prove to be an issue for the processing of deep-towed data because conventional marine seismic imaging algorithms are usually tailored for data presenting only small depth variations of the sources and receivers, usually neglected or corrected accurately enough with statics corrections. An analogy for such a geometry can be found in land seismic acquisition, where the altitude of the sources and receivers can differ greatly. Therefore, the processing of land seismic data commonly includes a datuming phase; that is, the sources and receivers are moved to a constant altitude.

One elementary way to perform datuming is to apply small static corrections to traveltimes in the simplest cases to correct for altitude deviations, for example, small deviations from the reference altitude and low raypath emergence angles (Barison et al., 2011). However, for significant topographic variations, an exact wavefield propagation is necessary to accurately upward or downward continue the data to a reference datum. This action of correcting the acquisition datum by wavefield continuation is called wave-equation datuming (WED) and was first introduced by Berryhill (1979).

The acoustic signal recorded at a single receiver can emerge from various angles. Therefore, if we were to propagate the wave to a distinct datum, different time corrections would be needed depending on the emergence angles. Based on this observation, Berryhill proposes a Kirchhoff integral formulation for his WED to propagate the seismic data to a reference datum while preserving the wavefield character of the data (Berryhill, 1979, 1984, 1986).

Theory of WED

For nonzero offset data, the Kirchhoff integral is applied in two successive stages (Bevc, 1996). The following notation is used in the description of the algorithm:

- "Input" traces — the original traces. The acoustic signals are emitted at the acquisition source positions and recorded at the acquisition receiver positions (x_r, z_r).
- "Intermediate" traces — the traces after the first stage of processing. The signals are emitted at the acquisition source positions and recorded at the datumed receiver positions.
- "Datumed" traces — the traces at the output of the algorithm. The signals are emitted at the datumed source positions and recorded at the datumed receiver positions.

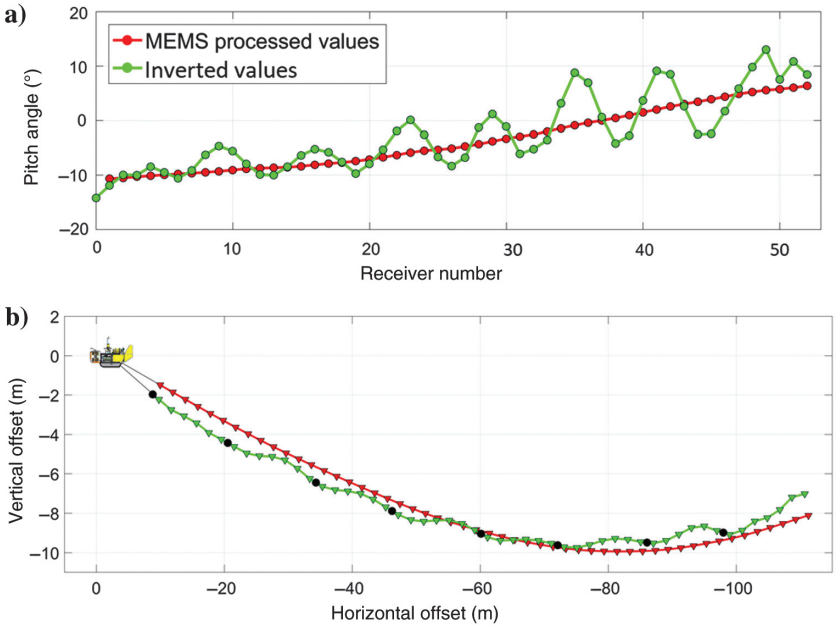

Figure 4. (a) Measured and inverted pitch values for shot 823. The inverted pitch value at the 0 abscissa corresponds to the lead-in cable. (b) Corresponding MEMS and inverted geometries (vertical exaggeration: 3.0).

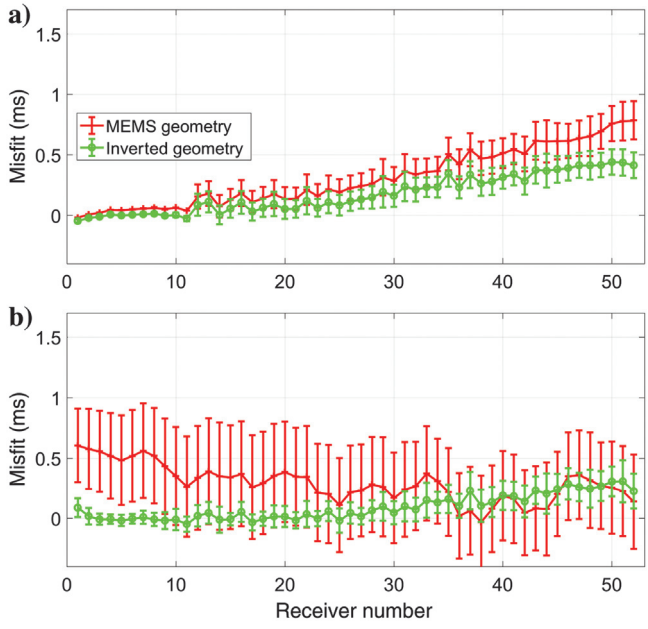

Figure 5. Average differences between t_{calc} computed using the MEMS geometry (the red curve) or the inverted geometry (the green curve) and t_{obs} for profile PL03PR06α, (a) direct wave and (b) seafloor-reflected wave. The vertical lines represent the standard deviation.

Downloaded 08/01/20 to 134.246.166.26. Redistribution subject to SEG license or copyright; see Terms of Use at https://library.seg.org/page/policies/terms
DOI:10.1190/geo2019-0686.1

The first stage consists of moving the receivers from their acquisition positions to the selected datum by summing the input traces P to intermediate traces p as follows:

$$p_j = \sum_{i=-M}^{M} A_{ij} \frac{\partial^{1/2}}{\partial t^{1/2}} P_i(t - \tau_{ij}), \tag{6}$$

where τ_{ij} is the traveltime between the acquisition receiver location i and the datumed receiver location j and M defines the limit of the contributing receivers located on either side of the datumed receiver. Note that M is to be determined based on the maximum geologic dip present and the maximum elevation change between the acquisition geometry and the final datum. In equation 6, A_{ij} is an amplitude correction term based on spherical divergence and obliquity:

$$A_{ij} = \frac{\Delta x}{2\pi r_{ij} v} \cos(\theta_{ij}), \tag{7}$$

where v is the datuming velocity, Δx represents the spatial sampling interval, and θ_{ij} is the angle between the normal to the input surface and the raypath path r_{ij} connecting the acquisition receiver i location and the datumed receiver j location (Bevc, 1995).

In the second stage of the algorithm, the sources are moved from their acquisition positions to the datum by summing the intermediate traces p to the final datumed traces P':

$$P'_k = \sum_{j=-N}^{N} A_{jk} \frac{\partial^{1/2}}{\partial t^{1/2}} p_j(t - \tau_{jk}), \tag{8}$$

where N defines the limits of the contributing traces, based on the positions of the sources located on either side of the datumed source, A_{jk} is defined according to equation 7 and the r_{jk} factor defines the distance between the acquisition and datumed source locations, and θ_{jk} is the corresponding angle.

An important aspect raised by Berryhill (1979, 1984, 1986) is the need of a split-spread acquisition geometry (with receivers on both sides of the source) to equally treat the layers dipping in either direction. Split-spread geometries are the standard in land acquisitions but not in marine surveys. Berryhill advises making use of the reciprocity between sources and receivers to circumvent this issue. Reciprocity states that, for a given seismic trace, interchanging the positions of the source and the receiver will result in an identical signal, assuming that the source and receiver have no directivity (Clærbout, 1976). Berryhill (1984) assumes that the streamer and the source share a common datum; thus, reciprocity can be used to design an artificial split-spread geometry.

In the case of a SYSIF acquisition, the depth of the tow fish is constantly adjusted according to the bathymetry to maintain a constant altitude. As a result, the source depth varies and the receiver offset fluctuates along the seismic line. They do not share a common datum; thus, reciprocity cannot be used to create a split-spread configuration. Therefore, the WED procedure has to be altered for deep-towed acquisition geometry.

Adaptation of WED to deep-towed data

The adaptation of the WED algorithm to deep-towed data aims at correcting the vertical variations of the source's positions and the vertical and horizontal variations of the receivers' positions relative to the source. These variations are caused by the deformations of the streamer following the motion of the tow fish. The inability to use reciprocity to form a split-spread configuration prevents the straightforward application of the WED procedure to SYSIF data. Nonetheless, our implementation of the datuming follows the same main steps:

1) Definition of the reference datum and of the datumed system geometry.
2) Moving the receivers to the reference datum — equation 6 is applied to the input data sorted in the common-shot-gather (CSG) domain.
3) Moving the shot positions to the reference datum — equation 8 is applied to the intermediate data sorted in the common receiver gather (CRG) domain.
4) Time-variant muting, to avoid angle extrapolations caused by the datuming, is applied on the data sorted in the CMP domain.

We now review these four steps.

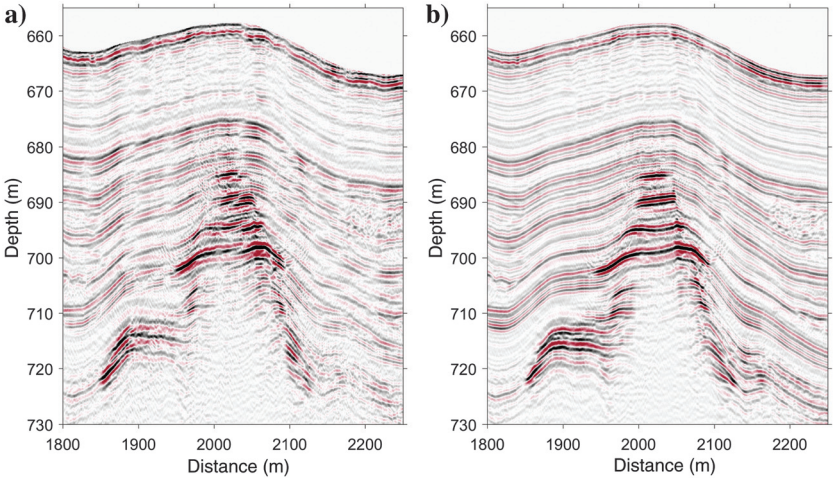

Figure 6. PL03PR06α: profiles processed with a PSDM using a constant velocity model. (a) Data processed using the MEMS geometry. (b) Data processed using the inverted geometry (vertical exaggeration: 7.3).

Step 1: Defining the datumed geometry

The reference datum is chosen higher (upward continuation) than the shallowest receiver or source position of the profile to avoid the datum crossing any velocity interface (i.e., the seafloor). We subtract 5.0 m from the shallowest position to ensure that there is no null, or close to zero, denominator in the amplitude correction factor (equation 7). Because the acquisition positions and the common datum are located above the seafloor, the seawater velocity is used to convert the distances to times.

The angle content of seismic data is defined by the maximum emergence angle for a given depth. The angle content drives the accuracy for later velocity analysis and therefore needs to be preserved during the datuming procedure. The depth and dip of the reflector, the length of the streamer

Downloaded 08/01/20 to 134.246.166.26. Redistribution subject to SEG license or copyright; see Terms of Use at https://library.seg.org/page/policies/terms
DOI:10.1190/geo2019-0686.1

and the velocity field, define the maximum emergence angle of a raypath. The largest angle recorded by the system for a shot is marked as θ_{max} in Figure 7a, which corresponds to the reflection on the seafloor measured at the last receiver.

The WED algorithm moves the acquisition system to a reference datum that is higher, hence, further away from the target. To compensate for this higher altitude and to preserve the angle content of the data, the length of the datumed streamer is increased (Figure 7a). We calculate, for each shot, the vertical shift Δz_{52} between the last (52nd) receiver's acquisition position and the datum. The prolongation of the ray defined by θ_{max} to the reference datum indicates the position of the last datumed receiver. This position can be calculated as

$$x'_{max} = x_{52} + \Delta z_{52} \tan(\theta_{max}), \quad (9)$$

where x'_{max} is the offset of the last datumed receiver and x_{52} is the horizontal offset of the last receiver.

We selected a datumed receiver spacing of 1 m, half that of the acquisition spacing because it interpolates the data in the angle domain. The longitudinal offset between the source and the first receiver causes a blind spot in the data in the angle domain. This blind spot is reproduced in the datumed data by offsetting the position of the first virtual receiver (Figure 7a). With the first and last receiver offsets known and the receiver spacing defined, the number of virtual receivers n'_r is calculated.

Step 2: Moving the receivers

The second step of the procedure consists of relocating the receivers from their acquisition positions to the reference datum. The data are sorted in the CSG domain, and each CSG is processed individually. The summation described by equation 6 is carried out for each virtual receiver on the reference datum. The contributing input traces are selected depending on the position of the receivers. Initially, the traces are summed between two boundaries $-M$ and M (equation 6), yet we cannot use these same boundaries in a deep-towed configuration because of the end-on spread geometry. Instead, we integrate the input traces between a trace 0 and a trace limit M. The trace 0 is associated to the input receiver located directly below the datumed receiver j ($\theta_{ij} = 0^\circ$ in equation 7, marked as "receiver 0" in Figure 7b). The upper bound of summation M corresponds to the trace associated to the input receiver that defines a maximum angle of θ_{max} (Figure 7a) between the input receiver location and the datumed receiver location, counted positive toward the source (marked as "receiver M" in Figure 7b). Hence, for a virtual receiver on the reference datum, the contributing input traces are selected if the corresponding receivers lay in a cone defined by a vertical axis and the angle θ_{max}. The traces are time corrected by the traveltimes τ_{ij} between the acquisition and datumed receiver positions (Figure 7b and equation 6). The input traces are corrected in amplitude by the factor A_{ij} described by Bevc (1995) in equation 7. Finally, the selected traces are summed to form the intermediate trace p_j.

The number of datumed receivers is increased from the native 52 to a number dependent on the vertical shift. The sources remain located at their acquisition positions.

Step 3: Moving the sources

In this third step, we move the sources from their acquisition locations to the reference datum. To that purpose, we need to reorganize the intermediate traces from the CSG domain into the CRG domain. To sort the data as CRGs, we divide the seismic profile in bins; each CRG is composed of the traces where the receiver's location falls into a given bin. The bins are 1 m wide to ensure that the CRGs contain a large enough number of traces.

By taking advantage of reciprocity to virtually invert the positions of the sources and receivers, we can observe that the geometry of the CRG is similar to that of an acquisition shotpoint as shown in Figure 7c. To preserve the angle content of the data, the length of the streamer (actually composed of shotpoints) is increased according to the CRG's maximum angle of reflection θ'_{max}, in a similar way as in step 2.

The correction of the sources' locations for each CRG is equivalent to the one applied to the receivers. For each datumed source, the contributing traces are selected from the CRG if the acquisition sources' positions lie in the area delimited by the vertical axis (i.e., 0 as lower bound of summation in equation 8) and θ'_{max} (Figure 7d). The first contributing source is marked as "source 0" in Figure 7d, and the last contributing source is marked as "source N." The selected traces are then time corrected by a factor of τ_{jk}, which corresponds to the distance between the acquisition sources' locations and the datumed source's position (Figure 7d). The amplitudes of the traces are corrected by the factor A_{jk} (equation 7). Finally, the corrected traces are summed to form the datumed trace P'.

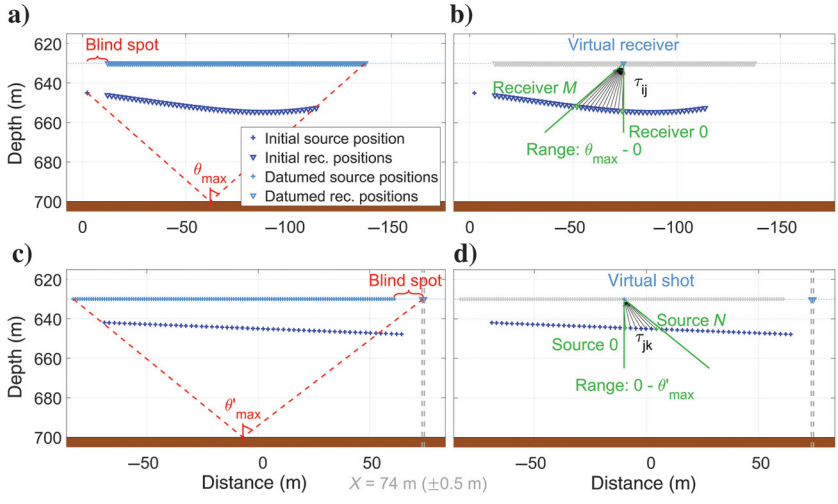

Figure 7. Representation of the first steps of the WED. (a) Definition of the geometry associated with the displacement of the receivers. The largest offset of the datumed receivers is defined by the vertical shift of the last receiver and by the maximum reflection angle θ_{max} on the seafloor. (b) Selection of the traces stacked to move the receivers to the datum. (c) Definition of the geometry associated with the displacement of the sources. The largest offset is defined by the offset of the last source and by the maximum reflection angle θ_{max} on the seafloor. In this example, the traces are gathered as CRGs at the bin X = 74 m (bin width 1 m). (d) Selection of the traces stacked to move the sources to the datum.

Downloaded 08/01/20 to 134.246.166.26. Redistribution subject to SEG license or copyright; see Terms of Use at https://library.seg.org/page/policies/terms
DOI:10.1190/geo2019-0686.1

At the end of this third step, the sources and receivers are now located at their final positions on the reference datum. The data set now consists of single-track data with a wide variety of offsets.

Step 4: Time-variant muting

An important aspect of WED procedure is to preserve the angle range, which means that reflection angles associated to the datumed geometry cannot be higher than the ones acquired by the deep-towed system. Because the maximum offset of the new datum geometry is defined by considering the maximum reflected angle at the seafloor, for deeper reflectors, the datuming procedure may extrapolate data and generate higher reflection angles than the ones actually acquired. To prevent any data extrapolation, a time-variant mute has to be applied to remove any samples of the seismic traces for which the associated datumed reflection angles exceed the maximum acquired reflection angles $\theta_{\max}(t)$. Before applying the time-variant mute, the data are first sorted into the CMP domain. For a given CMP, T defines the time beyond which a trace k is being muted:

$$\text{for } t > T, P'_k(t) = 0,$$
$$\text{where } T = \frac{x_r'^k}{V \sin[\theta_{\max}(t)]}. \tag{10}$$

Note that P'_k is the datumed trace k and $x_r'^k$ is the datumed trace k receiver offset. The term $\theta_{\max}(t)$ is evaluated from the acquisition source and receiver positions considering a homogeneous medium with a constant velocity V and a lithology parallel to the seafloor. The constant velocity V is set equal to the seawater velocity c because the depth-velocity profile is unknown at this stage of data processing. Although the different lithologic layers constituting the subsurface may refract the wavefield depending on their respective velocities and geometries, we consider our computation of $\theta_{\max}(t)$ accurate enough to perform the time-variant mute. The reflection angles are calculated by marching a 1 m window repeatedly from the seafloor down to the maximum imaged depth. A muted CMP is depicted in Figure 8. A comparison between two common-offset sections, before and after datuming, is presented in the Supplementary Material (supplementary information can be accessed through the following link: S1).

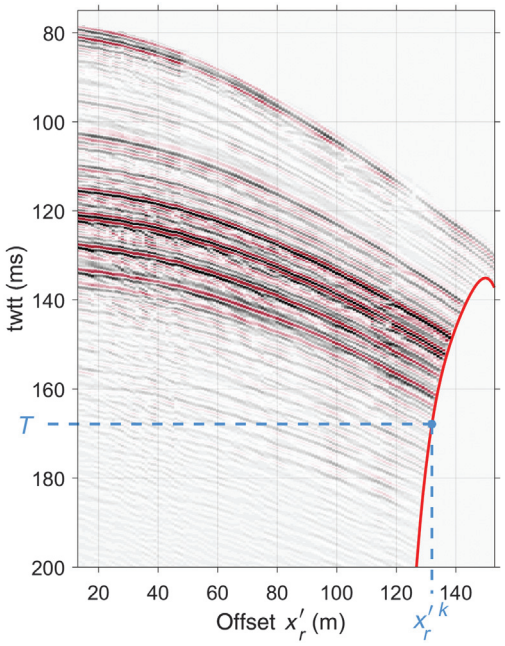

Figure 8. Datumed, muted traces sorted in the CMP domain. The traces are muted when the associated datumed reflection angles are greater than the acquired $\theta_{\max}(t)$, delimited by the red line. The muting time T is calculated according to the offset $x_r'^k$ (equation 10).

VHR VELOCITY ANALYSIS

The datuming of the deep-towed seismic data allows the sorting of traces into CMP gathers and performing of the velocity analysis using a standard NMO method. We first illustrate some results obtained from the deep-towed data acquired at the altitude of 50 m during the GHASS cruise. Nevertheless, during the cruise most acquisitions were performed at an altitude of 100 m above the seafloor for safety considerations. In that configuration, the angular content of the data is narrower, thus limiting the precision of the velocity analysis. Therefore, we investigate the impact of the altitude of the system on velocity determination. Finally, we use the velocity field to perform a PSDM revealing very fine details of the shallow gas system.

Semblance analysis

We perform the velocity analysis every 10 m by forming 5 m wide supergathers. The velocity analysis is performed by computing the semblance spectrum (Al-Chalabi, 1979). Computations are performed with a temporal step of 1 ms, and a velocity step of 1 m/s. The NMO velocity profile associated to a supergather is determined by picking the maximum semblance values. To ensure the lateral continuity of the picking from consecutive semblance panels, the semblance maxima are picked following notable reflectors where possible. Then, the NMO velocity is assimilated to the root-mean-square (rms) velocity (V_{rms}) and the interval velocity is computed using the Dix formula (Dix, 1955). The interval velocity uncertainties are estimated using the method developed by Hajnal and Sereda (1981), where the uncertainty is a function of V_{rms} and T_{rms}. The uncertainty on V_{rms} is given by taking the velocity interval corresponding to 98% of the picked semblance maximum (Dewangan and Ramprasad, 2007). The time uncertainty on the picking is set constant at 0.45 ms, which corresponds to the temporal resolution of the system obtained after array shape reconstruction.

The velocity analysis performed on the deep-towed data after datuming is illustrated on Figure 9a, where a semblance spectrum computed from CMP $X = 2023$ m is presented. The corresponding interval velocity profile converted in depth by calculating the zero-offset depth related to the picked times (Figure 9c). The interval velocity uncertainties increase with depth, which is related to the decrease of the angle range. The velocity estimation on the seafloor is in agreement with the seawater velocity measured using the xCTD probes, which validates the consistency of the applied workflow. The interval velocity distribution (Figure 9b) displays an anticline structure characterized by a drop in the P-wave velocity from 1450 m/s to approximately 1000 m/s associated with gas-charged layers.

Downloaded 08/01/20 to 134.246.166.26. Redistribution subject to SEG license or copyright; see Terms of Use at https://library.seg.org/page/policies/terms
DOI:10.1190/geo2019-0686.1

Impact of the acquisition altitude

Most profiles acquired during the GHASS cruise were obtained by setting the altitude of SYSIF's tow fish to 100 m to ensure the safety of the equipment. To assess the impact of the altitude on interval velocity estimations, a line was acquired twice with two different altitudes: profiles PL03PR06 (previously presented) and PL01PR11 obtained at altitudes of 50 and 100 m, respectively.

We apply the complete workflow that has been previously detailed for profile PL03PR06 (i.e., datuming and semblance analysis) to profile PL01PR11. Because acquiring data with a deep-towed system remains a challenging positioning task, both profiles do not share the exact same location with a maximum difference in lateral positioning of 48 m between the two profiles. The results are presented in Figure 10. If the semblance is less resolved with larger maxima (Figure 10a) due to the limited range of reflection angles, an rms velocity decrease is observed in relation to the presence of free gas. Interval velocities are similar to those obtained with an altitude of 50 m, but the uncertainty has doubled. Even with larger uncertainty in velocity estimates, deep-towed seismic data acquired at 100 m can be used to assess velocity variation trends in the first 70 m of sediments. In particular, the decrease in velocity related to the presence of free gas within the anticline is unambiguously revealed in both profiles.

Depth imaging of the shallow gas system in great water depth

The western Black Sea has been a long-term site for investigating the role of fluids in submarine landslides. The presence of numerous mounts (average diameter 80 m, average height 15 m), interpreted as inherited morphology resulting from the compressive bulge of a massive landslide has been reported (Riboulot et al., 2017). These mounts were surveyed using high-resolution surface-towed seismic during the GHASS cruise (Ker et al., 2019), but conventional seismic failed to determine their internal structure due to the water depth (650–1000 m) in the area. The deep-towed seismic data presented in this contribution are the result of a targeted seismic survey over these mounts during the GHASS cruise. The interval velocity distribution obtained after the processing of the profile PL03PR06α (Figure 9b) was used to perform a PSDM based on a Kirchhoff method detailed in Marsset et al. (2014, 2018). Figure 11 enables a qualitative comparison between the depth migrated profile processed with a constant velocity (Figure 11a) and one processed with

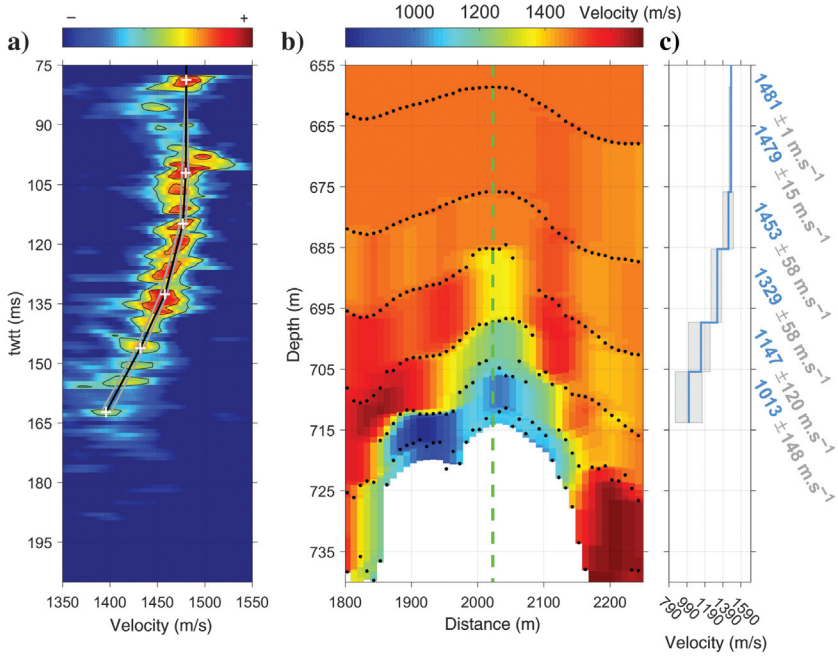

Figure 9. PL03PR06α: (a) semblance panel and picked V_{rms} velocities at the CMP $X = 2023$ m. The gray lines represent a ±2% velocity uncertainty on the semblance picks. (b) Interval velocity distribution where the dots indicate the position of the picked velocities. (c) Interval velocity profile and uncertainties at the CMP $X = 2023$ m (represented by the green dashed line in panel b).

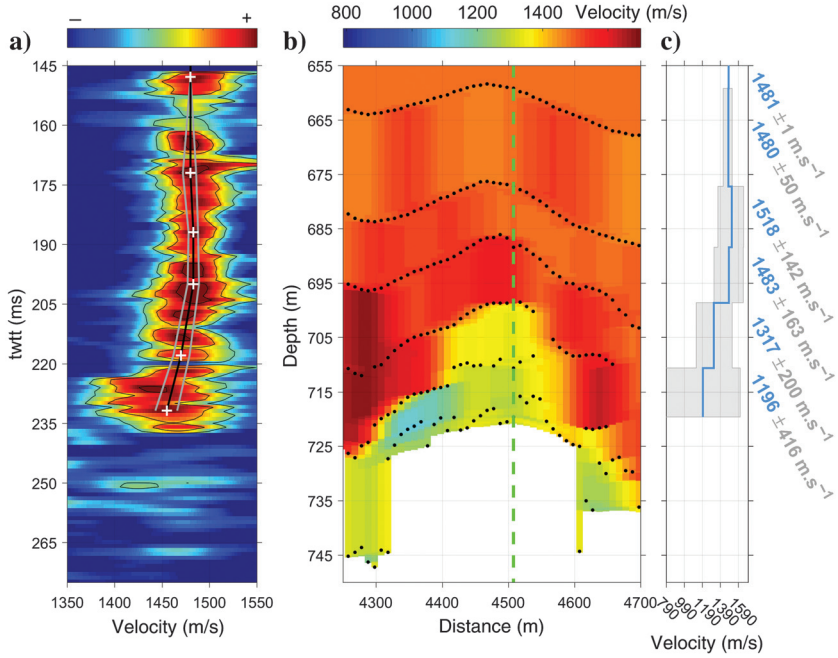

Figure 10. PL01PR11: (a) semblance panel and picked V_{rms} velocities at the CMP $X = 4508$ m. The gray lines represent a ±2% amplitude uncertainty on the semblance picks. (b) Interval velocity distribution where the dots indicate the position of the picked velocities. (c) Interval velocity profile and uncertainties at the CMP $X = 4508$ m (represented by the green dashed line in panel b).

Downloaded 08/01/20 to 134.246.166.26. Redistribution subject to SEG license or copyright; see Terms of Use at https://library.seg.org/page/policies/terms
DOI:10.1190/geo2019-0686.1

Figure 11. (a) Subprofile PL03PR06α, PSDM results. Using a constant seawater velocity model. (c) The same profile migrated using the variable velocity model presented in Figure 9b (vertical exaggeration: 10.0). (b and d) The same CMP located at the center of the anticline structure, marked by the green line, migrated at constant velocity and with the velocity model (respectively).

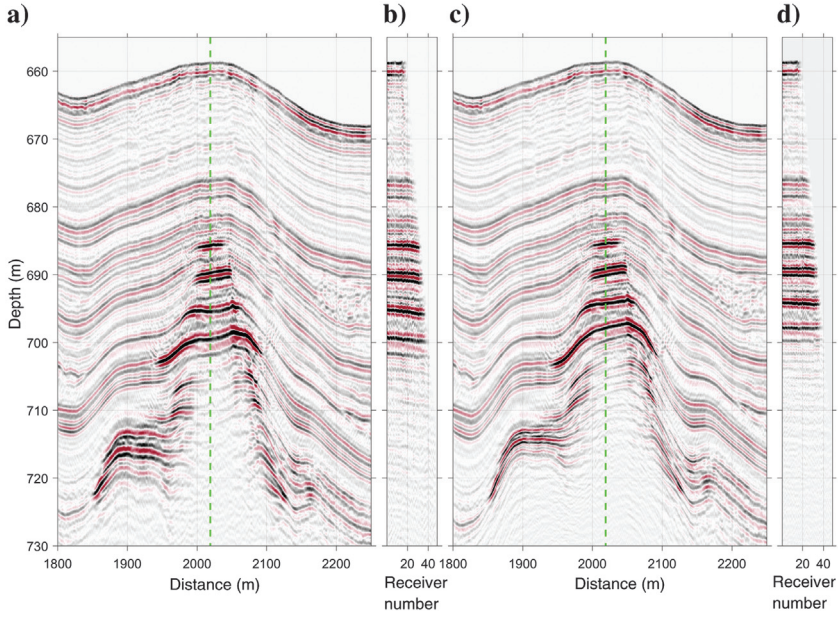

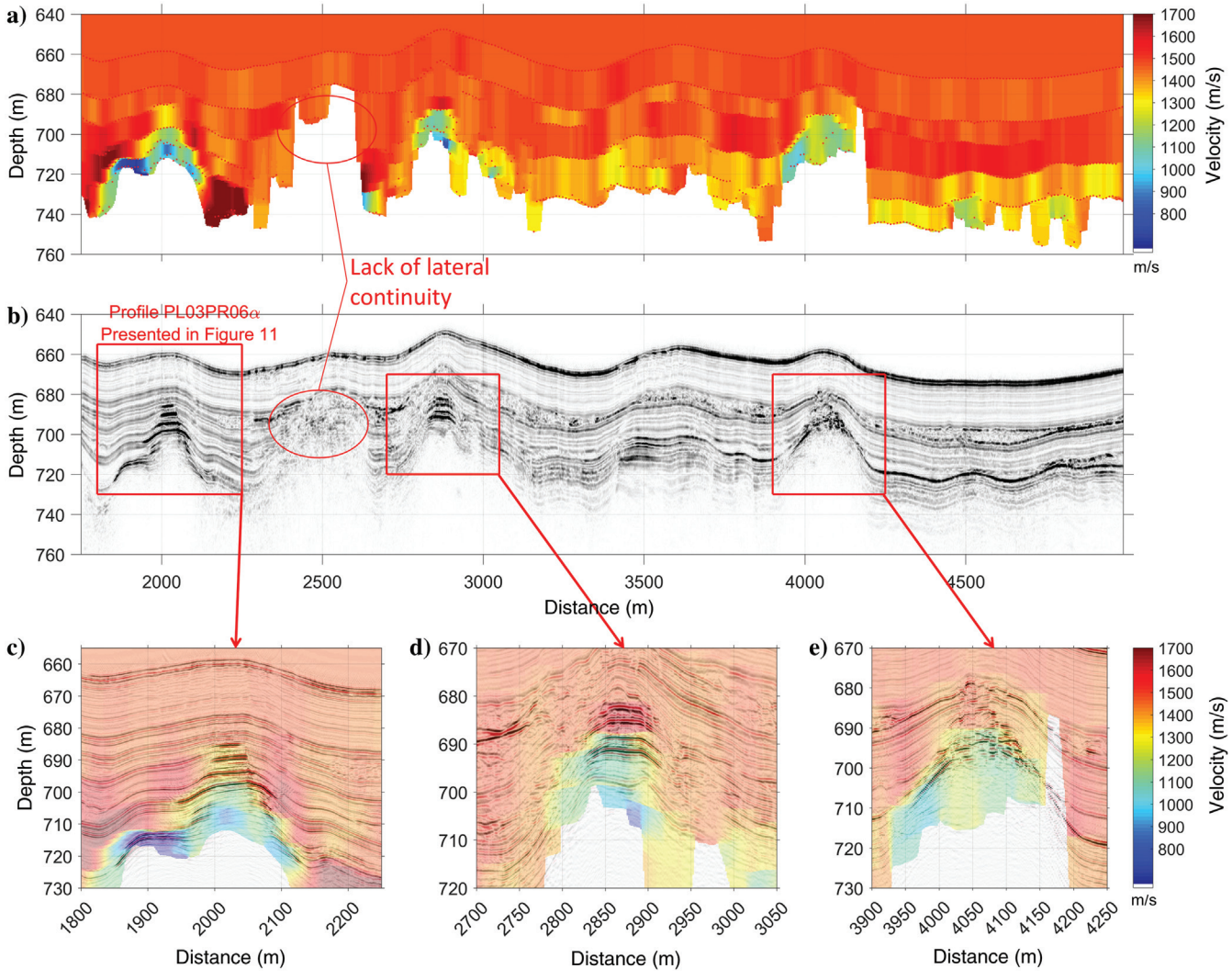

Figure 12. Profile PL03PR06β. (a) The interval velocity structures. (b) The seismic profile migrated using the velocity model presented in panel (a) (vertical exaggeration: 6.25). (c, d, and e) Low-acoustic-velocity areas corresponding to three anticline structures filled with free gas.

Downloaded 08/01/20 to 134.246.166.26. Redistribution subject to SEG license or copyright; see Terms of Use at https://library.seg.org/page/policies/terms
DOI:10.1190/geo2019-0686.1

the interval velocity distribution (Figure 11c). The CIG located at the center of the anticline structure is also presented in Figure 11b and 11d. The accuracy of the interval velocity estimates is demonstrated by the flatness of seismic reflections in CIG (Figure 11d) compared to the constant velocity case (Figure 11b). The resolution of the push-down associated with the presence of free gas illustrates the validity of the velocity model (the push-down is an artifact caused by a local low-velocity zone). The maximum vertical shift is 1.6 m, which corrects the positions of the reflectors in depth. This accuracy in the velocity model is due to the improved description of the streamer shape, followed by WED. Consequently, this workflow proves to be a powerful processing tool allowing the application of conventional algorithms to unconventional seismic data. The processing sequence, including NMO and PSDM, can be routinely applied to large data sets as illustrated in Figure 12. The velocity analysis performed on profile PL03PR06β shows three low-acoustic-velocity areas allowing the identification of three anticline structures filled with gas (Figure 12c–12e).

CONCLUSION

We have demonstrated the performance of the deep-towed multichannel seismic system SYSIF in terms of imaging capability and velocity characterization. The presented workflow allows the investigation of small-scale structures at great water depths. The processing of deep-towed data requires careful reconstruction of the variable streamer shape to make up for the deformations of the deep-towed streamer along the seismic profile. The inversion of the local pitch angles of the streamer based on traveltimes (direct and seafloor-reflected) improves the effective resolutions to 1.62 (horizontal) and 0.65 m (vertical), or 92% of that of the theoretical resolutions (1.5 m horizontal and 0.6 m vertical). Precise knowledge of the receiver locations enables datuming the data set to take advantage of conventional seismic processing algorithms. For extended deep-towed surveys over gently dipping geologic structures, NMO analysis after datuming provides small-scale velocity models at great water depths. We performed a velocity analysis and depth imaging of the profile PL03PR06β. Three anticline structures, corresponding to the mounts from the western Black Sea, were well identified; all were associated with low velocity (850–1100 m/s) and high amplitude reflectors. The velocity analysis allowed us to identify velocity changes within structures less than 10 m thick and less than 50 m wide. The joint interpretation of the velocity distribution and depth image highlighted that free gas has migrated from a deeper source and has been trapped in anticline structures preventing it from reaching the seafloor. Fine-scale push-down effects (< 2 m) within these anticline structures were successfully resolved when performing velocity analysis and depth imaging at 650 m of water depth. The accuracy in the final velocity distribution is, by definition, related to the angle content of the seismic data. Therefore, the quality of the acquired seismic data is a trade-off between safety considerations and the optimal acquisition altitude. The presented algorithms applied to the GHASS deep-towed data proved a mean of taking full advantage of the deep-towed multichannel seismic technology that brings a unique insight to the characterization of geohazards taking place at great water depths.

ACKNOWLEDGMENTS

The support by officers and crew during the GHASS cruise on board *R/V Pourquoi Pas?* (2015) is greatly appreciated as is the dedication of the Genavir and Ifremer technical staff during the cruise. We thank M. Noble and an anonymous reviewer for their comments that helped us to improve this paper. We thank Y. Thomas and S. Murphy for the insightful discussions.

DATA AND MATERIALS AVAILABILITY

Data associated with this research are available and can be obtained by contacting the corresponding author.

REFERENCES

Al-Chalabi, M., 1979, Velocity determination from seismic reflection data, *in* Developments in geophysical exploration methods — 1, Applied Science Publishers Ed.: Springer, 1–68.

Badhani, S., A. Cattaneo, S. Collico, R. Urgeles, B. Dennielou, E. Leroux, F. Colin, S. Garziglia, M. Rabineau, and L. Droz, 2020a, Integrated geophysical, sedimentological and geotechnical investigation of submarine landslides in the Gulf of Lions (Western Mediterranean): Geological Society, London, Special Publications, SP500–2019–175.

Badhani, S., A. Cattaneo, B. Dennielou, E. Leroux, F. Colin, Y. Thomas, G. Jouet, M. Rabineau, and L. Droz, 2020b, Morphology of retrogressive failures in the Eastern Rhone interfluve during the last glacial maximum (Gulf of Lions, Western Mediterranean): Geomorphology, **351**, 106894, doi: 10.1016/j.geomorph.2019.106894.

Barison, E., G. Brancatelli, R. Nicolich, F. Accaino, M. Giustiniani, and U. Tinivella, 2011, Wave equation datuming applied to marine OBS data and to land high resolution seismic profiling: Journal of Applied Geophysics, **73**, 267–277, doi: 10.1016/j.jappgeo.2011.01.009.

Berryhill, J. R., 1979, Wave-equation datuming: Geophysics, **44**, 1329–1344, doi: 10.1190/1.1441010.

Berryhill, J. R., 1984, Wave-equation datuming before stack: Geophysics, **49**, 2064–2066, doi: 10.1190/1.1441620.

Berryhill, J. R., 1986, Submarine canyons: Velocity replacement by wave-equation datuming before stack: Geophysics, **51**, 1572–1579, doi: 10.1190/1.1442207.

Bevc, D., 1995, Imaging under rugged topography and complex velocity structure: Ph.D. thesis, Stanford University.

Bevc, D., 1996, Flooding the topography: Wave-equation datuming of land data with rugged acquisition topography: Geophysics, **62**, 1558–1569, doi: 10.1190/1.1444258.

Byrd, R. H., R. B. Schnabel, and G. A. Shultz, 1988, Approximate solution of the trust region problem by minimization over two-dimensional subspaces: Mathematical Programming, **40**, 247–263, doi: 10.1007/BF01580735.

Chapman, N. R., J. F. Gettrust, R. Walia, D. Hannay, G. D. Spence, W. T. Wood, and R. D. Hyndman, 2002, High-resolution, deep-towed, multichannel seismic survey of deep-sea gas hydrates off western Canada: Geophysics, **67**, 1038–1047, doi: 10.1190/1.1500364.

Clare, M. A., M. E. Vardy, M. J. B. Cartigny, P. J. Talling, M. D. Himsworth, J. K. Dix, J. M. Harris, R. J. S. Whitehouse, and M. Belal, 2017, Direct monitoring of active geohazards: Emerging geophysical tools for deep-water assessments: Near Surface Geophysics, **15**, 427–444, doi: 10.3997/1873-0604.2017033.

Clærbout, J. F., 1976, Fundamentals of geophysical data processing: With applications to petroleum prospecting: Blackwell Scientific Publications.

de Prunelé, A., L. Ruffine, V. Riboulot, C. A. Peters, C. Croguennec, V. Guyader, T. Pape, C. Bollinger, G. Bayon, J.-C. Caprais, Y. Germain, J.-P. Donval, T. Marsset, G. Bohrmann, L. Géli, A. Rabiu, M. Lescanne, E. Cauquil, and N. Sultan, 2017, Focused hydrocarbon-migration in shallow sediments of a pockmark cluster in the Niger Delta (Off Nigeria): Geochemistry, Geophysics, Geosystems, **18**, 93–112, doi: 10.1002/2016GC006554.

de Souza, J. L., 2014, A method to estimate spatial resolution in 2-D seismic surface wave tomographic problems: International Journal of Geosciences, **5**, 757–770, doi: 10.4236/ijg.2014.58068.

Dewangan, P., and T. Ramprasad, 2007, Velocity and AVO analysis for the investigation of gas hydrate along a profile in the western continental margin of India: Marine Geophysical Researches, **28**, 201–211, doi: 10.1007/s11001-007-9027-4.

Dix, C. H., 1955, Seismic velocities from surface measurements: Geophysics, **20**, 68–86, doi: 10.1190/1.1438126.

Duarte, H., N. Wardell, and O. Monrigal, 2017, Advanced processing for UHR3D shallow marine seismic surveys: Near Surface Geophysics, **15**, 347–358, doi: 10.3997/1873-0604.2017022.

Gettrust, J. F., M. Grimm, S. Madosik, and M. Rowe, 1988, Results of a deep-tow multichannel survey on the Bermuda Rise: Geophysical Research Letters, **15**, 1413–1416, doi: 10.1029/GL015i012p01413.

Hajnal, Z., and I. T. Sereda, 1981, Maximum uncertainty of interval velocity estimates: Geophysics, **46**, 1543–1547, doi: 10.1190/1.1441160.

He, T., G. D. Spence, W. T. Wood, M. Riedel, and R. D. Hyndman, 2009, Imaging a hydrate-related cold vent offshore Vancouver Island from deep-towed multichannel seismic data: Geophysics, **74**, no. 2, B23–B36, doi: 10.1190/1.3072620.

Kallweit, R., and L. C. Wood, 1982, The limits of resolution of zero-phase wavelets: Geophysics, **47**, 1035–1046, doi: 10.1190/1.1441367.

Ker, S., Y. Le Gonidec, D. Gibert, and B. Marsset, 2011, Multiscale seismic attributes: A wavelet-based method and its application to high-resolution seismic and ground truth data: Multiscale seismic attributes: Geophysical Journal International, **187**, 1038–1054, doi: 10.1111/j.1365-246X.2011.05207.x.

Ker, S., B. Marsset, S. Garziglia, Y. Le Godinec, D. Gibert, M. Voisset, and J. Adamy, 2010, High-resolution seismic imaging in deep sea from a joint deep-towed/OBH reflection experiment: Application to a Mass Transport Complex offshore Nigeria: Geophysical Journal International, **182**, 1524–1542, doi: 10.1111/j.1365-246X.2010.04700.x.

Ker, S., and V. Riboulot, 2015, GHASS cruise, R/V Pourquoi Pas ? https://doi.org/10.17600/15000500.

Ker, S., Y. Thomas, V. Riboulot, N. Sultan, C. Bernard, C. Scalabrin, G. Ion, and B. Marsset, 2019, Anomalously deep BSR related to a transient state of the gas hydrate system in the western Black Sea: Geochemistry, Geophysics, Geosystems, **20**, 442–459, doi: 10.1029/2018GC007861.

Korotaev, G., T. Oguz, and S. Riser, 2006, Intermediate and deep currents of the Black Sea obtained from autonomous profiling floats: Deep Sea Research Part 2: Topical Studies in Oceanography, **53**, 1901–1910, doi: 10.1016/j.dsr2.2006.04.017.

Kvalstad, T., 2007, What is the current "best practice" in offshore Geohazard investigations? A state-of-the-art review: Presented at the Offshore Technology Conference, Offshore Technology Conference.

Le Gall, Y., and B. Marsset, 2007, Développements électroacoustiques en sismique marine Très Haute Résolution: Acoustique et Techniques, 17–22.

Markova, N., , Marine Hydrophysical Institute, Russian Academy of Sciences, Bagaev, A., and , Marine Hydrophysical Institute, Russian Academy of Sciences, 2016, The black sea deep current velocities estimated from the data of argo profiling floats: Physical Oceanography.

Marsset, B., S. Ker, Y. Thomas, and F. Colin, 2018, Deep-towed high-resolution seismic imaging 2: Determination of P-wave velocity distribution: Deep-Sea Research Part 1, **132**, 29–36, doi: 10.1016/j.dsr.2017.12.005.

Marsset, B., E. Menut, S. Ker, Y. Thomas, J.-P. Regnault, P. Leon, H. Martinossi, L. Artzner, D. Chenot, S. Dentrecolas, B. Spychalski, G. Mellier, and N. Sultan, 2014, Deep-towed high-resolution multichannel seismic imaging: Deep Sea Research 1, **93**, 83–90, doi: 10.1016/j.dsr.2014.07.013.

Podvin, P., and I. Lecomte, 1990, Finite difference computation of traveltimes in very contrasted velocity models: A massively parallel approach and its associated tools: Geophysical Journal International, **418**, 271–284, doi: 10.1111/j.1365-246X.1991.tb03461.x.

Reiche, S., B. Berkels, and B. Weiß, 2020, Automated static and moveout corrections of high-resolution seismic data from the Baltic Sea: Near Surface Geophysics, **18**, 23–37, doi: 10.1002/nsg.12068.

Riboulot, V., A. Cattaneo, C. Scalabrin, A. Gaillot, G. Jouet, G. Ballas, T. Marsset, S. Garziglia, and S. Ker, 2017, Control of the geomorphology and gas hydrate extent on widespread gas emissions offshore Romania: Bulletin de la Société géologique de France, **188**, 26, doi: 10.1051/bsgf/2017182.

Rowe, M. M., and J. F. Gettrust, 1993, Fine structure of methane hydrate-bearing sediments on the Blake Outer Ridge as determined from deep-tow multichannel seismic data: Journal of Geophysical Research: Solid Earth, **98**, 463–473, doi: 10.1029/92JB01706.

Sultan, N., B. Marsset, S. Ker, T. Marsset, M. Voisset, A. M. Vernant, G. Bayon, E. Cauquil, J. Adamy, J. L. Colliat, and D. Drapeau, 2010, Hydrate dissolution as a potential mechanism for pockmark formation in the Niger delta: Journal of Geophysical Research, **115**, 1–33, doi: 10.1029/2010JB007453.

Sultan, N., V. Riboulot, S. Ker, B. Marsset, L. Géli, J. B. Tary, F. Klingelhoefer, M. Voisset, V. Lanfumey, J. L. Colliat, J. Adamy, and S. Grimaud, 2011, Dynamics of fault-fluid-hydrate system around a shale-cored anticline in deepwater Nigeria: Journal of Geophysical Research, **116**, B12110, doi: 10.1029/2011JB008218.

Tóth, Z., V. Spiess, J. M. Mogollón, and J. B. Jensen, 2014, Estimating the free gas content in Baltic Sea sediments using compressional wave velocity from marine seismic data: Journal of Geophysical Research, Solid Earth, **119**, 8577–8593, doi: 10.1002/2014JB010989.

Vanneste, M., N. Sultan, S. Garziglia, C. F. Forsberg, and J.-S. L'Heureux, 2014, Seafloor instabilities and sediment deformation processes: The need for integrated, multi-disciplinary investigations: Marine Geology, **352**, 183–214, doi: 10.1016/j.margeo.2014.01.005.

Walia, R., and D. Hannay, 1999, Source and receiver geometry corrections for deep towed multichannel seismic data: Geophysical Research Letters, **26**, 1993–1996, doi: 10.1029/1999GL900402.

Ward, P., E. Asakawa, and S. Shimizu, 2004, High resolution, deep-tow seismic survey to investigate the methane hydrate stability zone in the Nankai Trough: Resource Geology, **54**, 115–124, doi: 10.1111/j.1751-3928.2004.tb00193.x.

Wood, W. T., J. F. Gettrust, N. R. Chapman, G. D. Spence, and R. D. Hyndman, 2002, Decreased stability of methane hydrates in marine sediments owing to phase-boundary roughness: Nature, **420**, 656–660, doi: 10.1038/nature01263.

Downloaded 08/01/20 to 134.246.166.26. Redistribution subject to SEG license or copyright; see Terms of Use at https://library.seg.org/page/policies/terms
DOI:10.1190/geo2019-0686.1